



The
University
Of
Sheffield.

Advanced Finite Element Strategies for Machining of Long Fibre Reinforced Polymer Composites

Fernando Cepero-Mejías

A thesis submitted in partial fulfilment of the requirements for the
degree of
Doctor of Philosophy

Supervised by
Dr. Jose Luis Curiel-Sosa and Dr. Kevin Kerrigan

The University of Sheffield
Department of Mechanical Engineering

25th November 2021

Declaration

I, the author, confirm that the Thesis is my own work. I am aware of the University's Guidance on the Use of Unfair Means (www.sheffield.ac.uk/ssid/unfair-means). This work has not been previously been presented for an award at this, or any other, university.

This work was supervised by Dr. Jose Luis Curiel-Sosa from the University of Sheffield as well as Dr. Vaibhav Phadnis and Dr. Kevin Kerrigan from the Advance Manufacturing Research Centre (AMRC) of Sheffield from September of 2016 to April of 2021.

List of publications

My PhD has been quite prolific for publishing papers. Among them, publications can be found in two of the top-5 leading journals in composite materials, such as two papers in Composite Structures (I.F = 5.407) and one paper in Composite Science and Technology (I.F = 8.528). Also, I have published another paper in an Open Access journal that is new "Composite Part C: Open Access". Three additional journal papers are expected to be published soon; two are under revision, and one in the writing process.

Three conference papers have been published in the journal "Procedia CIRP", which is the journal that collects the most relevant conference works in machining. Additionally, other four conference papers have been published in national and international conferences involving the research of composite materials and advanced materials fracture. Finally, I have presented six posters throughout my professional career in relevant conferences of materials fracture, machining and computational research. These contributions are listed below. Note that, most publications without doi link can be found in **Appendix A**.

Journal papers

1. F. Cepero-Mejías, V. A. Phadnis, K. Kerrigan, and J. L. Curiel-Sosa, "A finite element assessment of chip formation mechanisms in the machining of CFRP laminates with different fibre orientations," *Compos. Struct.*, vol. 268, no. April, 2021.
[doi:10.1016/j.compstruct.2021.113966](https://doi.org/10.1016/j.compstruct.2021.113966).
2. F. Cepero-Mejías, N. Duboust, V. A. Phadnis, K. Kerrigan, and J. L. Curiel-Sosa, "A novel finite element method approach in the modelling of edge trimming of CFRP laminates," *Appl. Sci.*, vol. 11, no. 11, 2021.
[doi:10.3390/app11114743](https://doi.org/10.3390/app11114743).
3. S. Karmakov, F. Cepero-Mejías, and J. L. Curiel-Sosa, "Numerical analysis of the delamination in CFRP laminates: VCCT and XFEM assessment," *Compos. Part C Open Access*, vol. 2, p. 100014, Oct. 2020.
[doi:10.1016/j.jcomc.2020.100014](https://doi.org/10.1016/j.jcomc.2020.100014).
4. F. Cepero-Mejías, J. L. Curiel-Sosa, A. Blázquez, T. T. Yu, K. Kerrigan, and V. A. Phadnis, "Review of recent developments and induced damage assessment in the modelling of the machining of long fibre reinforced polymer composites," *Compos. Struct.*, vol. 240, no. February, p. 112006, 2020.
[doi:10.1016/j.compstruct.2020.112006](https://doi.org/10.1016/j.compstruct.2020.112006).
5. F. Cepero, I. G. García, J. Justo, V. Mantič, and F. París, "An experimental study of the translaminal fracture toughnesses in composites for different crack growth

directions , parallel and transverse to the fiber direction,” *Compos. Sci. Technol.*, vol. 181, no. February, p. 107679, 2019.
[doi:10.1016/j.compscitech.2019.107679](https://doi.org/10.1016/j.compscitech.2019.107679).

6. F. Cepero-Mejías, J. L. Curiel-sosa, C. Zhang, and V. A. Phadnis, “Effect of cutter geometry on machining induced damage in orthogonal cutting of UD polymer composites: FE study,” *Compos. Struct.*, vol. 214, no. February, pp. 439–450, 2019.
[doi:10.1016/j.compstruct.2019.02.012](https://doi.org/10.1016/j.compstruct.2019.02.012).

Conference papers

1. F. Cepero-Mejías, J. L. Curiel-Sosa, K. Kerrigan, and V. A. Phadnis, “Study of the machining induced damage in UD-CFRP laminates with various fibre orientations: FE assessment,” *Procedia CIRP*, vol. 87, pp. 366–371, 2020.
[doi:10.1016/j.procir.2020.02.028](https://doi.org/10.1016/j.procir.2020.02.028).
2. F. Cepero-Mejías, V. A. Phadnis, and J. L. Curiel-sosa, “Machining induced damage in orthogonal cutting of UD composites: FEA based assessment of Hashin and Puck criteria,” *17th CIRP Conf. Model. Mach. Oper.*, vol. 82, pp. 332–337, 2019.
[doi:10.1016/j.procir.2019.04.241](https://doi.org/10.1016/j.procir.2019.04.241).
3. F. Cepero-Mejías, J. L. Curiel-Sosa, K. Kerrigan, and V. A. Phadnis, “Chip formation in machining of unidirectional carbon fibre reinforced polymer laminates: FEM based assessment,” *Procedia CIRP*, vol. 85, pp. 302–307, 2019.
[doi:10.1016/j.procir.2019.09.005](https://doi.org/10.1016/j.procir.2019.09.005).
4. F. Cepero-Mejías, J. L. Curiel-sosa, and V. A. Phadnis, “Análisis numérico de la formación de la viruta en operaciones de mecanizado de fibra de carbono,” *Congreso del Grupo Español de la Fractura 2019*, 2019, pp. 250–254.
5. F. Cepero-Mejías, I. G. García, J. Justo, V. Mantič, and F. París, “Comparación experimental de la tenacidad a fractura intralaminar en materiales compuestos para crecimiento de grietas en diferentes direcciones en el plano,” *Congreso del Grupo Español de la Fractura 2019*, 2019, pp. 255–260.
6. F. Cepero, I. G. García, J. Justo, V. Mantič, F. París, and A. Barroso, “Comparación experimental de la tenacidad a fractura transversal de laminados unidireccionales correspondientes al crecimiento longitudinal o transversal de grietas,” *Matcomp 15*, vol. Actas del, pp. 1165–1170, 2015.
7. F. Cepero, I. G. García, J. Justo, and V. Mantič, “Experimental comparison between the transverse fracture toughness of a unidirectional laminate corresponding to either longitudinal or transverse crack growth,” *16th Eur. Conf. Compos. Mater. ECCM 2014*, no. June, pp. 22–26, 2014.

Conference posters

1. F. Cepero-Mejías, N. Duboust, V.A. Phadnis, J. L. Curiel-Sosa and K. Kerrigan, “Finite Element Method investigation in the edge trimming of CFRP laminates,” 5th Annual Machining Science Student Conference, 2020.
2. F. Cepero-Mejías, J. L. Curiel-Sosa, K. Kerrigan, and V. A. Phadnis, “Chip formation in machining of UD polymer based composites: FEM based assessment,” 2nd CIRP Conference on Composite Material Parts Manufacturing (CIRP-CCMPM 2019), 2019.
3. F. Cepero, I. G. García, J. Justo, V. Mantič and F. París, “Comparación experimental de la tenacidad a fractura intralaminar en materiales compuestos para crecimiento de grietas en diferentes direcciones en el plano,” Congreso del Grupo Español de la fractura, 2019.
4. F. Cepero-Mejías, J. L. Curiel-Sosa and V. A. Phadnis, “Effect of cutter geometry on machining induced damage in orthogonal cutting of UD polymer composites : FE study,” Tech Fellows, 2018.
5. F. Cepero-Mejías, J. L. Curiel-Sosa and V. A. Phadnis, “Damage model design for composite materials,” Tech Fellows 2017.Tech Fellows, 2017
6. F. Cepero, I. G. García, J. Justo and V. Mantič, “Experimental comparison between the transverse fracture toughness of an unidirectional laminate corresponding to either longitudinal or transverse crack growth,” ECCM16 – 16th European Conference on Composite Materials, 2014.

Note that, various chapters of this thesis are based on the above work published during this PhD. The publications of reference and their corresponding chapters are specified below:

- **Chapter 2: Literature review and damage modelling approaches** is based on the journal article “**Review of recent developments and induced damage assessment in the modelling of the machining of long fibre reinforced polymer composites**”.
- **Chapter 4: Machining induced damage assessment** is based on the journal article “**Effect of cutter geometry on machining induced damage in orthogonal cutting of UD polymer composites: FE study**”.
- **Chapter 5: Chip formation modelling for various fibre orientations** is based on the journal article “**A finite element assessment of chip formation mechanisms in the machining of CFRP laminates with different fibre orientations**”.
- **Chapter 6: Composite machining application: Edge trimming** is based on the journal article “**A novel finite element method approach in the modelling of edge trimming of CFRP laminates**”.

Abstract

This thesis addresses a novel finite element study in machining of long-fibre-reinforced polymers (LFRP). For this sake, the development of sophisticated Fortran VUMAT user-subroutines is performed to insert a new composite damage algorithm in the modelling of composite machining, which accounts for damage propagation and chip fracture. These damage algorithms are based on continuous damage mechanics (CDM) theory linked to fracture computational techniques to simulate damage propagation, while chip fracture is induced using wisely strain-based element deletion criteria.

The modelling of two main topics in composite machining have been investigated during this research: composite cutting basics (machining induced damage and chip formation) and tool wear influence in machining forces.

The influence of cutting tool morphologies and material in the machining induced damage in composite was investigated using a novel method of inserting the spring-back phenomenon in the numerical analysis. Significant conclusions are extracted from this research. For instance, high relief angles reduce the sub-surface damage, or the tool wear incidence is found not to be critical in the studied range.

The following step was the modelling of chip formation mechanisms in composite machining. It was achieved by inserting a strain-based element deletion algorithm in the user-defined finite element (FE) code to allow chip fracture. The numerical assessment of sub-surface damage and chip formation was performed, implementing a strain-based continuum damage mechanics (CDM) approach. The study of five common machining configurations was addressed to model the governing chip fracture mechanism for several fibre orientations. This factor would include substantial improvements in the accuracy of the oncoming works.

Finally, a common composite edge trimming operation is successfully modelled to prove the damage algorithm's versatility. Edge trimming has barely been modelled so far because of its complexity and high computational cost required. It was developed an FE model to predict the tool wear influence on the machining forces' increment. Interesting technical applications could be achieved using this FE model. For instance, it could detect the point where the tool should be replaced by just checking the machining forces saving manufacturing time and optimising its use.

Acknowledgements

First of all, I would like to express my deep gratitude to my academical supervisor **Jose Luis Curiel-Sosa**. I will always be grateful to him for giving me the opportunity of developing my researcher skills in a highly prestigious university like the University of Sheffield is. His extensive experience in modelling composites and his great passion and wise advice in supervising this project has inspired me to improve my research skills.

Moreover, a special mention is deserved to my industrial supervisors **Vaibhav Phadnis and Kevin Kerrigan**. Their generous help to solve technical problems have been vital to the successful development of this project. I would also like to highlight the correct and pleasant treatment that I have received during these years from them; consequently, I now consider them two great friends in addition to two great professionals.

Besides, I would like to acknowledge to Industrial Doctoral Centre (IDC) and Engineering and Physical Sciences Research Council (EPSRC) for their practical financial and technical support in the development of this work (EP/L016257/1).

Thanks to my co-workers in Sheffield for helping me and making the four years of my PhD more enjoyable. I would like to make a special mention for **Marius, Marco, Max, Oscar and Dani** who have helped me achieve all the objectives that my PhD raised with their unwavering help.

I would like to remind my Latino friends who have given me some enjoyable times. I was delighted to have had the opportunity to share many experiences with these people full of vitality and joy. Special mention to my football teammates, I have shared unforgettable moments during these beautiful 4 years full of exciting matches.

Two phenomenal people like **Mauro and Jaime** deserve to be here. Together we spent unforgettable party nights during the first years of my PhD. I am delighted to have met them because I learned a lot from them. Although I have not had the opportunity to meet them in recent years, I still remember them with special affection. For many more special Jaleo nights!

It is impossible not to thank the unconditional support that I have always received from my group of Spanish friends in Sheffield. Thank you very much for all those unforgettable moments that we have lived together, trips, nights out, cafes, exciting days at Carmen's house... Each member of the group is special, and we make this group of friends unique. God save the **Pata Negra**!

I would like to highlight four exceptional members within this group: **Guille, Antonio, Marta and Chus**. They are four of the best people I have met in my life, who have helped me a lot in difficult moments during my PhD. I can never thank them enough for not letting me get discouraged in these difficult times that we live in. Thus, I am very

proud to be part of their lives and more than friends, I consider them my Sheffielder's family.

Of course, I would like to include my girlfriend **Stephanie** in this section. Our deep love makes me feel like the happiest man in the world. Although we have been together for a short time, we have overcome many difficult situations during this lockdown to build this lovely relationship. I can't wait to live thousand of experiences together in the years to come and enjoy our love. I love you my heart!

Besides, I would also like to acknowledge my Spanish friends who contact me almost every day, making me feel comfortable. Finally, I would like to thank my parents (**Fernando and Maria Luisa**) and brother (**Manuel**) for their tireless support and words of encouragement in the most challenging moments of my life. They always encourage me unconditionally to fight to achieve my goals. I feel fortunate to have them in my life. The achievement of this thesis would have been impossible without their support.

Nomenclature

α	Reduction parameter for considering non-linearities and instabilities
Δt	Step time increment
Δt_{sta}	Stable step time increment
δ_{eq}	Equivalent displacement at the composite ply interface
δ_{eq}^0	Equivalent displacement at the composite ply interface when damage initiation takes place
δ_{eq}^f	Equivalent displacement at the composite ply interface when total failure takes place
$\delta_{I,eq}$	Equivalent displacement at the composite ply of a determine damage mode
$\delta_{I,eq}$	Equivalent displacement at the composite ply of a specific damage mode
$\delta_{I,eq}^0$	Equivalent displacement at the composite ply of a determine damage mode when damage initiates
$\delta_{I,eq}^f$	Equivalent displacement at the composite ply of a determine damage mode when total failure takes place
δ_n	Normal displacement at the composite ply interface
δ_s	Shear displacement in the first direction at the composite ply interface
δ_t	Shear displacement in the second direction at the composite ply interface
η	Exponential factor used in Benzeggagh-Kenane criterion
η_m	Damage vector
λ	Angle between the cutting tool edge and the laminate thickness in an oblique cutting machining process
ν_{12}	Poisson's ratio in principal plane (1-2)
ν_{13}	Poisson's ratio in principal plane (1-3)
ν_{23}	Poisson's ratio in principal plane (2-3)
ϕ	Free energy

Ψ^ξ	Incremental damage parameter associated to the damage mode ξ
ρ_e	Element material density
σ	Stress tensor
σ_{eq}^0	Equivalent stress at the composite ply interface when damage initiation takes place
$\sigma_{I,eq}^0$	Equivalent stress at the composite ply of a determine damage mode when damage initiation takes place
σ_{ij}	Stress vector components in the direction “i” and “j” of the main axis
ε	Strain tensor
φ	Crack angle angle parameter
ξ	Damage mode
a_0, a_m, a_n	Exponential values used in the power law criterion
A_{del}	Total delaminated area
A_{ip}	Element characteristic area
A_{nom}	Nominal drill bit area
C	Stiffness matrix
c_e	Element wave speed
C_{ij}	Stiffness matrix
$D(d_{ij})$	Damage tensor
d^ξ	Directional damage vector associated to the damage mode ξ
d_f	Fibre damage
d_{ij}	Damage vector components in the direction “i” and “j” of the main axis
D_{max}	Maximum delaminated diameter
d_m	Matrix damage
D_{nom}	Nominal drill bit diameter
d_s	Shear damage
E_{11}	Fibre Young modulus
E_{22}	Matrix Young modulus in direction 2
E_{33}	Matrix Young modulus in direction 3
E_e	Element courant stiffnes

F_{fc}	Fibre compression failure exposure factor
F_{ft}	Fibre traction failure exposure factor
F_{mc}	Matrix compression failure exposure factor
F_{mma}	Matrix mode A failure exposure factor
F_{mmb}	Matrix mode B failure exposure factor
F_{mmc}	Matrix mode C failure exposure factor
F_{mt}	Matrix traction failure exposure factor
FD	Delamination factor based on the delaminated area
Fd	Delamination factor based on the delaminated diameter
G^ξ	Damage tensor associated to the damage mode ξ
g^ξ	Surface associated to the damage mode ξ
G^C	Critical energy release rate at the composite ply interface
G_{12}	Shear modulus in principal plane (1-2)
G_{13}	Shear modulus in principal plane (1-3)
G_{23}	Shear modulus in principal plane (2-3)
G_{fc}	Fibre compression energy release rate
G_{ft}	Fibre traction critical energy release rate
G_{II}	Instantaneous Mode II energy release rate at the composite ply interface
G_I	Instantaneous Mode I energy release rate at the composite ply interface
G_I^C	Critical energy release rate at the composite ply of a determine damage mode
G_{mc}	Matrix compression energy release rate
G_{mt}	Matrix traction energy release rate
G_n	Normal instantaneous energy release rate at the composite ply interface
G_n^C	Normal critical energy release rate at the composite ply interface
G_s	Shear instantaneous energy release rate in the first shear direction at the composite ply interface
G_s^C	Shear critical energy release rate in the first shear direction at the composite ply interface
G_T	Total instantaneous energy release rate at the composite ply interface

G_t	Normal instantaneous energy release rate in the first shear direction at the composite ply interface
G_t^C	Shear critical energy release rate in the second shear direction at the composite ply interface
K_{nn}	Normal artificial stiffness at the composite ply interface
K_{ss}	Shear artificial stiffness in the first shear direction at the composite ply interface
K_{tt}	Normal artificial stiffness in the first shear direction at the composite ply interface
L_c	Characteristic element size
l_e	Element characteristic length
n	Group of stress or strain domains consider
p	Experimental parameter in the damage propagation model proposed by Curiel-Sosa
$p_{\perp\perp}^-$	Slope of the fracture envelope (normal stress - transverse/transverse shear stress) curve in compression states when normal stress vanishes
$p_{\perp\parallel}^{(+)}$	Slope of the fracture envelope (normal stress - longitudinal/transverse shear stress) curve in traction states when normal stress vanishes
$p_{\perp\parallel}^-$	Slope of the fracture envelope (normal stress - longitudinal/transverse shear stress) curve in compression states when normal stress vanishes
$R_{\perp\perp}^A$	Fracture resistance of the fracture plane due transverse/transverse shear stresses
$R_{\perp\parallel}^A$	Fracture resistance of the fracture plane due longitudinal/transverse shear stresses
$R_{\perp}^{(+)A}$	Fracture resistance of the fracture plane due to transverse stresses
S_{12}	Shear strength in principal plane (1-2)
S_{13}	Shear strength in principal plane (1-3)
S_{23}	Shear strength in principal plane (2-3)
S_{ij}	Compliance matrix
t_n	Normal instantaneous stress value at the interface of the composite plies
t_n^0	Maximum normal instantaneous stress value at the composite ply interface
t_s	Shear instantaneous stress value in the first shear direction at the composite ply interface

t_s^0	Maximum shear instantaneous stress value in the first shear direction at the interface between composite plies with pure shear strain in the first shear direction
t_t	Shear instantaneous stress value in the second shear direction at the composite ply interface
t_t^0	Shear instantaneous stress values in the second shear direction at the interface between composite plies with pure shear strain in the second shear direction
X_C	Fibre compression strength
X_T	Fibre tensile strength
Y_C	Matrix compression strength
Y_T	Matrix tensile strength
Z_C	Matrix compression strength in direction 3
Z_T	Matrix tensile strength in direction 3
2D	Two dimensional
3D	Three dimensional
c	Convergence margin
CDM	Continuum damage mechanics
CFRP	Carbon fibre reinforced polymers
CZM	Cohesive zone model
FE	Finite element
FEM	Finite element method
GFRP	Glass fibre reinforced polymers
I	Internal forces
LEFM	Linear Elastic Fracture Mechanics
LFRP	Long fibre reinforced polymers
P	External forces
PMC	Polymer matrix composite
R	Residual forces
SBCB	Surface-based cohesive behaviour
UD	Unidirectional
VCCT	Virtual Crack Closure Technique
XFEM	eXtended Finite Element Method

Contents

Declaration	i
List of publications	ii
Abstract	v
Acknowledgements	vi
Nomenclature	viii
Contents	xiii
List of Tables	xiv
List of Figures	xiv
1 Introduction	1
1.1 Motivation	1
1.2 Aims and objectives	4
1.3 Scheme.....	5
2 Literature review and damage modelling approaches	8
2.1 Introduction.....	8
2.2 Finite element method (FEM)	9
2.3 Finite-element modelling of FRP materials.....	10
2.4 Composite modelling length scales	11
2.5 Implicit and explicit methods.....	15
2.6 Composite damage modelling approaches	17
2.6.1 Composite constitutive phases	18
2.6.1.1 Initial material response.....	18

2.6.1.2	Damage initiation	20
2.6.1.3	Damage evolution	23
2.6.2	Modelling of fibre/matrix debonding and delamination	26
2.6.3	Future modelling improvements	29
2.7	State of the art in the modelling of composite machining	29
2.7.1	Orthogonal cutting FEM based assessments	29
2.7.1.1	2D Macro-mechanical models	30
2.7.1.2	3D Macro- and Meso-mechanical models	34
2.7.1.3	Micro-mechanical models	36
2.7.2	Drilling FEM based assessments	40
2.8	Chapter summary	44
3	2D and 3D composite damage model	46
3.1	Introduction	46
3.2	2D and 3D machining damage algorithm fundamentals	47
3.2.1	Implementation of the damaged constitutive model	47
3.2.1.1	Implementation of the 2D damaged constitutive model	48
3.2.1.2	3D damaged stiffness matrix implementation	48
3.2.2	Minimisation of the mesh element size dependency	49
3.2.3	Damage initiation	51
3.2.4	Damage propagation	53
3.2.5	Chip fracture	54
3.3	User-defined VUMAT subroutine	54
3.4	Verification of FE damage model	59
3.4.1	Experimental trials description	59
3.4.2	Experimental trials	60
3.4.2.1	Experimental test of 0° laminates	60
3.4.2.2	Experimental test of 90° laminates	61
3.4.3	FE simulations description	63
3.4.3.1	Simulation of tensile test of 0° laminates	64
3.4.3.2	Simulation of tensile test of 90° laminates	65
3.4.3.3	Shear damage simulation	66
3.5	Concluding remarks	70
4	Machining induced damage assessment	72

4.1	Introduction	72
4.2	Model characteristics	73
4.2.1	Machining configurations and geometric analysis	74
4.2.2	Meshing parameters	75
4.2.3	Contact and friction modelling	77
4.3	Damage model particularities	78
4.4	Model validation	78
4.5	Results and discussion	82
4.5.1	Fibre orientation influence	82
4.5.2	Workpiece material influence	83
4.5.3	Tool edge radius influence	85
4.5.4	Relief angle influence	87
4.5.5	Rake angle influence	88
4.6	Concluding remarks	90
5	Chip formation modelling for various fibre orientations	91
5.1	Introduction	91
5.2	Model characteristics	93
5.2.1	General model features	93
5.2.2	Mesh and friction model performed	95
5.3	Damage model characteristics	96
5.4	Results and discussion	97
5.4.1	Element deletion strain-based criteria	97
5.4.2	Numerical assessment	103
5.4.2.1	Fibre orientation of 0°	103
5.4.2.2	Fibre orientation of 0° with 0° rake angle	104
5.4.2.3	Fibre orientation of 45°	105
5.4.2.4	Fibre orientation of 90°	106
5.4.2.5	Fibre orientation of 135°	108
5.5	Concluding remarks	109
6	Composite machining application: Edge trimming	111
6.1	Introduction	111
6.2	Experimental set-up	112
6.3	Model characteristics	115

6.4	Damage model	117
6.5	Results and discussion	117
6.5.1	Numerical FE model validation	120
6.5.2	Fibre orientation of 45°	125
6.5.3	Fibre orientation of 90°	130
6.6	Concluding remarks	133
7	Conclusions and future work	135
7.1	Thesis aims	135
7.2	Thesis outcomes	136
7.2.1	Modelling of sub-surface damage	136
7.2.2	Modelling of chip formation	137
7.2.3	Edge trimming numerical results	138
7.3	Future work	139
	Bibliography	140
	Appendices	152
A	Scientific publications	153
A.1	Conference papers	153
A.1.1	Paper 1	153
A.1.2	Paper 2	159
A.1.3	Paper 3	166
A.1.4	Paper 4	173
A.2	Conference posters	179
A.2.1	Poster 1	179
A.2.2	Poster 2	180
A.2.3	Poster 3	181
A.2.4	Poster 4	182
A.2.5	Poster 5	183
B	Matrix traction failure exposure factors F_{mt} images at the end of the simulation	184
C	Matrix compression failure exposure factors F_{mc} images at the end of the simulation	195

List of Tables

- 1.1.1 Machining industrial applications 2
- 2.7.1 Elastic properties available in the orthogonal cutting modelling of LFRP composites 31
- 2.7.2 Strength properties available in the orthogonal cutting modelling of LFRP composites 31
- 2.7.3 Intralaminar damage modelling in 2D FE macro mechanical models 31
- 2.7.4 Intralaminar and interlaminar damage modelling in 3D FE macro mechanical models 35
- 2.7.5 Intralaminar and interlaminar damage modelling in FE micro mechanical models 37
- 2.7.6 Elastic properties examples used in drilling modelling 40
- 2.7.7 Failure properties examples of the drilling modelling 40
- 2.7.8 Intralaminar damage modelling in 3D FE drilling models 41
- 2.7.9 Interlaminar damage modelling in 3D FE drilling models 41
- 2.7.10 Interlaminar artificial stiffness and strengths examples in the drilling modelling 41
- 3.2.1 Definitions of equivalent stresses ($\sigma_{eq,I}$) and displacements ($\delta_{eq,I}$) used in this research 51
- 3.4.1 Elastic properties of the tested CFRP laminate 63
- 3.4.2 Strength properties of the tested CFRP laminate 63
- 3.4.3 Elastic properties of the CFRP laminate [139] 67
- 3.4.4 Strength properties of the CFRP laminate [139] 67
- 4.2.1 Cutting variables employed in this work 74
- 4.2.2 Elastic properties of GFRP and CFRP materials used in this work 74
- 4.2.3 Strength properties of GFRP and CFRP materials used in this work 75
- 4.3.1 Critical fracture toughness extracted from [142] 78
- 4.4.1 Vertical speed, cutting tool displacements and simulation time obtained for every fibre orientation simulating the standard cutting configuration 79

5.2.1	Cutting variables employed in this work	94
5.2.2	Elastic properties of the CFRP laminate [81]	94
5.2.3	Strength properties of the CFRP laminate [81]	94
5.3.1	Critical fracture toughness employed in this work	96
5.4.1	Strain limits adopted to simulate the chip formation in all machining configurations studied	102
6.3.1	CFRP mechanical properties	115
6.3.2	CFRP strength properties.	115
6.4.1	Values of critical fracture toughness selected	117
6.5.1	Numerical errors obtained with respect the experimental average forces measured by Duboust et al Duboust2017.	125
6.5.2	Average forces and increments percentage because of the tool wear simulated	129
6.5.3	Average forces and increments percentage because of the tool wear simulated	132

List of Figures

1.1.1	Typical composite failure modes: (a) Fibre failures [25], (b) Fibre-matrix debonding [30] (c) Delamination [32] (d) Fibre pull-out [27] (e) Sub-surface damage [31] (f) Matrix crushing [33].	3
1.1.2	Machining operations illustrations: (a) orthogonal cutting (b) oblique cutting, (c) turning, (d) edge trimming, (e) milling and (f) drilling	4
1.3.1	Thesis layout	7
2.4.1	Representation of a macro-mechanical FE model [42]	12
2.4.2	Representation of a meso-mechanical FE model [43]	13
2.4.3	Representation of a RVE cell in a micro-mechanical FE model [44]	14
2.4.4	Schematic representation of the test simulated in a RUC cell to obtain the composite mechanical properties: (a) E11, (b) E22, (c) E33, (d) G12, (e) G13 and (f) G23	15
2.6.1	Schematic representation of different matrix and fibre damage types: (a) matrix cracking, (b) matrix crushing, (c) fibre breakage and (d) fibre buckling	18
2.6.2	Representation of stress tensor components in the main axis of a cubic composite cell	21
2.6.3	Failure envelopes of various composite famous failure criteria adapted from Pinho et al. [87] for unidirectional composites E-Glass/LY556 and the experimental data obtained in the WWFE [86]	23
2.6.4	CDM approaches schemes using (a) linear and (b) exponential stiffness degradations	25
2.6.5	Bilinear traction-separation response representation	28
2.7.1	Matrix crushing damage area (HSNMCCRT=1) for CFRP and GFRP laminates with a fibre orientation of 45° performed by Santiuste et al. [85]	32
2.7.2	(a) Sub-surface damage and (b) chip length with different fibre orientations simulated by Lasri et al. [84]	33
2.7.3	Examples of the the measure techniques of (a) cutting force (experimentally measurements and filtered results using a Matlab code) and (b) sub-surface matrix damage obtained in the simulations carried out by Zenia et al. [120]	33

2.7.4	Simulation of the cutting process of CFRP/Ti stack simulated (a) cutting CFRP laminate, (b) approaching to the interface, (c) a moment after passing away the interface, (d) Titanium chip formation [123]	34
2.7.5	Contour plot of stress σ_{12} with a rake angle of 15° and a depth of cut of 0.1 mm simulated by Rao et al. [42]	35
2.7.6	Representation of fibre compression, matrix compression and delamination with laminates configurations of [45/45/0/90] and [90/0/45/45] simulated by Santiuste et al. [91]	36
2.7.7	Sub-surface damage for different tool geometries (a) original tool and (b) new tool geometry obtained by Calzada et al. [128]	38
2.7.8	Damage in matrix(m1, m2 and m3), fibre (f1 and f2) and fibre-matrix interface with a fibre orientation of 30° and a depth of cut of 0.2 mm for different tool displacements (a) $0 \mu\text{m}$, (b) $21.2 \mu\text{m}$ and (c) $21.41 \mu\text{m}$ assessed by Rao et al. [111]	38
2.7.9	Chip formation mechanism and cohesive damage (SDEG) obtained with the new approach developed by Abena et al. [127] for fibre orientations of (a) 90° and (b) 135°	39
2.7.10	Laminate stresses and chip fragment simulated in [44] for laminates with fibre orientations of (a) 60° , (b) 90°	40
2.7.11	Numerical drilling model developed by Phadnis et al [81]	42
2.7.12	(a) Complete and (b) simplified FE models simulated by Feito et al [109] .	42
2.7.13	Drill bits geometry studied by Feito et al [82]	43
2.7.14	Delamination extension at entry and exit of the laminate after drilling using step drill bits with different stage ratio obtained by Islibir et al. [90]	43
3.2.1	Tensile test simulated by Lapczyk and Hurtado [93] to show the reduction of the mesh size dependency in a composite behaviour with a linear softening (a) Strain localised band, (b) Stress-strain graphs obtained for different number of elements.	49
3.2.2	Determination of the angle (φ) when the crack advances with a fibre orientation angles of: (a) $\theta=0^\circ$, (b) $0^\circ < \theta < 45^\circ$, (c) $\theta=45^\circ$, (d) $45^\circ < \theta < 90^\circ$, (e) $\theta=90^\circ$ and (f) $90^\circ < \theta < 135^\circ$	50
3.2.3	Damage model scheme carried out for every damage mode.	54
3.3.1	VUMAT algorithm flowchart.	56
3.3.2	Damage algorithm flowchart.	57
3.3.3	Damage evolution algorithm flowchart.	58
3.3.4	Element removal algorithm flowchart.	58
3.4.1	Tensile test set-up (a) Instron 8501 machine, (b) Hydraulic machine pressure controls and (c) Extensometer and specimen disposition in Instron 8501 machine.	59
3.4.2	Specimen breakage in tensile test with a fibre orientation of 0°	60

3.4.3	Stress-strain graph obtained from: (a) Trial 1, (b) Trial2, (c) Trials 1 and 2 superposition and (d) Calculated average stress-strain evolution.	61
3.4.4	Specimen breakage in tensile test with a fibre orientation of 90°.	62
3.4.5	Stress-strain graph obtained from: (a) Trial 1, (b) Trial2, (c) Trials 3 and (d) Calculated average stress-strain evolution.	62
3.4.6	Partitions modelled in specimens with fibre orientations of (a) Strain localised band, (b) Stress-strain graphs obtained for different number of elements.	64
3.4.7	Fibre and matrix damage (d_f and d_m) distribution of the 0° laminates for 2D and 3D FE models: (a) d_f of 2D FE model, (b) d_f of 3D FE model, (c) d_m of 2D FE model and (d) d_m of 3D FE model.	65
3.4.8	Numerical and experimental stress-strain graphs of 0° laminates obtained for various element sizes (ES) in (a) 2D FE predictions, (b) 3D FE predictions.	65
3.4.9	Fibre and matrix damage (d_f and d_m) distribution of the 90° laminates for 2D and 3D FE models: (a) d_m of 2D FE model and (b) d_m of 3D FE model.	66
3.4.10	Numerical and experimental stress-strain graphs of 90° laminates obtained for various element sizes (ES) in (a) 2D FE predictions, (b) 3D FE predictions.	66
3.4.11	Iosipescu test simulated geometry	67
3.4.12	Shear stress-strain curves obtained in experiment and the damage proposed damage model	68
3.4.13	Mesh distribution of the simulated Iosipescu specimen model: (a) 2D FE model, (b) 2D FE model central zoom ,(c) 3D FE model and (d) 3D FE model central zoom	69
3.4.14	Shear damage simulated in the 2D FE iosipescu model	69
3.4.15	Shear damage simulated in the 3D FE iosipescu model: (a) Perspective and (b) Front view	70
4.2.1	(a) Tool and (b) workpiece cutting parameters.	73
4.2.2	Workpiece boundary conditions.	74
4.2.3	Evolution of the internal energy, hourglass energy and kinetic energy during the simulation with the standard cutting configuration and a fibre orientation of 90	75
4.2.4	Mesh distributions with a maximum element size of (a) 50 μm , (b) 100 μm and (c) 150 μm	76
4.2.5	Mesh convergence study of (a) machining forces and (b) sub-surface damage.	77
4.2.6	Mesh convergence study with different element size around the tool tip of (a) machining forces and (b) sub-surface damage.	77
4.2.7	Mesh convergence study with different element size around the tool tip of (a) machining forces and (b) sub-surface damage.	78

4.4.1	(a) Spring back phenomenon representation and (b) example of machining forces record for the simulation of the standard cutting configuration and a fibre orientation of 0°	79
4.4.2	Thrust forces obtained in the proposed numerical simulation and other publications.	80
4.4.3	Detailed illustrations of the matrix damage modes causes at final simulation time with the standard configuration and a fibre orientation of 90° : (a) Matrix traction damage (d_{mt}), (b) Matrix compression damage d_{mc} , (c), (d), (e) σ_{22} , σ_{12} , d_{mt} and d_{mc} predicted in position (1), (2) and (3), respectively and (f) Damage modes allocation using the Puck's matrix failure criterion in different laminate positions	81
4.4.4	Sub-surface damage obtained in the numerical simulation proposed and Bhatnagar et al. [118] numerical and experimental results	82
4.5.1	F_{mt} obtained for fibre orientations (a) 0° (b) 15° , (c) 30° , (d) 45° , (e) 60° , (e) 75° and 90° at final simulation time with the standard cutting configuration.	83
4.5.2	F_{mc} illustration of (a) UD-CFRP composites and (b) UD-GFRP composites at final simulation time and fibre orientation of 45°	84
4.5.3	Sub-surface damage obtained for all the workpiece materials and fibre orientations studied at the final simulation time.	84
4.5.4	(a) Cutting and (b) thrust forces obtained for all the workpiece materials and fibre orientations studied at the final simulation time.	85
4.5.5	Sub-surface damage obtained for all the tool edge radius and fibre orientations studied at the final simulation time.	86
4.5.6	F_{mc} obtained for tool edge radius of (a) $15 \mu m$ (b) $30 \mu m$, (c) $50 \mu m$ at final simulation time for a fibre orientation of 90°	86
4.5.7	(a)Sub-surface damage and (b) thrust forces obtained for all the relief angles and fibre orientations studied at the final simulation time.	87
4.5.8	F_{mt} obtained for relief angles (a) 4° (b) 6° , (c) 8° and (d) 10° at final simulation time for a fibre orientation of 75°	88
4.5.9	Sub-surface damage obtained for all the rake angles and fibre orientations studied at the final simulation time.	89
4.5.10	F_{mc} obtained for rake angles (a) -5° (b) 0° , (c) 5° and (d) 10° at final simulation time for a fibre orientation of 30°	89
5.1.1	Representation of the different chip fracture scenarios studied in this research: (a) Fibre orientation of 0° , (b) Fibre orientation of 0° with a rake angle of 0° , (c) Fibre orientation of 0° with a rake angle of 0° , (d) Fibre orientation of 90° and (e) Negative fibre orientations or superior to 90° . .	92
5.2.1	Representation of the FE model simulated: (a) 3D perspective view (b) Boundary conditions and relevant cutting parameters modelled	94
5.2.2	Material directions assigned in Abaqus graphic (90° laminate)	95

5.2.3	Representation of meshed areas of the model: (a) Laminate and tool mesh distribution (b) Mesh distribution in the thickness	96
5.4.1	Fibre compression damage evolution	98
5.4.2	Matrix traction damage evolution	99
5.4.3	Shear fibre damage evolution	99
5.4.4	Shear matrix damage evolution	99
5.4.5	Matrix compression damage evolution	100
5.4.6	Fibre traction damage evolution	100
5.4.7	Matrix traction damage evolution in the laminate thickness direction (3) .	101
5.4.8	Matrix compression damage evolution in the laminate thickness direction (3). The strain limit imposed (2) exceed the strain level to reach the total failure ($d_{mc} = 1$)	101
5.4.9	Fibre shear damage evolution in plane 1-3	101
5.4.10	Matrix shear damage evolution in planes 1-3 and 2-3	102
5.4.11	Maximum damage calculated in the ideal configuration for matrix traction damage in the machining simulation of 0° with positive rake angle.	102
5.4.12	Representation of the FE model simulated with a fibre orientation of 0° : (a) 3D perspective view (b) Front view	103
5.4.13	Representation of a representative meshed element deleted to simulate the chip of a laminate with a fibre orientation of 0° : (a) Meshed element selected before deletion (b) Evolution of d_{mt2} and ε_{22} during the simulation time.	104
5.4.14	Representation of the FE model simulated with a fibre orientation of 0° and a rake angle of 0° : (a) 3D perspective view (b) Front view	104
5.4.15	Representation of a representative meshed element deleted to simulate the chip of a laminate with a fibre orientation of 0° and a rake angle of 0° : (a) Meshed element selected before deletion (b) Evolution of d_{fc} and ε_{11} during the simulation time.	105
5.4.16	Representation of the FE model simulated with a fibre orientation of 45° : (a) 3D perspective view (b) Front view	105
5.4.17	Representation of a representative meshed element deleted to simulate the chip of laminates with a fibre orientation of 45° : (a) Meshed element selected before deletion (b) Evolution of d_{m2} and ε_{12} during the simulation time.	106
5.4.18	Representation of the FE model simulated with a fibre orientation of 90° : (a) 3D perspective view (b) Front view	107

5.4.19	Representation of a representative meshed element deleted to simulate the chip of laminates with a fibre orientation of 90°: (a) Meshed element selected in front of the cutting tool before deletion, (b) Evolution of d_{mc2} and ε_{22} during the simulation time, (c) Meshed element selected below of the cutting tool before deletion, (d) Evolution of d_{mt2} and ε_{22} during the simulation time.	107
5.4.20	Representation of the FE model simulated with a fibre orientation of 135°: (a) 3D perspective view (b) Front view	108
5.4.21	Illustration of the fibre compression damage previous to the chip release in laminates with a fibre orientation of 135°.	109
5.4.22	Representation of a representative meshed element deleted to simulate the chip of laminates with a fibre orientation of 135°: (a) Meshed element selected before deletion (b) Evolution of d_{fc} and ε_{12} during the simulation time.	109
6.2.1	Relative fibre orientation change in edge trimming - orange stripes = fibre, green stripes = matrix.	113
6.2.2	Five axis CNC machine tool, Cincinnati FTV5-2500.	113
6.2.3	Edge Trimming Set-up: (a) separate pieces and (b) assembled set.	114
6.2.4	Three flute Polycrystalline Diamond (PCD) Cutting Tool with Optical Edge Radius Measurements.	114
6.3.1	Mesh sensitivity analysis of horizontal machining forces (F_X).	115
6.3.2	Mesh sensitivity analysis of vertical machining forces (F_Y).	116
6.3.3	Mesh zoom of the closed area next to the cutter tool edge.	116
6.3.4	Meshed elements distribution in the modelled laminate.	116
6.5.1	Representation of the characteristic edge trimming cutting mechanisms using a (a) new tool and (b) worn tool	118
6.5.2	Representation of relevant machining parameters analysed in this research: (a) FE model machining parameters employed and (b) tool tooth forces representation	118
6.5.3	Representation of relevant machining parameters analysed in this research: (a) spring back phenomenon (b) machining relative angle scheme, (c) machining relative angle distribution in the machining of 45° laminates and (d) machining relative angle distribution in the machining of 90° laminates	120
6.5.4	Validation of FE predictions with $f_r=800$ mm/min, $w=6000$ rpm and fibre orientation of (a) 45° and (b) 90°	121
6.5.5	Validation of FE predictions with $f_r=800$ mm/min, $w=8000$ rpm and fibre orientation of (a) 45° and (b) 90°	122
6.5.6	Validation of FE predictions with $f_r=1200$ mm/min, $w=6000$ rpm and fibre orientation of (a) 45° and (b) 90°	123

6.5.7	Validation of FE predictions with $f_r=1200$ mm/min, $w=8000$ rpm and fibre orientation of (a) 45° and (b) 90°	124
6.5.8	F_X and F_Y forces simulated in laminates with a fibre orientation of 90° and tool edge radius of (a) $10\ \mu m$, (b) $20\ \mu m$, (c) $40\ \mu m$, (d) $50\ \mu m$	126
6.5.9	F_X representation in 45° laminates and element sizes of $10\ \mu m$ for several tool edge radius: (a) $10\ \mu m$, (b) $20\ \mu m$, (c) $30\ \mu m$, (d) $40\ \mu m$, (e) $50\ \mu m$ and (f) $10\text{-}50\ \mu m$	127
6.5.10	F_X representation in 45° laminates and tool edge radius of $10\ \mu m$ for several element sizes: (a) $10\ \mu m$, (b) $20\ \mu m$, (c) $40\ \mu m$, (d) $5\text{-}10\ \mu m$	128
6.5.11	F_T and F_N forces simulated in laminates with a fibre orientation of 45° and tool edge radius of (a) $10\ \mu m$, (b) $20\ \mu m$, (c) $40\ \mu m$, (d) $50\ \mu m$	129
6.5.12	Representation of the average machining foces simulated with a fibre orientation of 45° : (b) F_X and F_Y (b) F_T and F_N	130
6.5.13	F_X and F_Y forces simulated in laminates with a fibre orientation of 90° and tool edge radius of (a) $10\ \mu m$, (b) $20\ \mu m$, (c) $40\ \mu m$, (d) $50\ \mu m$	131
6.5.14	F_T and F_N forces simulated in laminates with a fibre orientation of 90° and tool edge radius of (a) $10\ \mu m$, (b) $20\ \mu m$, (c) $40\ \mu m$, (d) $50\ \mu m$	132
6.5.15	Representation of the average machining foces simulated with a fibre orientation of 90° : (b) F_X and F_Y (b) F_T and F_N	133
B.0.1	F_{mt} obtained for fibre orientations (a) 0° (b) 15° , (c) 30° , (d) 45° , (e) 60° , (e) 75° and 90° at final simulation time with the standard cutting configuration.	185
B.0.2	F_{mt} obtained for fibre orientations (a) 0° (b) 15° , (c) 30° , (d) 45° , (e) 60° , (e) 75° and 90° at final simulation time using a rake angle of -5°	186
B.0.3	F_{mt} obtained for fibre orientations (a) 0° (b) 15° , (c) 30° , (d) 45° , (e) 60° , (e) 75° and 90° at final simulation time using a rake angle of 0°	187
B.0.4	F_{mt} obtained for fibre orientations (a) 0° (b) 15° , (c) 30° , (d) 45° , (e) 60° , (e) 75° and 90° at final simulation time using a rake angle of 10°	188
B.0.5	F_{mt} obtained for fibre orientations (a) 0° (b) 15° , (c) 30° , (d) 45° , (e) 60° , (e) 75° and 90° at final simulation time using a relief angle of 4°	189
B.0.6	F_{mt} obtained for fibre orientations (a) 0° (b) 15° , (c) 30° , (d) 45° , (e) 60° , (e) 75° and 90° at final simulation time using a relief angle of 8°	190
B.0.7	F_{mt} obtained for fibre orientations (a) 0° (b) 15° , (c) 30° , (d) 45° , (e) 60° , (e) 75° and 90° at final simulation time using a relief angle of 10°	191
B.0.8	F_{mt} obtained for fibre orientations (a) 0° (b) 15° , (c) 30° , (d) 45° , (e) 60° , (e) 75° and 90° at final simulation time with a UD-CFRP workpiece.	192
B.0.9	F_{mt} obtained for fibre orientations (a) 0° (b) 15° , (c) 30° , (d) 45° , (e) 60° , (e) 75° and 90° at final simulation time with a tool edge radius of $15\ \mu m$	193
B.0.10	F_{mt} obtained for fibre orientations (a) 0° (b) 15° , (c) 30° , (d) 45° , (e) 60° , (e) 75° and 90° at final simulation time with a tool edge radius of $30\ \mu m$	194

C.0.1	F_{mc} obtained for fibre orientations (a) 0° (b) 15° , (c) 30° , (d) 45° , (e) 60° , (e) 75° and 90° at final simulation time with the standard cutting configuration.	196
C.0.2	F_{mc} obtained for fibre orientations (a) 0° (b) 15° , (c) 30° , (d) 45° , (e) 60° , (e) 75° and 90° at final simulation time using a rake angle of -5°	197
C.0.3	F_{mc} obtained for fibre orientations (a) 0° (b) 15° , (c) 30° , (d) 45° , (e) 60° , (e) 75° and 90° at final simulation time using a rake angle of 0°	198
C.0.4	F_{mc} obtained for fibre orientations (a) 0° (b) 15° , (c) 30° , (d) 45° , (e) 60° , (e) 75° and 90° at final simulation time using a rake angle of 10°	199
C.0.5	F_{mc} obtained for fibre orientations (a) 0° (b) 15° , (c) 30° , (d) 45° , (e) 60° , (e) 75° and 90° at final simulation time using a relief angle of 4°	200
C.0.6	F_{mc} obtained for fibre orientations (a) 0° (b) 15° , (c) 30° , (d) 45° , (e) 60° , (e) 75° and 90° at final simulation time using a relief angle of 8°	201
C.0.7	F_{mc} obtained for fibre orientations (a) 0° (b) 15° , (c) 30° , (d) 45° , (e) 60° , (e) 75° and 90° at final simulation time using a relief angle of 10°	202
C.0.8	F_{mc} obtained for fibre orientations (a) 0° (b) 15° , (c) 30° , (d) 45° , (e) 60° , (e) 75° and 90° at final simulation time with a UD-CFRP workpiece.	203
C.0.9	F_{mc} obtained for fibre orientations (a) 0° (b) 15° , (c) 30° , (d) 45° , (e) 60° , (e) 75° and 90° at final simulation time with a tool edge radius of $15\mu m$	204
C.0.10	F_{mc} obtained for fibre orientations (a) 0° (b) 15° , (c) 30° , (d) 45° , (e) 60° , (e) 75° and 90° at final simulation time with a tool edge radius of $30\mu m$	205

Chapter 1

Introduction

1.1 Motivation

Carbon fibre reinforced polymers (CFRP) and glass fibre reinforced polymers (GFRP) are the most used composite materials in the industry because of their excellent strength-to-weight properties. It makes composite materials an excellent choice for applications where weight reduction is essential. For example, the aerospace industry achieved a considerable aircraft weight reduction by increasing composite materials in their airframes. Aeroplanes such as the Boeing 787 [1] reached about a 50% of composite content on their structural weight. Besides, composite materials offer high corrosive resistance, damage tolerance fatigue and excellent impact absorption properties, making them a great candidate for achieving high-performance applications required in industrial sectors such as automotive, sports, or maritime [2, 3].

The most used machining processes used in the composite industry are drilling, milling and turning. Drilling operations are used to create blind, through, and countersunk holes to aid the assembly between different components. Concerning milling operations, many variants are developed to reach the part morphology required. For example, it is used to remove edges (edge trimming or edge milling), form grooves (groove milling), insert circular orifices (circular milling) or generate a flat surface (face milling). Edge burr of laminates are usually removed employing straight cuts using sawing wheels [4, 5].

In the case of turning, the shafts machining to adjust the diameter of the desired section is the most used application [6]. Orthogonal cutting is highly researched because it genuinely represents the basis of the 2D cutting mechanisms that occur in the laminate under the tooling tooth's action in drilling, turning, and milling [7]. Finally, oblique cutting is a variant of orthogonal cutting that reflects with more fidelity the 3D cutting mechanisms due to the angle of inclination with the cutting direction applied to the tool edge [8]. Applications and use of previous mention machining processes are highlighted in Table 1.1.1.

Table 1.1.1. Machining industrial applications

Operation	Use	Applications
Milling	Adjust the dimensional parts demand	Grooves, edge trimming, circular holes [9–12] ...
Drilling	Assembly of high performance parts	Countersunk or through holes [13, 14]
Turning	Industrial shaft tolerances adjustment	High speed shafts, CFRP tubes, tool spindles [6, 15, 16] ...
Orthogonal cutting	Study of 2D machining parameters (straight tool edge)	Academical [7]
Oblique cutting	Study of 3D machining parameters (oblique tool edge)	Academical [8]

Other non-conventional machining processes, out of this document's scope, are commonly used in the industry. For instance, the abrasive waterjet machining process cuts the material under the influence of a high pressurised water jet mixed with abrasive particles over the laminate [17]. Another case is laser machining, where an orientated laser's thermal energy is used to remove the material [18]. Moreover, electrical discharge machining removes the material utilising electrical discharges [19]. Finally, ultrasonically assisted machining uses the tool vibration and abrasives to cut through the composite laminates [20, 21]. More detailed information could be obtained about machining composite processes in Sheikh-Ahmad's book [22].

Generally, composites parts are used in high-performance applications; thereby, strict dimensional tolerances and surface roughness are commonly necessary [23, 24]. Hence, machining processes should be widely investigated to accomplish these previous specifications. However, composite machining encompasses several laminate failures such as fibre failures [25, 26], fibre pull-out [27], delamination [28, 29], matrix-fibre debonding [30] or sub-surface damage [31] (refer to Fig. 1.1.1); causing significant obstacles to the fulfilment of quality and strength demands. Therefore, the study of appropriate cutting parameters which reduce undesired part defects becomes crucial.

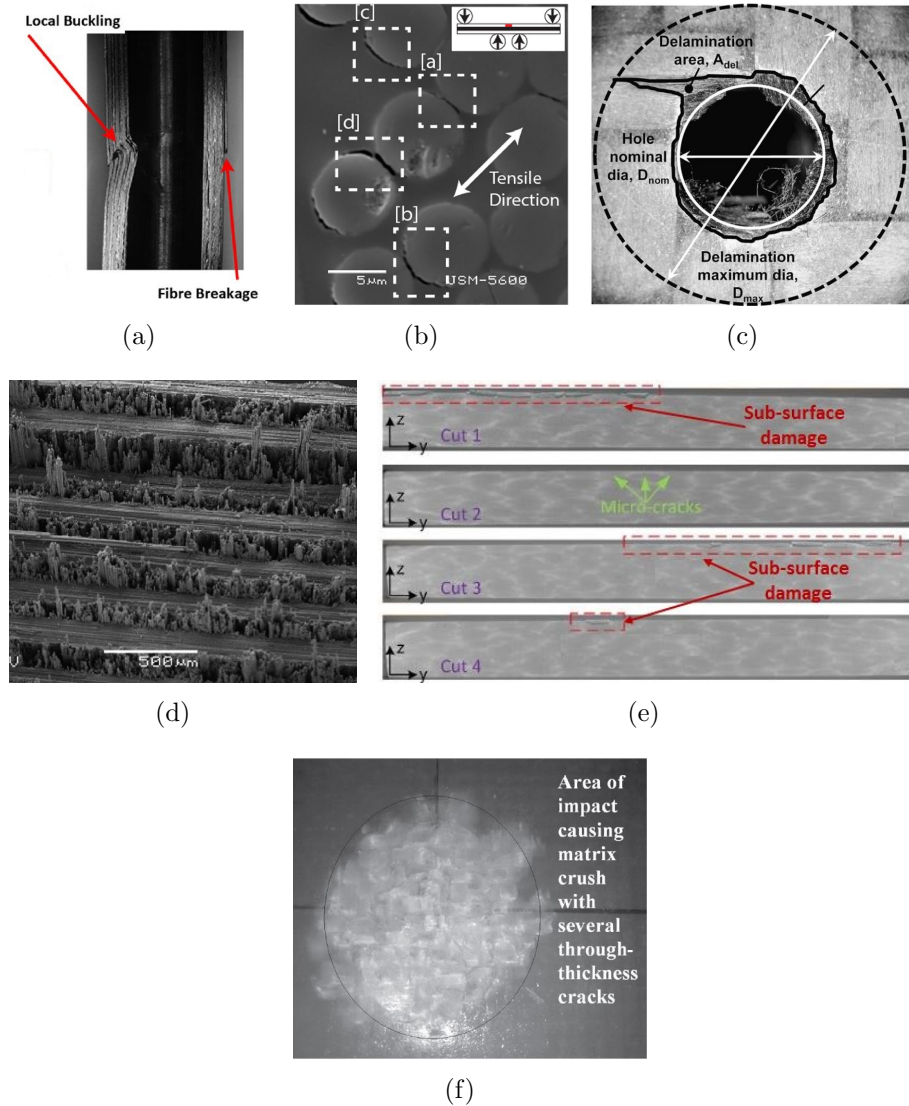


Fig. 1.1.1. Typical composite failure modes: (a) Fibre failures [25], (b) Fibre-matrix debonding [30] (c) Delamination [32] (d) Fibre pull-out [27] (e) Sub-surface damage [31] (f) Matrix crushing [33].

Many differences are appreciated in the physics of the conventional composite machining processes studied (refer to Fig. 1.1.2). In milling, the material is removed using an advancing rotary cutter moving in the machining direction through a fixed workpiece [9, 10]. In turning processes, the workpiece rotates while the cutting tool moves in a 2D plane to cut the material [15, 16]. Edge trimming removes the material from the laminate edges, moving a rotatory tool around the laminate periphery [11, 12].

Orthogonal cutting and oblique cutting are another two machining processes to remove the defective edges. In the first case, orthogonal cutting is based on machining the laminate edge with the linear movement of a sharp razor with the tool edge perpendicular to the cutting direction [7]. In the case of oblique cutting, the most significant difference is that the cutting edge is positioned in an oblique position concerning the cutting direction. Finally, the drilling operation is based on a laminate perforation by penetrating with a rotating drill into the laminate, parallel to the laminate thickness direction [13, 14].

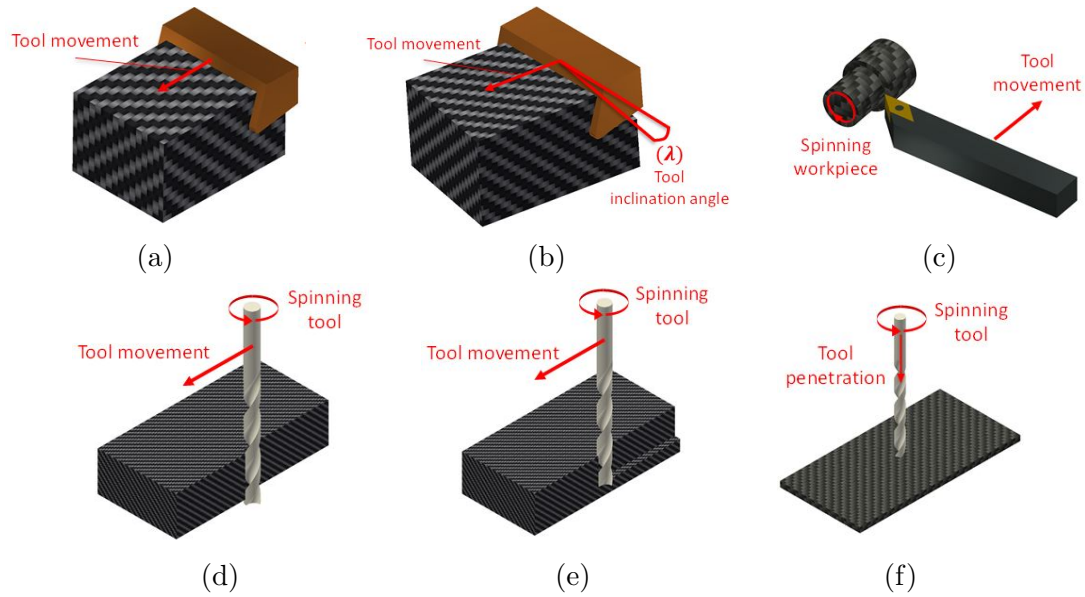


Fig. 1.1.2. Machining operations illustrations: (a) orthogonal cutting (b) oblique cutting, (c) turning, (d) edge trimming, (e) milling and (f) drilling

Despite a plethora of previous scientific efforts to address composite machining challenges using machining trials, there is still a sizeable scope to understand the effect of composite design variables (such as fibre orientations and layout) and machining process parameter (such as cutting feed/speed, cutter geometry, etc.) on the machining response of composites. The high cost of the composite materials and tooling make expensive these trials; thus, it is convenient the development of cheaper alternatives to investigate this matter. The use of FE analysis offers an attractive alternative as it is a very cost-effective method to design machining strategies to reduce cost and increase the quality of composite parts.

Drilling and orthogonal cutting are the most common machining operations simulated so far, reaching significant findings in both processes. However, this research is still quite limited because of the cumbersome cutting tool/workpiece interaction and the high computational cost required in these FE analyses. Additionally, various conventional composite machining processes such as milling, edge trimming, oblique cutting, or turning have not been widely modelled up to now [34, 34–37]. Thereby, more FE simulations are still required to understand all the crucial factors of these processes.

1.2 Aims and objectives

The aim of this thesis is the effective modelling of composite machining operations such as orthogonal cutting, drilling or edge trimming using a finite element approach. In general terms, implementing a numerical model capable of obtaining reliable predictions of the influence of cutting parameters such as tool edge radius, helix angle, feed rate, or other machining responses such as chip fracture, cutting forces or machining induced damage is sought.

The development of a customised composite damage model capable of modelling distinct fibre and matrix failures will be proposed to achieve this purpose. This damage model is implemented in the software package Abaqus/Explicit through a user-defined Fortran

VUMAT subroutine. This investigation aims to address the reasons that produce the chip fractures and underlying crack propagation typical from composite machining operation. This information will guide the selection of the most effective cutting parameters in terms of time and cost without affecting the final component's structural integrity. As a result, the below objectives are set out in this research.

1. Revision of all relevant publications in the modelling of machining operations with polymer matrix composites (PMCs) highlighting their strong points and their limitations to reach accurate predictions. From this review, all the unexplored areas in this field will be detected to lead this project's research direction.
2. Selection and development of a customised and effective composite damage model to simulate several aspects of PMCs machining with high accuracy levels. This damage model should have great versatility since it will be useful to simulate machining operations with a distinct cutting tool/workpiece interactions such as edge trimming or orthogonal cutting.
3. Development of a 2D FE model to analyse the influence of cutting parameters such as rake angle, tool edge radius, or relief angle on the remainder damage underlying the machined surface. Additionally, the development of a 3D FE model will be performed to provide the basis to mimic this study for cross-ply laminates in further investigations.
4. Implementation of a novel strain-based element deletion algorithm to simulate the chip fracture in PMCs machining. This will allow analysing in detail the distinct chip formation mechanism with several fibre orientations.
5. Simulation of more complex machining operations such as edge trimming. Notable improvements in comparison with the numerical predictions obtained so far are expected.

1.3 Scheme

This section summarises the outlines obtained in this document to generate a global idea of the research methodology developed here. Eight chapters are developed to carry out a complete and exhaustive analysis of five main research blocks: (1) introduction, (2) literature review, (3) development of numerical investigations and (4) conclusions and future work. Clear visualisation of this thesis's layout is provided in Fig. 1.3.1. A brief description of the objective of these research blocks is presented below.

1. **Introduction:** In this block, the motivation, objectives and research methodology of this project are conveniently described to enhance the comprehension of the entire manuscript.
2. **Literature review:** Firstly, a general review of the finite element approaches to model composite damage is offered to particularise in their possible applications in composite machining subsequently. The relevant achievements and numerical approaches employed in the relevant investigations developed so far are discussed. The

current scope and possible future improvements in composite machining modelling are critically discussed in this section.

3. **Development of numerical investigations:** Predicted results and their implications in composite machining are explained in detail. These numerical results are obtained through the implementation of a novel composite damage model in this field. Basics in the study of sub-surface damage and chip formation with several fibre orientations are assessed. Typical industrial machining applications such as drilling or edge trimming are investigated.
4. **Conclusions and future work:** An extensive and explanatory discussion of this thesis's content is provided in this block. All relevant novelties and findings extracted in this work are highlighted to conclude the document.

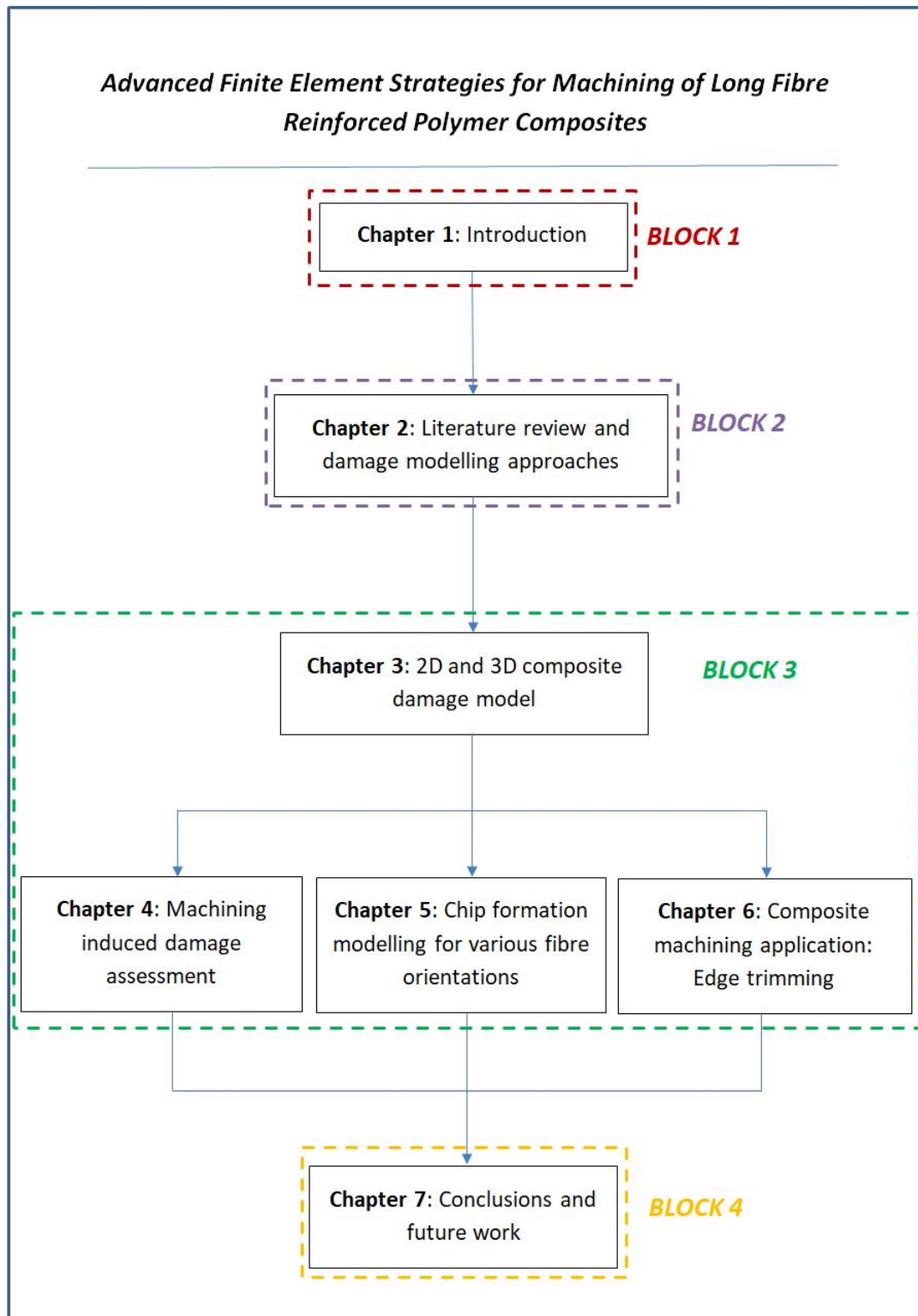


Fig. 1.3.1. Thesis layout

Chapter 2

Literature review and damage modelling approaches

2.1 Introduction

In recent decades, numerical simulations have become increasingly important in the study of composite machining. This is due to the low reliability and high economic cost derived from the detection of internal damage induced by machining operations in laminates with the use of non-destructive techniques. In contrast, the finite element numerical modelling technique offers a cheap and efficient alternative to predict this type of damage at different scales with great accuracy.

Another alternative to address these types of problems are analytical solutions. These solutions are obtained by carrying out some experiments where the influence that each variable has on the rest of the variables studied is analysed. This technique is very useful to obtain extensive information on the machining process by performing a small number of experiments. From the results of these experiments, the evolution of the damage in the laminates during their machining is inferred in a wide range of cutting parameters from where the optimal cutting parameters are found. However, due to the difficult interaction of the constituents of the composite with the tool and together with the concatenation of the different damages that occur in the laminate due to its anisotropy, these types of solutions have a low degree of accuracy. Therefore, the use of more complex techniques such as finite elements which take into account the progressive development of damage such as fibre breakage, matrix cracking, delamination or fibre/matrix debonding and their interactions is recommended to obtain more accurate predictions.

Despite the great convenience of using finite elements in composite machining research for the reasons previously mentioned, its development to date is still limited. This fact is mainly due to the high computational cost and the challenges of modelling with great precision the different damages and their interactions in this type of process. Therefore, the continuous advance in the development of modelling techniques and the increase in computational capacity has allowed during the last decades the progressive development of increasingly complex finite element models to address this matter. Therefore, the objective of this chapter is to analyse the achievements of the scientific community to date on this topic using the different numerical techniques available and how future improvements could be obtained in these models.

2.2 Finite element method (FEM)

The Finite Element Method (FEM) is the most employed approach to solve engineering problems. As a general rule, all the problems related to deformable solids, including the traditional heat transfer fields, structural analysis, fluid flow, or electromagnetism, can be perfectly formulated to obtain their corresponding solving equations. However, partial differential equations or the studied system's complicated geometry make it impossible to find an analytical solution to the problem. Therefore, with the substantial increase of the computers' computational power, the FEM has constituted a great alternative to provide approximate solutions to continuum-mechanics problems in which it is not possible to find an analytical solution.

The finite element approach subdivides a large domain into smaller and simpler several finite parts of the domain called elements constructing a mesh. These elements are connected in points called nodes where all forces and displacements are processed. The method approximates the complex solution of a continuum boundary value problem with large algebraic systems to obtain the nodal solutions demanded. It is achieved by obtaining the weak formulation of the problem by integrating the governing partial differential equations using variational principles.

Typically, the finite element approach uses the Eulerian or Lagrangian frameworks to model the problem's kinematic. The Lagrangian approach keeps the mass constant in the meshed element throughout the simulation even when large volume changes occur, not allowing the mass trespassing the element's boundaries. Conversely, in an Eulerian mesh, the elements keep the same volume and the mass travel throughout them during the simulation. As both approaches are distinct, their capabilities adjust better in the simulation of different kind of problems. In general terms, the Eulerian meshes represent an excellent election to simulate problems with large deflections or fluid dynamics. Lagrangian meshes are suitable for small deformation problems, and different materials or layers need to be modelled. However, the problems derived from the high deformation obtained in the highly distorted elements using this kind of formulation have been reasonably reduced using the numerical techniques implemented in the current numerical software packages. Furthermore, the use of this framework is convenient to model the contact between two or more solids. Therefore, because all the aforementioned Lagrangian capabilities are essential in composite machining, this formulation is employed to develop this thesis.

Other issues to consider to resolve problems using the finite-element method are the accuracy of the solutions and the numerical model's computational cost. On the one hand, obtaining results with a high degree of accuracy is required to make the simulated phenomena similar to reality and draw relevant conclusions. On the other hand, reducing the computational cost is necessary to avoid the industry's undesired delays that require the simulations of heavy FE composite machining models that often involve days, weeks, or even months. Generally speaking, the implementation of smaller element sizes or the use of more integration points obtain more precise results, but at the same time, it significantly increases the computational cost of the simulation. Therefore, implementing a mesh that reaches the right balance between these two variables is highly necessary.

Although, as it is well known in the research community, the methodology to obtain an optimal mesh is an art because there are no clear rules to achieve this purpose, there are some guidelines that help its design. In general, to increase the numerical results'

accuracy, regions with high field gradients such as crack edges, sharp reentrant corners, or areas where the loads are applied require a refinement commonly called h-refinement. Another action denominated as p-refinement to increase the accuracy of the results is to increment the use of elements with higher-order shape functions. Additionally, the size of the elements allocated in regions separated from the region of study should be raised compared to the studied areas' elements to reduce the computational time. This strategy is possible because it does not contribute significantly to the accuracy of the numerical results. Note that the problem's solution is mesh dependant, so a mesh sensitivity analysis is always required to guarantee that the problem's convergence was achieved. Therefore, the correct implementation of these previous strategies leads to an optimal mesh design to develop numerical simulations.

Finally, the modelling of composite machining requires the use of specific FE codes to model various characteristic features involved in these complex processes such as the orthotropic mechanical response of a ply, the bonding between plies, the modelling of various matrix and fibre failure types, or the cutting tool/workpiece contact among others. Commonly, 2D and 3D FE models have been developed to model this field's interesting research aspects. Various length scales FE models have been developed in the last decades to analyse the causes of local fibre and matrix failures and global ply damages, respectively, in composite machining. Despite the plethora of computational analyses performed so far, modelling the complex failures in a composite laminate during a machining operation is still limited. Thereby, several numerical approaches need to be investigated in-depth to increase the quality of the numerical predictions. The following sections will analyse all the relevant information associated with these topics in more detail.

2.3 Finite-element modelling of FRP materials

The significant difference in the mechanical properties exhibited by the fibres and resins that make up a composite sheet causes it to exhibit anisotropic behaviour that is highly dependent on the fibres' orientation. Laminates are manufactured by stacking a sequence of thin sheets with suitable fibre orientations to achieve the required mechanical properties. As a general rule, the length of the thickness in these laminates is much smaller than the laminate extension in its other two directions, so applying two-dimensional simplified mechanical theories is recommended in cases where this is possible. Because they considerably reduce the complexity of the problem. For this reason, the use of 2D shell element based models is widespread in many studies where composite modelling is performed. However, not all problems can be addressed with these numerical models due to their limitations, so using 3D Solid element based models is essential in many investigations encompassed in this field. Relevant characteristics of both FE models are discussed below.

2D Shell element based models (2D FEM)

This type of numerical models uses finite shell elements which formulation is based on the classical lamination theory (CLT). This theory is suitable in laminates where the thickness is small, and out-of-plane deformation is low [38]. It assumes that the evolution of in-plane displacements are linear throughout the thickness while the out-of-plane displacement keeps constant in the laminate. Because in this formulation, the bonding between plies is not considered, the stress distribution is discontinuous from one ply to another as their constitutive behaviour is distinct for plies with different fibre orientations [39]. The

formulation of two types of shell elements, continuum and conventional, which use the same kinematics, are commonly employed in the most popular finite element packages such as Abaqus or Ansys. The laminate geometry is designed in a 2D, or 3D space framework where all plies are included in the area occupied by a single 2D planar element [40]. Thereby, all plies share the same degrees of freedom because the number of elements required in this FE models is considerably reduced the computational cost and the pre-processing time are low. However, they cannot simulate problems correctly where severe delamination or high transverse shear deformations occurs because the bonding between plies is not modelled using this formulation.

3D Solid element based models (3D FEM)

Composite is commonly modelled using 2D shell element based FE analysis due to their simplicity and reduced computational cost. However, they are quite limited to model the through-thickness laminate behaviour because crucial factors such as the delamination between plies or large transverse shear deformations are not considered. The 3D solid elements can resolve these limitations mentioned above to predict relevant laminate variables such as delamination, normal stresses and interlaminar shear stresses. It is achieved because plies are modelled explicitly, meshing one or more brick elements through its thickness [39]. Later, the element is grouped in a section containing the lamina's material properties and the fibre orientation of each ply is assigned, defining the mechanical properties of every single ply modelled [40].

Additionally, between two adjacent plies, a thin layer with cohesive elements with at least one element in the out-of-plane direction is inserted to predict these resin-rich areas' behaviour, which susceptible to undergo in severe delamination cracks. As a result of these factors, the accuracy of 3D FE models in problems subjected to high delamination and interlaminar shear stresses is much higher than the results obtained in 2D FE models. However, because of the high number of elements with their DOFs and the creation of sections necessary to simulate the plies, the pre-processing time and the computational cost are substantially high.

2.4 Composite modelling length scales

One of FRP composites' most relevant characteristics lies in the high degree of heterogeneity of their constituents that can be seen in their micro-structure. Fibres and matrices are in clearly separated phases and show different mechanical properties assigned the desired mechanical properties for lamination by combining them correctly. Since a different mechanical behaviour is appreciated both at the microscopic and macroscopic levels, the study of mechanical behaviours at various scales and their interactions must be studied in detail.

Micro-mechanics is the science responsible for establishing the connection between the laminate's behaviour at different scales, studying the relationships between the physical properties of the laminate as a whole and its constituents. This achievement is achieved by introducing the mechanics of the different constituents that form the investigated composite material in the most advanced computational techniques. Afterwards, the micro-mechanical properties of these micro-constituents are homogenised to extrapolate the macro-mechanical properties of the laminate. Talreja et al. [41] defined three types

of scale analyses at different levels in composite modelling: (1) Macro-scale, (2) Meso-scale and (3) Micro-scale. The characteristics of these scale analyses are briefly described below.

- Macro-scale analysis:** In this type of analysis the laminate is treated as a continuum medium of a homogeneous material with anisotropic mechanical properties. These anisotropic properties introduced are the representative or average mechanical properties offered by the laminate in all spatial directions. This type of analysis's main advantages are its simplicity and high capacity to study parts with complex shapes and all kinds of fibre reinforcement structures. However, since this approach does not explicitly model the different constituents of the composite material, the local damage of the matrix and the fibre is not simulated, which considerably reduces the numerical results' physical significance. A good example of this type of model is represented in Fig. 2.4.1.

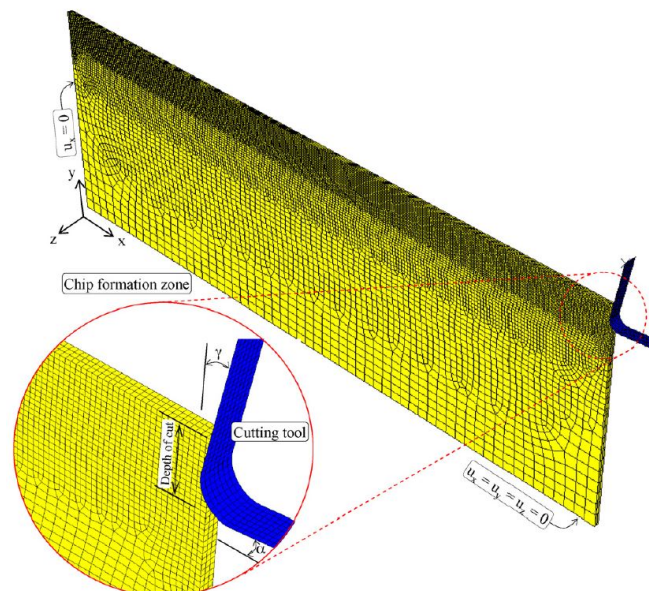


Fig. 2.4.1. Representation of a macro-mechanical FE model [42]

- Meso-scale analysis:** These analyses focus on the study of the mechanical behaviour and subsequent failure of a ply. Each of the sheets is modelled as a continuous homogeneous entity with orthotropic properties, as shown in Fig. 2.4.2. In this case, as in the macro-scale models, the fibres and matrices' local failures cannot be represented, considering the ply as a homogeneous entity. However, unlike macro-scale models, the delamination between plies can be high accurately predicted. These models are efficient in computational cost, so they are recommended for modelling representative laminate dimensions.

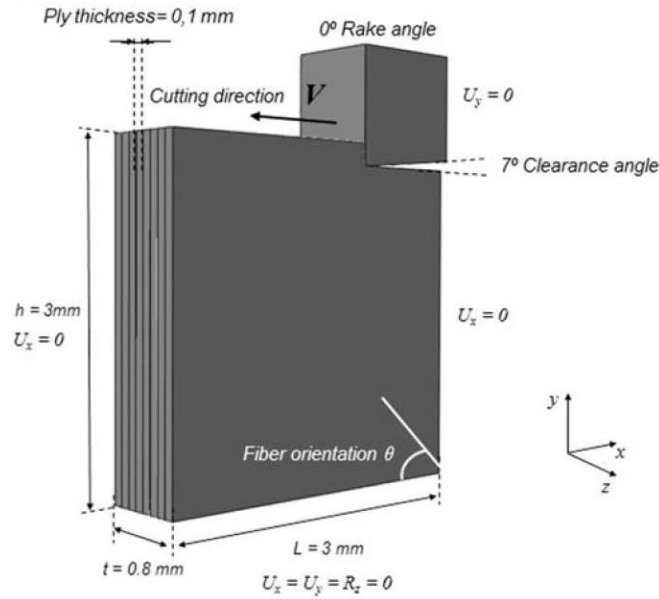


Fig. 2.4.2. Representation of a meso-mechanical FE model [43]

- Micro-scale analysis:** The micro-scale analyses focus on the study of the local constituents' failure and micro-deformations in a small area of the laminate. Here, the matrix and the fibre and fibre/matrix interfaces are modelled explicitly, implementing for each component distinct constitutive behaviours. As a consequence, this kind of FE models can accurately offer meaningful constituents' failure types predictions. However, the small dimensions of the fibre diameters, around $5\text{-}10\ \mu\text{m}$ together with the necessity of meshing these small areas using several elements to achieve convergence, use tiny element sizes and increase remarkably the computational cost of the FE model.

All these previous commented analyses are performed in a multi-scale analysis to correlate their results using continuum mechanic considerations and acquire a reliable global image of a process. Two different techniques, denominated localisation and homogenisation, are developed in multi-scale analyses. The homogenisation technique calculates the macro-mechanical properties analysing the average mechanical properties obtained from the micro-scale FE simulation of a representative cell of the material called **Representative Volume Element** (RVE), see Fig. 2.4.3. This statistical RVE cell should be large enough to represent the behaviour of the material reliably; typically this cell should include a cubic side lengths from 2 to 5 times the fibre diameters [41].

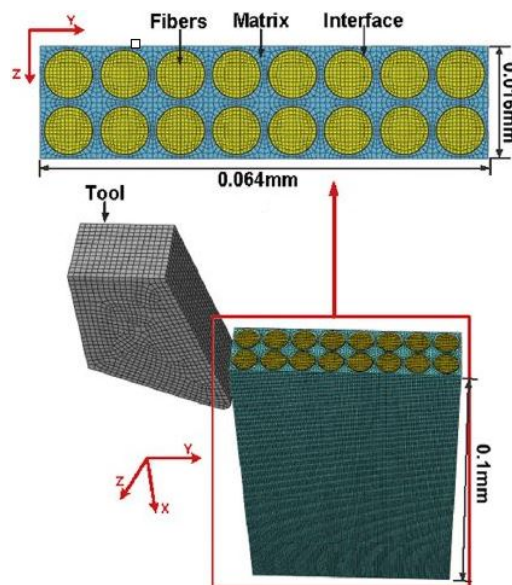


Fig. 2.4.3. Representation of a RVE cell in a micro-mechanical FE model [44]

However, this RVE cell does not localise properly the local fibre or matrix damage initiation and progression triggered at stress concentration points. Then, to better capture physics at the micro-level, a periodic micro-field technique based on smaller cells than RVE called a repetitive unit cell (RUC) is developed. The matrix and the fibre are uniformly distributed, and periodic boundary conditions and prescribed loads are selected to determine the macro-mechanical properties. Localised damage such as matrix cracking, fibre/matrix or fibre breakage is accurately captured using this approach. A good representation of the simulations developed in a RUC to determine the mechanical properties of a CFRP composite is provided in Fig. 2.4.4.

Multi-scale modelling predicts laminate damage by implementing the information obtained from micro-level simulations in macro-level simulations. In this way, the accuracy of predicting damage on a macroscopic scale in common problems such as impact or composite machining is substantially increased. However, the computational cost involved in simulating multiple meshes at different scales is still high, even for the increasing computational power available in advanced computational units. For this reason, the implementation of this type of analysis in composite machining is not currently approachable. Besides, the small size of the elements to reliably reproduce the fibres' mechanical behaviour and the typical dimensions of cutting in machining sharply increase the computational cost of micro-mechanical models. This thesis tries to approach real machining problems simulation, obtaining simulations with an outstanding balance between accuracy and computational cost. Thus, the use of macro-mechanical models is decided in the investigations developed in this work.

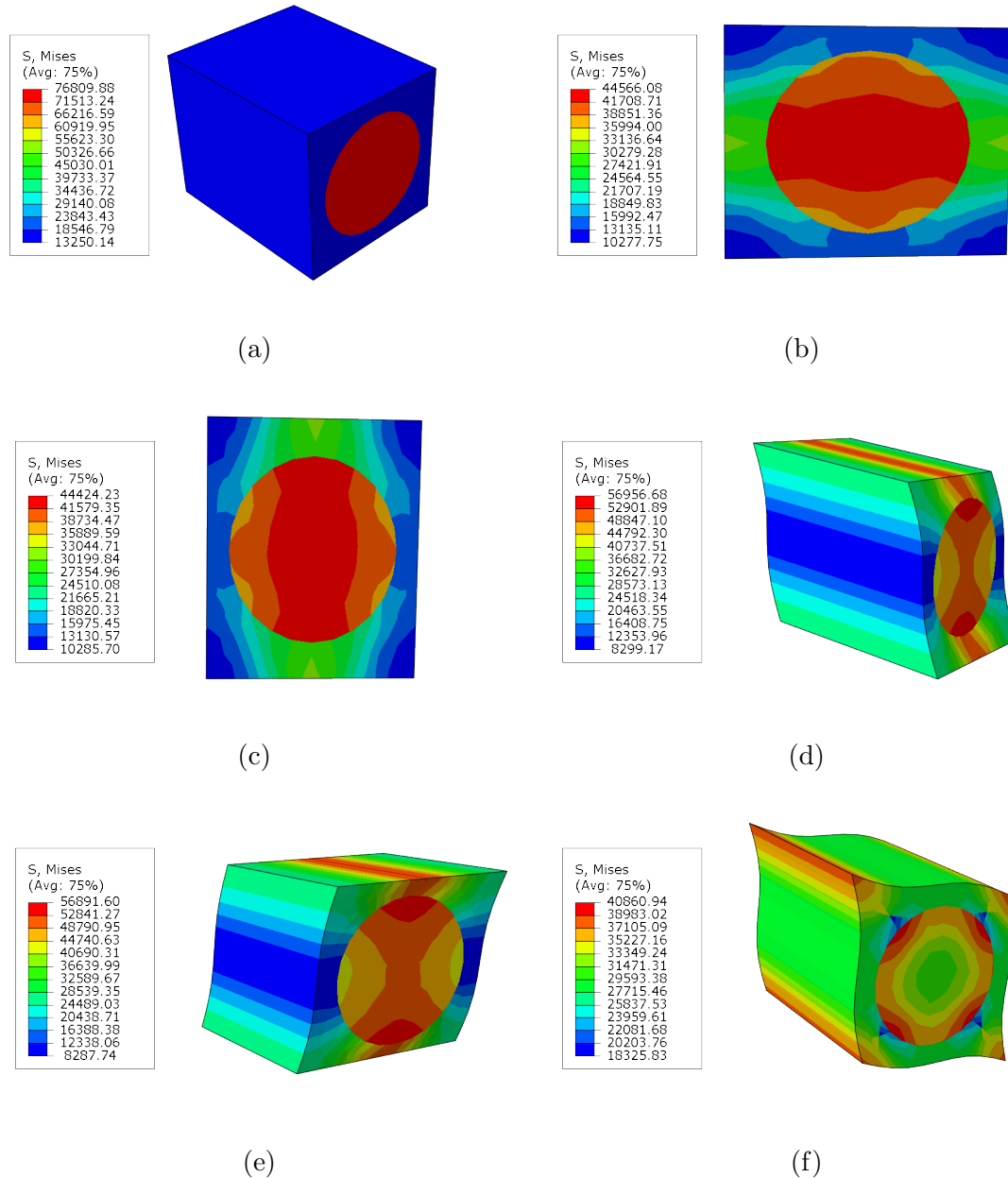


Fig. 2.4.4. Schematic representation of the test simulated in a RUC cell to obtain the composite mechanical properties: (a) E_{11} , (b) E_{22} , (c) E_{33} , (d) G_{12} , (e) G_{13} and (f) G_{23}

2.5 Implicit and explicit methods

Typically, implicit and explicit solvers are used in finite element to simulate static and dynamic problems, respectively [45]. These methods resolve a huge system of equations using two different approaches. Implicit methods are suitable for resolving static problems because they are based on the static equilibrium principle. This principle states that the sum of all forces at the internal nodes (I) should be balanced with the external forces (P) applied via external loads or contact problems. Commonly, the static equilibrium is

formulated as reads,

$$P - I = 0 \quad (2.5.1)$$

These problems usually require an iterative process to achieve the convergence of the problem, which is reached when the residual forces (R) are below a small quantity (c), see Eq. (2.5.2). This magnitude is usually controlled by the numerical settings of the numerical software employed. Long increment step times could be reached because this problem is unconditionally stable. However, several iterations are usually required to achieve the convergence of the problem, and with every new iteration, the increment of the step time notably reduces the increment of the step time. Another aspect to consider is that this method requires constantly updating the tangent stiffness matrix every step to achieve the convergence of the numerical problem. Implementing this stiffness matrix to reproduce the typical non-linear orthotropic material behaviour of a lamina via user-defined subroutines is required.

Compared with the explicit method, the implicit method's computational cost to simulate a time step is much higher because it is processing large matrix sizes and resolving loads of algebraic equations for every iteration. Finally, the Implicit simulations do not deal with simulations where unstable crack propagations or large deformation rates occur due to these phenomena excessively complicating the convergence of the problem.

$$R = \frac{|I - P|}{P} \leq |c| \quad (2.5.2)$$

The explicit method is used to resolve dynamic problems because it is based on the dynamic equilibrium principle. The main differences regarding the static equilibrium condition are the consideration of the inertial forces in the problem, see Eq. (2.5.3). Therefore, the required nodal velocities and accelerations to evaluate these inertial forces ($m\ddot{u}$) are calculated using the central difference rule. This method calculates the velocities (\dot{u}) and accelerations (\ddot{u}) using an algorithm where the time step increments are variable during the simulation.

$$P - I = m\ddot{u} \quad (2.5.3)$$

As opposed to the implicit method, the explicit method is conditionally stable, and thus, the achievement of the convergence at the end of a step is not a problem in this kind of analysis. However, it implies that the time step (Δt) needs to be small enough for not allowing the wave propagation exceed one element length during this step. Time step length is determined using the Courant-Friedrichs –Lewy convergence condition. This condition considers the mass, size, and stiffness of the meshed elements, as shown in Eq. (2.5.4). Therefore, the computational cost of one step is much higher in an Implicit analysis. Nevertheless, the large number of steps require due to the short step increment time imposed in an Explicit framework make that the total computational time of a simulation is much longer in Explicit analysis than in Implicit simulations.

$$\Delta t = \alpha \Delta t_{sta} \quad \Delta t_{sta} = \min \frac{l_e}{c_e} \quad c_e \cong \sqrt{\frac{E_e}{\rho_e}} \quad (2.5.4)$$

In the above equation, the parameter Δt is the time increment. α represents a reduction factor lower than 1 ($0.8 \leq \alpha \leq 0.98$) which consider the instabilities of nonlinearities of the problem [45]. The stable time step (Δt_{sta}) is the time that guarantee that the solution will grow bounded. The terms l_e and c_e denote the characteristic length and the wavespeed of the element e , respectively. Finally, E_e and ρ_e represent the Courant stiffness and the density of the element e .

This method does not need to update the tangent stiffness matrix. Thus the implementation of complex non-linearities becomes more feasible via in-built Abaqus commands or user-defined subroutine. Additionally, in quasi-static problems (problems with inertial forces close to 0), the element mass can be notably increased, reducing the computational time without significantly affecting the numerical results' accuracy. This issue occurs because the term of the inertial force ($m\ddot{u}$) is closed to 0. Thus, when the mass increment, the result of this term keeps close to zero without modifying the dynamic equilibrium.

In general, the explicit method is better suited to the simulation of composite machining processes. This fact is correct because these processes are highly dynamic, occurring in milliseconds. Thus, it is necessary the consideration of the inertial forces. Furthermore, the complex simulation of the tool/composite interaction is necessary to mitigate numerical convergence problems using an explicit method.

2.6 Composite damage modelling approaches

Composite materials suffer many types of damage due to their anisotropy. Damages in the fibres and matrix and their interactions occur at the same time [46–49]. These damages are responsible for progressively degrading the mechanical properties of the pieces until their total breakage. Generally, small cracks appear first in the matrix in areas with small imperfections [50–52]. Subsequently, these small cracks expand with the plies delamination or fibre/matrix debonding, weakening the strength of the laminate [53–65]. Finally, the final breakage of the laminate occurs by the massive breakage of fibres [27, 66–69].

These failure mechanisms entail considerable difficulties to implement them in a simultaneous numerical simulation. Furthermore, the simulation of the interaction between the laminate and the cutting tool exposes a difficult contact problem to simulate. Therefore, the use of sophisticated numerical approaches is necessary to address these types of problems.

Various length-scale approaches (meso- and micro-scale) have been developed to simulate the laminate machining response depending upon the composite damage type addressed in the investigation. Macro-scale FE models are more efficient in predicting laminate composite failure types such as delamination or machining-induced damage, while micro-scale FE models provide accurate predictions of the distinct local damage types.

These local damages could be listed in four types: (1) matrix cracking, (2) matrix crushing, (3) fibre breakage and (4) fibre buckling. For matrix cracking and crushing, an evident fracture of the matrix is produced in tensile and compression tensional states, respectively. The fibre breakage produces a clear fracture surface in the fibres under tensile tensional states. Finally, the fibre buckling typically breaks fibres in an oblique band with a specific angle θ denominated as "Kink band" due to the instabilities that the fibre experiences in

compressive tensional states [70]. A representation of these local damages is offered in Fig. 2.6.1

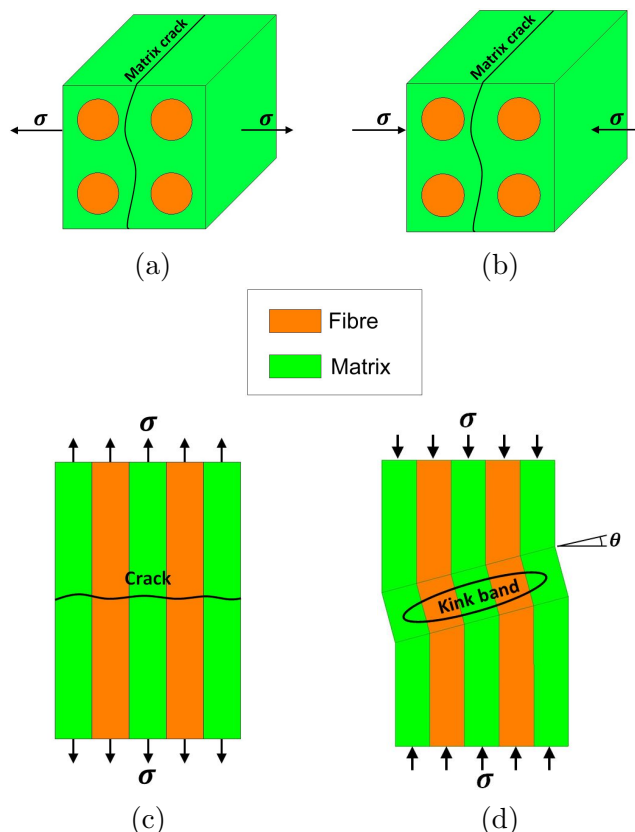


Fig. 2.6.1. Schematic representation of different matrix and fibre damage types: (a) matrix cracking, (b) matrix crushing, (c) fibre breakage and (d) fibre buckling

Two main sections are distinguished to analyse the damages modelled in composite machining: (1) intralaminar damage and (2) fibre/matrix debonding and delamination. More details about the approaches to model composite damages are identified below.

2.6.1 Composite constitutive phases

Normally, all composite damages can be implemented via user-defined subroutines or through the in-built commands of the numerical software employed. Typically, the modelling of composite damages is treated in three separate phases: (1) initial material response, (2) damage initiation and (3) damage evolution.

2.6.1.1 Initial material response

Although there is no damage at this stage, it is essential to simulate the posterior damage initiation and damage evolution accurately. This phase is treated using different considerations in macro- and micro-scale FE models to reflect the distinct composite damages in their constituents and plies.

- Macro-scale FE models

It is well known that polymer-based composites exhibit excellent resistant performance and high stiffness in the fibre's direction, while, in the transverse direction, they offer low resistance and low stiffness to external loads, typical of the resins. For simulating this particular behaviour, transversely isotropic models are used to introduce high stiffness in the fibre direction, and low Young's modulus in the perpendicular direction [35].

$$\begin{bmatrix} \sigma_{11} \\ \sigma_{22} \\ \sigma_{33} \\ \sigma_{12} \\ \sigma_{13} \\ \sigma_{23} \end{bmatrix} = \begin{bmatrix} \frac{1-\nu_{23}\nu_{32}}{E_{22}E_{33}\Delta} & \frac{\nu_{12}-\nu_{32}\nu_{13}}{E_{11}E_{33}\Delta} & \frac{\nu_{13}-\nu_{12}\nu_{23}}{E_{11}E_{22}\Delta} & & & \\ \frac{\nu_{12}-\nu_{32}\nu_{13}}{E_{11}E_{33}\Delta} & \frac{1-\nu_{13}\nu_{31}}{E_{22}E_{33}\Delta} & \frac{\nu_{23}-\nu_{21}\nu_{13}}{E_{11}E_{22}\Delta} & & & \\ \frac{\nu_{13}-\nu_{12}\nu_{23}}{E_{11}E_{22}\Delta} & \frac{\nu_{23}-\nu_{21}\nu_{13}}{E_{11}E_{22}\Delta} & \frac{1-\nu_{12}\nu_{21}}{E_{11}E_{22}\Delta} & & & \\ \hline & & & G_{12} & & \\ & & & & G_{13} & \\ & & & & & G_{23} \end{bmatrix} \begin{bmatrix} \varepsilon_{11} \\ \varepsilon_{22} \\ \varepsilon_{33} \\ \gamma_{12} \\ \gamma_{13} \\ \gamma_{23} \end{bmatrix} \quad (2.6.1)$$

where $\Delta = \frac{1 - \nu_{12}\nu_{21} - \nu_{23}\nu_{32} - \nu_{31}\nu_{13} - 2\nu_{21}\nu_{32}\nu_{13}}{E_{11}E_{22}E_{33}}$

In the above equations, the variables σ_{ij} denotes the stresses components in directions "i" and j of the main axis, while normal and shear strains are represented for variables ε_{ii} and γ_{ij} respectively. E_{ii} and G_{ij} represent the Young's modulus and the shear modulus in principal plane directions "i" and "j", respectively. Finally, ν_{ij} is the Poisson coefficient in "i" and "j" directions.

For simplicity, the ply behaviour is usually modelled in the elastic regime, not considering the plastic deformations in epoxy resins during the machining processes. Other factors such as matrix thermal degradation or tool-workpiece friction, which affects the material behaviour considerably in machining [71], have been poorly investigated without considering a defined variable to account for this damage [43] so far. Therefore, more sophisticated FE models these material factors should be addressed in the future to enhance numerical results accuracy.

- Micro-scale FE models

In this approach, carbon and glass fibres, as well as epoxy resins, are separately modelled. Both carbon and glass fibres are studied in the elastic domain as the plastic deformations developed in these materials are negligible. Carbon fibres are modelled as transversely isotropic materials to consider the different responses shown in this material in longitudinal and transverse directions [72], while glass fibres are commonly treated as an isotropic material [73]. Due to the epoxy resins plasticity, matrix behaviour is simulated through elasto-plastic FE models.

$$\begin{bmatrix} \sigma_{11} \\ \sigma_{22} \\ \sigma_{33} \\ \sigma_{12} \\ \sigma_{13} \\ \sigma_{23} \end{bmatrix} = \begin{bmatrix} \lambda - 2\mu & \lambda & \lambda & & & \\ \lambda & \lambda - 2\mu & \lambda & & & \\ \lambda & \lambda & \lambda - 2\mu & & & \\ \hline & & & \mu & & \\ & & & & \mu & \\ & & & & & \mu \end{bmatrix} \begin{bmatrix} \varepsilon_{11} - \varepsilon_{11}^{pl} \\ \varepsilon_{22} - \varepsilon_{22}^{pl} \\ \varepsilon_{33} - \varepsilon_{33}^{pl} \\ \gamma_{12} - \gamma_{12}^{pl} \\ \gamma_{13} - \gamma_{13}^{pl} \\ \gamma_{23} - \gamma_{23}^{pl} \end{bmatrix} \quad (2.6.2)$$

In the above equations, the terms λ and μ represents the Lamé constants, while normal and shear plastic strains are denoted for variables ε_{ii}^{pl} and γ_{ij}^{pl} respectively. These type of FE models achieve better machining force predictions than macro-scales FE models due to the inclusion of plastic deformations in the matrix. However, the introduction of these non-linearities increases notably the FE model's complexity using more sophisticated numerical algorithms such as the returning mapping algorithm [74]. However, factors that affect matrix behaviour, such as the strain rate dependency or thermal effects, have not been widely investigated. Therefore, more significant effort needs to be made to insert these material characteristics, affecting the final simulated damage results.

2.6.1.2 Damage initiation

Prediction of the failure in composites is one of the biggest challenges because of its constituent heterogeneity. The cohabitation of fibre and matrix usually produces several damage modes simultaneously under different tensional states. For this reason, it is essential to obtain accurate composite failure prediction models to accurately capture the overall integrity of laminates in all possible stress configurations. Many famous failure criteria by experimented researchers such as Tsai-Wu, Tsai-Hill [75], Hashin [76, 77] or Puck [78] have been proposed to date to address these problems with higher accuracy [79].

Several of these failure criteria have been implemented in FE models to predict machining operations' damage via user-defined subroutines. Various models based on material strength (maximum stress) or polynomial (Tsai-Hill 2D, 3D) criteria have been used in several works because of their simplicity. However, these models are not accurate because they are inspired in metal formulations treating composites as a homogenous material without considering the heterogeneity and the nature and interactions of their constituents. Maximum stress and 2D Tsai-Hill criteria are formulated in Eqs. (2.6.3) and (2.6.4), respectively.

- Maximum stress criterion [75]

$$\sigma_{ij} \leq \sigma_{ij}^{max} \quad (2.6.3)$$

- 2D Tsai-Hill [75]

$$\left[\frac{\sigma_{11}}{X}\right]^2 - \frac{\sigma_{11}\sigma_{22}}{X^2} + \left[\frac{\sigma_{22}}{Y}\right]^2 + \left[\frac{\sigma_{12}}{S}\right]^2 \leq 1 \quad (2.6.4)$$

In the above equations, X , Y and S correspond to the fibre, matrix and ply shear strength of the composite, respectively.

Physically based failure criteria are the most suitable to predict the damage in composites, because they distinguish between fibre and matrix failure types accurately. In machining FE models, Hashin and Hou [77, 80] criteria are the most used because of their formulation simplicity, refer to Tables 2.7.3, 2.7.4 and 2.7.8. Four different damage modes are considered in Hashin criterion: fibre traction, fibre compression, matrix traction and matrix compression. In the case of Hou criteria an additional expression for predicting the delamination is employed. Hou and Hashin 3D failure criteria read:

- Hashin [77]

$$\left(\frac{\sigma_{11}}{X_T}\right)^2 + \frac{\sigma_{12}^2 + \sigma_{13}^2}{S_{12}^2} < 1 \Rightarrow \text{Fibre traction } (\sigma_{11} > 0) \quad (2.6.5)$$

$$\left(\frac{\sigma_{11}}{X_C}\right)^2 < 1 \Rightarrow \text{Fibre compression } (\sigma_{11} < 0) \quad (2.6.6)$$

$$\frac{(\sigma_{22} + \sigma_{33})^2}{Y_T} + \frac{\sigma_{23}^2 - \sigma_{22}\sigma_{33}}{S_{23}^2} + \frac{\sigma_{12}^2 + \sigma_{13}^2}{S_{12}^2} < 1 \Rightarrow \text{Matrix traction } (\sigma_{22} + \sigma_{33} > 0) \quad (2.6.7)$$

$$\left[\left(\frac{Y_C}{2S_{23}}\right)^2 - 1 \right] \left(\frac{\sigma_{22} + \sigma_{33}}{Y_C}\right) + \frac{(\sigma_{22} + \sigma_{33})^2}{4S_{23}^2} + \frac{\sigma_{23}^2 - \sigma_{22}\sigma_{33}}{S_{23}^2} + \frac{\sigma_{12}^2 + \sigma_{13}^2}{S_{12}^2} < 1 \quad (2.6.8)$$

$$\Rightarrow \text{Matrix compression } (\sigma_{22} + \sigma_{33} < 0)$$

- Hou [80]

$$\left(\frac{\sigma_{11}}{X_T}\right)^2 + \left(\frac{\sigma_{12}^2 + \sigma_{13}^2}{S_{12}^2}\right) \leq 1 \Rightarrow \text{Fibre traction } (\sigma_{11} > 0) \quad (2.6.9)$$

$$\left(\frac{\sigma_{11}}{X_C}\right)^2 + \left(\frac{\sigma_{12}^2 + \sigma_{13}^2}{S_{12}^2}\right) \leq 1 \Rightarrow \text{Fibre compression } (\sigma_{11} < 0) \quad (2.6.10)$$

$$\left(\frac{\sigma_{11}}{Y_T}\right)^2 + \left(\frac{\sigma_{12}}{S_{12}}\right)^2 + \left(\frac{\sigma_{23}}{S_{23}}\right)^2 \leq 1 \Rightarrow \text{Matrix traction } (\sigma_{22} + \sigma_{33} > 0) \quad (2.6.11)$$

$$\frac{1}{4} \left(\frac{-\sigma_{22}}{S_{23}}\right)^2 + \left(\frac{\sigma_{22}Y_C}{4S_{23}}\right) - \frac{\sigma_{22}}{Y_C} + \left(\frac{\sigma_{12}}{S_{12}}\right)^2 \leq 1 \Rightarrow \text{Matrix compression } (\sigma_{22} + \sigma_{33} < 0) \quad (2.6.12)$$

In the above equations, σ_{ij} are the stress components in the components "i" and "j" of the principal axes, refer to Fig. 2.6.2. X_T and X_C are the fibre tensile and compression strength, respectively. Y_T is the matrix tensile strength, Y_C is the matrix compression strength. S_{12} is the shear strength and in principal planes (1-2), while S_{23} is the shear strengths in the principal plane (2-3).

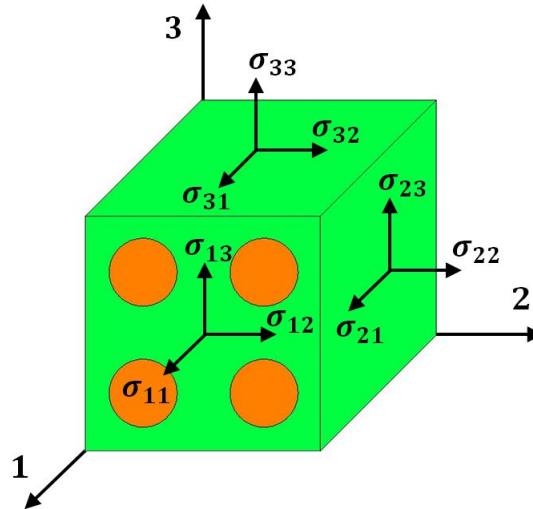


Fig. 2.6.2. Representation of stress tensor components in the main axis of a cubic composite cell

Additionally, other expressions have been used to enhance the failure predictions capabilities in composite UD laminates. For instance, Phadnis et al. [81] implemented an expression derived from the Puck criterion to predict the matrix failure, which reads.

$$\left[\left(\frac{\sigma_{11}}{2X_T} \right)^2 + \frac{\sigma_{22}^2}{|Y_C Y_T|} + \left(\frac{\sigma_{12}}{S_{12}} \right)^2 \right] + \sigma_{22} \left(\frac{1}{X_T} + \frac{1}{X_C} \right) = 1 \quad (2.6.13)$$

$(\sigma_{22} + \sigma_{33} \geq 0) \Rightarrow$ *Matrix cracking* $(\sigma_{22} + \sigma_{33} < 0) \Rightarrow$ *Matrix crushing*

Other failure criteria have been inserted to consider the structural particularities in woven composites. For instance, Feito et al. [82] implemented to predict the failure in the laminate thickness direction (d_{m3}), see Eq. (2.6.14).

$$d_{m3} = \frac{1}{4} \left(\frac{\sigma_{33}}{Z_C} \right)^2 + \frac{Z_C \sigma_{33}}{4S_{13}S_{23}} + \left| \frac{\sigma_{33}}{Z_C} \right| + \max \left[\frac{\sigma_{13}^2}{S_{13}}, \frac{\sigma_{23}^2}{S_{23}} \right] \quad (2.6.14)$$

,where Z_C represents the matrix strength in the thickness direction.

For the analysis of matrix behaviour in micro-scale FE models, the failure is deemed when meshed stress element achieve a maximum von Mises yield stress [83] or it is controlled by a plastic damage variable [73] (refer to Table 2.7.5).

In general terms, matrix damage modes dominate machining problems [84,85]. Therefore, the insertion of precise matrix failure criteria is essential to enhance the quality of results. In matrix cracking, most of the failure criteria provide similar results that adjust reasonably with experimental findings, see Fig. 2.6.3. Nevertheless, matrix crushing failure criteria differ in their predictions; it is vital to correct a failure model to obtain more accurate results.

The effectiveness of several failures criteria to predict damage in real components were assessed in the well-known exercise denominated as "World-Wide Failure Exercise (WWFE)" [86]. Fig. 2.6.3 represent a few of the failure evaluated in this study, observing that Puck [78] and LARC04 [87] offer the most accurate predictions, while Hashin predictions are quite conservative, as shown in Fig. 2.6.3.

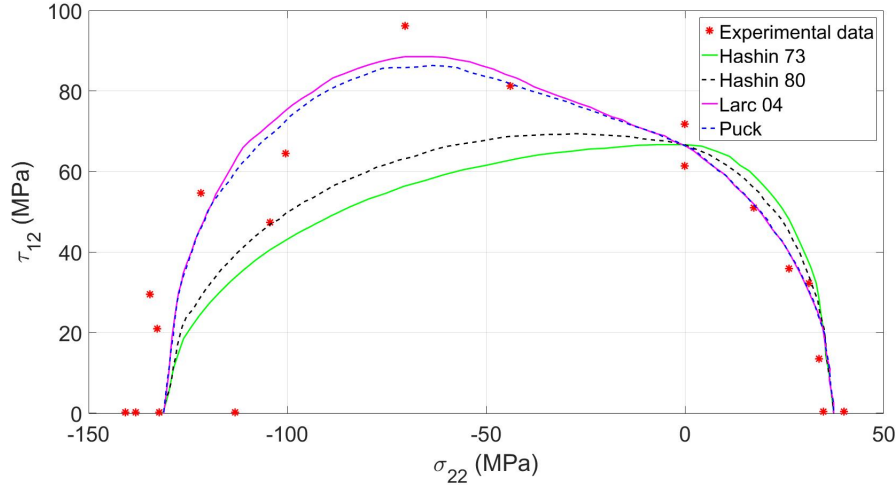


Fig. 2.6.3. Failure envelopes of various composite famous failure criteria adapted from Pinho et al. [87] for unidirectional composites E-Glass/LY556 and the experimental data obtained in the WWFE [86]

Therefore, the use of failure criteria that fit better with experimental results in compression modes is convenient for improving the accuracy of the FE machining models. However, note that the evaluation of failure criteria was carried out under static conditions, without considering any dynamic effects. Thus, the introduction of dynamic terms, such as typical in machining processes, might modify failure models' computational accuracy. For this reason, further investigations need to be performed to achieve a better understanding of this subject [88].

2.6.1.3 Damage evolution

Damage evolution in composite machining are usually modelled using continuum damage mechanics (CDM) approaches, where the initial stiffness is degraded through a damage coefficient d , see Eq. (2.6.15). This variable is initiated immediately after the damage initiation criterion is achieved and evolves from 0 (no damage) to 1, where the damage is developed.

$$X = X_0(1 - d) \tag{2.6.15}$$

where X represents the current damaged property and X_0 is the initial property value.

Two types of damage propagations are found in machining FE models: "ply discount approach" and "energy-based models". Different algorithms are developed in both approaches to reduce stiffness matrix parameters.

- Ply discount approach

The ply discount approach applies discrete damage by the evolution of the damage variable d from 0 to 1 immediately after the damage initiation condition is reached. Because of its simplicity, this is the computational technique most used in FE machining models [89–92].

However, this technique is not suitable for modelling machining problems. The main reason is that this technique introduces serious meshed element distortion problems that

need to be mitigated with the insertion of a remaining stiffness, which is not a real feature of the real-world physical interaction [84]. Additionally, it eliminates the meshed elements before their bearing capacity is reached, thus not achieving accurate results.

- Energy based models

In this kind of models, stresses and strains change following a consistent damage propagation law to dissipate all the energy required to expand a crack. Typically, the energy release term (G_i) for every damage mode is measured considering the displacement (u_i) and stresses (σ_i) at every step as indicated in Eq. (2.6.16).

$$G_i = \int_0^{u_i} \sigma_i du_i \quad (2.6.16)$$

Material behaviour is based on free energy principles. Ignoring plasticity and thermal effects the free energy could be formulated in function of the strain tensor (ε), as shown in Eq. (2.6.17).

$$\Phi := \frac{1}{2} \varepsilon : C : \varepsilon \quad (2.6.17)$$

where the stiffness matrix (C) and stress (σ) can be calculated as:

$$C := 2 \frac{\partial \phi}{\partial (\varepsilon \otimes \varepsilon)} ; \quad \sigma = \frac{\partial \phi}{\partial \varepsilon} \quad (2.6.18)$$

Stiffness degradation properties are inserted using several damage variables (d_{ij}), which are included in a damage tensor (D). These factors are incorporated in the stiffness matrix as shown below:

$$\hat{\sigma} = D(d_{ij})\sigma \quad (2.6.19)$$

A damage propagation law governs the evolution of these damage factors. Most used in the literature for its simplicity are linear [93,94] and exponential [95,96] (refer to Fig. 2.6.4). Other more sophisticated damage algorithms may be selected to capture the fracture material behaviour [29,97,98]. For example, the model proposed by Curiel-Sosa et al. [98] based on surface damage gradient, and strain rate evolution considers the interaction of 6 different damage modes.

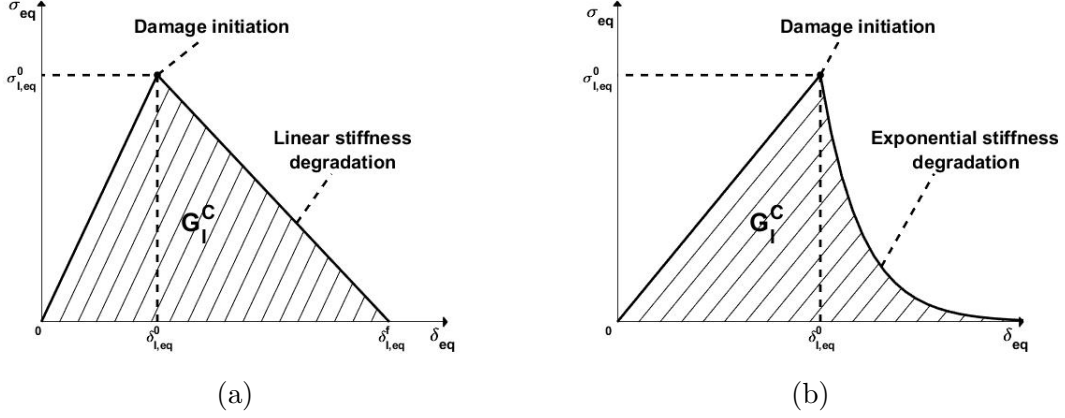


Fig. 2.6.4. CDM approaches schemes using (a) linear and (b) exponential stiffness degradations

$$\dot{\eta}_n = \sum_{\xi=1}^m \Psi_n^\xi d_n^\xi ; \Psi_n^\xi = (\nabla_\varepsilon g_n^\xi \dot{\varepsilon}_n)^{1/p} ; d_n^\xi = \varepsilon_n^T (G_n^{\xi T} + G_n^\xi) / \|\nabla_\varepsilon g_n^\xi\| \quad (2.6.20)$$

In the above equation, n denotes the stress or strain domain's component considered ξ represents the damage mode studied, η is the damage vector associated with the damage mode ξ . Variable g^ξ is the surface on the strain domain, G^ξ refers to the tensor associated with the damage ξ on the strain domain. Ψ^ξ is the increment of the damage variable for a determined damage mode, d^ξ denotes the damage directional vector and p a particular parameter from the composite used that should be adjusted for every particular problem.

Although the implementation of the CDM approach in machining numerical studies is highly recommended to simulate the fracture behaviour in composite materials realistically, it is not widely extended in the existing FE models identified in this literature review. A few 2D FE works covering micro- and macro-scale lengths have used this method [83, 85, 99]. Mostly, the in-built linear law degradation available in Abaqus commands is employed. Damage evolution is controlled by the meshed element displacement, as indicated in Eq. (3.2.17).

$$d_I = \frac{\delta_{I,eq}^f (\delta_{I,eq} - \delta_{I,eq}^0)}{\delta_{I,eq} (\delta_{I,eq}^f - \delta_{I,eq}^0)} \quad (d_I \in [0, 1] \text{ and } I = (ft, fc, mt, mc)) \quad (2.6.21)$$

where $\delta_{I,eq}$ refers to the interfacial equivalent displacement that accounts normal and shear relative displacements components. Final ($\delta_{I,eq}^f$) and initial ($\delta_{I,eq}^0$) equivalent displacements are calculated immediately after a damage initiation condition if one damage mode is reached. The variable I is an indicator of every damage mode processed in this equation - ft = fibre traction, fc = fibre compression, mt = matrix traction and mc = matrix compression.

More advanced investigations in this direction need to be performed to implement the advantages of various previous energy-based CDM approaches in drilling and orthogonal cutting 3D FE models through user-defined subroutines.

Other displacement-based damage approaches could be used, but they are not recommended as post-damage initiation behaviour is not very well-defined the machining of composite behaviour with high strain rates [100].

Another consideration to improve the FE models accuracy is the correct selection of critical fracture toughness properties. It is quite complex to obtain accurate values for every damage mode because of the aforementioned high heterogeneity found in this material; for the fibre and matrix failure modes [70, 101]. Therefore, the use of accurate machined material values should be extracted through experimental studies.

2.6.2 Modelling of fibre/matrix debonding and delamination

The prediction of fibre/matrix debonding and delamination damage play a relevant role in the modelling of composite machining; fibre/matrix debonding is present in all processes, while delamination is significant in drilling applications. Because of these damage types' similar nature, they are modelled following the characteristics of the same principle of an interfacial crack. The most extended fracture mechanics methods employed in machining is the cohesive zone model (CZM). This method offers superior capabilities to predict these damage modes than other methodologies such as crack tip opening displacement (CTOD) or linear elastic fracture mechanics (LEFM) [102].

Cohesive zone modelling (CZM) approach

CZM approach is a well-recognised modelling technique to simulate the crack propagation in Mode I, Mode II and mixed-mode [103]. Cohesive behaviour is mainly implemented in machining works using a bilinear traction separation law [35] (refer to Fig. 2.6.5). It is composed of the same three distinct phases explained previously in composite constituent damage, including a few particularities, which are broken down below.

In the initial elastic response, the interfacial stresses are calculated with a diagonal artificial stiffness matrix that multiplies the displacement, as shown below.

$$\begin{bmatrix} T_n \\ T_s \\ T_t \end{bmatrix} = \begin{bmatrix} K_{nn} & 0 & 0 \\ 0 & K_{ss} & 0 \\ 0 & 0 & K_{tt} \end{bmatrix} \begin{bmatrix} U_n \\ U_s \\ U_t \end{bmatrix} \quad (2.6.22)$$

Here, T_n, T_s and T_t represent the instantaneous stresses in either normal and shear directions to the interface, respectively; K_{nn}, K_{ss} and K_{tt} refer to the instantaneous artificial stiffnesses and U_n, U_s and U_t denote the instantaneous interfacial relative displacements. Artificial stiffness values are recommended to be high enough to simulate the interface behaviour faithfully and prevent crack faces interpenetration [104]. Furthermore, the correct interlaminar strength selection is essential to model the components debonding for mixed-mode fractures [105].

Subsequently, damage initiation is typically determined using a quadratic-nominal stress criterion (Eq. (2.6.23)). The same linear stiffness degradation represented in Eq. (2.6.24) is employed to insert the cohesive behaviour. The critical fracture toughness is calculated using power-law or Benzeggagh-Kenane (BK) criteria, represented in Eqs. (2.6.25) and (2.6.26).

$$\left(\frac{t_n}{t_n^0}\right)^2 + \left(\frac{t_s}{t_s^0}\right)^2 + \left(\frac{t_t}{t_t^0}\right)^2 = 1 \quad (2.6.23)$$

$$d = \frac{\delta_{eq}^f (\delta_{eq} - \delta_{eq}^0)}{\delta_{eq} (\delta_{eq}^f - \delta_{eq}^0)} \quad (d \in [0, 1]) \quad (2.6.24)$$

$$\left(\frac{G_n}{G_n^C}\right)^{a_0} + \left(\frac{G_s}{G_s^C}\right)^{a_n} + \left(\frac{G_t}{G_t^C}\right)^{a_m} = 1 \quad (2.6.25)$$

$$G^C = G_n^C + (G_s^C - G_n^C) \left(\frac{G_s + G_t}{G_n + G_s + G_t}\right)^\eta \quad (2.6.26)$$

In the above equations, t_n , t_s and t_t represent the instantaneous stress values in either normal and shear directions to interface, respectively. t_n^0 , t_s^0 and t_t^0 are the maximum nominal stress when the strain is either purely normal or shear directions to interface, respectively. G_n , G_s and G_t refer to the instantaneous energy release rate in normal shear directions to interface. G_n^C , G_s^C are the critical energy release rate values in normal and first shear direction to the interface. Variables a_0 , a_n and a_m represents the constant exponents of the power law function. The factor G^C represents the critical energy release rate to allow the crack propagation and η is an exponential value.

Although the CZM approach is the modelling technique used in the modelling of composite machining, it has serious difficulties simulating faithfully mixed-mode fracture scenarios as the crack front tends to deviate its stable growth direction and the crack path has to be predefined in this approach. This matter could be solved using other relative novel modelling approaches that treat the modelling of crack deviation more effectively. For instance, eXtended FEM (XFEM) allowing crack propagation through elements with the use of enriched elements or phase field methods (PFM) that crack propagation is governed by the minimisation of the free energy have been proved to model the crack front propagation with high accuracy [106, 107].

The use of XFEM or PFM modelling approaches would simulate the chip release in more detail, which is not studied so far, as modelling strategies erode the laminate elements in contact with the tool using the current strategies to delete meshed elements.

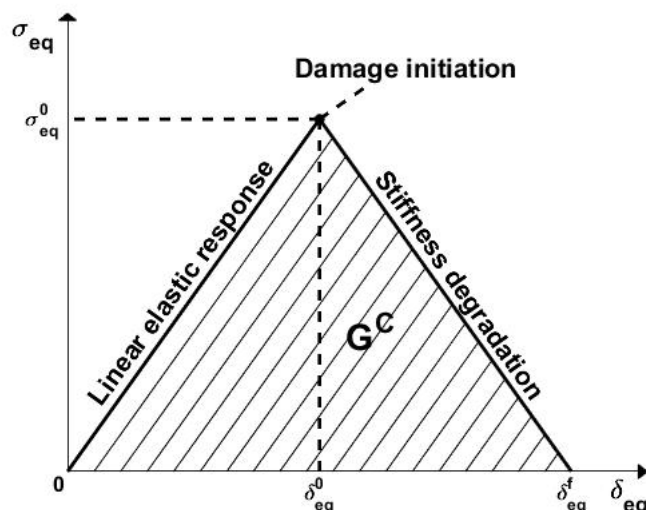


Fig. 2.6.5. Bilinear traction-separation response representation

The cohesive behaviour can be modelled in Abaqus/Explicit using two distinct alternatives:

- Cohesive element.
- Surface-based cohesive behaviour (SBCB) interaction.

Cohesive element

To model cohesive zones, the use of specific interface elements to simulate an adhesive connection is physically inserted with cohesive elements. As a result, it offers remarkable benefits for modelling the debonding process faithfully [102,108]. Non-initial crack or use of cumbersome remeshing techniques is required with this approach, as required in other common crack modelling techniques, such as VCCT [103].

Excellent debonding predictions can be obtained using this technique [35]. The use of small elements to achieve accurate results is required; typical thickness implemented are between 5-10 μm [35]. Thus, this small element size decreases the step time considerably, increasing the computational cost. Another factor to consider is the high peak forces produced by the high artificial stiffness implemented in the cohesive elements at the contact with the tool; these high forces predicted by the model are not realistic and need to be manually removed, increasing notably the post-processing time.

Cohesive elements have been widely used in the computational machining of composites. For instance, drilling [81,82,109] or micro-mechanical orthogonal cutting [72,73,110,111] works simulated successfully laminate delamination or fibre/matrix debonding, respectively using cohesive elements.

Surface-based cohesive behaviour (SBCB) interaction

SBCB interaction is a simplified surface-based method to model the cohesive adhesion of a negligible interface thickness. Results accuracy of the adhesion is higher modelling with cohesive elements. In contrast, SBCB interaction obtains less accurate solution but offers faster solutions and lower computational cost.

This technique mitigates the undesired peak forces obtained with the contact between the cutting tool and cohesive elements due to these elements' high artificial stiffness. It reduces considerably the post-processing time of filtering this undesired force peaks to read the numerical results. These advantages make this approach quite attractive from an industrial point of view, where obtaining quick results is essential.

This technique is mainly used to predict plies debonding; for example, three FE drilling studies [89,90,112] obtained outstanding delamination predictions using cohesive interactions. Another orthogonal cutting simulation [113] remarked the high accuracy predicting delamination of cohesive surfaces compared to the use of user-defined elements using the Hou model.

2.6.3 Future modelling improvements

A fundamental part of the modelling of composites is the simulation of the fracture of cracks. This can be done using numerical software in-built commands or by implementing user-defined subroutines. This fracture is simulated by removing the damaged elements when the failure criterion is met. However, element removal does not effectively emulate the crack fracture physics by roughly removing a large material's area. This factor means that the transmission of contact loads or heat between the elements cannot be developed correctly, reducing the predictions' accuracy. Apart from this statement, this methodology cannot accurately measure the stress concentrations at crack's vicinity that determine its growth direction. As a consequence, significant deviations from the experimental evidence are predicted for crack propagation.

These problems could be solved with the use of other relative novel modelling approaches which treat the modelling of crack deviation more effectively. For instance, eXtended FEM (XFEM) allows crack propagation through elements with the use of enriched degrees of freedom [28,114] or phase field methods (PFM) that models the crack front propagation using minimisation of the free energy principle [106,107,115,116]. The use of XFEM and PFM would notably increase the quality of numerical prediction in terms of machining forces, chip fracture and machining induced damage. This is achieved because both approaches simulate both chip-laminate interaction physics and chip fracture mechanisms with high accuracy. However, the high complexity of these methodologies to simulate unstable crack growths or multiple damage modes difficult their implementation in composite machining. Therefore, an important effort developing effective codes that will allow to implement both approaches in composite machining FE models must be addressed in the future.

2.7 State of the art in the modelling of composite machining

2.7.1 Orthogonal cutting FEM based assessments

Despite orthogonal cutting not being widely employed in composite machining, this operation has been extensively modelled in several publications. The reason for this issue is that these FE models can faithfully study the cutting mechanism which takes place in

other more usual and complex machining operations such as milling [117] or turning [36] with a significant reduction of modelling complexity.

Because of this machining operations' simplicity, most computational studies are developed using 2D FE plane stress models. Two types of FE models are distinguished, macro and micro-mechanical models. Macro mechanical models are relatively simple FE models which have a low pre-processing and low computational cost. Numerical results obtained with these models provide general information about the induced laminate damage formed from machining. Micro-mechanical models, in general, are complex and require high modelling skills to thrive in this kind of analysis. These analyses are potent and can accurately simulate the internal damage inflicted to the fibre and matrix and the debonding between them. In other words, micro-mechanical analysis are more suitable to accurately simulate the composite constituents' damage modes cause in detail, while macro mechanical models are employed for the study of laminate damage modes using heavy FE models.

Macro mechanical models are mainly focused on the analysis of the sub-surface damage causes and chip formation. Several analyses of the influence of cutting parameters, such as rake angle, depth of cut, relief angle, tool edge radius, have been successfully carried out using 2D FE models. However, the damage laws employed in these simulations are basic, and validation of results is carried out through force analysis. The use of sophisticated CDM approaches and the validation of the sub-surface damage's numerical results are highly recommended to enhance the oncoming numerical results' quality.

Few 3D FE models are developed so far because of the high computational time and complexity of this type of analysis. The delamination assessment is still limited in these investigations. An exhaustive literature review in this field revealed that only two publications analysed this variable, see Table 2.7.4. Therefore, an important effort for developing 3D FE models to measure characteristics such as out-of plane-effect, stacking sequence or delamination effects in laminates is required in the future. Furthermore, the use of complex CDM approaches via Vumat and SBCB interaction or cohesive elements is recommended to enhance the intralaminar and interlaminar damage predictions, respectively.

In micro-mechanical models, sophisticated intralaminar and interlaminar modelling approaches have been employed. These FE models require high computational expertise. Typically, the use of zero-thickness cohesive elements using a complex CZM approach and the insertion of elastoplastic or linear stiffness degradation elements is carried out. Good agreement with experimental forces is achieved in these models. Besides, accurate information about the fibre and matrix failure and the fibre matrix debonding is obtained. In the future, the development of 3D FE models could contribute to a better understanding of the delamination or chip formation process in machining.

2.7.1.1 2D Macro-mechanical models

Typically these kind of models are heavy and require long times to run one simulation. For this reason, composites properties are modelled as equivalent homogeneous material (EHM) to reduce the computational cost. An illustration of the composites' elastic and failure properties in various publications is represented in Table 2.7.1 and Table 2.7.2, respectively. Simulation of intralaminar damage is carried out degrading element stresses

to zero when a failure criterion is reached to erode the meshed element under strain-based criteria.

Table 2.7.1. Elastic properties available in the orthogonal cutting modelling of LFRP composites

Material	$E_{11}(GPa)$	$E_{22}(GPa)$	$G_{12}(GPa)$	ν_{12}
GFRP [85, 118]	48	12	6	0.28
CFRP [91, 113]	136.6	9.6	5.2	0.29
CFRP [85]	126	11	6.6	0.28
Gr/Ep [119]	166.9	8.55	5.83	0.33

Table 2.7.2. Strength properties available in the orthogonal cutting modelling of LFRP composites

Material	$X_T(MPa)$	$X_C(MPa)$	$Y_T(MPa)$	$Y_C(MPa)$	$S_{12}(MPa)$
GFRP [85, 118]	1200	800	59	128	25
CFRP [91, 113]	1500	900	27	200	80
CFRP [85]	1950	1480	48	200	79
Gr/Ep [119]	2330	1850	60	90	60

Various approaches have been employed to model the intralaminar damage in 2D FE macro mechanical models, as it is showcased in Table 2.7.3. This table reveals that this field's primary works did not quantify the measured damage in their models. Different enhancements were implemented later to improve the FE models quality, such as using a ply discount approach or elastoplastic model developed by Lasri et al. [84] and Zenia et al. [120], respectively. The composite damage algorithm implemented in the numerical software Abaqus/Cae for modelling these problems deserves a special mention, as it is often used in composite machining modelling, see Table 2.7.3. This algorithm accounts for the Hashin failure criteria to determine the damage initiation. After that, a linear softening of the properties involved in the damage mode is applied to finally erode the element when the fibre is totally damaged ($d_f = 1$). More recently, more sophisticated damage algorithms to improve the numerical accuracy have been implemented as it is visualised in Zhang and Strenkowski [121] investigation.

Table 2.7.3. Intralaminar damage modelling in 2D FE macro mechanical models

Publications	Damage initiation	Damage propagation	Element deletion
Arola et al. [119]	Tsai-Hill and maximum stress	No damage propagation	No element deletion
Bhatnagar et al. [118]	Tsai-Hill	No damage propagation	No element deletion
Lasri et al. [84]	Hoffman, Hashin. . .	Ply discount approach (5%)	No element deletion
Santiuste et al. [85]	Hashin	Linear	Damage controlled ($d_f = 1$)
Soldani et al. [99]	Hashin	Linear	Damage controlled ($d_f = 1$)
Zenia et al. [120]	Yield stress	Controlled by an elastoplastic model	Not specified
Xu et al. [122]	Hashin	Linear	Damage controlled ($d_f = 1$)
Xu and El Mansori [123]	Hashin	Linear	Damage controlled ($d_f = 1$)
Benhassine et al. [124]	Hashin	Linear	Damage controlled ($d_f = 1$)
Zhang and Strenkowski [121]	Hashin	Damage model proposed by Van der Meer and Sluys [125]	Eulerian formulation

The first publication on this topic is carried out by Arola et al. [119] to simulate the machining of a UD GFRP laminate. Several computational analyses with different fibre orientations and rake angles are simulated. Cutting forces are found to be in good agreement with experimental results. For the thrust force, a significant mismatch is obtained between the experimental and numerical results.

Bhatnagar et al. [118] developed an experimental and numerical work of UD-GFRP composites analysing several fibre orientations and depth of cuts. It is found that sub-surface damage increased noticeably for fibre orientations higher than 60° . Besides, an important increment of the sub-surface damage with the increment of the depth-of-cut is appreciated.

Experimental machining forces from Bhatnagar's work [118] are taken to validate other computational publications [84, 85]. Lasri et al. [84] analysed cutting variables such as the sub-surface damage or chip length produced in a UD-GFRP laminate. Three failure criteria are analysed in this work Hashin, Hoffman and Maximum stress. No element erosion is considered, and stiffness degradation of 95% of material properties is applied after one failure criterion is reached. Generally, a high dependency of the studied variables with the fibre orientation is found, see Fig. 2.7.2.

Santiuste et al. [85] compared the sub-surface damage and chip formation of UD-GFRP and UD-CFRP laminates. It is found that UD-CFRP laminates presented brittle behaviour with small sub-surface damaged areas. In the case of UD-GFRP composites, a ductile behaviour with significant sub-surface damage areas is obtained, see Fig. 2.7.1.

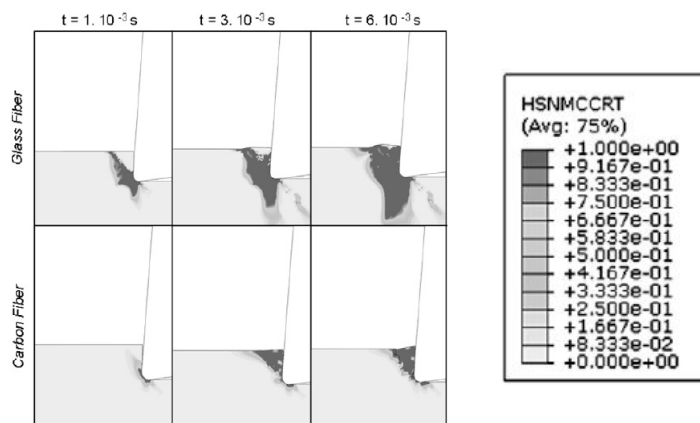


Fig. 2.7.1. Matrix crushing damage area (HSNMCCRT=1) for CFRP and GFRP laminates with a fibre orientation of 45° performed by Santiuste et al. [85]

Soldani et al. [99] performed an analysis of different parameters such as rake angle, tool edge, mesh shape and fracture energy in UD-GFRP composites. Machining forces and sub-surface damage are assessed for several simulations carried out in this work. Interesting conclusions such as the importance of using a sharp tool angle to reduce machining forces and laminate damage are reported.

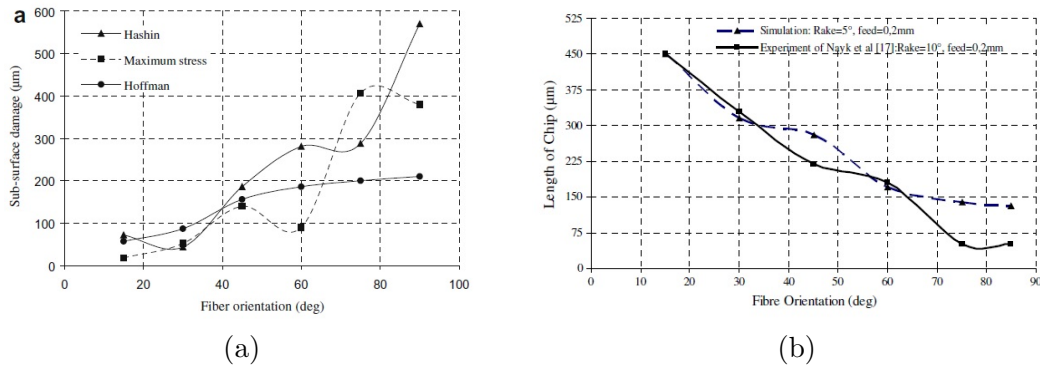


Fig. 2.7.2. (a) Sub-surface damage and (b) chip length with different fibre orientations simulated by Lasri et al. [84]

Zenia et al. [120] measured the influence that cutting parameters have in the sub-surface damage and cutting force of UD-CFRP laminates, see Fig. 2.7.3. Taguchi’s method is used to minimise the number of simulations required. Cutting force and sub-surface damage decreased with an increment of fibre orientation and depth of cut. In contrast, higher rake angles are noted to increase the cutting force and sub-surface damage.

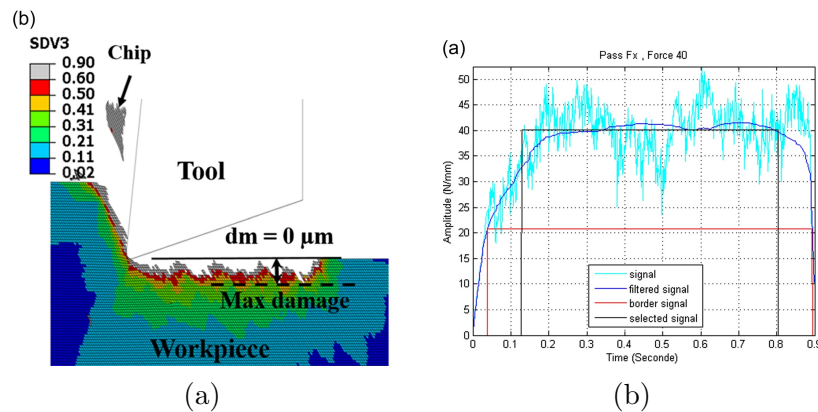


Fig. 2.7.3. Examples of the the measure techniques of (a) cutting force (experimentally measurements and filtered results using a Matlab code) and (b) sub-surface matrix damage obtained in the simulations carried out by Zenia et al. [120]

The machining of CFRP/Ti stack is performed in two publications [122, 123]. The well-known Johnson-Cook constitutive law is employed to model the plasticity and chip removal of the titanium alloy studied. Xu et al. [122] reported that high cutting velocities and low feed rates reduce the sub-surface damage and interface delamination. Xu and El Mansori [123] figured out that the best machining sequence is CFRP → Ti to obtain better surface morphology and less damage on the laminate, see Fig. 2.7.4.

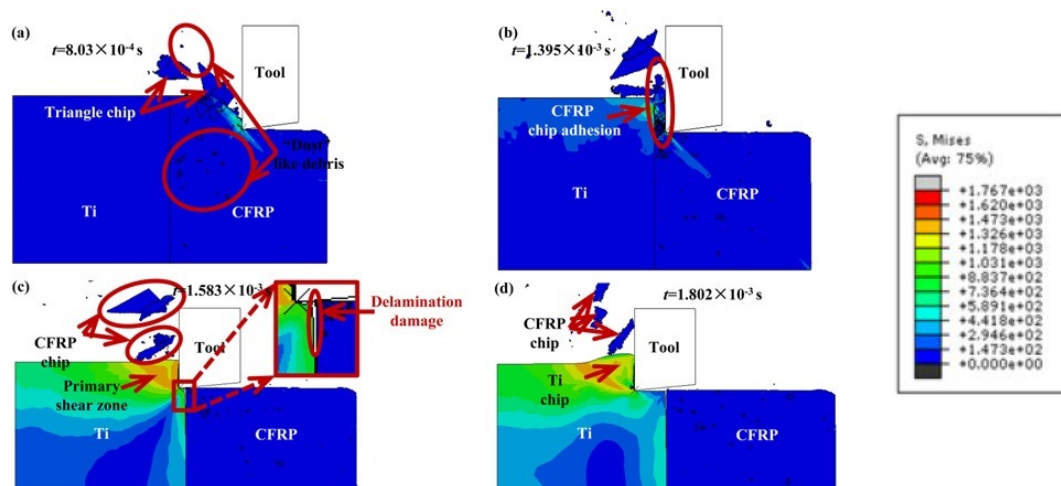


Fig. 2.7.4. Simulation of the cutting process of CFRP/Ti stack simulated (a) cutting CFRP laminate, (b) approaching to the interface, (c) a moment after passing away the interface, (d) Titanium chip formation [123]

Benhassine et al. [124] performed a 2D FE orthogonal cutting model to assess the influence of different rake angles in the machining response of CFRP composites. For this purpose, rake angles of 5° , 10° , 15° and 20° were studied. In general, cutting forces were not changing significantly for the different rake angles studied, while chip formation time is generally delayed using higher rake angles. Sub-surface damage is considerably large for laminates with a fibre orientation of 90° , which should be avoided in a machining process.

Zhang and Strenkowski [121] simulated an Eulerian analysis of UD-CFRP composites combining the FEM with the discontinuous Galerkin method (DGM) to obtain high accuracy in the results. Two damage types are distinguished: (1) interface failure and (2) fibre bending. To compute the fibre bending, a corrector factor that considers the fibre curvature was included, finding that the fibre bending effect is determinant to predict the sub-surface damage accurately.

2.7.1.2 3D Macro- and Meso-mechanical models

Few 3D FE models are developed so far because of the high computational time and complexity of these analyses. Plies delamination is only assessed in two works related to this field, as shown in Table 2.7.4. Therefore, an important effort for developing 3D FE models to measure characteristics such as out-of-plane effect, stacking sequence or delamination effects in laminates is required in the future. Furthermore, the use of complex CDM approaches via user-subroutines and SBCB interaction or cohesive elements is recommended to enhance the intralaminar and interlaminar damage predictions, respectively.

Various 3D FE models have been published in the literature to analyse different machining aspects [42, 43, 91, 113, 126]. As illustrated in Table 2.7.4, these kinds of FEA works focus on the modelling of intralaminar damage, applying different failure criteria via user-defined VUMAT subroutines. Material mechanical properties degradation using a ply discount approach with the subsequent element erosion based on maximum strain criteria is the numerical methodology more implemented. Just a few contributions have studied delamination between plies so far in this kind of FE models. For instance, Santiuste et

al. [91,113] developed a study to predict laminate delamination with the use of user-defined VUMAT subroutines to implement the Hou criterion and the use of SBCB interaction, as shown in Table 2.7.4.

Table 2.7.4. Intralaminar and interlaminar damage modelling in 3D FE macro mechanical models

Publications	Intralaminar damage			Interlaminar damage	
	Damage initiation	Damage propagation	Element deletion	Delamination	
Rao et al. [42]	3D Tsai-Hill	-	Failure criteria is achieved	-	
Santiuste et al. [91]	Hou	Ply discount approach	Maximum strain criteria	Hou criteria	
Santiuste et al. [113]	Hou	Ply discount approach	Maximum strain criteria	Hou criteria and SBCB interaction	
Santiuste et al. [43]	Hou	Ply discount approach	Maximum strain criteria	-	
Wang et al. [126]	Hashin	-	Failure criteria is achieved	-	

Rao et al. [42] simulated the chip formation process in UD-CFRP composites successfully, see Fig. 2.7.5. Various machining variables as rake angle, fibre orientation or depth of cut are assessed in this work. It is found that cutting forces incremented with higher fibre orientations and depth of cuts. The influence of the rake angle in the machining forces is found not to be significant.

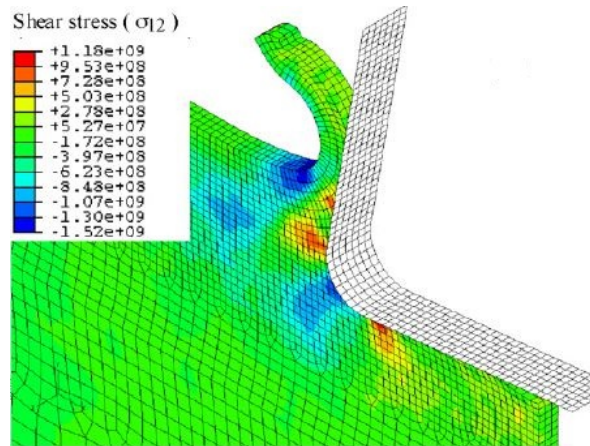


Fig. 2.7.5. Contour plot of stress σ_{12} with a rake angle of 15° and a depth of cut of 0.1 mm simulated by Rao et al. [42]

Santiuste et al. [113] predicted the delamination of a CFRP laminate phenomenon with two models (Hou criteria and SBCB interactions). More realistic delamination results are obtained with the use of SBCB interactions. The more delaminated areas are obtained for interfaces between $0/90^\circ$ and $0/\pm 45^\circ$.

Furthermore, Santiuste et al. [91] developed a delamination study in various CFRP cross-ply laminate to take into account the out of plane effects, refer to Fig. 2.7.6. It is found in thin laminates very similar sub-surface damage to the damage obtained in 2D FE models, while for wide laminates, outer plies suffered a higher deformation. It is concluded that external plies should be composed of plies with low sub-surface damage to avoid future crack nucleation problems.

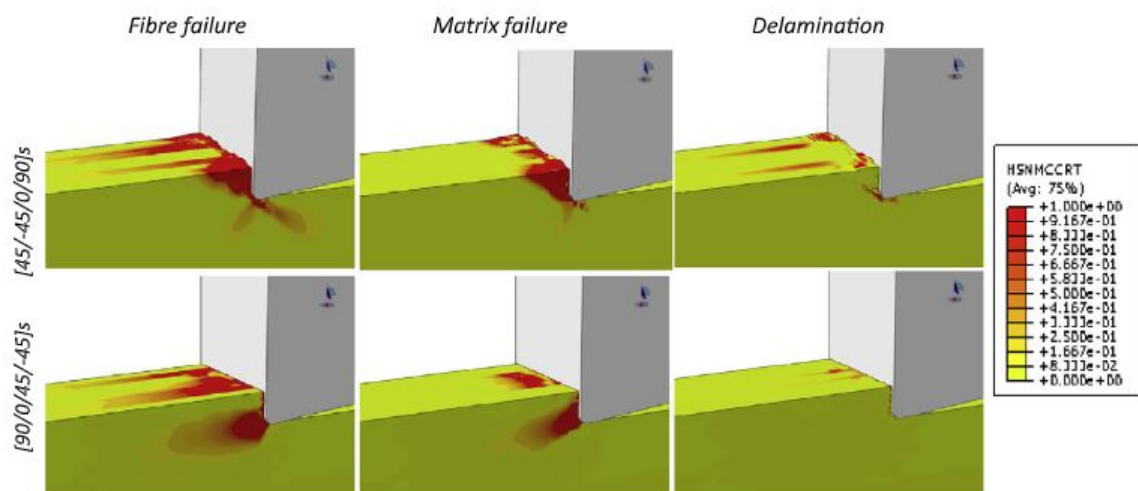


Fig. 2.7.6. Representation of fibre compression, matrix compression and delamination with laminates configurations of [45/45/0/90] and [90/0/45/45] simulated by Santiuste et al. [91]

The same FE model developed in [91] was used to analyse the sub-surface thermal damage developed during an orthogonal cutting process [43]. The thermal damage zone was considered the area enclosed by meshed elements whose temperature exceeded the 150 °C. Despite the heat conduction process is limited for the element deletion, interesting conclusions were extracted from this work. For fibre orientation of 90° and -45° and increment of thermal damage, depth was observed for higher frictional coefficients, while the opposite trend was obtained for fibre orientations of 0° and 45°. Increments in cutting speed were concluded to raise the sub-surface thermal damage for all fibre orientations studied.

Wang et al. [126] developed a 3D FE orthogonal cutting model to assess the machining responses for several fibre orientations of CFRP laminates. Two damage variables were used to evaluate two types of sub-surface damage: vertical depth damaged (F_{dep}) and damaged area (F_a). Because of the different nature of the cutting process in laminates with different fibre orientations, for fibre orientations lower than 90°, F_{dep} provides more representative predictions. In contrast, for fibre orientations superior to 90°, F_a was observed to provide more accurate damage predictions because of the low surface quality obtained in these samples. It was found that high cutting speed and low depth of cuts reduce considerable machining induced damage.

2.7.1.3 Micro-mechanical models

In these models, three separated phases are typically simulated: fibre, matrix and matrix-fibre interface. Commonly glass fibre and matrix are modelled as an isotropic material, while carbon fibre is generally treated as a transversally isotropic material. Simple modelling of fibre damage behaviour is employed, with the meshed element's erosion immediately after maximum stress is reached. The use of CDM approaches with linear stiffness degradations is applied to simulate the matrix's behaviour in various FE investigations [73,111]. However, the highest complexity to develop this kind of works is found in the modelling of fibre/matrix debonding. This matter is mainly addressed using zero-thickness cohesive

elements using various cohesive zone model (CZM) approaches.

Various approaches have been implemented to model the initiation and evolution of the damage via VUMAT [127], or VUEL [73] user-subroutines of Abaqus/Explicit or in-built Abaqus/Explicit commands [72, 111, 128]. Regarding the damage evolution implemented in these model, an exponential degradation is observed to be the preferred option; remarking the degradation employed by Calzada et al. [128] which accounted separately two damages -normal and tangential damage- and degrade mechanical properties with the amount of the highest maximum damage calculated.

These three separated phases are modelled in a small area next to the laminate/tool contact zone to reduce the computational cost. The rest of the model is simulated as an EHM to reduce the computational cost. Few computational works developing micro-mechanical FE models have been modelled due to the high expertise level and high computational cost related to these numerical simulations. Advances obtained in this kind of computational works are exposed in the following lines.

Table 2.7.5. Intralaminar and interlaminar damage modelling in FE micro mechanical models

Fibre behaviour modelling						
Publications	Material behaviour	Damage initiation	Damage propagation	Element deletion		
Cheng et al. [44]	Carbon fibre, transversally isotropic	Maximum stress	-	Failure condition is achieved		is
Abena et al. [127]	Carbon fibre, transversally isotropic	Maximum stress	-	Failure condition is achieved		is
Rao et al. [73]	Carbon fibre, transversally isotropic		Not specified			
Rao et al. [73]	Glass fibre, isotropic		Not specified			
Rao et al. [111]	Glass fibre, isotropic	Maximum stress	-	Failure condition is achieved		is
Calzada et al. [128]	Carbon fibre, transversally isotropic	Maximum stress	-	Failure criteria is achieved		is
Dandekar et al. [72]	Carbon fibre, transversally isotropic		Marigo et al. [129] brittle failure model			
Dandekar et al. [72]	Glass fibre, isotropic	-	-			Shear failure
Matrix behaviour modelling						
Publications	Material behaviour	Damage initiation	Damage propagation	Element deletion		
Cheng et al. [44]	Elastoplastic	Linear	Matrix damage reach 1 ($d_m = 1$)			
Abena et al. [127]	Elastoplastic	Maximum Von stress	misses	-		Failure is achieved
Rao et al. [73]	Elastoplastic	Maximum Von stress	misses	Linear		Maximum plasticity ($\epsilon_{pl} = 0.5$)
Rao et al. [111]	Zero thickness cohesive elements	Maximum Von stress	misses	Linear with plasticity		Matrix damage reach 1 ($d_m = 1$)
Calzada et al. [128]	Zero thickness cohesive elements			Not specified		
Dandekar et al. [72]	Zero thickness cohesive elements	-	-			Shear failure
Fibre/matrix debonding modelling						
Publications	Numerical approach	Traction separation law	Damage initiation	Damage evolution		
Cheng et al. [44]	Zero thickness cohesive elements	Linear-exponential	Maximum interfacial normal and tangential displacements	Quadratic stress criterion	Exponential respect normal or tangential maximum damage	
Abena et al. [127]	Cohesive element, SBCB interaction and user defined behaviour	Bilinear	Maximum interfacial normal and tangential displacements	Quadratic stress criterion	Power law	
Rao et al. [73]	User defined behaviour	Tvergaard's proach [130]	Maximum interfacial normal and tangential displacements	Quadratic stress criterion	Exponential	
Rao et al. [111]	Zero thickness cohesive elements	Bilinear	Maximum interfacial normal and tangential displacements	Quadratic stress criterion	Power law	
Calzada et al. [128]	Zero thickness cohesive elements	Linear-exponential	Maximum interfacial normal and tangential displacements	Quadratic stress criterion	Exponential respect normal or tangential maximum damage	
Dandekar et al. [72]	Zero thickness cohesive elements	Not specified	Maximum interfacial normal and tangential displacements	Quadratic stress criterion	Energy based evolution	

Dandekar and Shin [72] simulated an entire model with three distinctive separated phases. A CZM approach based on Tvergaard's traction separation law [130] is used for predicting the matrix-fibre debonding. Marigo brittle failure model [129] is implemented to predict the carbon fibre damage, reproducing faithfully the fibre behaviour observed in the experiments. The model achieved good machining forces, debonding at front and rear sides

of the interface and fibre failure predictions. Various limitations are found in this work. For instance, the matrix damage is not taken into account.

Calzada et al. [128] considered two failure damage modes: (1) bending dominated and (2) crushing dominated. For fibre orientations of 0° and 135° , the crushing dominated failure is predominant, while fibres at 45° and 90° the crushing dominated failure mode is taken place. Finally, a modelled new tool demonstrated that the use of high rake angle (50°) and sharp tool nose radius ($1\mu\text{m}$) reduce the sub-surface damage considerably, see Fig. 2.7.7).

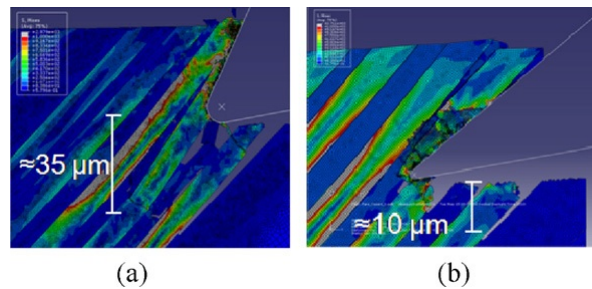


Fig. 2.7.7. Sub-surface damage for different tool geometries (a) original tool and (b) new tool geometry obtained by Calzada et al. [128]

Rao et al. [73] modelled a two-phase orthogonal cutting FE model of UD-GFRP and UD-CFRP composites to analyse the cutting forces in a range of fibre orientations, rake angles and depth of cuts. Thrust and cutting forces are accurately predicted in this model. Fibre failure is found to be a combination of crushing and bending modes. Bending effects are observed to become more critical for fibre orientations from 90° to 15° for both composites studied. In the case of 90° in UD-GFRP composites, the failure is caused by the crushing at the cutting tooltip and the adjacent fibre's bending. While for UD-CFRP laminate with a fibre orientation of 90° , fibre bending is the most critical fracture mode.

Rao et al. [111] studied the chip formation mechanism for UD-GFRP composites. It is found that the matrix failure occurred first, then a fibre failure of the adjacent to the failed matrix took place, as shown in Fig. 2.7.8. Chip length is found to be dependent on the height of the tool-workpiece contact and the machined surface. The higher this height is, the less damage is obtained. Thus, chip length is observed to decrease from fibre orientation from 15° to 90° .

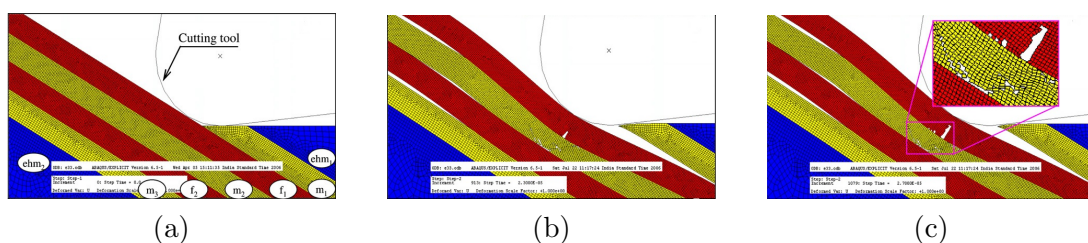


Fig. 2.7.8. Damage in matrix (m_1 , m_2 and m_3), fibre (f_1 and f_2) and fibre-matrix interface with a fibre orientation of 30° and a depth of cut of 0.2 mm for different tool displacements (a) $0\ \mu\text{m}$, (b) $21.2\ \mu\text{m}$ and (c) $21.41\ \mu\text{m}$ assessed by Rao et al. [111]

Finally, a new trend in the modelling of machining composites is the development of 3D micro-mechanical models. More sophisticated FE strategies capable of reducing the high

computational cost necessary to solve these numerical analyses must better understand the machining parameters' influence in the local damage development in cross-ply laminates.

Abena et al. [127] implemented a novel approach in a 3D FE model to simulate the matrix-fibre interface delamination in a UD-CFRP laminate, see Fig. 2.7.9. The new modelling approach deleted the interface elements after the surrounding failed for compressive modes. It is compared with other well-known modelling delamination approaches such as SBCB and cohesive elements. In general terms, the computational cost is considerably reduced, and accurate delamination predictions are obtained.

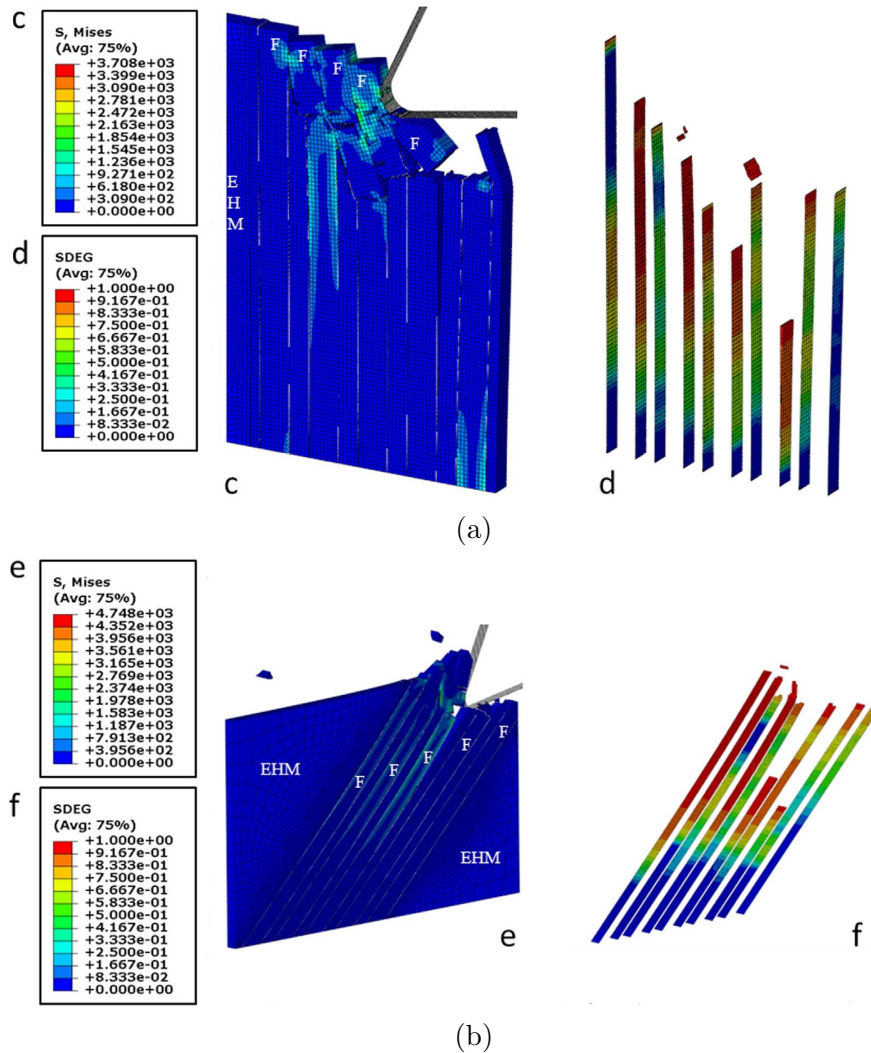


Fig. 2.7.9. Chip formation mechanism and cohesive damage (SDEG) obtained with the new approach developed by Abena et al. [127] for fibre orientations of (a) 90° and (b) 135°

Thermal matrix effects were considered in the thermo-mechanical coupled FE model proposed by Cheng et al. [44], see Fig. 2.7.10. This novel approach achieves predictions in the machining of UD-CFRP laminates an excellent agreement with experimental cutting forces. Interesting conclusions are extracted from this work, such as that interfacial and matrix damage are more severe than fibre damage or negative fibre orientations increase the fibre abruptly bending and surface roughness.

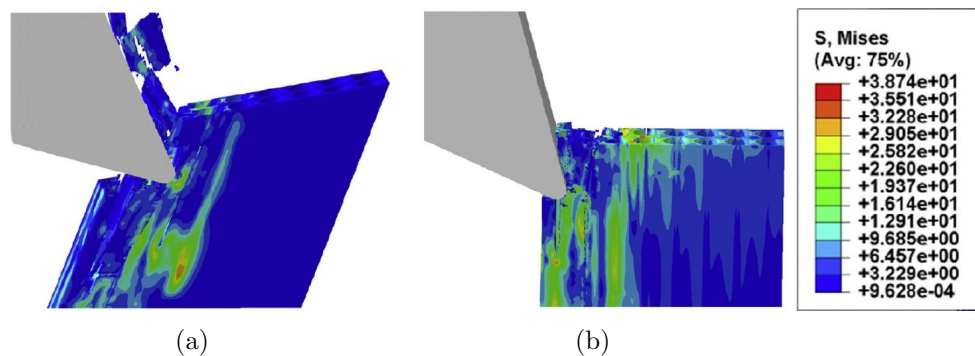


Fig. 2.7.10. Laminate stresses and chip fragment simulated in [44] for laminates with fibre orientations of (a) 60° , (b) 90° .

2.7.2 Drilling FEM based assessments

Due to the complex interaction between drill bits and workpiece, any spatial component effects can be neglected in the modelling of drilling operations. Hence, it is not recommendable to model this machining operation with a 2D FE model. Nevertheless, simplifications could be taken as, for instance, the modelling of the tool as a solid rigid body or the development of simplified models to reduce the high computational time required for the simulation of these numerical models. In addition, a high pre-processing cost should be assumed to model the complex drill bit morphologies using advanced design software packages such as Catia or Solid work.

Good examples of the values of elastic and failure properties used in drilling modelling investigations are collected in Table 5.2.1 and Table 5.2.2, respectively. Mostly, the intralaminar damage is implemented via VUMAT user-subroutine using a ply discount approach. Meshed elements erosion is performed immediately after a maximum strain is achieved to avoid distortional problems.

Table 2.7.6. Elastic properties examples used in drilling modelling

Publications	E_{11}	$E_{22} = E_{33}$	$G_{12} = G_{13}$	G_{23}	$\nu_{12} = \nu_{13}$	ν_{23}
Wang et al [112]	153GPa	10.3GPa	6 GPa	3.7GPa	0.3	0.4
Phadnis et al [81]	127GPa	9.1GPa	5.6GPa	4GPa	0.31	0.45
Isbilir et al [89]	112GPa	8.2GPa	4.5GPa	3GPa	0.3	0.4
Makh dum et al [21]	115GPa	14GPa	4GPa	3.2GPa	0.29	-

Table 2.7.7. Failure properties examples of the drilling modelling

Publications	X_T	X_C	Y_T	Y_C	S_{12}	S_{23}
Wang et al [112]	2537MPa	1580MPa	82MPa	236MPa	90MPa	40MPa
Phadnis et al [81]	2720MPa	1690MPa	111MPa	214MPa	115MPa	115MPa
Isbilirr et al [89]	1900MPa	1000MPa	84MPa	250MPa	60MPa	110MPa

Table 2.7.8. Intralaminar damage modelling in 3D FE drilling models

Publications	Damage initiation	Damage propagation	Element deletion
Phadnis et al. [81]	Hashin for fibre and Puck for matrix Eq. (2.6.13)	-	Failure criteria is achieved
Feito et al. [109]	Hou	Ply discount approach	Maximum strain criteria
Feito et al. [82]	Maximum stress Eq. (2.6.14)	+	Ply discount approach Maximum strain criteria
Feito et al. [131]	Maximum stress Eq. (2.6.14)	+	Ply discount approach Maximum strain criteria
Islibir et al. [90]	Hashin	Ply discount approach	Not specified
Islibir et al. [89]	Hashin	Ply discount approach	Not specified
Wang et al. [112]	Hashin	-	Failure criteria is achieved

Delamination is modelled using both cohesive elements, and cohesive interactions approach to implement a bilinear traction-separation response (refer to Fig. 2.6.5). In all works exposed in this section, damage initiation is assessed via the quadratic stress criterion (Eq. (2.6.23)), while delamination grow is mostly determined by the power law energy criterion- refer to Eq. (2.6.25)- as shown in Table 2.7.9.

Table 2.7.9. Interlaminar damage modelling in 3D FE drilling models

Publications	Modelling approach	Damage initiation	Damage propagation	Damage evolution
Phadnis et al. [81]	Cohesive elements	Quadratic stress criterion	Linear	Power law
Feito et al. [109]	Cohesive elements	Quadratic stress criterion	Linear	Power law
Feito et al. [82]	Cohesive elements	Quadratic stress criterion	Not specified	Power law
Feito et al. [131]	Cohesive elements	Quadratic stress criterion	Not specified	Power law
Islibir et al. [90]	SBCB interaction	Quadratic stress criterion	Linear	Power law
Islibir et al. [89]	SBCB interaction	Quadratic stress criterion	Linear	Power law
Wang et al. [112]	SBCB interaction	Quadratic stress criterion	Linear	Benzeggagh-Kenane

Thrust force, torque and Fd are assessed for several cutting speeds and feed rates. Influence of drill bit geometry, tool wear, feed rate or thrust forces or stacking sequence on laminate delamination have been performed up to now. However, delamination effects of special drill bits, tool wear or resin thermal analysis have not been extensively investigated up to date. Hence, significant effort is required in the future to cover these unexplored areas as well as simplify FE models complexity.

Because of the high complexity involved in modelling these machining operations, not many publications have been published so far. Most papers are focused on the investigation of delamination at entry and exit of the laminate causes. Various researchers modelled delamination between plies using cohesive elements [81, 82, 109, 131]. Values of relevant variables to model delamination used in the literature are presented in Table 5.2.3.

Table 2.7.10. Interlaminar artificial stiffness and strengths examples in the drilling modelling

Publications	t_n	$t_s = t_t$	K_{nn}	$K_{ss} = K_{tt}$	G_n^c	$G_s^c = G_t^c$
Wang et al [112]	60MPa	110MPa	$10^6 N/mm^3$	$236 N/mm^3$	90N/mm	40N/mm
Phadnis et al [81]	60MPa	90MPa	$4x10^6 N/mm^3$	$214 N/mm^3$	115N/mm	115N/mm
Feito et al [109]	60MPa	90MPa	$4x10^6 N/mm^3$	$250 N/mm^3$	60N/mm	110N/mm

Phadnis et al. [81] studied the delamination at entry and exit of a cross-ply CFRP laminate with a stacking sequence of $[0_4/90_8/0_4]$. The drill bit simulated is a jobber carbide TiN-coated twist drill bit, and a back-up plate to reduce delamination at laminate exit is added,

as shown in Fig. 2.7.11. Numerical delamination at entry and exit results is obtained in good agreement with experimental results to validate the model. It is found that low feed rates and high cutting speeds reduced delamination, thrust force and torque.

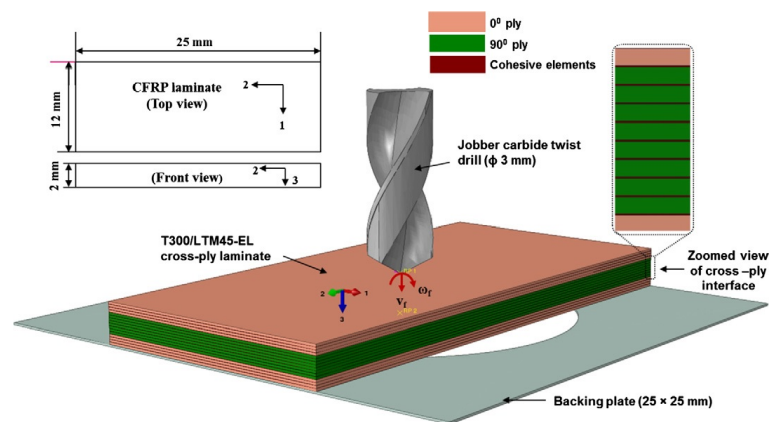


Fig. 2.7.11. Numerical drilling model developed by Phadnis et al [81]

Feito et al. [109] carried out a simplified numerical model to considerably reduce the simulation's computational time. This simplified model only took into account the vertical movement of a twist drill. Simplified model results are validated, obtaining similar results of the delamination simulated with the standard FE model, which considered the tool feed and rotatory movements, as shown in Fig. 2.7.12. Thrust force, below clamping area and stacking sequence effects on delamination are successfully assessed with the simplified model. Computational time is reduced from several days needed for the complete model to some hours required for the simplified model.

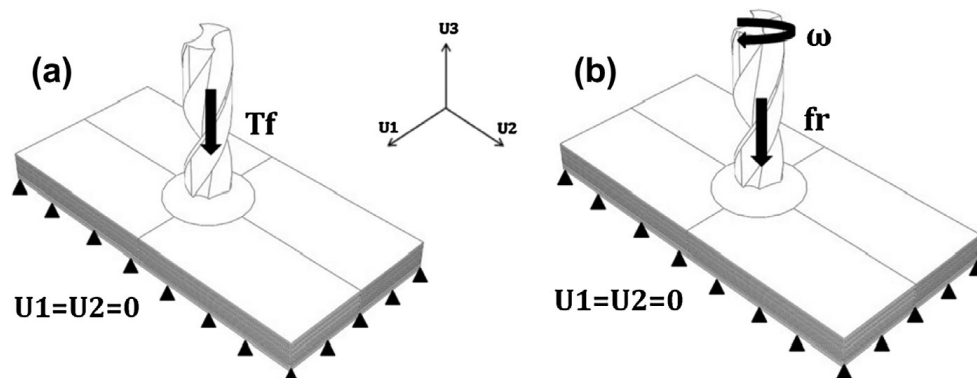


Fig. 2.7.12. (a) Complete and (b) simplified FE models simulated by Feito et al [109]

Feito et al. [82] assessed the tool wear delamination effects on woven carbon fibre laminates. New and honed edge twist drill and step drill bits are successfully simulated, see Fig. 2.7.13. Significant higher thrust force and delamination values are obtained for the honed edge drill bit compared to the new drill bit results. Low feed rates are demonstrated to reduce delamination and thrust force. High cutting velocities are observed to reduce the delamination and thrust force for the edge honed drill bit. The cutting velocity effects on delamination and thrust force are not relevant for the new drill bit. It is remarked that the modelling scheme proposed in this work could be used for other tool wear modes.

Feito et al. [131] investigated the effect of machining settings on thrust force and delamination of woven CFRP laminates using a step drill. The numerical values obtained in this analysis are used to adjust mechanic models to rapidly predict the delamination and thrust forces expected under a determined machining configuration. The authors concluded that with increasing feed rate and cutting speed, the delamination and thrust forces are steadily incremented.

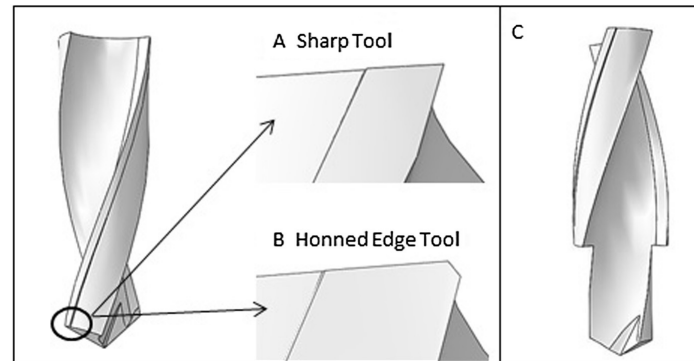


Fig. 2.7.13. Drill bits geometry studied by Feito et al [82]

SBCB interaction is used in other publications obtaining interesting insights in the modelling of composite drilling [89, 90, 112]. Isbilir et al. [89] developed a 3D FE model to simulate a CFRP laminate drilling. Numerical results of entrance delamination, thrust force and torque are found in good agreement with experimental results. A detailed convergence mesh study is performed to avoid numerical errors, reaching a final fine mesh around the hole with an element size of 0.26 mm and an aspect ratio of 1.

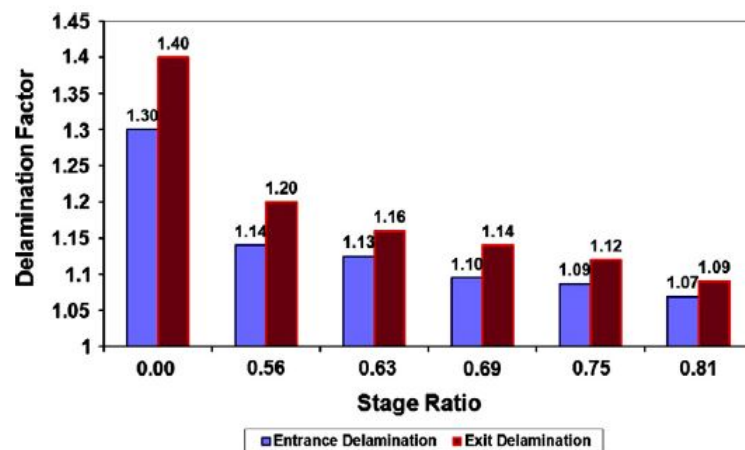


Fig. 2.7.14. Delamination extension at entry and exit of the laminate after drilling using step drill bits with different stage ratio obtained by Islibir et al. [90]

Wang et al. [112] measured the delamination at the top and bottom of CFRP/Al laminates of various stacking sequences. It is found that between the three stacking sequences studied, the configuration $[-45/90_4/45_2/-45]_{3s}$ achieved the lower level of delamination. Finally, Isbilir et al. [90] conducted a numerical investigation of the effect that the stage ratio of step drill bits has in the machining responses of CFRP laminates. Authors

concluded from their numerical simulations that operating with a high step ratio is vital to reduce delamination levels considerably, as shown in Fig. 2.7.14.

2.8 Chapter summary

The advantages and disadvantages of the composite laminates' finite element modelling using 2D shell-based models and 3D solid element models were analysed. In general terms, 2D FE models provide high in-ply accuracy solutions with low pre-processing and low computational cost, while 3D models offer a high accuracy to predict interlaminar stresses and through-thickness damages.

The characteristics of FE models to simulate composite discrete damage at different length scales is discussed. Micro-mechanical models offer a high accuracy to predict, visualise and analyse local failure types, but in exchange, high pre-processing time and high computational cost are demanded in these models. In contrast, meso-mechanical and macro-mechanical models reduce notably the simulation's computational cost, although they cannot visualise the local fibre or matrix failure types. Considering that there must be a balance between the available computational resources and the computational cost required by the model, the selection of the macro-mechanical models developed in this thesis is justified.

The characteristics of Implicit and Explicit solvers to obtain a numerical solution were discussed. This discussion aims to analyse which method should be more suitable to model composite machining operations. It was concluded that an Explicit framework offers better capabilities because it considers the inertial forces and the facility to achieve the convergence in complicated contacts characteristic of composite machining.

This document has provided a comprehensive review of the computational machining FEM studies available so far. A discussion of the advantages and disadvantages of FEM modelling approaches applied to predict composite damage modes in machining applications has been performed. Computational composite drilling analysis has required the use of complex and high computational cost FE models. These works have been focused on investigating cutting parameters influence on the delamination between plies. In the case of orthogonal cutting, they have been more focused on studying the causes that produce the machining induced damage. Two types of FE have been distinguished: macro-mechanical and micro-mechanical models. Both FE models have decreased their computational cost with the use of 2D FE models. Several conclusions have been extracted from this article:

- More sophisticated FE model needs to be developed to simulate more complex composite machining operations such as edge trimming, oblique cutting or milling to optimise these processes.
- Implementation of the relative novel modelling approaches such as XFEM or PFM has the potential to improve the quality of numerical simulations in the prediction of chip formation and damage incrementally.
- Cutting process variables such as tool wear, ply stacking sequence or cutting tool type influence on delamination and other forms of composite-specific damage are not widely investigated in drilling models and should be studied in more detail.

- Development of thermo-mechanical coupled FE models and inclusion of matrix plasticity on the computational composite machining analyses is required to improve the numerical results' reliability.
- The use of subroutines to introduce advanced CDM approaches and the measurement of critical energy release rates are necessary to enhance numerical predictions.
- Use of user-defined subroutines to model delamination is highly recommended to insert customised properties in the elements such as thermal or non-linear stiffness degradation.
- The use of advanced computational techniques such as SBCB interaction to model delamination is highly recommended to increase numerical prediction accuracy in orthogonal cutting macro mechanical models.
- The development of 3D FE micro-mechanical models is necessary to understand better the fibre-matrix debonding in machining processes.
- In order to establish the reliability and accuracy of future models in accurately predicting chip formation and damage, further validation beyond typical cutting force measurements should be undertaken. The sub-surface damage could be experimentally validated through either destructive or non-destructive methods.

In this thesis, a methodology for studying the basis of the machining of composites will be developed. A damage algorithm based on a continuum damage mechanics (CDM) approach will be applied to macro mechanical models to study the sub-surface damage and chip formation causes in composite machining. Additionally, an investigation of a typical industrial edge trimming process will be addressed to show the damage model's capabilities to provide attractive solutions in real machining problems.

In the following chapter, the damage model proposed to simulate the FE models proposed in this research will be explained. The details to include this damage model in the simulation via a user-defined VUMAT Fortran subroutine will be explained. Finally, the validation of the proposed damage model will be assessed, comparing the numerical results obtained from two tensile test simulations with fibre orientations of 0° and 90° with experimental findings.

Chapter 3

2D and 3D composite damage model

3.1 Introduction

In this research, a constitutive composite damage model based on the CDM approach is developed due to its high capabilities to simulate composite damage types' onset and posterior evolution accurately. The complex interaction between composite constituents and the coalescence of several damage types makes the modelling of composite behaviour a cumbersome venture. Therefore, the numerical problems listed below need to be dealt with to achieve a robust and accurate FE model.

- The implementation of a massive amount of parameters and equations is usually necessary, which entails a considerable increase in computational cost.
- The implementation of complex parameters is usually required.
- The physical meaning of the variables to determine the constitutive law is insufficient in many cases.
- Mesh size dependency is generally high in this kind of FE models
- The usual brittle behaviour simulated in this kind of models usually does not account for the total fracture energy

This material model should implement all the necessary parameters to introduce a ply behaviour's physics accounted in a CDM approach. Additionally, these parameters should have a rigorous physical meaning and be easily obtained or induced from the experimental trials. Note that it does not exist an exact CDM model to model the composite ply behaviour during machining operations. Hence, the implementation of specific considerations in the constitutive law must be performed to model a single ply's mechanical response and fracture reliably. Hence, to guarantee the development of a useful material constitutive law in the modelling of composite machining applications, the fulfilment of the following objectives have been addressed in this research.

- The parameters used should be the minimum as possible to simulate the material constitutive law.

- The parameters' values to determine the strength or mechanical properties of a ply should have a definite physical meaning.
- The mesh sensitivity should be low to guarantee the accuracy of the numerical results.
- The mechanical properties degradation and element deletion should be included in the material damage to recreate the chip formation and the laminate's mechanical response.
- Separate fibre and matrix damage types are evaluated separately, degrading the properties of their corresponding stiffness matrix coefficients.

This chapter encompasses all fundamentals of the numerical damage algorithms implemented during the development of this thesis. Two damage algorithms have been performed damage progression during machining operation in 2D and 3D FE models. These damage algorithms have been implemented in Abaqus/Explicit software package via Fortran user-defined VUMAT subroutine. More detailed information about the particularities implemented in different machining investigations can be found in the following chapters.

3.2 2D and 3D machining damage algorithm fundamentals

In this section, a clear explanation of the damage algorithms implemented during this thesis's development is provided. 2D and 3D damage algorithms have been carried out to study different insights into the machining of composites. The four most relevant characteristics for the right understanding of these algorithms are: (1) implementation of the damaged constitutive model, (2) damage initiation, (3) damage propagation and (4) element deletion. More detail information is broken down in the following lines.

3.2.1 Implementation of the damaged constitutive model

It is public domain that a deformable solid's stress and strain are intimately linked by the constitutive equations of the material investigated. If one of these magnitudes, strain or stress is known, the unknown magnitude could be easily inferred using the compliance matrix or the stiffness matrix, respectively.

$$[\varepsilon_{ij}] = [S_{ij}] [\sigma_{ij}] \quad (3.2.1)$$

$$[\sigma_{ij}] = [C_{ij}] [\varepsilon_{ij}] \quad (3.2.2)$$

Abaqus strains are inputs at every simulation step, and the damaged stiffness matrix needs to be calculated to update the stresses at the end of every simulated step. Stiffness matrix (C_{ij}) is obtained as the inverse of the compliance matrix (S_{ij}^{-1}), as showcased in Eq. (3.2.3). This relation will be used in the following subsections to obtain the final damaged stiffness matrix used for the simulations covered in this thesis.

$$C_{ij} = S_{ij}^{-1} \quad (3.2.3)$$

3.2.1.1 Implementation of the 2D damaged constitutive model

In the case of 2D FEM analysis, the damage model is initially inserted in the compliance matrix using the same methodology proposed by Lapczyk and Hurtado [93]. In this formulation, four different damage modes are present: fibre traction (d_{ft}), fibre compression (d_{fc}), matrix traction (d_{mt}) and matrix compression (d_{mc}). Hereafter, the combination of these damage modes inside the compliance matrix (S_{ij}) is showcased in Eq. (2.6.22).

$$[S_{ij}] = \begin{bmatrix} \frac{1}{(1-d_f)E_{11}} & \frac{\nu_{12}}{E_{11}} & 0 \\ \frac{\nu_{21}}{E_{22}} & \frac{1}{(1-d_m)E_{22}} & 0 \\ 0 & 0 & \frac{1}{(1-d_s)G_{12}} \end{bmatrix} \quad (3.2.4)$$

, where $d_s = 1 - (1-d_{ft})(1-d_{fc})(1-d_{mt})(1-d_{mc})$ $d_f = \max\{d_{ft}, d_{fc}\}$; $d_m = \max\{d_{mt}, d_{mc}\}$
 $d_I \in [0, 1]$ and $I = (ft, fc, mt, mc)$

However, for Abaqus strains are inputs at every simulation step and the damaged stiffness matrix needs to be calculated to update the stresses at the end of every simulated step. Stiffness matrix (C_{ij}) is obtained as the inverse of the compliance matrix (S_{ij}^{-1}), leaving the follow expression,

$$[C_{ij}] = \frac{1}{D} \begin{bmatrix} (1-d_f)E_{11} & (1-d_f)(1-d_m)\nu_{21}E_{11} & 0 \\ (1-d_f)(1-d_m)\nu_{12}E_{22} & (1-d_m)E_{22} & 0 \\ 0 & 0 & D(1-d_s)G_{12} \end{bmatrix} \quad (3.2.5)$$

, where $D = 1 - (1-d_f)(1-d_m)\nu_{12}\nu_{21}$

3.2.1.2 3D damaged stiffness matrix implementation

For the 3D case, the same idea to implement the damage model used for 2D simulations is kept. Six different damages are studied in this model: two for fibres (d_{ft} and d_{fc}), two for matrix in the ply plane -transverse to the fibre- (d_{mt2} and d_{mc2}) and two for matrix in the thickness direction (d_{mt3} and d_{mc3}). All these damages are combined in the compliance matrix as follows,

$$[S_{ij}] = \begin{bmatrix} \frac{1}{(1-d_f)E_{11}} & -\frac{\nu_{12}}{E_{11}} & -\frac{\nu_{13}}{E_{11}} & 0 & 0 & 0 \\ -\frac{\nu_{21}}{E_{22}} & \frac{1}{(1-d_{m2})E_{22}} & -\frac{\nu_{23}}{E_{22}} & 0 & 0 & 0 \\ -\frac{\nu_{31}}{E_{33}} & -\frac{\nu_{32}}{E_{33}} & \frac{1}{(1-d_{m3})E_{33}} & 0 & 0 & 0 \\ 0 & 0 & 0 & \frac{1}{(1-d_{s1})G_{12}} & 0 & 0 \\ 0 & 0 & 0 & 0 & \frac{1}{(1-d_{s2})G_{13}} & 0 \\ 0 & 0 & 0 & 0 & 0 & \frac{1}{(1-d_{s2})G_{23}} \end{bmatrix} \quad (3.2.6)$$

Here, $d_{s1} = 1 - (1-d_{ft})(1-d_{fc})(1-d_{mt2})(1-d_{mc2})$; $d_{s2} = 1 - (1-d_{ft})(1-d_{fc})(1-d_{mt3})(1-d_{mc3})$

$d_{s3} = 1 - (1-d_{mt2})(1-d_{mc2})(1-d_{mt3})(1-d_{mc3})$

$d_f = \max\{d_{ft}, d_{fc}\}$; $d_{m2} = \max\{d_{mt2}, d_{mc2}\}$; $d_{m3} = \max\{d_{mt3}, d_{mc3}\}$

$$d_I \in [0, 1] \text{ and } I = (ft, fc, mt2, mc2, mt3, mc3)$$

Operating the following terms are the components of the final damaged stiffness matrix.

$$\begin{aligned}
 C_{11} &= E_{11}(1 - d_f) [1 - (1 - d_{m2})(1 - d_{m3})\nu_{23}^2] / A \\
 C_{12} &= E_{22}(1 - d_f)(1 - d_{m2}) [(1 - d_{m3})\nu_{13}\nu_{23} + \nu_{12}] / A \\
 C_{22} &= E_{22}(1 - d_{m2}) [1 - (1 - d_f)(1 - d_{m3})\nu_{13}\nu_{13}] / A \\
 C_{13} &= E_{33}(1 - d_f)(1 - d_{m3}) [(1 - d_{m2})\nu_{12}\nu_{23} + \nu_{13}] / A \\
 C_{33} &= E_{33}(1 - d_{m3}) [1 - (1 - d_f)(1 - d_{m2})\nu_{12}\nu_{21}] / A \\
 C_{23} &= E_{33}(1 - d_{m2})(1 - d_{m3}) [(1 - d_f)\nu_{12}\nu_{31} + \nu_{23}] / A \\
 C_{44} &= G_{12}(1 - d_f)(1 - d_{m2}) \\
 C_{55} &= G_{13}(1 - d_f)(1 - d_{m3}) \\
 C_{66} &= G_{23}(1 - d_{m2})(1 - d_{m3})
 \end{aligned} \tag{3.2.7}$$

$$\begin{aligned}
 \text{with } A &= 1 - (1 - d_f)(1 - d_{m2})\nu_{12}\nu_{21} - (1 - d_{m2})(1 - d_{m3})\nu_{23}^2 - (1 - d_f)(1 - d_{m3})\nu_{13}\nu_{31} \\
 &\quad - 2(1 - d_f)(1 - d_{m2})(1 - d_{m3})\nu_{12}\nu_{31}\nu_{23}
 \end{aligned}$$

3.2.2 Minimisation of the mesh element size dependency

Typically, in continuum mechanics, models with strain-softening behaviour show high mesh-size sensitivity. This statement occurs due to the strain localisation in a determine area when this reaches the peak stress value, which starts the mechanical degradation. Subsequently, all the strain accumulated in the surrounded elements tends to migrate to these damaged elements. Thus, all the energy dissipation is concentrated in small areas leading to a drastic reduction of the global fracture energy simulated in the FE model. The idea developed in this paragraph could be visualised in the tensile test developed by Lapczyk and Hurtado [93], refer to Fig. 3.2.1(b). In this model, after damage onset occurs, all the strain is confined in elements allocated in a line perpendicular to the load direction, as shown in Fig. 3.2.1(a).

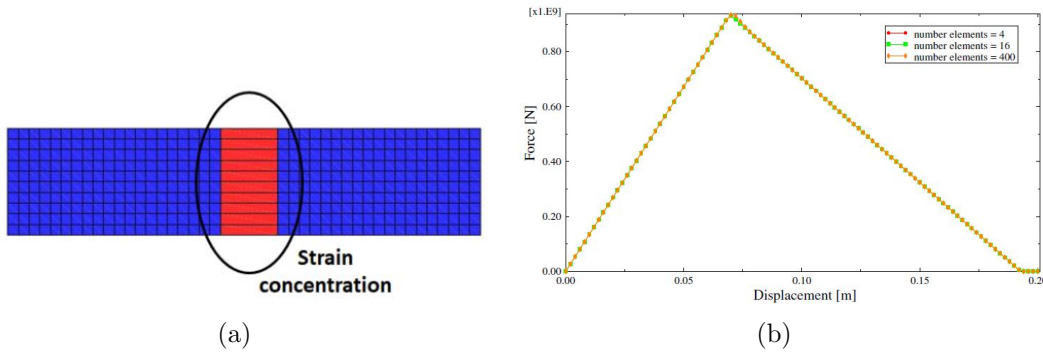


Fig. 3.2.1. Tensile test simulated by Lapczyk and Hurtado [93] to show the reduction of the mesh size dependency in a composite behaviour with a linear softening (a) Strain localised band, (b) Stress-strain graphs obtained for different number of elements.

The Bazant's crack band model and Oh [132] is employed to alleviate this high mesh size dependency. It is achieved by making the equivalent fracture strain dependant on every

mesh element's characteristic element size (L_c). In other words, this model adjusts the value of the equivalent failure strain (ε_f) to keep constant the fracture energy using the relation expressed below.

$$\varepsilon_{eq}^f = \frac{2G_f}{\sigma_{eq}^f L_c} \quad (3.2.8)$$

The magnitude of L_c is calculated in this research using the approach proposed by Bazant and Oh [132]. This approach assembles the area of a material integration point (A_{ip}) and the angle between a mesh element line and the crack advancing direction φ , refer to Eq. (3.2.9). This angle is calculated taking different considerations depending on the crack orientation. Note that, for describing the crack advance orientation the same reference taken for determining the fibre orientation (θ) will be used. When the crack advances horizontally or vertically the value of φ is 0 because the extension that the crack advance through this element is a line length in a square element, see Figs. 3.2.2(a) and 3.2.2(e). For a crack angle advance lower than 45° the crack angle (φ) keeps this value (Fig. 3.2.2(b)). If the crack angle exceeds 45° the value of the parameter φ is determined as the angle between the crack line and the vertical axis, as shown in Figs. 3.2.2(d) and 3.2.2(f). For a crack propagation of 45° or 135° degrees the value of φ is 45° . The meshed elements where the crack propagates in this thesis are modelled as square elements with an element ratio of 1. Additionally, they are horizontally aligned to increase the prediction's quality.

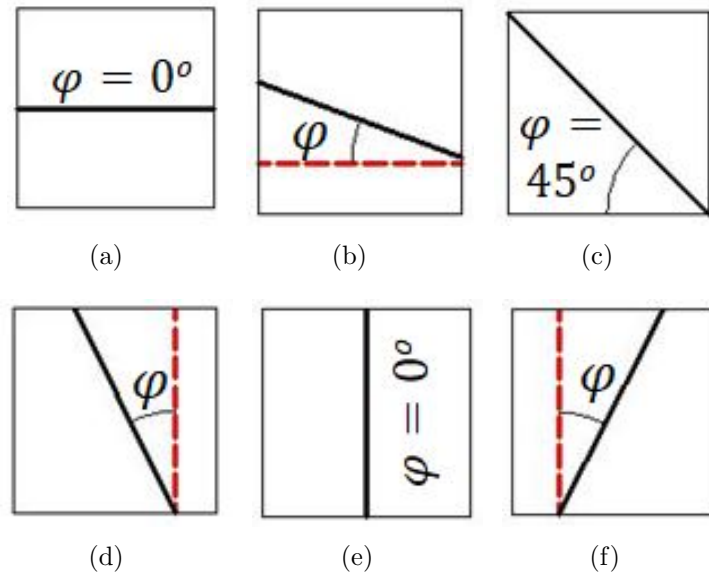


Fig. 3.2.2. Determination of the angle (φ) when the crack advances with a fibre orientation angles of: (a) $\theta=0^\circ$, (b) $0^\circ < \theta < 45^\circ$, (c) $\theta=45^\circ$, (d) $45^\circ < \theta < 90^\circ$, (e) $\theta=90^\circ$ and (f) $90^\circ < \theta < 135^\circ$

$$L_c = \frac{\sqrt{A_{ip}}}{\cos(\varphi)} \quad ; \quad |\varphi| \leq 45^\circ \quad (3.2.9)$$

Additionally, to keep the consistency of the damage algorithm, the equivalent displacements and equivalent stresses are represented in Table 3.2.1 where the operator $\langle x \rangle$ is

defined as $\langle x \rangle = (x + |x|)/2$ and β takes a value of 1 for 3D models and a value of 0 for 2D models.

Table 3.2.1. Definitions of equivalent stresses ($\sigma_{eq,I}$) and displacements ($\delta_{eq,I}$) used in this research

Damage mode	$\delta_{eq,I}$	$\sigma_{eq,I}$
Fibre traction ($\sigma_{11} \geq 0$)	$L_c \sqrt{\langle \varepsilon_{11} \rangle^2 + \varepsilon_{12}^2 + \beta \varepsilon_{13}^2}$	$\frac{L_c(\langle \sigma_{11} \rangle \langle \varepsilon_{11} \rangle + \sigma_{12} \varepsilon_{12} + \beta \sigma_{13} \varepsilon_{13})}{\delta_{eq,ft}}$
Fibre compression ($\sigma_{11} < 0$)	$L_c \langle -\varepsilon_{11} \rangle$	$\frac{L_c \langle -\sigma_{11} \rangle \langle -\varepsilon_{11} \rangle}{\delta_{eq,fc}}$
Matrix traction ($\sigma_{22} \geq 0$)	$L_c \sqrt{\langle \varepsilon_{22} \rangle^2 + \varepsilon_{12}^2 + \beta \varepsilon_{23}^2}$	$\frac{L_c(\langle \sigma_{22} \rangle \langle \varepsilon_{22} \rangle + \sigma_{12} \varepsilon_{12} + \beta \sigma_{23} \varepsilon_{23})}{\delta_{eq,mt2}}$
Matrix compression ($\sigma_{22} < 0$)	$L_c \sqrt{\langle -\varepsilon_{22} \rangle^2 + \varepsilon_{12}^2 + \beta \varepsilon_{23}^2}$	$\frac{L_c(\langle -\sigma_{22} \rangle \langle -\varepsilon_{22} \rangle + \sigma_{12} \varepsilon_{12} + \beta \sigma_{23} \varepsilon_{23})}{\delta_{eq,mc2}}$
Matrix traction ($\sigma_{33} \geq 0$)	$\beta L_c \sqrt{\langle \varepsilon_{33} \rangle^2 + \varepsilon_{13}^2 + \varepsilon_{23}^2}$	$\beta \frac{L_c(\langle \sigma_{33} \rangle \langle \varepsilon_{33} \rangle + \sigma_{13} \varepsilon_{13} + \beta \sigma_{23} \varepsilon_{23})}{\delta_{eq,mt3}}$
Matrix compression ($\sigma_{22} < 0$)	$\beta L_c \sqrt{\langle -\varepsilon_{22} \rangle^2 + \varepsilon_{12}^2 + \varepsilon_{23}^2}$	$\beta \frac{L_c(\langle -\sigma_{22} \rangle \langle -\varepsilon_{22} \rangle + \sigma_{12} \varepsilon_{12} + \sigma_{23} \varepsilon_{23})}{\delta_{eq,mc3}}$

3.2.3 Damage initiation

Because of composite brittle behaviour, matrix plasticity is not taken into account. Besides, isothermal conditions are contemplated in this work for simplicity. Composites material behaviour is modelled with an initial linear elastic response until damage initiation took place. The maximum stress failure criterion is selected to determine the fibre damage initiation, while for the matrix, the Puck plane stress failure criterion is chosen. Five distinct damage modes are considered, fibre traction, fibre compression, matrix mode A, matrix mode B and matrix mode C.

Equations to reach the fibre traction and fibre compression damage initiation criteria are represented in Eqs. (3.2.10) and (3.2.11).

- Fibre traction ($\sigma_{11} > 0$)

$$F_{ft} = \left(\frac{\sigma_{11}}{X_T} \right) \geq 1 \quad (3.2.10)$$

- Fibre compression ($\sigma_{11} < 0$)

$$F_{fc} = \left| \frac{\sigma_{11}}{X_C} \right| \geq 1 \quad (3.2.11)$$

Where F_{ft} and F_{fc} represents the fibre traction and compression damage activation functions, respectively. Henceforth, these damage activation functions are named only activation functions for simplicity. Plane stress failure Puck criteria modes are chosen because it offers good matrix failure predictions in comparison with other extended composites failure criteria [79]. In this document, the basics of this failure are provided. For completion, a brief explanation of the Puck matrix failure modes variables is given. The interested reader is referred to [78] for more detailed information.

Matrix plane stress Puck failure criteria are composed of three failure modes: (1) Mode A, (2) Mode B and (3) Mode C. In Mode A matrix rupture is occasioned under traction

conditions, while Mode B and Mode C are taken place under normal compressive stresses. Mode A and Mode B cut the laminate parallel with thickness direction while Mode C split the laminate with a certain angle. Puck matrix failure modes predictions contain a high complexity level as appreciated in Eqs. (3.2.12) to (3.2.14).

F_{mma} , F_{mb} and F_{mmc} represents the Mode A, Mode B and Mode C damage activation functions, respectively. To clarify the analysis of results only a matrix traction activation function (F_{mt}) and matrix compression activation function (F_{mc}) are analysed. Value of (F_{mt}) is assigned to be the same than F_{mma} , while (F_{mc}) is established as the maximum of F_{mb} and F_{mmc} in every element ($F_{mc} = \max\{F_{mb}, F_{mmc}\}$).

- Matrix Mode A ($\sigma_{22} \geq 0$)

$$F_{mma} = \sqrt{\left(\frac{\sigma_{12}}{R_{\perp\parallel}^A}\right)^2 + \left(1 - \frac{p_{\perp\parallel}^{(+)}}{R_{\perp\parallel}^A} R_{\perp}^{(+A)}\right)^2 \left(\frac{\sigma_{22}}{R_{\perp}^{(+A)}}\right)^2} + \frac{p_{\perp\parallel}^{(+)}}{R_{\perp\parallel}^A} \sigma_{22} \geq 1 \quad (3.2.12)$$

- Matrix Mode B ($\sigma_{22} < 0$ and $\sigma_{22} > -R_{\perp\perp}^A$)

$$F_{mb} = \sqrt{\left(\frac{\sigma_{12}}{R_{\perp\parallel}^A}\right)^2 + \left(\frac{p}{R}\right)^2 \sigma_{22}^2 + \left(\frac{p}{R}\right) \sigma_{22}} \geq 1 \quad (3.2.13)$$

- Matrix Mode C ($\sigma_{22} \leq -R_{\perp\perp}^A$)

$$F_{mmc} = \frac{1}{2 \left[1 + \left(\frac{p}{R}\right) R_{\perp\perp}^A\right]} \left[\left(\frac{\sigma_{12}}{R_{\perp\parallel}^A}\right)^2 + \left(\frac{\sigma_{22}}{R_{\perp\perp}^A}\right)^2 \right] \frac{R_{\perp\perp}^A}{-\sigma_{22}} \geq 1 \quad (3.2.14)$$

Here, all terms with R represent the strength components associated with the fracture plane. Term $R_{\perp}^{(+A)}$ is equal to the transverse matrix traction strength (Y_T), $R_{\perp\parallel}^A$ corresponds to the intralaminar shear strength (S_{12}). Variable $R_{\perp\perp}^A$ is the transverse/transverse shear strength and generally this variable is quite difficult to measure, so the value is normally extracted indirectly from Eq. (3.2.15). Term $p_{\perp\parallel}^{(+)}$ is the Puck failure envelope slope when $\sigma_{22} > 0$ at point $\sigma_{22} = 0$. Recommendable values for this variable are 0.35 for carbon fibre composites and 0.3 for glass fibre composites [133]. Expression $\left(\frac{p}{R}\right)$ is calculated using the equation formulated in Eq. (3.2.16).

$$R_{\perp\perp}^A = \frac{Y_C}{2 \left(1 + p_{\perp\perp}^{(-)}\right)} \quad (3.2.15)$$

$$\left(\frac{p}{R}\right) = \frac{p_{\perp\parallel}^{(-)}}{R_{\perp\parallel}^A} \quad (3.2.16)$$

In the above equations, values recommended for the variables $p_{\perp\perp}^{(-)}$ and $p_{\perp\parallel}^{(-)}$ are 0.3 for carbon fibre composites and 0.25 for glass fibre composites [133].

3.2.4 Damage propagation

After damage onset is achieved, a linear continuum damage mechanics (CDM) approach is performed. The expression used to calculate the damage modes quantity in every step is shown in Eq. (3.2.17).

$$d_I = \frac{\delta_{I,eq}^f (\delta_{I,eq} - \delta_{I,eq}^0)}{\delta_{I,eq} (\delta_{I,eq}^f - \delta_{I,eq}^0)} \quad (d_I \in [0, 1] \text{ and } I = (ft, fc, mt, mc)) \quad (3.2.17)$$

Final ($\delta_{I,eq}^f$) and initial ($\delta_{I,eq}^0$) equivalent displacements are calculated immediately after the damage initiation condition of one damage mode is reached. These terms are determined by Eq. (5.4.1) and Eq. (3.2.19), respectively.

$$\delta_{I,eq}^f = \frac{2G_I^c F_I}{\sigma_{I,eq}} \quad (3.2.18)$$

$$\delta_{I,eq}^0 = \frac{\delta_{I,eq}}{F_I} \quad (3.2.19)$$

In the above equations, coefficient F_I with $I = (ft, fc, mt, mc)$ represents the correspondent damage mode's activation function value. $\sigma_{I,eq}$ and $\delta_{I,eq}$ are the equivalent stress and displacements of a damage mode, respectively. Expressions assigned to obtain the value of these variables are showcased in section 4.2.5.

Finally, the maximum damage of 0.95 is allowed for the matrix and 0.999 for the fibre damage modes. These maximum values are chosen to avoid numerical errors [84] and simulate the remaining stiffness that a total failure ply supply to adjacent laminate plies [133]. After this damage level was achieved, a second linear elastic response is introduced with the remaining stiffness. An illustration of the material behaviour scheme is represented in Fig. 3.2.3.

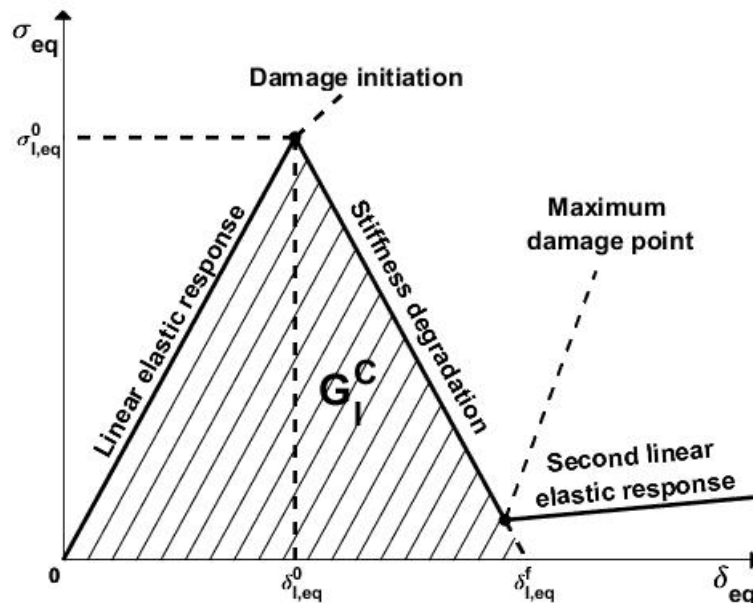


Fig. 3.2.3. Damage model scheme carried out for every damage mode.

3.2.5 Chip fracture

The chip formation process has been barely studied because of the intrinsic difficulty of addressing this matter in macro mechanical FE models. In this document, four types of failures are accounted shear, fibre/matrix debonding, matrix crushing and fibre buckling. The fracture is induced after a significant amount of deformation is produced enough to allow the total fibre or matrix damage degradation and avoid element distortion problems. The strain limits selected in this research are selected to guarantee that the damaged elements consumed most part of one damage mode fracture energy. This statement is explained in more detail in Section 5.4.1.

3.3 User-defined VUMAT subroutine

The link of Fortran user-defined VUMAT subroutines with the Abaqus/Explicit module is employed for developing all simulations performed in this research. Abaqus/Explicit is selected because of its high capabilities to simulate dynamic problems with contact interactions and important inertial forces, as discussed in Section 2.5. The user-defined VUMAT subroutine is in charge of processing all the data coming from the Abaqus/Explicit at every step time to customise the material constitutive law following the methodology described below.

1. Call from Abaqus/Explicit to the user-defined VUMAT subroutine passing the strain increment calculated for this time increment of the evaluated meshed element.
2. Update the total strain summing to the total strain at the previous step time incrementing strain calculated in this time increment.

3. Calculate the undamaged stiffness matrix and update the stresses
4. Calculate the equivalent displacements and evaluate if the initiation of any damage mode is reached.
5. In case one condition of the onset of a composite damage initiation is achieved, the variables are calculated.
6. In the following steps, the damage variable affected previously will be updated, degrading the studied element's mechanical properties progressively.
7. It is evaluated if the strain reached this element exceeds the maximum strain condition for element deletion. In case this condition has reached the element is deleted, this loop will be repeated at the next step time.
8. Finally, the damaged matrix is constructed, and the updated stresses are passed to Abaqus/Explicit, finishing the composite damage algorithm implemented in the subroutine

Finally, the flowcharts representing the methodology of the damage algorithm used in this research is shown next. Fig. 3.3.1 shows the entire methodology implemented in the VUMAT to introduce the performed composite constitutive law. In Fig. 3.3.2 is represented the loop to update the material damages in the simulation. Finally, the steps are taken in damage evolution, and element erosion algorithms are represented in Figs. 3.3.3 and 3.3.4.

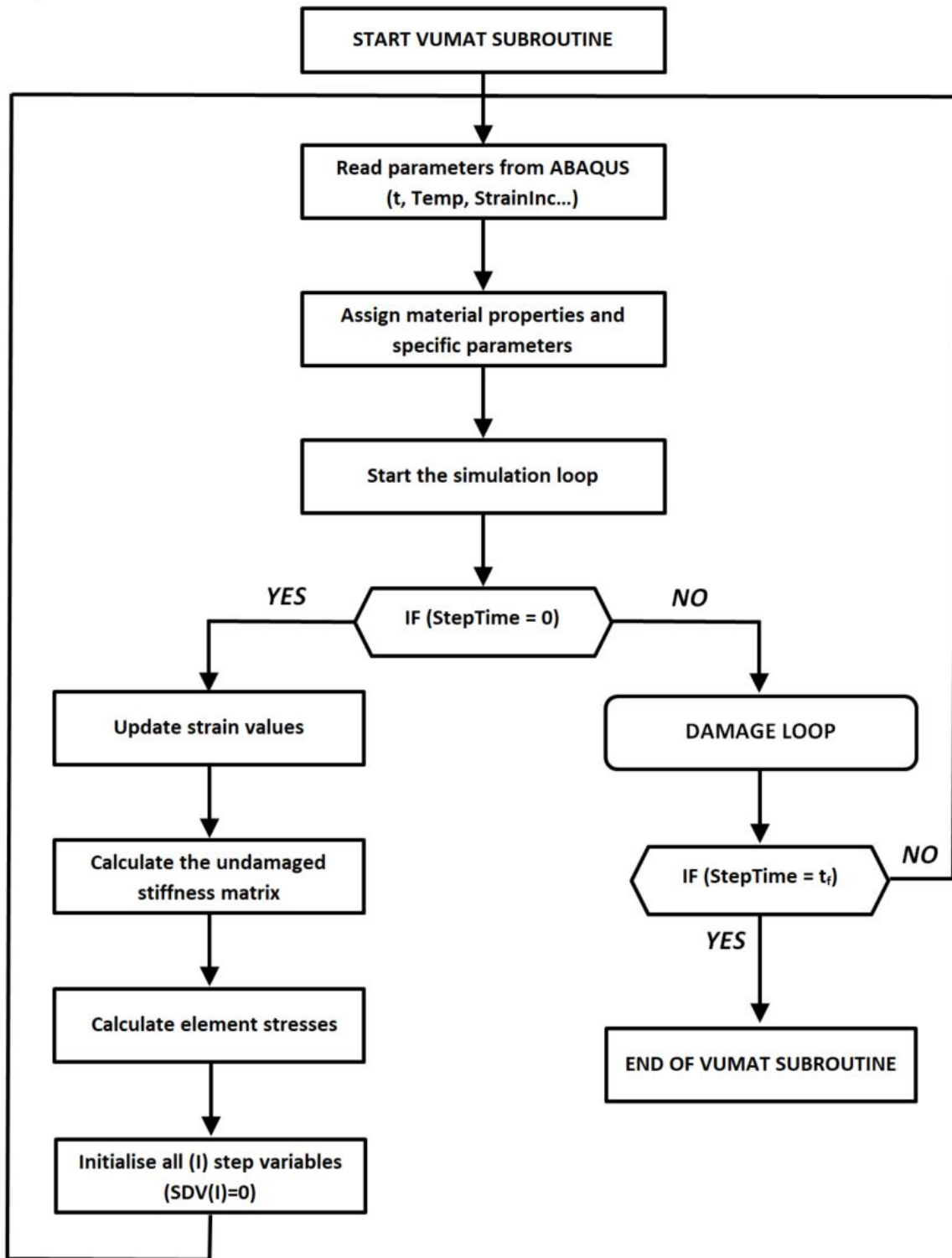


Fig. 3.3.1. VUMAT algorithm flowchart.

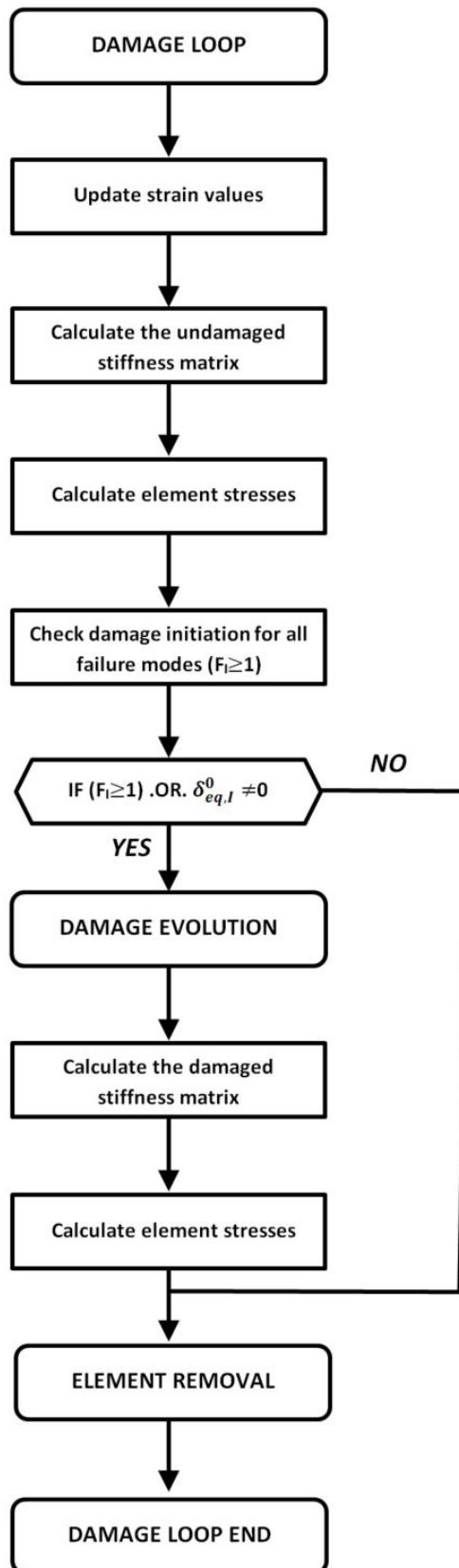


Fig. 3.3.2. Damage algorithm flowchart.

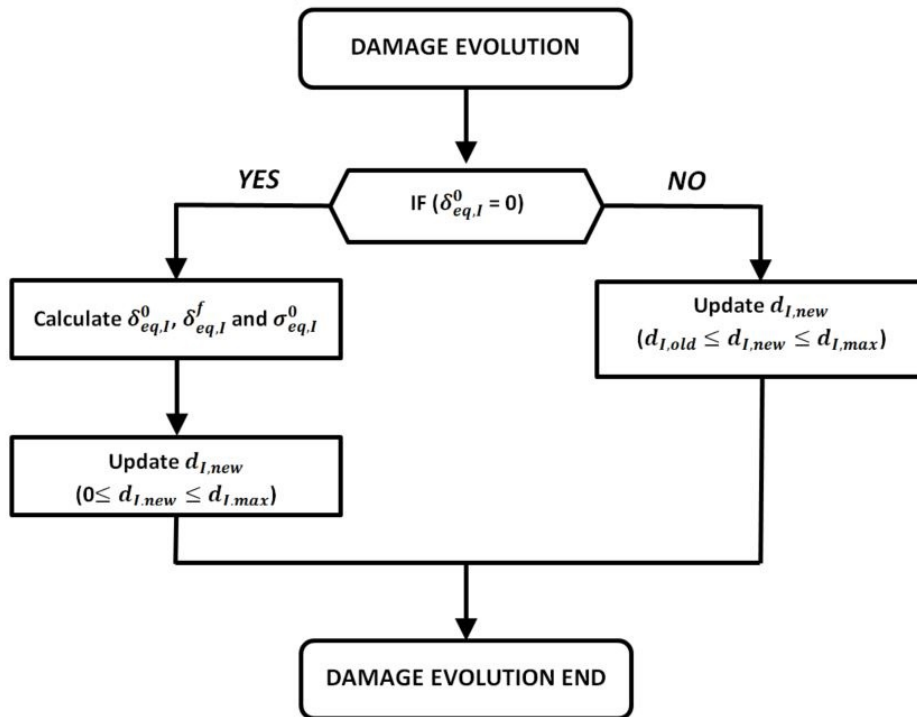


Fig. 3.3.3. Damage evolution algorithm flowchart.

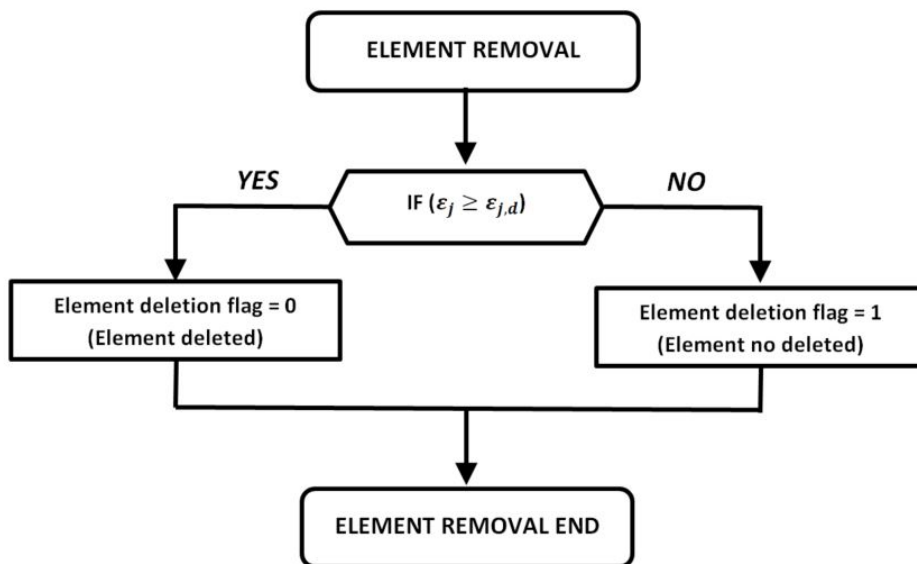


Fig. 3.3.4. Element removal algorithm flowchart.

3.4 Verification of FE damage model

3.4.1 Experimental trials description

Two simple tensile tests have been carried out experimentally to verify that the numerical predictions obtain similar results to demonstrate the proper introduction of the damage model explained above. Two tensile tests with fibre orientations of 0° and 90° are selected to check that the damage model is capable of simulating these particular cases where the fibre governs the fracture mechanism in the 0° laminates and by the matrix in the 90° laminates. In this manner, it can be confirmed that the damage model correctly predicts fibre and matrix damage separately, ensuring the model capability to simulate more complex load configurations where combinations of both damages occur with high accuracy.

For the experiments' design, the parameters established in the standard ASTM D3039 [134] have been taken into consideration. The trials were developed in the servo-hydraulic universal machine Instron 8501 with a load cell of 100 kN, see Fig. 3.4.1(a). This decision is taken because this machine is ideal to obtain strain-stress curves in a test where high loads are required. In the case of 90° specimens, this factor is not important, but it is essential for 0° specimens because of the fibres' high strength. The tensile test is performed moving up the upper grip and fixing the bottom grip; both grips use the high hydraulic pressure to clamp the specimen extremes, see Fig. 3.4.1(b). Finally, an axial extensometer with a gauge length (GL) of 25 mm, is installed in the specimen's centre to measure the strains accurately far from the clamped area. It occurs because the strains generated in the clamped area are distorted for the grips' compressive action, see Fig. 3.4.1(c).

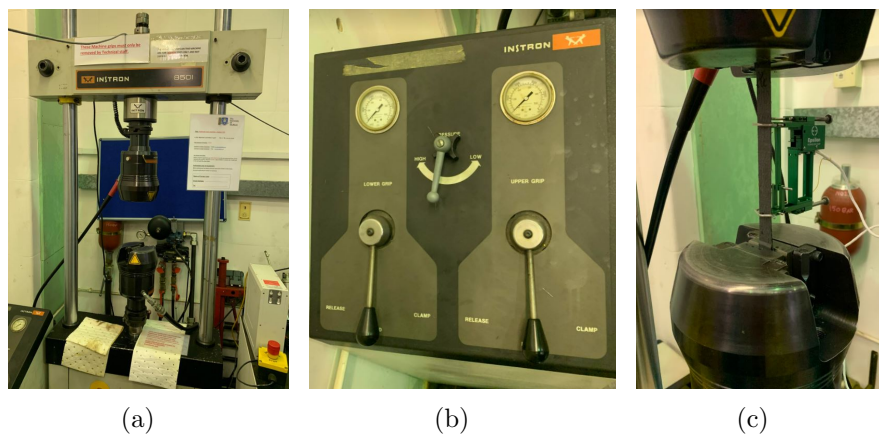


Fig. 3.4.1. Tensile test set-up (a) Instron 8501 machine, (b) Hydraulic machine pressure controls and (c) Extensometer and specimen disposition in Instron 8501 machine.

The specimens have been manufactured following a novel resin transfer infusion system developed at the University of Sheffield. In the tested specimens, the matrix and the fibre have a 50% volume fraction. The matrix is obtained from the mixture of Bisphenol A epoxy resin with Aradur 2954 hardener, while the carbon fibre used is a standard modulus T700. Both specimens studied are manufactured with the stacking of four lamina laminates with a thickness of 1.2 mm and dimensions of 250 x 15 mm for the 0° specimens and 175 x 25 mm for the 90° specimens. End-tabs are placed on these specimens' edges

to soften the contact between the grips and the specimens. These end tabs cover the specimens' full width and dispose of an angle of 7° in the edge closer to the specimen centre. This action is necessary to reduce the contact area's stress concentration between the specimen and the edge of the end-tabs and avoid a premature break in that area.

3.4.2 Experimental trials

A low cross-head displacement rate of 2 mm/min was applied to guarantee static conditions during all test development. Although the same methodology is used in the tested specimens, the results obtained notably differ in the specimens for the two fibre orientations considered. More detailed information on each type of test performed and the post-processing of data performed is given below.

3.4.2.1 Experimental test of 0° laminates

In this type of test, the specimen breaks abruptly when the strength of the fibres is reached. For this type of test, the use of safety glasses is necessary because this break releases many fragments of the specimen at high speed in all directions, and the impact of one of them on the eye could have catastrophic consequences, see Fig. 3.4.2. This failure mechanism is due to achieve the fibre breakage; the specimen has to reach a high level of stress, storing a large amount of internal energy that is abruptly released at the moment of breakage.



Fig. 3.4.2. Specimen breakage in tensile test with a fibre orientation of 0° .

This abrupt failure reduces the accuracy of the strain measured when a bundle of fibre breaks because it introduces disturbances in the specimen, causing movements in the strain gauge gauges at the breaking point. As a result, the stress-strain curves show a horizontal displacement at those moments when a bundle of a fibre break. Nevertheless, this fact does not change the linear growth trend observed before the fibre breakage. Therefore, these horizontal displacements must be corrected from the stress-strain curves because they are due to errors in the extensometer's measurement and do not take place in the laminate, see Figs. 3.4.3(a) to 3.4.3(c). Only two experiments yielded conclusive data for this type of specimen because the instability caused by a premature fibre breakage distorted the data obtained in several experiments.

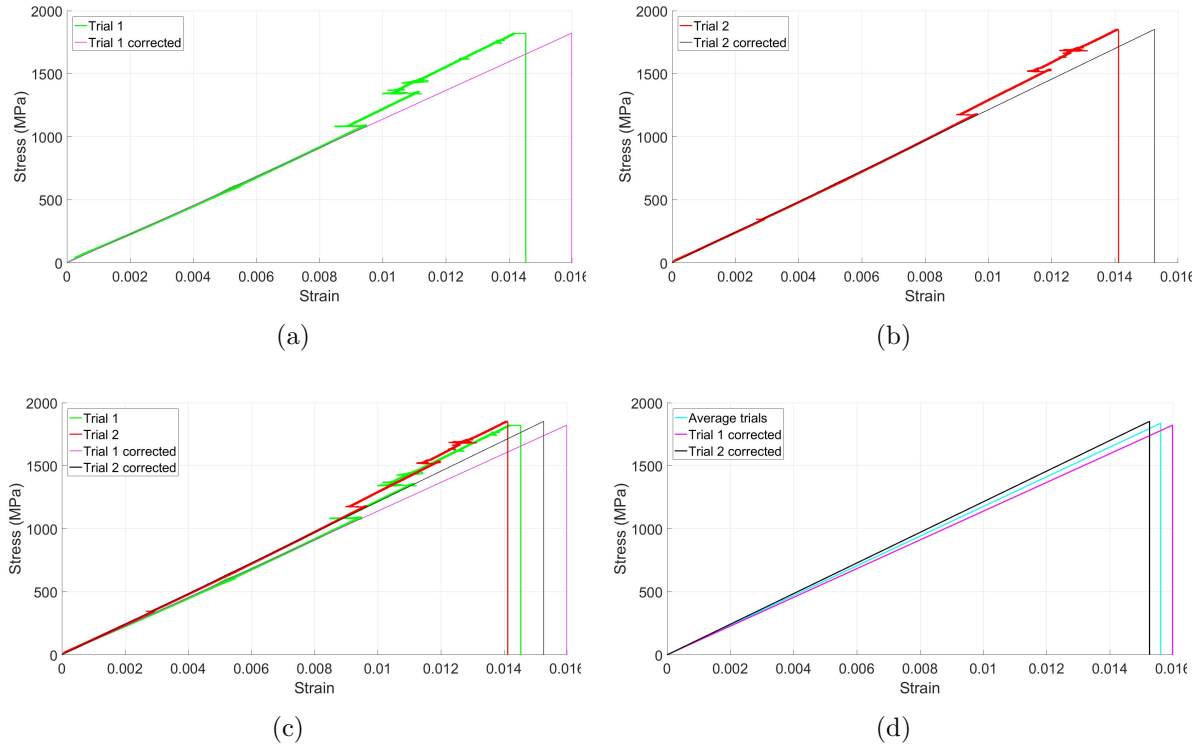


Fig. 3.4.3. Stress-strain graph obtained from: (a) Trial 1, (b) Trial2, (c) Trials 1 and 2 superposition and (d) Calculated average stress-strain evolution.

Finally, the average of the fibre Young modulus (E_{11}) and fibre traction strength (X_T) extracted from the experiments is 117.7 GPa and 1842.5 MPa , respectively.

3.4.2.2 Experimental test of 90° laminates

In the tensile tests for this class of specimens, a clear fracture perpendicular to the load direction is observed due to the matrix's rupture in this direction, as shown in Fig. 3.4.4. Even though this rupture occurs abruptly, the specimen's fragments are not obtained as occurs in the tensile tests with fibres at 0 degrees. It is because the stress required to break the matrix is significantly lower than that required to break the fibres. Consequently, the energy stored in the specimen instantly before its rupture is significantly lower than the energy required to collapse the tested sample.



Fig. 3.4.4. Specimen breakage in tensile test with a fibre orientation of 90° .

Regarding the stress-strain curves obtained, a clear elastic linear trend is observed throughout the three tests performed, refer to Fig. 3.4.5. This factor indicates that this type of matrix only works in an elastic regime and does not work in the plastic zone for static loads. Therefore, it can be inferred that the matrix will only have an elastic behaviour during its machining because the high strain rate experienced by the matrix in these operations tend to stiffen the behaviour of the material observed in static loads. From this conclusion, it is verified that the hypothesis of not considering plasticity taken in the damage algorithm proposed in this thesis is valid for many thermoset composites.

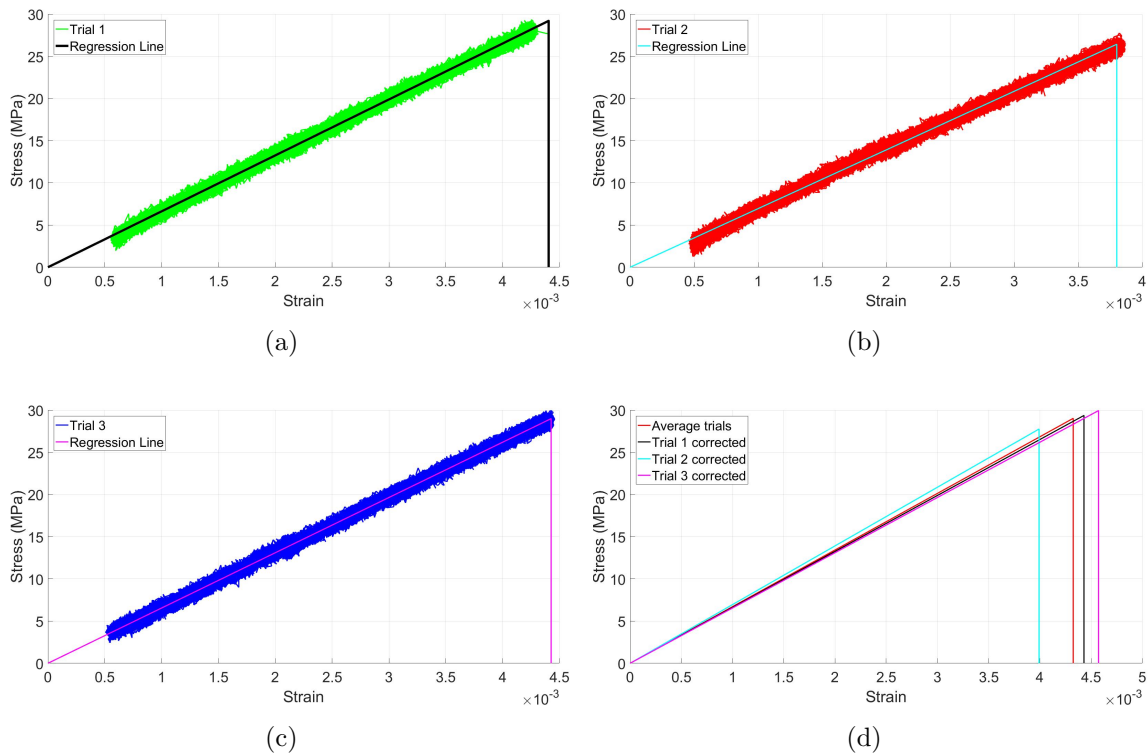


Fig. 3.4.5. Stress-strain graph obtained from: (a) Trial 1, (b) Trial2, (c) Trials 3 and (d) Calculated average stress-strain evolution.

Finally, the average of the matrix Young modulus ($E_{22} = E_{33}$) and matrix traction strength ($Y_T = ZT$) extracted from the experiments is 6.7 GPa and 29 MPa , respectively.

3.4.3 FE simulations description

Other mechanical properties such as the fibres and matrix's compressive strength, the Poisson's coefficient and shear strength, and young modulus must be implemented in Abaqus. These properties were obtained with the performance of tests based on the standards ASTM D3410 [135] and ASTM D3518 [136] resulting in the values illustrated in Tables 3.4.1 and 3.4.2. Therefore, all the composite parameters required in the proposed damage model are known, and numerical simulations can be carried out.

Table 3.4.1. Elastic properties of the tested CFRP laminate

$E_{11}(GPa)$	$E_{22} = E_{33}(GPa)$	$G_{12} = G_{13} = G_{23}(GPa)$	$\nu_{12} = \nu_{13}$	ν_{23}
118	6.7	5.39	0.33	0.04

Table 3.4.2. Strength properties of the tested CFRP laminate

$X_T(MPa)$	$X_C(MPa)$	$Y_T = Z_T(MPa)$	$Y_C = Z_C(MPa)$	$S_{12} = S_{13} = S_{23}(MPa)$
1837.5	900	29	199.8	192.3

Definitions provided ahead are applicable for 2D, and 3D FE models developed to simulate the tensile test. Element sizes (ES) of 0.75, 1, 1.5 and 2 mm were chosen to check the simulations' convergence. Only the part of the specimen that is not compressed by the grips is simulated. The dimensions modelled for 0° specimens are 138 x 15 mm, while dimensions of 90° specimens are 125 x 25 mm and thickness of 1 mm for both specimens in 3D FE models. The conditions imposed by the grips are added to the model imposing the correct boundary conditions at the modelled specimen's top and bottom surfaces. The displacements at the bottom surface are fixed and the displacements that are not vertical in the top surface are restricted. All the strength properties shown in Table 3.4.2 in the areas of the specimen extremes is increased a 10%, see Fig. 6.3.3, to concentrate the damage in the central area of the laminate.

Additionally, this mitigates the stress concentration effect that boundary conditions produce at the top and bottom specimen areas. Because the fracture observed in both experiments is different, the central area dimensions selected for 0° specimen and 90° specimen change. In the case of 0° specimens, the central covers 70 mm to reflect the massive damage that is obtained experimentally, as shown in Fig. 3.4.6(a), while for 90° specimen, the central area has the length of the element size to reflect the slight crack generated after failure, see Fig. 3.4.6(b).

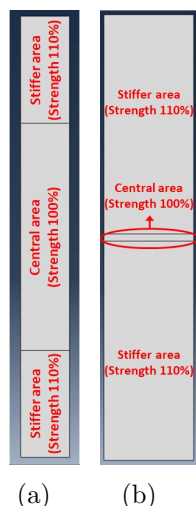


Fig. 3.4.6. Partitions modelled in specimens with fibre orientations of (a) Strain localised band, (b) Stress-strain graphs obtained for different number of elements.

3.4.3.1 Simulation of tensile test of 0° laminates

The election of a precise fibre tensile fracture energy is essential to obtain accurate numerical results due to it affects notably predicted magnitudes such as forces or damage propagation. However, the measurement of this magnitude is cumbersome and it is out of the scope of this project. Therefore, the fracture energy calculated in a similar CFRP panel need to be implemented in the simulation. A fracture energy of 81.5 N/mm calculated for a IM7/8552 laminate [95, 137] is used in this FE model.

The damage to the fibre and the matrix registered in the simulations expands in large areas of the laminate after the collapse of the specimen, as shown in Fig. 3.4.7. In the matrix's case, it can be seen that almost all the central and upper region of the laminate high damage values are reached, refer to Figs. 3.4.7(c) and 3.4.7(d), which would explain the formation of fragments that detach after failure in the experimental tests. The fibres are mainly damaged in two horizontal stripes that would simulate the damage of the fibres in these areas, as shown in Figs. 3.4.7(a) and 3.4.7(b).

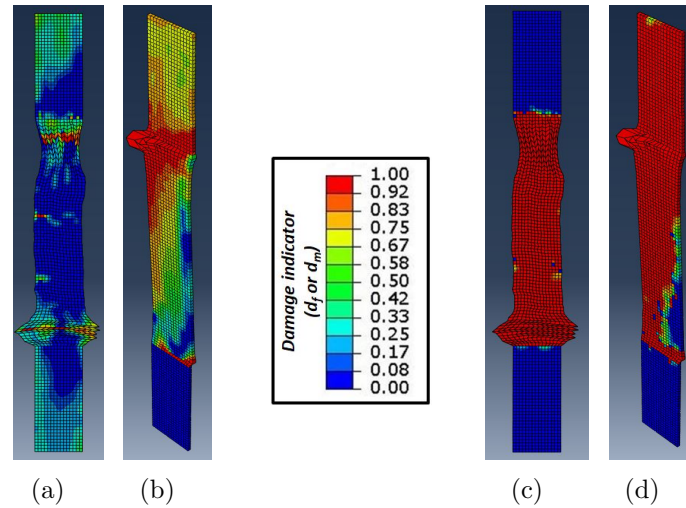


Fig. 3.4.7. Fibre and matrix damage (d_f and d_m) distribution of the 0° laminates for 2D and 3D FE models: (a) d_f of 2D FE model, (b) d_f of 3D FE model, (c) d_m of 2D FE model and (d) d_m of 3D FE model.

The evolution of the laminate stress obtained in the simulations fits perfectly with the experimentally recorded data, as shown in Fig. 3.4.8. Note that all the curves obtained overlap, indicating the convergence of the problem in all the simulated models and the high accuracy in the experimental tests' predictions. Because of this factor, it is possible to conclude the validity of the damage model proposed to simulate this type of damage.

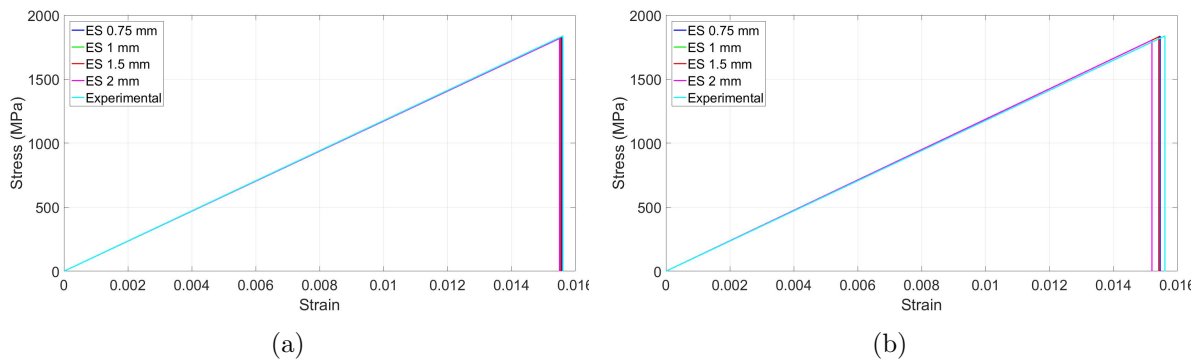


Fig. 3.4.8. Numerical and experimental stress-strain graphs of 0° laminates obtained for various element sizes (ES) in (a) 2D FE predictions, (b) 3D FE predictions.

3.4.3.2 Simulation of tensile test of 90° laminates

In this type of specimen, the matrix's damage is concentrated in the central strip, producing the horizontal fracture of the matrix, as shown in Fig. 3.4.9. The damage evolves from 0 to 1 abruptly in the failure band's elements, concentrating all the transversal strain in these elements. The matrix tensile fracture energy calculated for IM7/8552 [95, 137] is implemented in the simulation. Furthermore, no fibre or matrix damage is obtained outside the break zone resembling the stable fracture observed in the experiments.

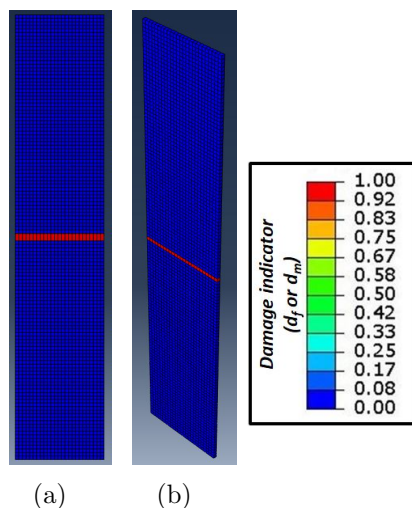


Fig. 3.4.9. Fibre and matrix damage (d_f and d_m) distribution of the 90° laminates for 2D and 3D FE models: (a) d_m of 2D FE model and (b) d_m of 3D FE model.

Besides, the stresses of the laminate registered in the simulations are superimposed with the data collected experimentally, refer to Fig. 3.4.10; showing that the damage model used predicts matrix failures with high accuracy. In conclusion, it has been shown that the 2D and 3D FE models used to predict fibre and matrix damage with high reliability in simple load configurations such as tensile tests. Therefore, the model's validity can be inferred to predict matrix and fibre damages from more complex loading scenarios in machining operations.

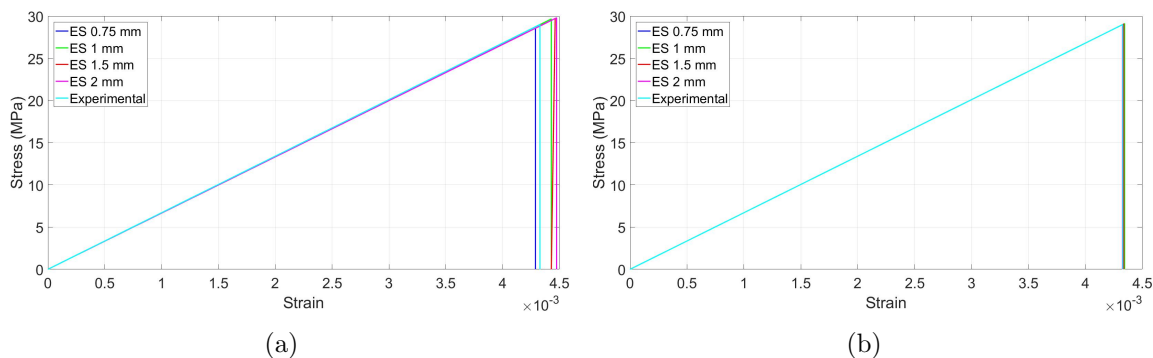


Fig. 3.4.10. Numerical and experimental stress-strain graphs of 90° laminates obtained for various element sizes (ES) in (a) 2D FE predictions, (b) 3D FE predictions.

3.4.3.3 Shear damage simulation

Beforehand, the capabilities of the damage model to predict fibre and matrix damage modes were successfully assessed to check the validity of the model to simulate composite machining operations. However, these capabilities are not sufficient to simulate machining operations because they present significant shear damage. Therefore, it is necessary to analyse the capacity of the model to predict this type of damage. As a general rule, shear

strength is usually measured using the Iosipescu test [138]. For this reason, this research uses the results of the Iosipescu test carried out by Odegard and Kumosa [139] to validate the model. Qualitative analysis is performed in 2D and 3D FE models to check if the damage model can predict the characteristic shear damage of this test.

The dimensions of the specimens are specified in the standard ASTM D5379 [140]. Generally, these specimens have two notches in their central part where the stress concentrators are located. The high shear stresses are achieved in these by the vertical movement of the grips. These grips infer a negative and positive vertical displacement of equal magnitude on the sides of the specimen to induce shear stresses in its central region. The measurements of the specimen and the grips of the experiment reported by Odegard and Kumosa [139] are simulated to validate the damage model. Fig. 3.4.11 shows the dimensions of the simulated specimen and grips.

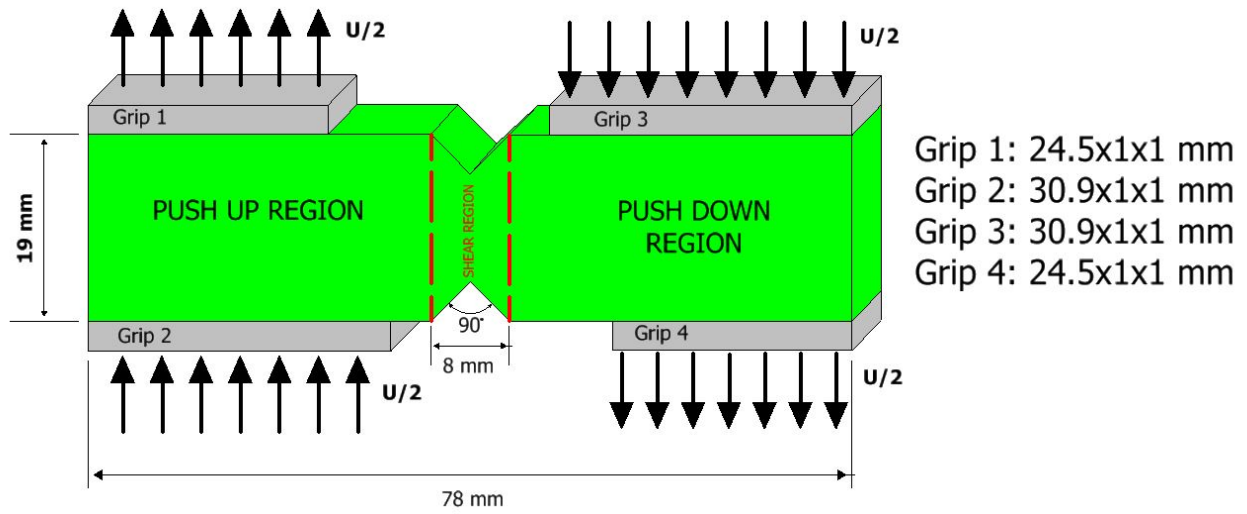


Fig. 3.4.11. Iosipescu test simulated geometry

The mechanical properties used in this model are specified in and illustrated in Tables 3.4.3 and 3.4.4. Since there is no data on fracture energy in the paper from which the results are extracted, the shear fracture energy of 0.79 N/mm calculated for an IM7-8552 laminate [95] is used.

Table 3.4.3. Elastic properties of the CFRP laminate [139]

$E_{11}(GPa)$	$E_{22} = E_{33}(GPa)$	$G_{12} = G_{13} = G_{23}(GPa)$	$\nu_{12} = \nu_{13}$	ν_{23}
140	11	6	0.38	0.4

Table 3.4.4. Strength properties of the CFRP laminate [139]

$X_T(MPa)$	$X_C(MPa)$	$Y_T = Z_T(MPa)$	$Y_C = Z_C(MPa)$	$S_{12} = S_{13} = S_{23}(MPa)$
1000	700	40	120	71.5

The behaviour of the simulated composite is linearly elastic and does not contemplate the plastic deformation that is observed in the experiments. It means that more fracture

energy will be dissipated in the experiments than in the damage model when the failure stress is reached. However, in the damage model, the propagation of the damage is progressive, adding fracture toughness that compensates for the higher fracture toughness observed in the experiments upon reaching the maximum stress peak. This statement is appreciated in the stress-strain curves represented in Fig. 3.4.12.

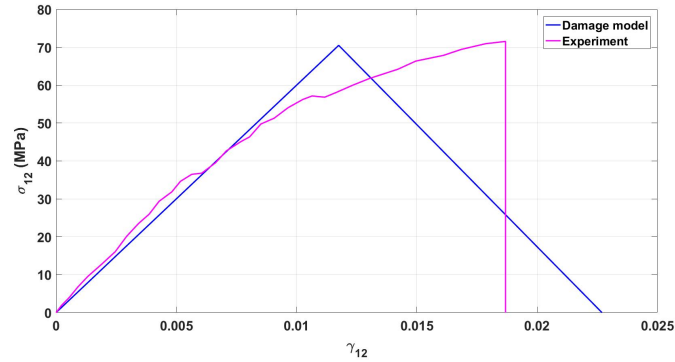


Fig. 3.4.12. Shear stress-strain curves obtained in experiment and the damage proposed damage model

The grips are modelled as rectangles with the dimensions specified in Fig. 3.4.11. These grips are modelled as rigid solids for simplicity. 2D models have shell elements CPS4R and 3D solid elements C3D8R models to ensure compatibility between Abaqus/Explicit and the Vumat Fortran subroutine.

The mesh used guarantees the precision of the numerical predictions and an acceptable computational cost. Both models have a mesh with an element size of 50 microns in their central region. These elements are progressively increased to 0.5 mm along the notch to the area where the specimen is gripped. Finally, the gripped zone is modelled with a uniform element size of 0.5 mm, as shown in Fig. 3.4.13.

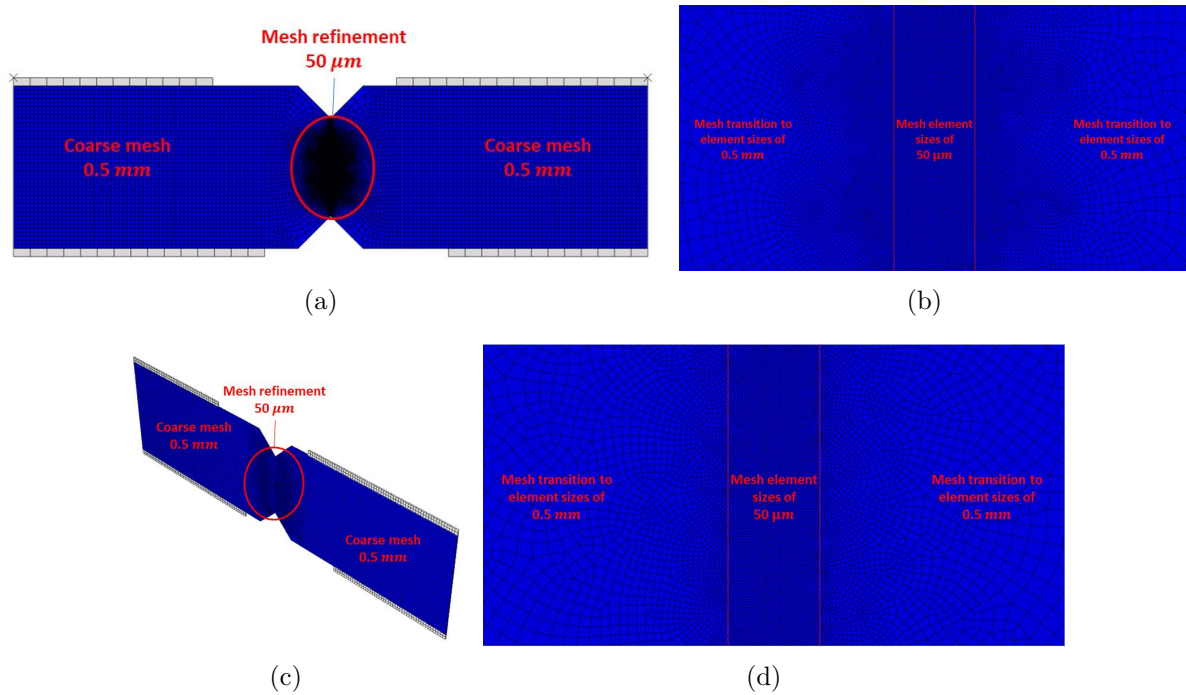


Fig. 3.4.13. Mesh distribution of the simulated Iosipescu specimen model: (a) 2D FE model, (b) 2D FE model central zoom, (c) 3D FE model and (d) 3D FE model central zoom

In the 2D FE model results, it can be seen how the model predicts the failure of the central section. It can be seen how the shear damage spreads abruptly in the central line that joins the two notches, Fig. 3.4.14. This damage would cause the total collapse of the specimen, as observed in the experiments.

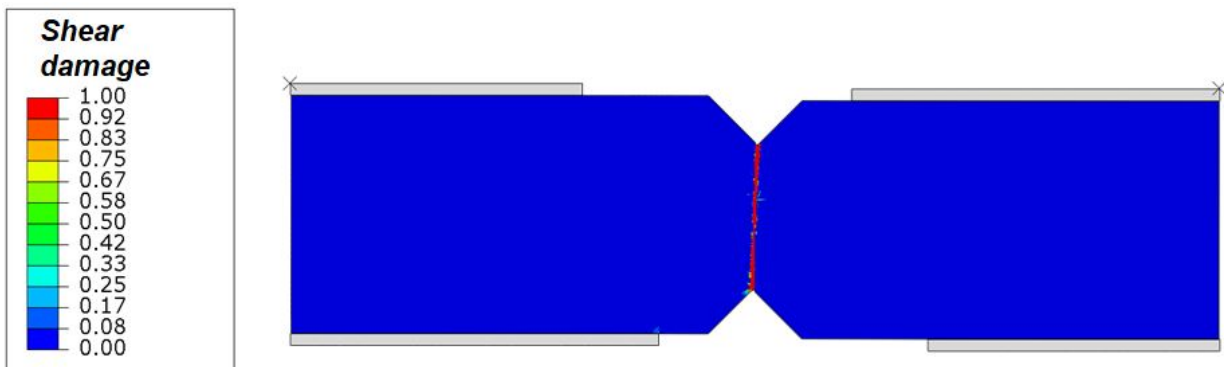


Fig. 3.4.14. Shear damage simulated in the 2D FE Iosipescu model

Regarding the 3D FE model, the propagation of the damage obtained is different from that observed in the 2D model. In this case, it is observed how the shear damage begins in the notches with two parallel lines forming an angle of 10 degrees with the vertical axis. Later, when the damage spreads across the width of the specimen, both lines connect in the middle. It causes the collapse of the specimen in its central zone, as shown in Fig. 3.4.15.

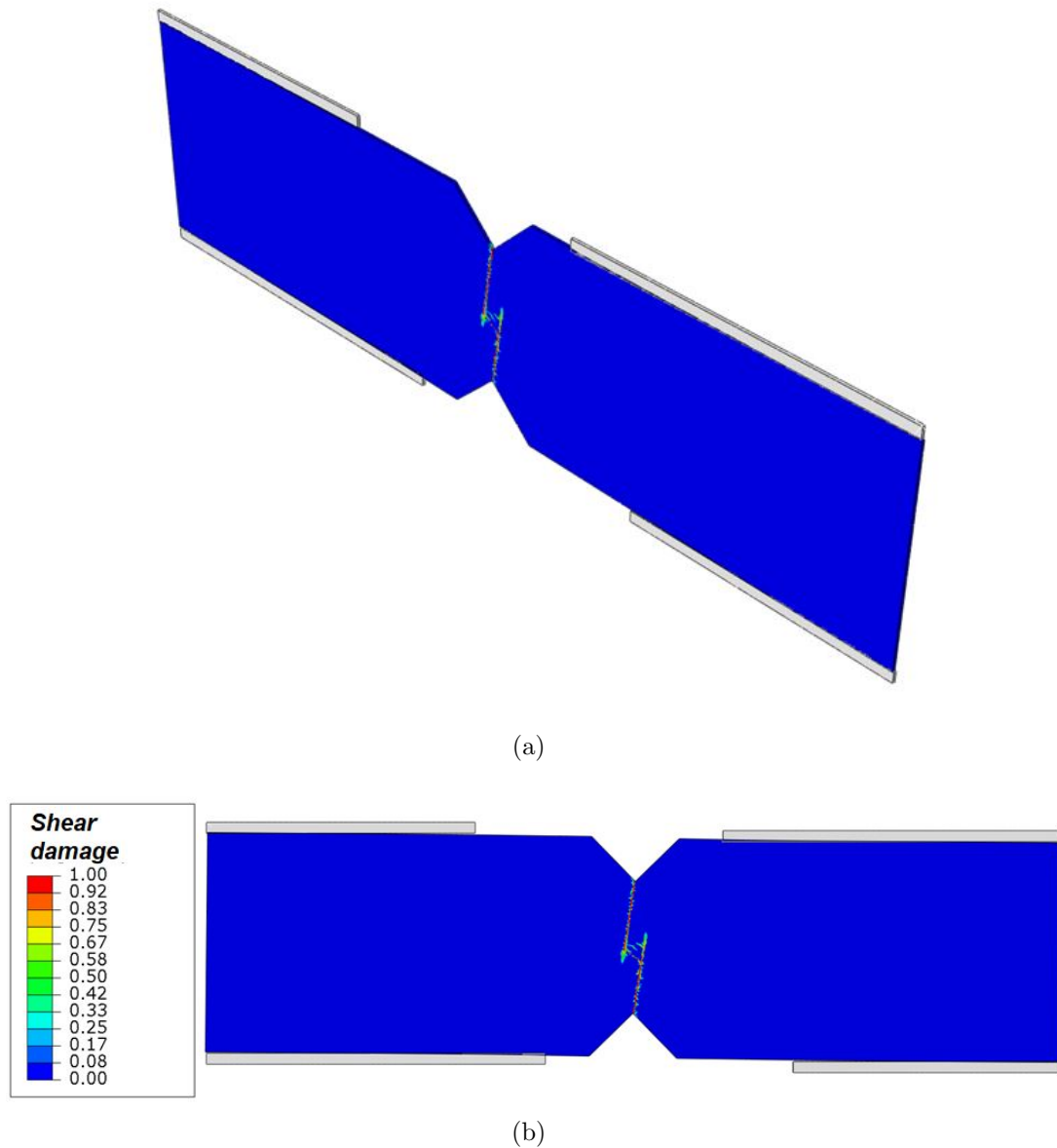


Fig. 3.4.15. Shear damage simulated in the 3D FE iosipescu model: (a) Perspective and (b) Front view

These divergences between 2D and 3D models could be explained due to formulation differences between 3D brick and shell elements and the influence of intralaminar stresses in 3D models. However, both models predict shear failure in the central section of the specimen in experimental trials. Thus, it could be concluded that the damage model can also predict shear failure with an excellent accuracy.

3.5 Concluding remarks

In this chapter, a continuum damage mechanic (CDM) approach is proposed to simulate the different characteristic fibre and matrix damages while cutting a composite ply. This type of methodology represents an advance in the modelling of machining operations be-

cause it introduces a progressive degradation of the mechanical properties of the element, guaranteeing that the fracture energy is reached before the failure of each element. The damage model includes the initiation of damage, progressive degradation of mechanical properties, and subsequent final failure to fulfil this task.

A hybrid damage criterion has been developed that combines the advantages of the well-known damage criteria proposed by Hashin and Puck. For the initial prediction of fibre failure, the Hashin model has been used due to its simplicity. The Puck model predicts the matrix failures due to its high accuracy in its predictions, especially in compression mode failures that play a very relevant role in this simulation type.

The mechanical properties of the matrix or fibre are progressively degraded using a strain-based linear degradation law. This law considerably reduces the mesh sensitivity of the simulations by including variables such as stress equivalent and equivalent displacement that depend on the element's characteristic size. Finally, a strain-based element removal algorithm is developed that removes the element when a failure mode is completed and simulates the laminate fracture in that area.

The proposed damage model is implemented in a user-defined VUMAT Fortran subroutine linked to the numerical software package Abaqus/Explicit. The use of these subroutines gives it great versatility in modelling composites' mechanical behaviour due to its high customisation power. For example, it could be modelled several unidirectional or cross-ply laminates by making small changes to the Abaqus interface and simulating woven composites with a simple modification of the material properties.

The numerical and experimental results of two simple tensile tests of laminates at 0 and 90 degrees are compared to validate the damage model. In general lines, the simulations show stress-strain curves similar to the experimental ones, reproducing the fragile and abrupt fibre breakage of the 0° laminates and the stable matrix fracture the 90° laminates. These simulations show the effectiveness of the model to predict matrix and fibre failure with simple load configurations. Finally, the capability of the proposed model to predict shear damage is assessed. A qualitative shear damage analysis is performed simulating a Iosipescu shear tests. The shear damage predicted in the centre of the specimen for both 2D and 3D FE models is in good agreement with the experimental findings. Therefore, it is concluded that this model can predict these damages in complex load configurations that take place in machining operations.

In the next chapter, the proposed damage model will analyse sub-surface damage in machining processes. The different factors that cause the change of this variable will be analysed and discussed in detail.

Chapter 4

Machining induced damage assessment

4.1 Introduction

An advanced FE model is developed in the present work to predict sub-surface damage in composite machining accurately. Although this variable plays a fundamental role in the laminates' surface quality and structural integrity, the quality of the predictions made so far is low because they are not validated with experimental results. In numerical simulations, they have characteristics that considerably reduce the accuracy of these predictions. The main problems for the correct development of this type of simulation are shown below.

- The computational cost of FE models is usually too high due to the small element size required for modelling and the large number of simulations required.
- The high degradation of the mechanical properties generally produces high deformation rates for the laminate elements in contact with the cutting tool, introducing severe convergence problems.
- Although the element deletion techniques used to constitute a solution to avoid element distortion problems, this technique limits the tool-workpiece load transfer, reducing the accuracy of shear forces' predictions and sub-surface damage.
- The difficulty of introducing the spring-back phenomenon (partial thickness recovery of the machined surface) makes thrust forces generally very low compared to the experimental evidence.

The numerical predictions obtained in this research are validated with the experimental data obtained by Bhatnagar et al. [118]. Fibre orientations of 0° , 15° , 30° , 45° , 60° , 75° and 90° are studied here. Seventy simulations were performed to analyse the influence of the cutting parameters studied has on the machining induced damage. The below features are added to the FE models to mitigate or at least reduce the above problems.

- All simulations will be developed in 2D FE models applying a mass scaling factor to considerably reduce the simulations' computational cost and maintain the accuracy of the numerical results.
- The maximum degradation of mechanical properties that is allowed in the damage of the matrix is 95 % to avoid that the problems of distortion of elements prevent the convergence of the problem.
- The element deletion is not considered in this work to increase the sub-surface damage predictions.
- A linear vertical penetration of the tool is introduced to simulate the spring-back phenomenon and significantly improve the thrust force predictions.

In other words, this work is focused on improving the predictions of numerical thrust force and induced machining damage. The main objective is to know how different cutting parameters such as tool edge radius, rake and relief angles, or fibre orientation affect post-machining surface cracks nucleation. Section 4.2 describes the modelling settings used in the simulations. Validation of numerical results is carried out in section 5.4 using the results extracted from Bhatnagar et al. [118] experiments. Section 5.5 exposed and discussed the induced machining damage numerical results obtained from all the machining configurations studied. Finally, conclusions obtained from this work are illustrated in section 6.

4.2 Model characteristics

Several 2D FEM plane stress quasi-static analysis is performed with the numerical software package Abaqus/Explicit. Positive fibre orientations of 0° , 15° , 30° , 45° , 60° , 75° and 90° are assessed in this work. A standard cutting configuration coherent with parameters used for Bhatnagar et al. [118] in their experiments is considered to validate the numerical results. Fig. 4.2.1 shows a schematic illustration of cutting parameters treated ahead.

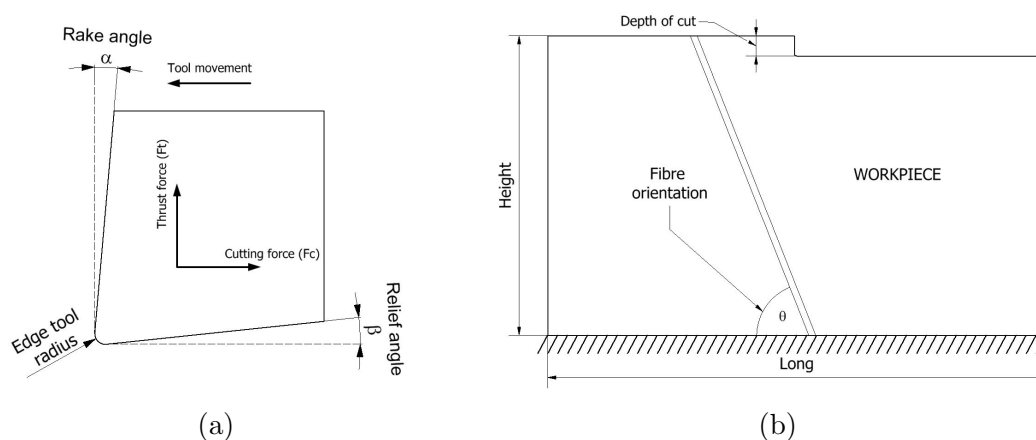


Fig. 4.2.1. (a) Tool and (b) workpiece cutting parameters.

4.2.1 Machining configurations and geometric analysis

Ten cutting configurations are simulated to evaluate the induced damage influence of rake angle, relief angles, tool edge radius and workpiece material. The desired cutting variable studied is changed to keep the rest of the cutting variables the same values with the standard configuration. In Table 4.2.1 a representation of all cutting variables values examined in this work is offered.

Table 4.2.1. Cutting variables employed in this work

Cutting variables	Standard configuration	Cutting variables values studied
Rake angle (α)	5°	-5°, 0°, 10°
Relief angle (β)	6°	4°, 8°, 10°
Tool edge radius (μm)	50	30, 15
Depth of cut (mm)	0.2	-
Workpiece material	GFRP	CFRP
Cutting speed (mm/s)	8.33	-

A 5 mm long and 3 mm height workpiece are investigated. As a boundary condition, the workpiece bottom side is fixed, while for lateral sides, the horizontal displacement is restricted as shown in Fig. 4.2.2. Elastic and strength properties of UD-GFRP and UD-CFRP used in this work are extracted from the Santiuste et al. [85] and Phadnis et al. [20] publications, respectively. Table 4.2.2 and Table 4.2.3 collect the elastic and strength properties of the studied UD-GFRP and UD-CFRP composites.

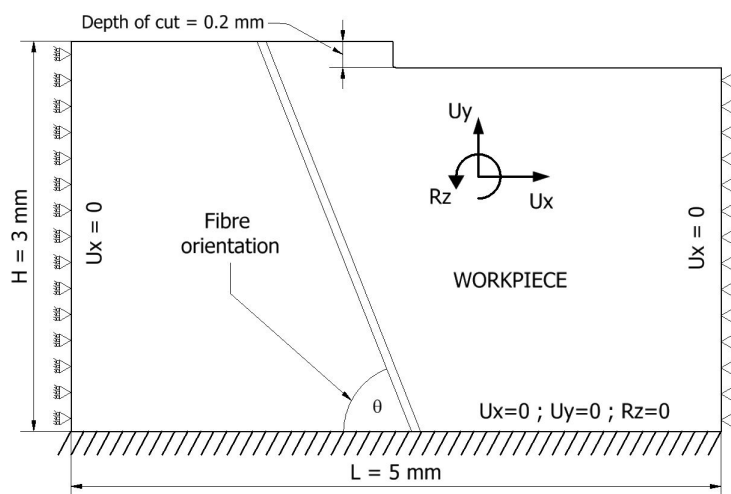


Fig. 4.2.2. Workpiece boundary conditions.

Table 4.2.2. Elastic properties of GFRP and CFRP materials used in this work

Material	$E_{11}(GPa)$	$E_{22}(GPa)$	$G_{12}(GPa)$	ν_{12}
GFRP [85]	48	12	6	0.28
CFRP [20]	136.6	9.6	5.2	0.29

Table 4.2.3. Strength properties of GFRP and CFRP materials used in this work

Material	$X_T(MPa)$	$X_C(MPa)$	$Y_T(MPa)$	$Y_C(MPa)$	$S(MPa)$
GFRP [85]	1200	800	59	128	25
CFRP [20]	2720	1690	111	214	115

4.2.2 Meshing parameters

Quadrilateral elements with linear interpolation and reduced integration, and enhanced hourglass control (CPS4R) were selected. Deletion of elements was not considered in this work. Besides, the low cutting speed applied in the simulation makes the FEM analysis could be considered as a quasi-static problem. Therefore, the composite density could be increased keeping the model kinematic energy stands in low values without affecting the final results and reducing the computational cost. A mass scaling factor of 500 is used in this research to guarantee a substantial reduction of the computational cost.

In general terms, it is recommended that the hourglass energy should be as maximum a 5% of the internal energy to consider valid the numerical results obtained. Apart, from that the kinetic energy should be lower than the 10% of the internal energy to guarantee that not additional dynamic effect are introduced in the simulation. In all simulations developed in this research were checked that both energies were below the 1% of the internal energy calculated. A good example of this statement is show in Fig. 4.2.3.

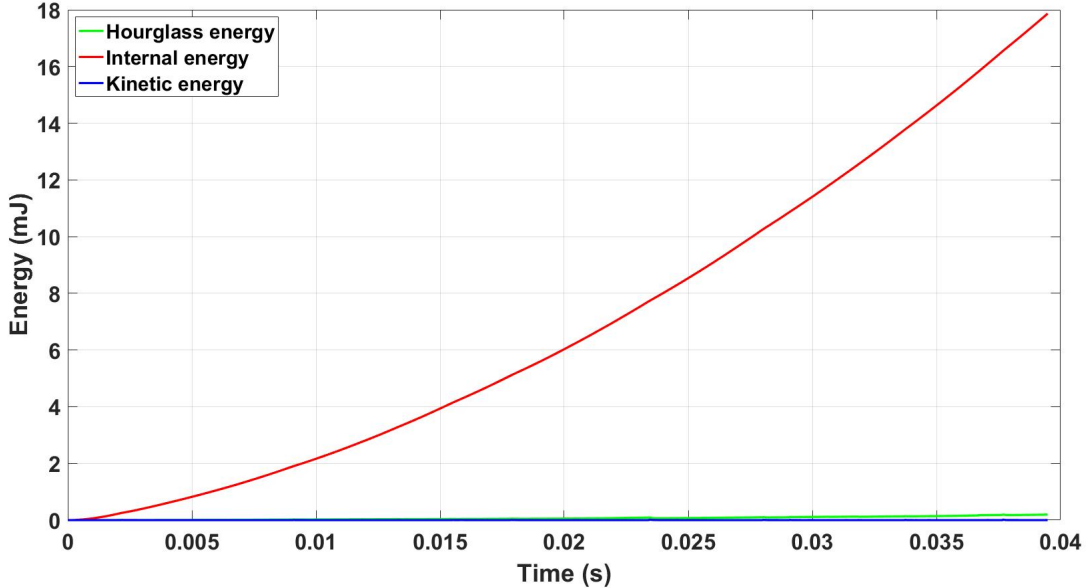


Fig. 4.2.3. Evolution of the internal energy, hourglass energy and kinetic energy during the simulation with the standard cutting configuration and a fibre orientation of 90

Mesh element size was selected to reach the right time-accuracy combination. Next to the cutting tool, a rectangular zone was meshed with an element size of $10\mu m$. The remaining area was more coarsely mesh using partitions which increase the element size progressively from the $10\mu m$ in the vicinity of the refined mesh to the $100\mu m$ of the outer edges. The

distribution of these partitions allowed to avoid the excessive distortion of elements and improve the numerical results' quality.

A mesh convergence study was performed to assure the effectiveness of the mesh employed. It was decided to develop this analysis with a fibre orientation of 45° . This decision was taken because the damage obtained with this fibre orientation was considerable, and the computational time was not excessive in this case. Therefore, bright and relatively quick conclusions about how the mesh distribution affected every fibre orientation's results were extracted by analysing the fibre orientation of 45° .

Eleven meshes were analysed, advancing from a coarser mesh with 9638 elements to a refined mesh with 26975 elements. The refined element size of $10\mu m$ near the tooltip was maintained to obtain accurate prediction in the surrounding tool-workpiece contact zone. The maximum element size was modified, passing from $50\mu m$ to $150\mu m$. In Fig. 4.2.4 an illustration of the mesh distribution obtained with maximum element sizes of $50\mu m$, $100\mu m$ and $150\mu m$ are depicted, observing a remarkable reduction of elements used for larger maximum element sizes.

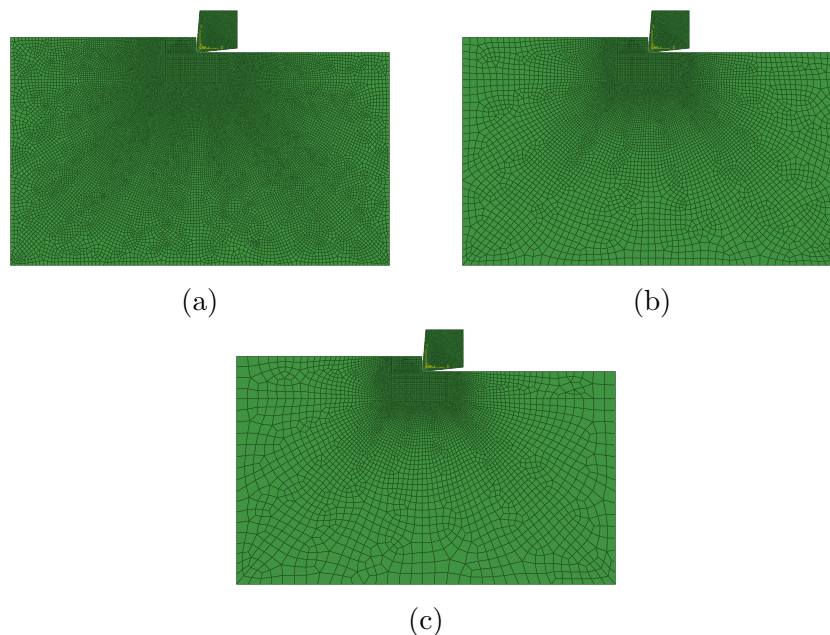


Fig. 4.2.4. Mesh distributions with a maximum element size of (a) $50\mu m$, (b) $100\mu m$ and (c) $150\mu m$

As it is observed in Fig. 4.2.5 in meshes with a more significant number of elements than the mesh used (maximum element size of $100\mu m$), the values of machining forces and sub-surface damage converged. Therefore, high accuracy and low computational time are achieved with the mesh distribution selected. Relevant information about how sub-surface damage and machining forces were measured is provided in subsections 6.2 and 6.3, respectively.

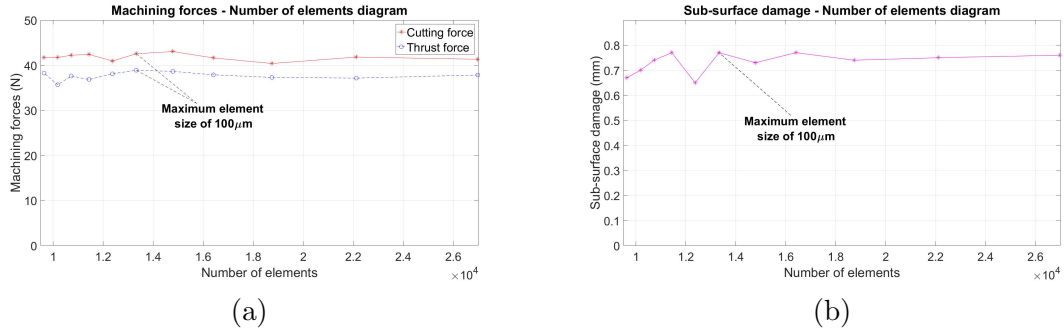


Fig. 4.2.5. Mesh convergence study of (a) machining forces and (b) sub-surface damage.

Additionally, a convergence study of the influence of the element size next to the tooltip has been performed to check the numerical results' robustness. As it is appreciable in Fig. 4.2.6 all results, machining force and damage measured keep a flat tendency for element sizes smaller than 10 μm , while in the case of thrust forces, they are observed to experience an important decrement for larger element sizes. Hence, it is concluded that the results obtained are accurate with an optimisation of the required computational time.

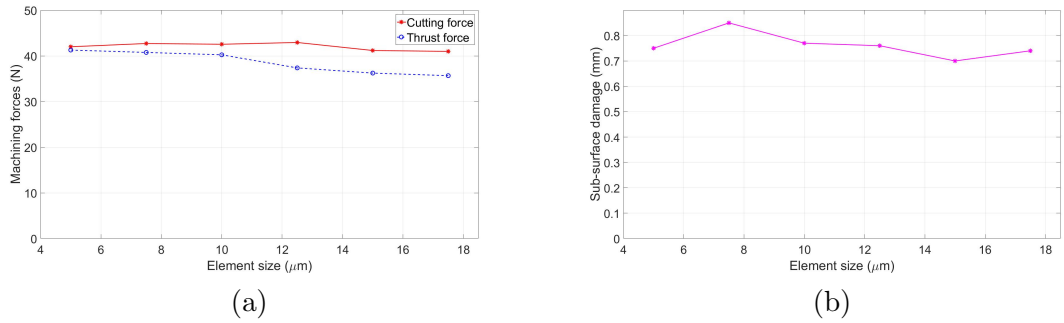


Fig. 4.2.6. Mesh convergence study with different element size around the tool tip of (a) machining forces and (b) sub-surface damage.

4.2.3 Contact and friction modelling

The tool is considered a solid rigid body. The contact between the tool and the workpiece is performed with a surface-node surface contact property. A constant Coulomb friction coefficient of 0.2 is employed in all simulations, as Koplev et al. [141] measured similar values in his research as an overall value for fibre orientations of 0 and 90. It is not the best method to model the contact because the friction coefficient should vary with the fibre orientation. However, because of the lack of information in this matter, other authors have been using this methodology [84, 85, 120].

The friction coefficient's efficiency is proved with a parametric study with a range between 0.2-0.8. Coefficients higher than 0.2 are found to adjust better to the experimental results used to validate the model. Between coefficients from 0.2 to 0.8, it is kept a flat tendency in sub-surface damage, while slight positive and negative slopes are appreciated for cutting and thrust forces, respectively. Coefficients between 0 to 0.2 increase the cutting force and sub-surface damage and keep stable the thrust forces predicted, as shown in Fig. 4.2.7.

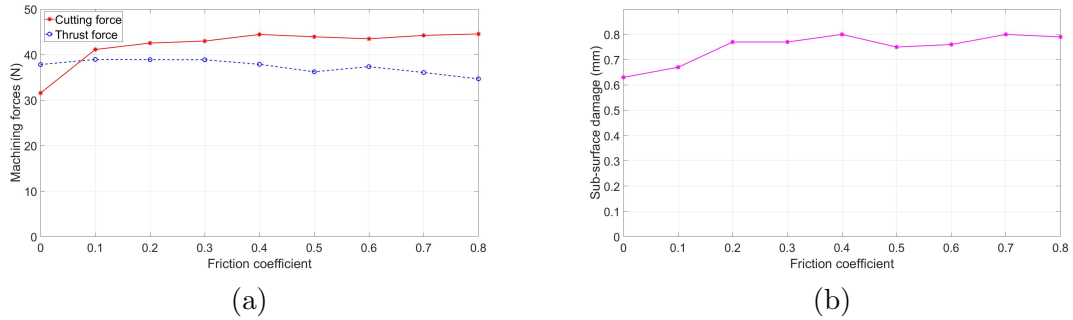


Fig. 4.2.7. Mesh convergence study with different element size around the tool tip of (a) machining forces and (b) sub-surface damage.

4.3 Damage model particularities

The 2D FE damage model described in Chapter 3 is selected to fulfil all the requirements demanded in this analysis. The maximum stress failure criterion is selected to determine the fibre damage initiation ($\alpha = 0$). No element deletion is considered in this research due to this factor reduce the predictions accuracy limitation the load transfer and mitigating the evolution of the underlying machine surface damage. The fracture energies used to calculate the damage evolution is extracted from [142] and the terms are visualised in Table 6.4.1.

Table 4.3.1. Critical fracture toughness extracted from [142]

N/mm	G_{ft}^c	G_{fc}^c	G_{mt}^c	G_{mc}^c
Critical fracture toughness	10	10	1	1

Finally, the maximum damage of 0.95 is allowed for the matrix and 0.999 for the fibre damage modes. These maximum values are chosen to avoid numerical errors [84] and simulate the remaining stiffness that a total failure ply supply to adjacent laminate plies [133]. After this damage level was achieved, a second linear elastic response is introduced with the remaining stiffness. An illustration of the material behaviour scheme is represented in Fig. 3.2.3.

4.4 Model validation

The standard cutting configuration model is validated by comparing the experimental results obtained by Bhatnagar et al. [118]. The chip is assumed to be formed when the simulated cutting force and thrust force reach the experimental values observed in experimental findings. Maximum cutting and thrust forces simulated are chosen as the machining forces to analyse the numerical results.

This assumption is considered reasonable because the non-deletion of elements carried out in the simulations avoid the apparition of the natural machining forces fluctuations [84].

An example of one simulation records of the cutting and thrust forces is provided in Fig. 4.4.1.

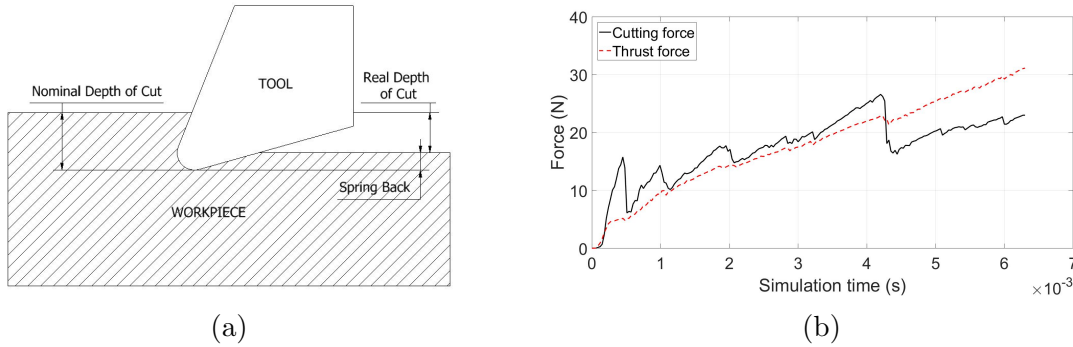


Fig. 4.4.1. (a) Spring back phenomen representation and (b) example of machining forces record for the simulation of the standard cutting configuration and a fibre orientation of 0° .

Spring back phenomenon, which considers the partial laminate thickness recovery that always takes place after the tool pass away (Fig. 4.4.1), is taken to improve the numerical damage predictions. This phenomenon is introduced, imposing a vertical penetration in the laminate; the values employed are shown in Table 4.4.1. These values were selected to calibrate the predicted thrust force and simulate the machining induced damage with higher accuracy. The real depth of cut considered is 0.2 mm, while to calculate the nominal depth-of-cut, the vertical tool penetration (Table 4.4.1) should be added, see Table 4.4.1.

Lasri et al. [84] and Santiuste et al. [85] validated their simulations using the cutting force obtained in Bhatnagar et al. [118] experiments. However, the thrust force is poorly predicted due to not including the spring-back phenomenon effects on composite machining response. This work proves this phenomenon's importance on thrust force enhancing previous numerical predictions, as shown in Fig. 4.4.1.

In addition, the machining sub-surface damage is assessed through the activation functions (F_{ft} , F_{fc} , F_{mt} and F_{mc}) introduced previously. Sub-surface damage is assumed to be the distance between the lowest element where it is equalised or exceeded the damage initiation condition and the machining trim surface. In this work the damage initiation condition is achieved after reaching or exceed F_{mt} and F_{fc} a value of 0.75 or F_{mc} and F_{ft} a value of 1. This decision is taken because fibre experience buckling problems in compression states, and matrix have properties degradation problems in traction states [133]. Therefore, it is decided to be conservative with fibre compression and matrix traction damage modes.

Table 4.4.1. Vertical speed, cutting tool displacements and simulation time obtained for every fibre orientation simulating the standard cutting configuration

Fibre orientation	0°	15°	30°	45°	60°	75°	90°
Vertical penetration (mm)	0.0313	0.0226	0.0411	0.0395	0.0407	0.0439	0.0600
Nominal depth of cut (mm)	0.2313	0.2226	0.2411	0.2395	0.2407	0.2439	0.2600
Horizontal displacement (mm)	0.0521	0.0236	0.0381	0.0366	0.0679	0.1465	0.3202
Simulation time (s)	0.0063	0.0029	0.0046	0.0044	0.0082	0.0176	0.0394

From the results it is observed that the fibre damage initiation criterion is not reached

in low laminate locations. Hence, the matrix damage modes determine the sub-surface damage in all simulations. In Fig. 4.4.3 the evolution of matrix damage modes and shear and transverse stresses in different laminate areas is assessed. Three distinct matrix-induced damage modes are distinguished in different workpiece positions: (1) beneath, (2) behind and (3) in front of the tool.

As shown in Fig. 4.4.3(d), d_{mt} is found behind, while d_{mc} occurs in front positions as illustrated in Fig. 4.4.3(e). Both matrix damage modes are obtained in low laminate positions (Fig. 4.4.3(c)). For clarification, failure allocations in Puck's failure envelope is provided in Fig. 4.4.3(f). Main reasons to obtain these results are:

- Zone 1: Shear stresses are predominant, allocating the failure point in the boundary between traction and compression failure modes.
- Zone 2: Important traction transverse stresses are obtained because the tool tip's pulling effect produces a Mode A or matrix traction failure.
- Zone 3: Mode C or matrix compression damage is detected due to the high compressive transverse stresses produced by the tool's pushing action.

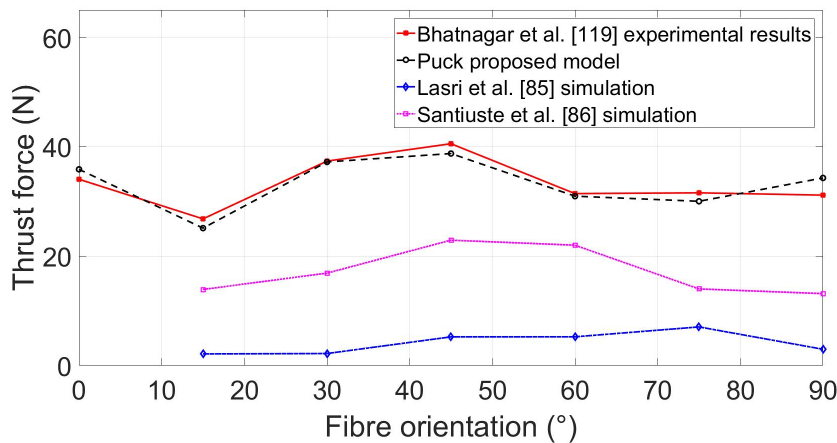


Fig. 4.4.2. Thrust forces obtained in the proposed numerical simulation and other publications.

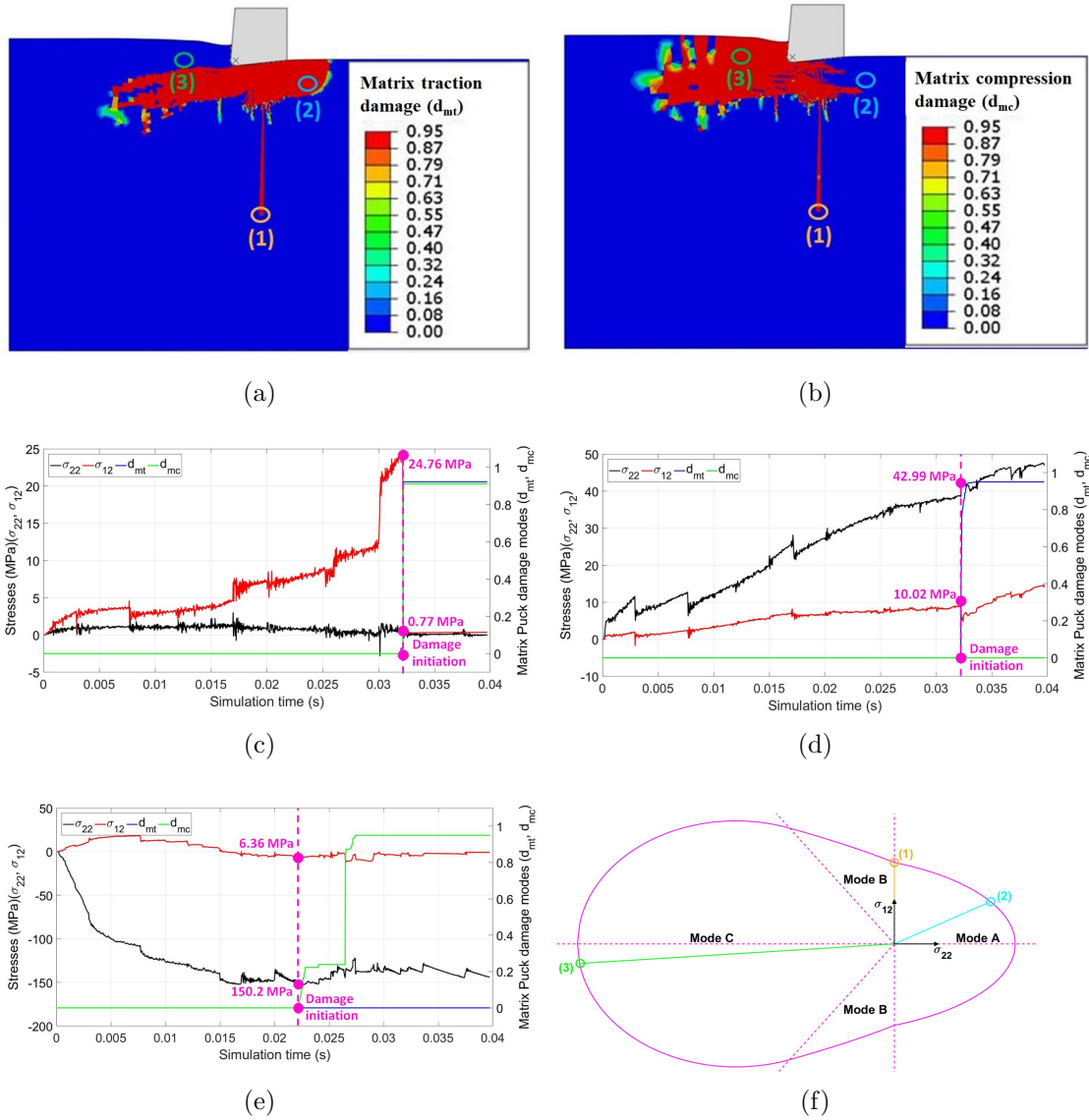


Fig. 4.4.3. Detailed illustrations of the matrix damage modes causes at final simulation time with the standard configuration and a fibre orientation of 90° : (a) Matrix traction damage (d_{mt}), (b) Matrix compression damage d_{mc} , (c), (d), (e) σ_{22} , σ_{12} , d_{mt} and d_{mc} predicted in position (1), (2) and (3), respectively and (f) Damage modes allocation using the Puck's matrix failure criterion in different laminate positions

Note that, although they are the most repeated trends appreciated in all fibre orientations, they are other trends appreciated in the simulated results. For instance, the machining of 0° laminates is a particular case where the transverse direction is perpendicular to the cutting tool movement. Therefore the stress σ_{22} is fluctuating around 0 making the shear contribution the principal cause of the matrix damage. In the cases of 15° and 30° laminates, the matrix tensile damage area observed in front of the tool is the chip fracture zone where the shear stresses are predominant, refer to Fig. 4.5.1. It occurs because the matrix stresses fluctuates around 0 for the dynamic effects providing both tensile and compression matrix damage predictions in the model. Bigger damage compression areas are predicted with significant matrix compression underneath the tool due to the tool penetration. It occurs because this tool penetration is compressing the matrix in these

areas.

The maximum sub-surface damage measured in the simulations achieved a significant improvement in comparison with Bhatnagar et al. [118] results, as depicted in Fig. 4.4.4. For all fibre orientations excepting 90° , the predicted values are closer to experimental ones than Bhatnagar's predictions achieved. It could be explained because the model does not include the fibre/matrix debonding, that occurs when fibre bends, and the shear matrix plastic energy which play a vital role in the damage extension for high fibre orientations. Further investigations will deal with this matter shortly. However, the increasing experimental sub-surface damage tendency for this fibre orientation is achieved in this simulation.

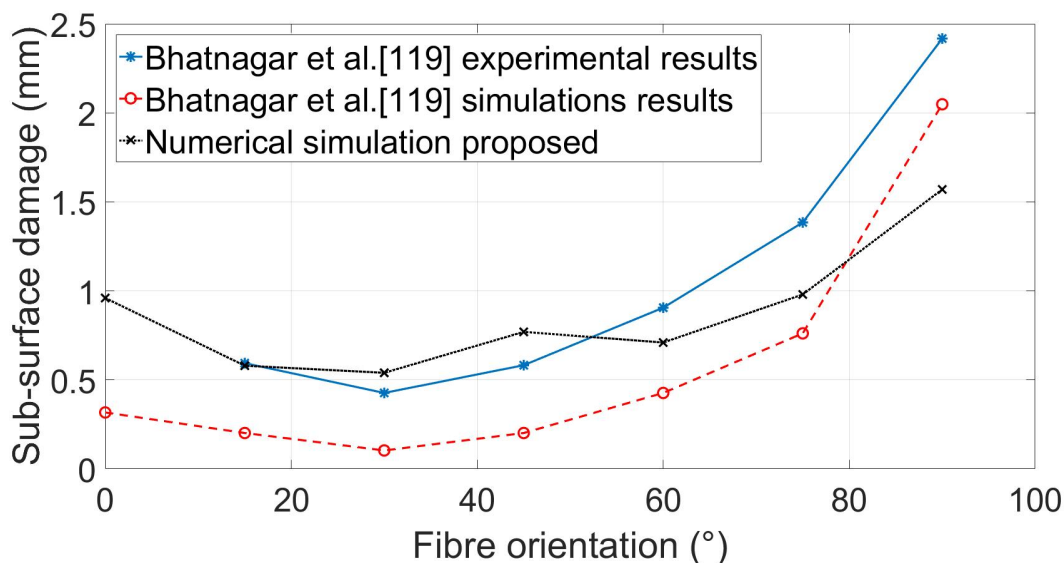


Fig. 4.4.4. Sub-surface damage obtained in the numerical simulation proposed and Bhatnagar et al. [118] numerical and experimental results

4.5 Results and discussion

The main contributions in this chapter are summarised in this section. Only one of the desired cutting parameters is changed for all simulations performed, keeping the rest with the standard configuration values (refer to Table 4.2.1). Ten cutting configurations are assessed to compare the influence of cutting parameters on the induced machining damage. They are performed applying the same tool displacement and velocities used for the standard cutting configuration (refer to Table 4.4.1). The illustration of all the matrix traction and matrix compression laminate damages simulated in this research are presented in **Appendix B** and **Appendix C**, respectively

4.5.1 Fibre orientation influence

Fig. 4.4.4 shows the induced damage contours for different fibre orientations. It can be seen that the induced damage is highly dependant on the fibre orientation. The damage is mainly propagated in parallel and perpendicular fibre direction as represented in Fig. 4.5.1.

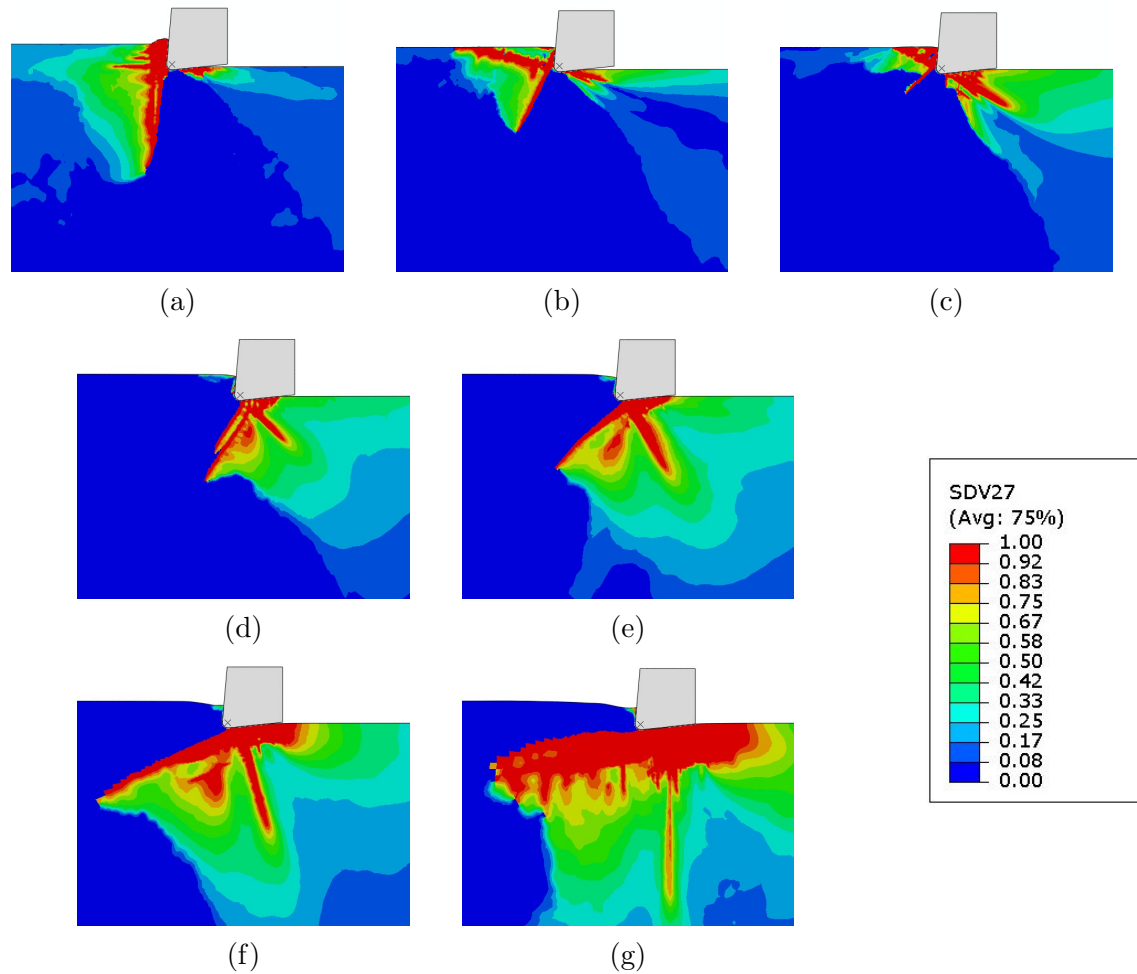


Fig. 4.5.1. F_{mt} obtained for fibre orientations (a) 0° (b) 15°, (c) 30°, (d) 45°, (e) 60°, (f) 75° and 90° at final simulation time with the standard cutting configuration.

Lower induced damages are achieved for 15° and 30° fibre orientations, while higher values are obtained for 75° and 90°. The implication of high tool-workpiece contact stiffness for low fibre orientations produced a fragile chip rupture without excessive damage propagation. For a fibre orientation of 0° the fibre buckling effects are detected, introducing unstable damage propagation effects.

For higher fibre orientations, the tool-workpiece contact stiffness is mainly governed by the matrix; thereby, it is softer than the contact produces with low fibre orientations. Due to this fact, a significant energy increment is required to achieve chip generation. As a result, the sub-surface damage extension is deeper for these unidirectional composite laminates. Lastly, for a fibre of 90° a fine line of the sub-surface in the thickness direction is appreciated. This finding reveals a significant fibre-matrix debonding, which increase the damage extension because the tool pushed the fibre away.

4.5.2 Workpiece material influence

UD-CFRP and UD-GFRP composites are simulated to assess the influence of different material properties. It is found that induced damage levels are significantly lower for UD-CFRP in all fibre orientations, see Fig. 4.5.3. In the case of UD-CFRP composites, fragile

damage behaviour is appreciated while UD-GFRP laminates show ductile behaviour. This behaviour is explained because of the higher contact stiffness properties between the tool and UD-CFRP composites.

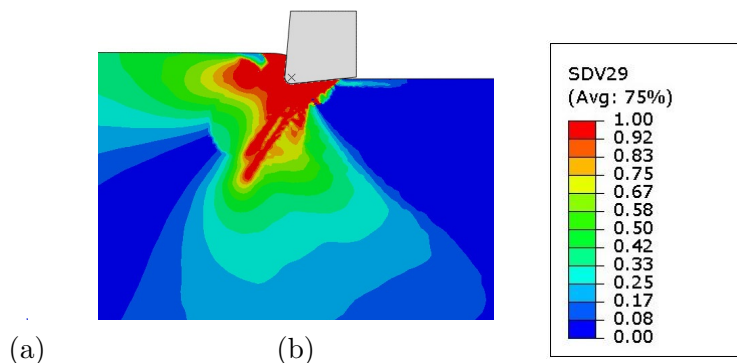


Fig. 4.5.2. F_{mc} illustration of (a) UD-CFRP composites and (b) UD-GFRP composites at final simulation time and fibre orientation of 45° .

The UD-GFRP composites increased more than 144.83% the machined induced damage simulated in UD-CFRP composites. For most fibre orientations, the UD-GFRP composites sub-surface damage exceeded the 200% or even the 300% damage obtained for UD-CFRP composites, reaching the maximum difference of a 375.76% for fibre orientation of 90° . Hence, it is concluded that CFRP composites are better materials to machine than GFRP composites in induced machining damage response. An illustration of the matrix compression damage extension (F_{mc}) for both materials with 45° fibre orientation is presented in Fig. 4.5.2.

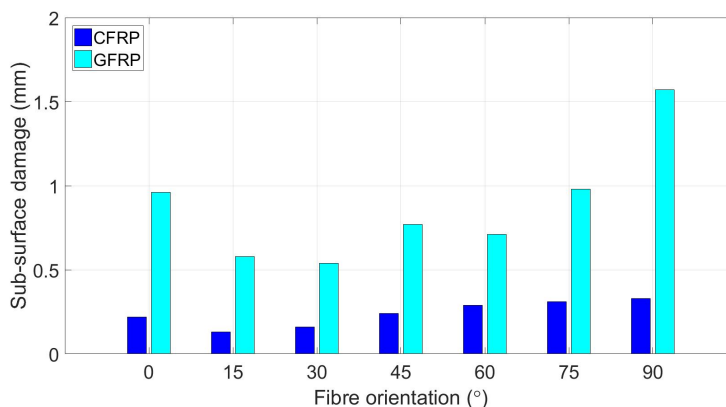
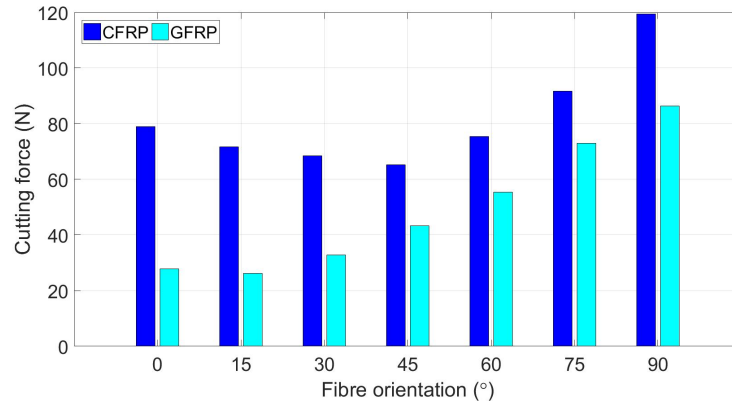
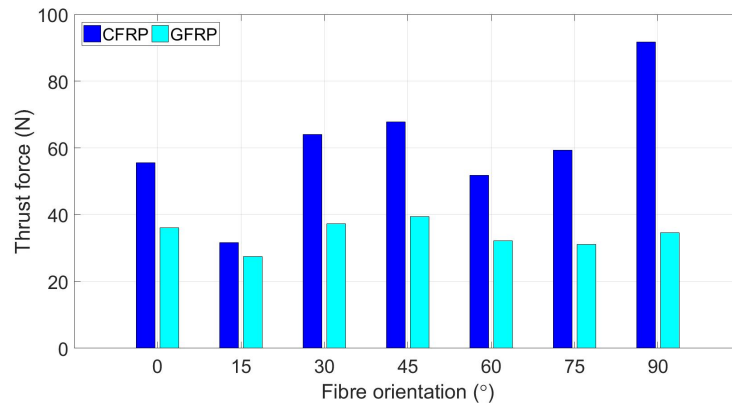


Fig. 4.5.3. Sub-surface damage obtained for all the workpiece materials and fibre orientations studied at the final simulation time.

Note that, because of the high stiffness of CFRP composites, the machining peak forces are substantially incremented compared to GFRP composites, as shown in Fig. 4.5.4.



(a)



(b)

Fig. 4.5.4. (a) Cutting and (b) thrust forces obtained for all the workpiece materials and fibre orientations studied at the final simulation time.

4.5.3 Tool edge radius influence

In Fig. 4.5.5 the induced damages obtained with the $15\ \mu\text{m}$, $30\ \mu\text{m}$ and $50\ \mu\text{m}$ edge tool radius simulated are plotted. This increment of edge tool radius chosen is simulated to observe the laminate damage that tool wear causes. An edge radius of $15\ \mu\text{m}$ represents the geometry of a new cutting tool faithfully. Whereas the radius of $30\ \mu\text{m}$ and $50\ \mu\text{m}$ model the increased edge radius of the cutting tools after several machining operations.

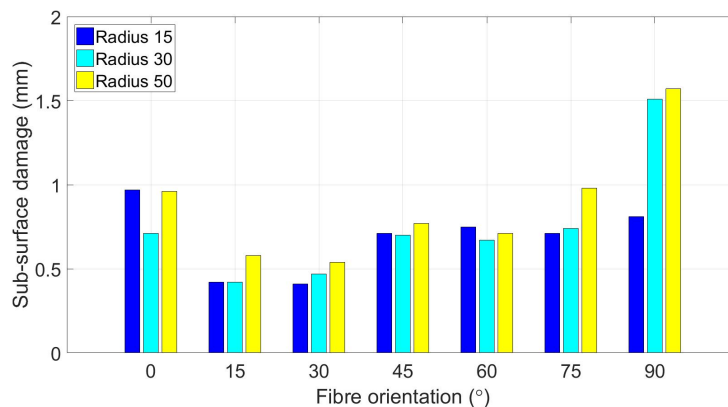


Fig. 4.5.5. Sub-surface damage obtained for all the tool edge radius and fibre orientations studied at the final simulation time.

For fibre orientations of 15° and 75° tool edge radius $15\mu m$ and $30\mu m$ reduce the sub-surface damage extension obtained with a tool edge radius of $50\mu m$. For 30° , 45° and 60° fibre orientations, the tool edge radius influence on the subsurface damage is observed to be negligible in the studied radius range.

In the case of 0° , a significant damage reduction is obtained with a tool edge radius of $30\mu m$. This damage reduction is reached due to the fibre buckling effects that occurred with this fibre orientation. For this reason, this laminate damage reduction in comparison with edge tool radius $15\mu m$ is obtained. For 90° fibre orientation, the use of a low tool edge radius is highly recommended to significantly reduce the laminate damage significantly, see Fig. 4.5.6.

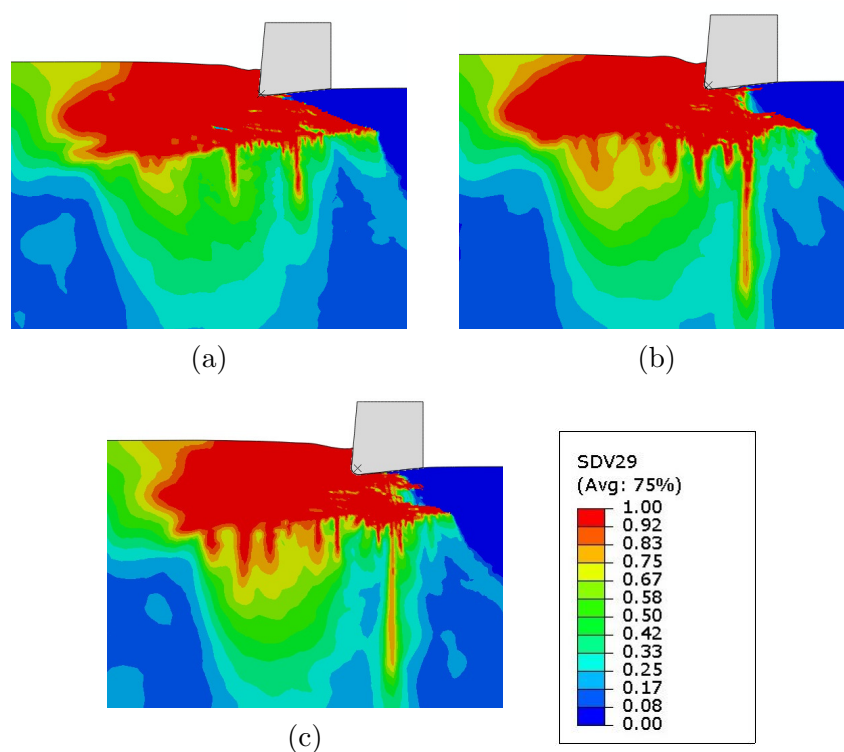


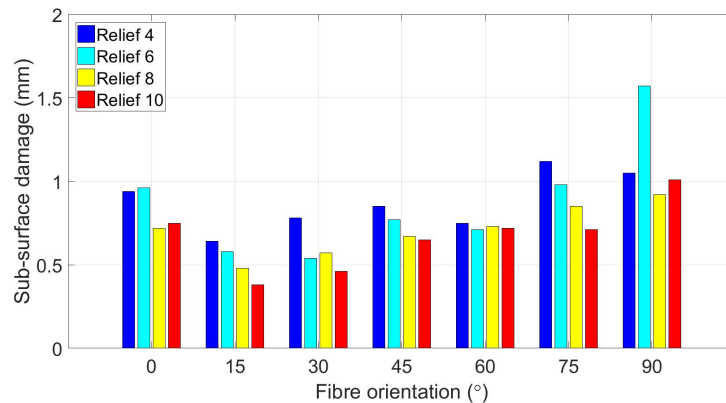
Fig. 4.5.6. F_{mc} obtained for tool edge radius of (a) $15\mu m$ (b) $30\mu m$, (c) $50\mu m$ at final simulation time for a fibre orientation of 90° .

It is concluded that the lower tool edge radius produces better machining surfaces than cutting tools with a higher edges radius. However, the maximum sub-surface damage increment is observed small (below the 40%) for fibre orientations between 0° and 75° . Hence, it is determined that the tool wear until $50 \mu\text{m}$ does not increase the sub-surface damage critically for fibre orientations between 0° and 75° .

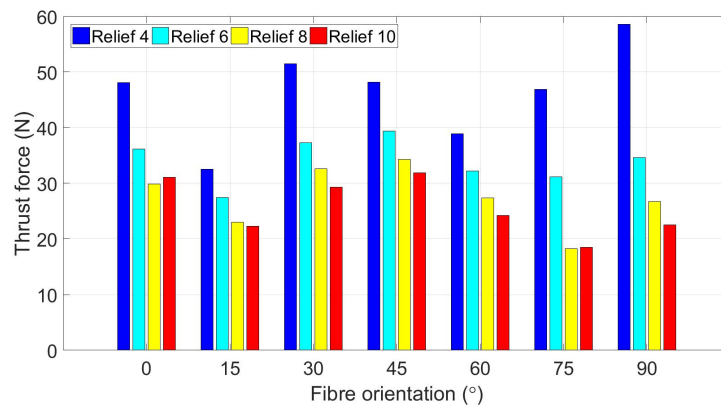
4.5.4 Relief angle influence

Machining configurations with 4° , 6° , 8° and 10° are analysed, see Fig. 4.5.7. In general terms, higher relief angles are beneficial to minimise the sub-surface damage, as shown in Fig. 4.5.7(a). The same tendency is appreciated for thrust forces due to the tool-workpiece contact area reduction behind the tooltip (refer to Fig. 4.5.7(b)). Therefore, it is concluded that thrust force and induced damage are intimately related; the less thrust force is achieved, the less induced damage is obtained.

Relief angle 10° is found to reduce the damage for fibre orientations of 15° , 30° and 75° considerably. Besides, it is observed that relief angles of 8° and 10° minimised the induced damage compared with the rest of the angles for 0° and 45° fibre orientations. For 60° fibre orientation, the relief angle effects are negligible, and for 90° the relief angle of 6° , a significant induce damage is achieved compared with the rest of the angles simulated.



(a)



(b)

Fig. 4.5.7. (a) Sub-surface damage and (b) thrust forces obtained for all the relief angles and fibre orientations studied at the final simulation time.

The simulation results show that the most serious sub-surface damage exceeds more than 50% the lowest sub-surface damage for fibre orientations of 15° , 30° , 75° and 90° . Thus, it is concluded that the election of correct high relief angles is essential for not affecting the structural integrity of the laminate considerably. The factor F_{mt} is depicted in Fig. 4.5.8 for 75° fibre orientation to show the reduction of sub-surface damage with higher relief angles.

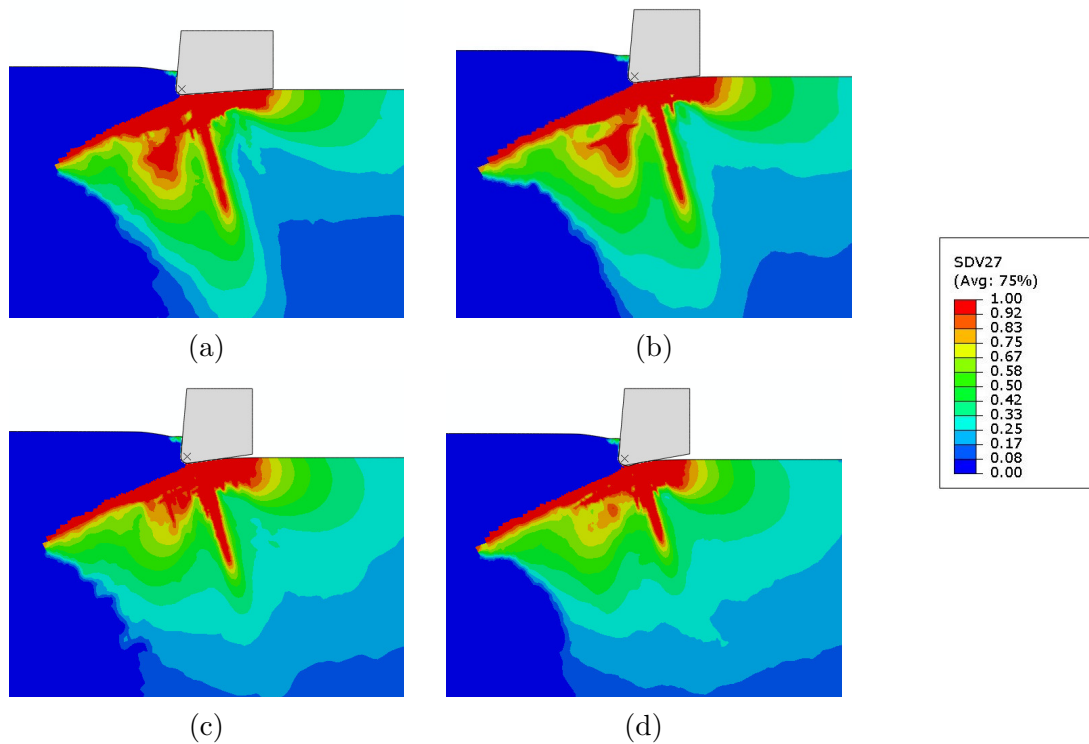


Fig. 4.5.8. F_{mt} obtained for relief angles (a) 4° (b) 6° , (c) 8° and (d) 10° at final simulation time for a fibre orientation of 75° .

4.5.5 Rake angle influence

From the numerical results obtained in this work, no clear rake angle tendency is observed to reduce the sub-surface damage. It is found that the rake angle which produced less sub-surface damage is fluctuating with the fibre orientation, see Fig. 4.5.9. Therefore, the best rake angle to reduce the level of damage in composite laminates should be analysed for each fibre orientation.

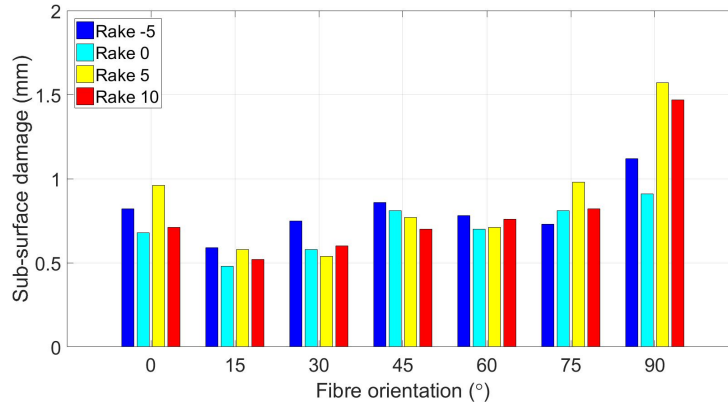


Fig. 4.5.9. Sub-surface damage obtained for all the rake angles and fibre orientations studied at the final simulation time.

Fig. 4.5.9 reveals that the rake angle of 0° obtains a low laminate induced damage for all fibre orientations. This rake angle is the best machining option for fibre orientations of 0°, 15°, 60° and 90°. However, significantly induced damage increments are not seen for fibre orientations between 0° and 75°, which the maximum differences are around 40%. Therefore, the rake angle is considered not essential to reduce the remaining laminate damage compared to other cutting factors such as workpiece material or relief angle.

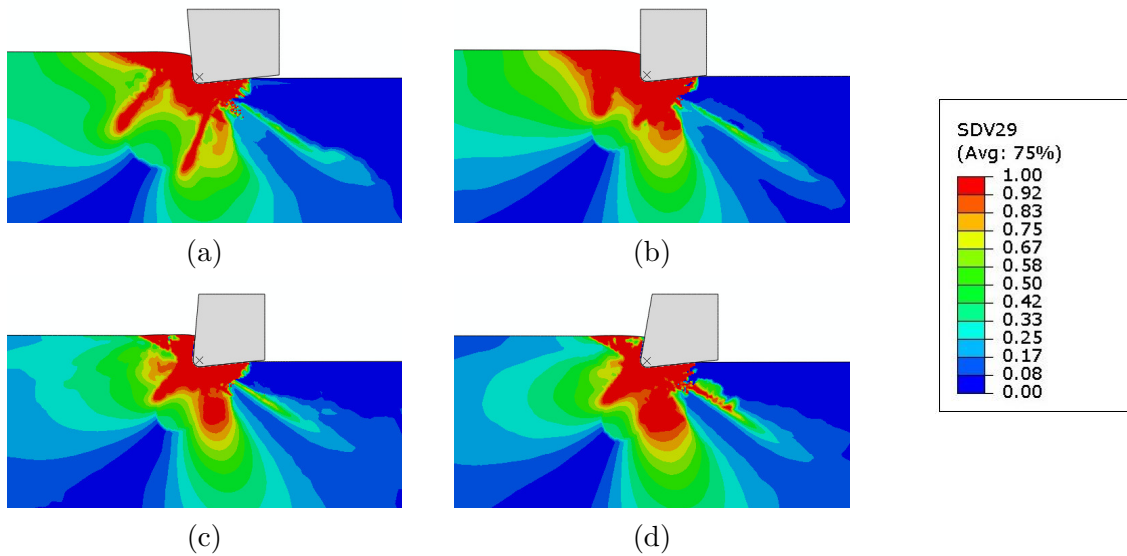


Fig. 4.5.10. F_{mc} obtained for rake angles (a) -5° (b) 0°, (c) 5° and (d) 10° at final simulation time for a fibre orientation of 30°.

As shown in Fig. 4.5.9, rake angles of 5° and 10° are not a suitable solution for machining laminates with 90° as it produces higher damage levels. Finally, Fig. 4.5.10 represents the matrix compression activation function F_{mc} calculated at the final of the simulation for a fibre orientation of 30° as a mode of example.

4.6 Concluding remarks

This investigation offers a novel orthogonal cutting FEM study of the effect of cutter parameters on machining induced damage. The Spring-back effect included adding a cutting tool vertical movement during the simulation, improving the thrust force predictions. The use of a new damage algorithm composed of linear stiffness degradation and a maximum damage limit for fibres and matrix has been demonstrated to improve previous sub-surface damage predictions. It has been demonstrated that matrix damage modes delimit the induced damage machining depth, distinguishing three main areas: (1) beneath, (2) behind and (3) in front of the cutting tool.

- Zone 1: Shear stress is predominant, and as a result, both matrix damages, cracking and crushing, are developed.
- Zone 2: Cracking matrix mode is produced because the tool-workpiece friction effect pulls the material in this area.
- Zone 3: Crushing mode occurs due to the high compressive loads produced by the cutter tool's pushing action.

Ten cutting configurations related to fibre orientation, material properties, edge radius, relief angle, and rake angle are simulated, concluding in the below statements.

- The low fibre orientations, i.e., 15° and 30° , show less induced damage than the higher fibre orientations, i.e., 75° and 90° . The low fibre orientations are experiencing fragile chip ruptures, while higher orientations show more ductile chip rupture.
- The UD-CFRP composites experience more fragile chip fractures and provide much lower induced damages than the UD-GFRP composites for all fibre orientations. Machining forces are considerably higher for CFRP composites because of their superior stiffness.
- In general, the tool wear effects do not generate severe induced damage, except for edge radius higher than $15 \mu m$ for 90° fibre orientation.
- High relief angles produce low sub-surface damages for all fibre orientations. It is noted that thrust forces are intimately related to the sub-surface damage observing that the less thrust force is achieved, the less induced damage is obtained.
- The rake angles studied does not affect considerably into the machining induced damage. A rake angle of 0° is recommended to obtain lower induced damage levels on the laminate for every fibre orientation.

Chapter 5

Chip formation modelling for various fibre orientations

5.1 Introduction

Mostly, there are five different chip fracture scenarios in composite machining [143–145]. The main factor which controls the chip fracture process is fibre orientation. In this investigation, cutting tools with positive rake angles are selected as a reference. Four distinct chip classifications according to the fibre orientation in the composite machining with positive rake angles (superior to 0°) can be distinguished: (1) 0° , (2) positive fibre orientations ($0^\circ < \theta < 90^\circ$), (3) 90° and (4) negative fibre orientations ($\theta > 90^\circ$). Additionally, the particular micro-buckling of the fibres observed in the machining using cutting tools with 0° rake angle introduce a new chip fracture mechanism.

A brief description of the particularities of every chip formation mechanism aforementioned is provided in the following lines. All these cases are visualised in Fig. 5.1.1.

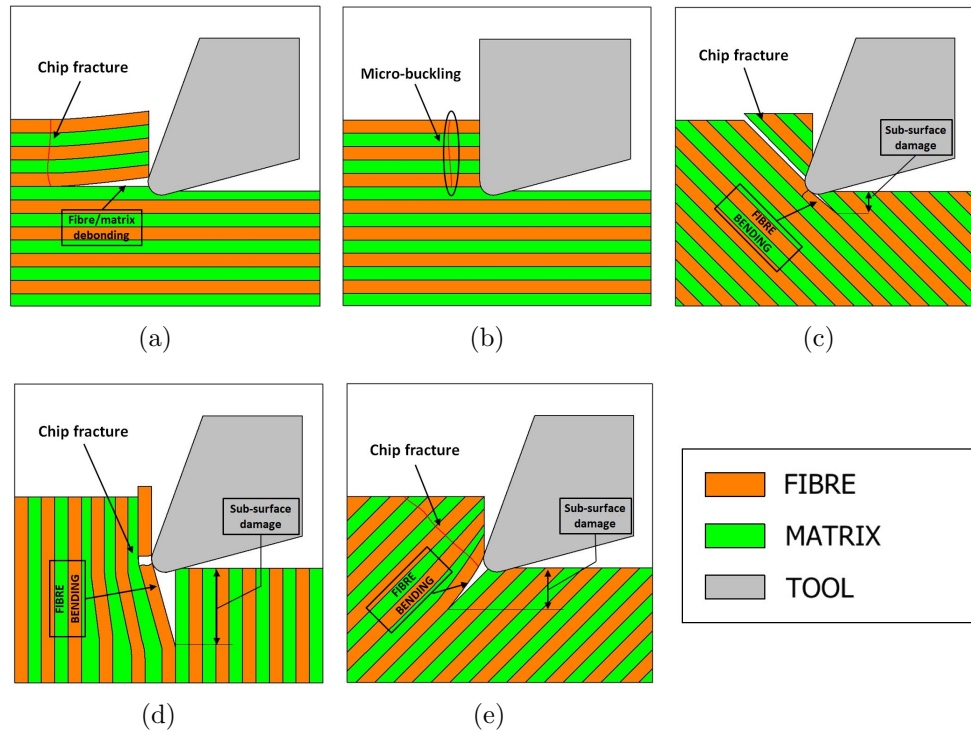


Fig. 5.1.1. Representation of the different chip fracture scenarios studied in this research: (a) Fibre orientation of 0° , (b) Fibre orientation of 0° with a rake angle of 0° , (c) Fibre orientation of 0° with a rake angle of 0° , (d) Fibre orientation of 90° and (e) Negative fibre orientations or superior to 90°

- **Fibre orientation of 0° :** firstly, a mode I fracture parallel to the fibre peel the laminate from the tool edge radius, creating a separate layer that slides over the rake face. This fracture occurs because the matrix's tensile strength is much lower than the fibre's strength under compression loadings. Secondly, the cutter advance induces a notable increase in the bending moment of the separate layer. Finally, the chip breaks perpendicularly to the fibre direction because the fibre bending strength is exceeded, as shown in Fig. 5.1.1(a).
- **Fibre orientation of 0° with 0° rake angle:** the high fibre compression occasioned by the rigid tool/workpiece contact originate the micro-buckling of the fibres with a small chip length. This mechanism is visualised in Fig. 5.1.1(b).
- **Positive fibre orientations $0^\circ < \theta < 90^\circ$:** the chip slides parallel to the fibre orientation, inducing a matrix shear fracture because produced by the high compressive forces induced with the cutting tool's advancement, as represented in Fig. 5.1.1(c).
- **Fibre orientation of 90° :** small fragments of fibre and matrix are sheared away parallel to the fibre orientation. The fibre is cut in this configuration because of the high compression induced by the tool. This contact produces a high bending moment in the fibre, which induce a mode I fracture, obtaining substantial sub-surface damage [35], refer to Fig. 5.1.1(d).
- **Negative fibre orientations $\theta > 90^\circ$:** the chip is removed with a mode II fracture perpendicular of the fibre because of the bending of fibre induced by severe compressive forces produced by the cutting tool. As a consequence of the fibre bending

moment generated with the tool's contact, significant underlying machining damage is induced in the laminate, as represented in Fig. 5.1.1(e).

A critical review of the state-of-art revealed that despite chip fracture is intimately connected with the prediction of machining responses, it has not been widely modelled up to date [34, 36]. Most of the current investigations developed in this field present several limitations. It occurs because they are developed in simplified 2D FE models and not all fibre orientations are successfully simulated [84]. 2D FE model are limited to the study of orthogonal cutting operations because it does not take into account the out-of-plane effect of the process; thus excluding more complex machining operations such as drilling, milling or turning. The study of these machining processes is of great interest to the industry and can only be addressed using 3D finite element models. Therefore, the development of more complex 3D FE models is required to enhance the machining response predictions' quality in the oncoming investigations.

This chapter develops an original methodology to model in 3D FE models the chip fracture in a composite orthogonal cutting process with several fibre orientations. The chapter layout is as follows. Section 5.2 provides a description of more important numerical aspects accounted for in this work. Details of the linear energy-based composite damage model employ in this investigation are given Section 5.3. A thorough discussion of the particularities modelled at each fibre orientation simulated is encountered in Section 5.4. Finally, Section 5.5 offers a general view of this research remarking the most relevant findings extracted from this numerical assessment.

5.2 Model characteristics

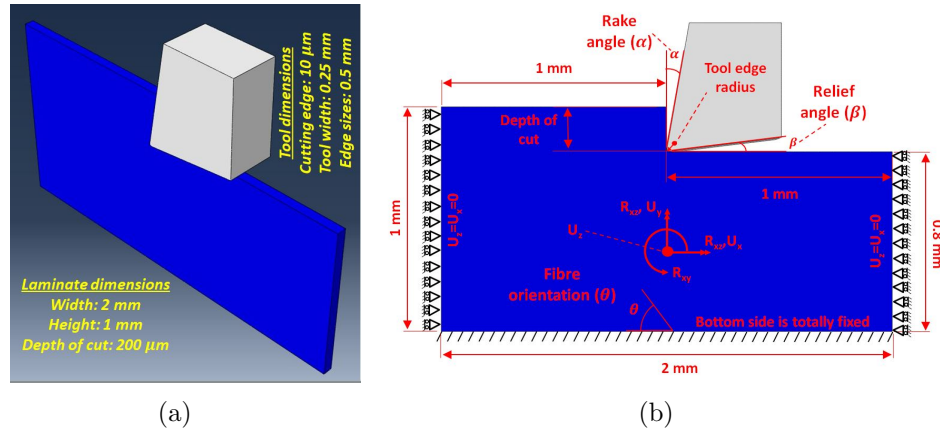
This section aims to clarify the most relevant aspects of the 3D FE model developed in this research. A 3D FE model is selected because Abaqus commands provides the self-contact iteration in 3D elements, but it is not provided for shell elements. This property does not allow the chip penetration in the laminate providing a higher physical meaning. This information is collected in two separate sections where numerical details regarding mesh distribution, geometry, material and friction model employed are described.

5.2.1 General model features

A representative portion of the laminate of 1 mm height, 2 mm long and 50 μm width is assessed in this work, see Fig. 5.2.1(a). The model's height and longitudinal dimensions allow recreating the chip release without the interaction of the imposed boundary conditions at the edges. A small thickness of 50 μm is selected to reach a reasonable computational time because the out-of-plane effect is negligible in the developed simulations. The cutting tool is positioned in the middle of the laminate to accurately emulate cutting conditions when the tool moves along the laminate edge. Additionally, two different boundary conditions are implemented to mimic a clamped laminate: horizontal displacement of laminate is restricted in lateral sides, while the bottom surface of the laminate fully fixed as shown in Fig. 5.2.1(b). The cutting parameters modelled in this investigation, which are visualised in Fig. 5.2.1(b). are collected in Table 5.2.1.

Table 5.2.1. Cutting variables employed in this work

Rake angle (α)	Relief angle (β)	Tool edge radius	Depth of cut	Cutting speed
10 °	10 °	10 μm	200 μm	100 mm/s

**Fig. 5.2.1.** Representation of the FE model simulated: (a) 3D perspective view (b) Boundary conditions and relevant cutting parameters modelled

Four fibre orientations are simulated in this research to assess several possible scenarios in composite machining: 0°, 45°, 90° and 135°. The mechanical properties of the CFRP laminate modelled in this research are extracted from [81] and listed in Tables 5.2.2 and 5.2.3, respectively. The cutting tool is assumed to be rigid because its elastic stiffness is remarkably higher than the CFRP's stiffness. This approach is considered to be valid for two reasons: firstly, magnitudes of cutting process parameters (especially depth-of-cut and cutting speed as these govern the cutter-workpiece contact area at any given instance) in this study are not large enough to cause a noticeable deformation to the cutter. Secondly, the modelling of tool wear is out-of-scope of the current study; this factor will be a matter of future consideration.

Table 5.2.2. Elastic properties of the CFRP laminate [81]

$E_{11}(\text{GPa})$	$E_{22} = E_{33}(\text{GPa})$	$G_{12} = G_{13} = G_{23}(\text{GPa})$	$\nu_{12} = \nu_{13}$	ν_{23}
136.6	9.6	5.2	0.29	0.4

Table 5.2.3. Strength properties of the CFRP laminate [81]

$X_T(\text{MPa})$	$X_C(\text{MPa})$	$Y_T = Z_T(\text{MPa})$	$Y_C = Z_C(\text{MPa})$	$S_{12} = S_{13} = S_{23}(\text{MPa})$
2720	1690	111	214	115

The principal material directions are calculated using the in-built Abaqus commands for every element of the laminate. In general terms, a local material coordinate system is created with axis 1, 2 and 3. Axis 1 refers to the fibre direction, axis 2 defines the

transversal fibre direction inside the lamina, and axis 3 is the out-of-plane (laminate thickness) direction, see Fig. 5.2.2. Abaqus pass the principal material directions to a user-defined VUMAT Fortran subroutine to calculate the laminate's mechanical behaviour.

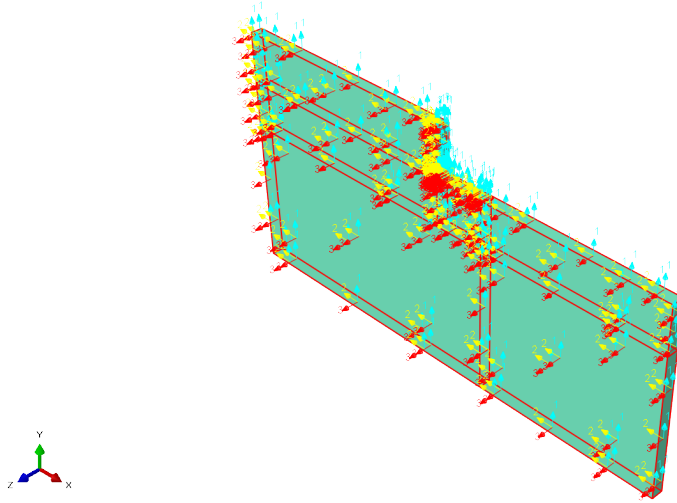


Fig. 5.2.2. Material directions assigned in Abaqus graphic (90° laminate)

5.2.2 Mesh and friction model performed

Hexagonal C3D8R meshed elements available in Abaqus/Explicit are used in this investigation. A thorough distribution of the element sizes is meshed to guarantee the results' accuracy in a reasonable computational time.

In the cutting tool, the elements are refined around the cutting edge to recreate the cutting edge morphology accurately with element sizes of $2 \mu m$, while for the rest of the cutting tool, they are around $10 \mu m$. Three mesh regions are distinguished in the composite laminate: one refined mesh, two intermediate meshes and one coarse mesh. The refined mesh is allocated in the cutting area in front of the tool with an element size $5 \mu m$. Both intermediate meshes increase gradually one dimension of the element size from $5 \mu m$ to $100 \mu m$, while the coarse mesh element sizes are steadily incremented from $5 \mu m$ to $100 \mu m$, refer to Fig. 5.2.3(a).

Along the tool width, only five partitions are modelled to reduce the number of meshed elements and reduce the model's computational cost. In the case of the composite laminate, ten partitions are carried out to have elements in the cutting region with an aspect ratio of 1, as shown in Fig. 5.2.3(b). This aspect ratio notably enhances the accuracy of the numerical results [89].

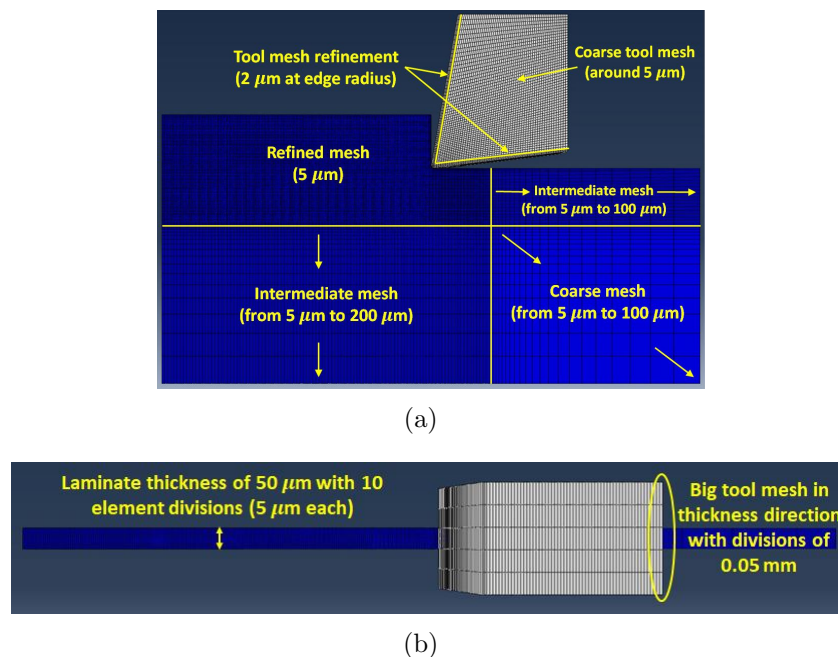


Fig. 5.2.3. Representation of meshed areas of the model: (a) Laminate and tool mesh distribution (b) Mesh distribution in the thickness

A constant coulomb friction coefficient of 0.1 is employed to simulate the laminate/tool contact. This coefficient is selected because several investigations concluded that the friction coefficients between CFRP laminates and PCD tools are close to this magnitude [146,147].

5.3 Damage model characteristics

The 3D FE damage model described in Chapter 3 is selected to fulfil all the requirements demanded in this analysis. The variables α and β Hashin failure criterion is set to 1 to consider the shear stresses contribution in the fibre failure. The critical fracture toughness values (G_I^C) used in this research to calculate the damage evolution following the methodology described in chapter 4 are shown in Table 5.3.1.

Table 5.3.1. Critical fracture toughness employed in this work

N/mm	G_{ft}^c	G_{fc}^c	G_{mt}^c	G_{mc}^c
G_I^C	100	100	1	1

A maximum damage of 0.99 is allowed for matrix damage modes and 0.999 for the fibre damage modes. These maximum values are chosen to avoid the problems given by element with an excessive deformation [84]. The mechanical properties degradation lead to rapid increments in the deformation of the damaged meshed elements that are eroded after achieving a maximum value to emulate the chip formation process. The maximum strain criteria chosen in this research is different for every case studied to mimic the particularities of every machining configuration. These criteria are explained in detail in the following section.

The strain limit values that simulate the chip fracture in every cutting configuration studied are implemented in a VUMAT Fortran subroutine. This subroutine inserts the required features in the FE simulations to simulate the chip formation of the cases investigated in this research. Note that, because of the aim of this research is to address a methodology to model chip formation in composite machining, the strain levels selected are determined using numerical considerations without considering an empirical basis. However, to study a particular process the measurement of maximum strains before collapse could improve significantly the accuracy in the predictions of other machining parameters such as machining forces or sub-surface damage. Finally, a high strain limit of 2 for all strain components which are not previously mentioned (ε_{11} , ε_{33} , ε_{13} , and ε_{23}) is assigned to avoid distortional problems of damaged elements. All strain limits used in this research are visualised in Table 5.4.1.

5.4 Results and discussion

Five chip fracture scenarios are successfully assessed implementing a strain-based element deletion criteria. The model's modelling of the chip fracture scenarios is explained; these simulations are in the right balance with experimental findings previously defined. This section explains the overall strain-based element deletion criteria implemented to simulate all the studied machining scenarios. Finally, the numerical details and particularities employed in every investigated case are provided

5.4.1 Element deletion strain-based criteria

The previous strain limit values that simulate the chip fracture in every cutting configuration studied are implemented in a VUMAT Fortran subroutine. This subroutine inserts the required features in the FE simulations to simulate the chip formation of the cases investigated in this research. Because this chapter aims to address a methodology to model chip formation in composite machining, the strain levels selected are determined using numerical considerations without considering an empirical basis. However, to study a particular process, the measurement of maximum strains before collapse could improve the accuracy significantly in the predictions of other machining parameters such as machining forces or sub-surface damage. The methodology employed to determine the strain limits used in this research is explained below.

Since the dominant failure mechanisms in the studied simulations are d_{fc} , d_{mt} and d_s , the selected strain limit values will be calculated to allow these damage to reach levels close to the maximum damages allowed. Ideal conditions will be assumed to calculate these values. It means that only longitudinal strain (ε_{11}) is considered for fibre failures, transverse strain (ε_{22}) for matrix failures and shear strain (ε_{12}) governs shear failures.

It is decided to find these strain components' values that make these damages reach values in the range between [0.9 - 0.95]. This decision is made since these calculations are carried out because the equivalent displacements will always be smaller to reach the strain levels required to eliminate the element in the ideal conditions. In real fracture conditions, other components of strain are added to the calculation of the equivalent displacement ($\delta_{I,eq}$), increasing the level of damage calculated until reaching the maximum damage

values allowed in most cases.

First, the initial equivalent displacement ($\delta_{I,eq}^0$) is calculated considering the element's stiffness, strength, and characteristic size. Then, the final equivalent displacement ($\delta_{I,eq}^f$) is calculated considering the damage mode's fracture energy and its strength. Finally, the evolution of the damage with the equivalent displacement is represented using Eq. (3.2.17) of the manuscript, and a strain value in the range of damage sought is sought. As an example, the calculation of the limit $|\varepsilon_{11}|$ to simulate the fibre compression failure is shown below.

$$\delta_{f_c,eq}^0 = \frac{X_C}{E_{11}} 0.005 \quad ; \quad \delta_{f_c,eq}^f = \frac{2G_{f_c}^c}{X_C} \quad ; \quad d_{f_c} = \frac{\delta_{f_c,eq}^f (\delta_{f_c,eq} - \delta_{f_c,eq}^0)}{\delta_{f_c,eq}^f (\delta_{f_c,eq}^f - \delta_{f_c,eq}^0)} \quad ; \quad -\varepsilon_{11} = \frac{\delta_{f_c,eq}}{0.005} \quad (5.4.1)$$

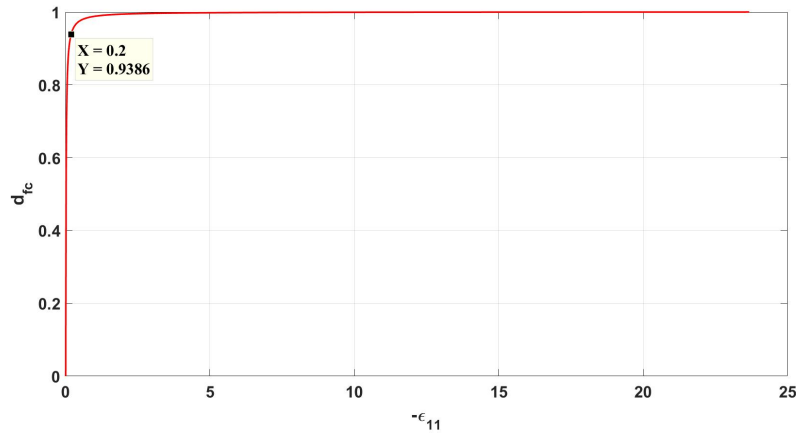


Fig. 5.4.1. Fibre compression damage evolution

In the above figure can be visualised that using the strain value of 0.2, a damage level inside the expected range is reached [0.9 – 0.95]. Therefore, the same procedure is repeated to obtain the correspondent maximum strain values for the matrix traction and fibre shear and matrix shear damages. In Figs. 5.4.2 to 5.4.4, it could be visualised how this matter was successfully achieved.

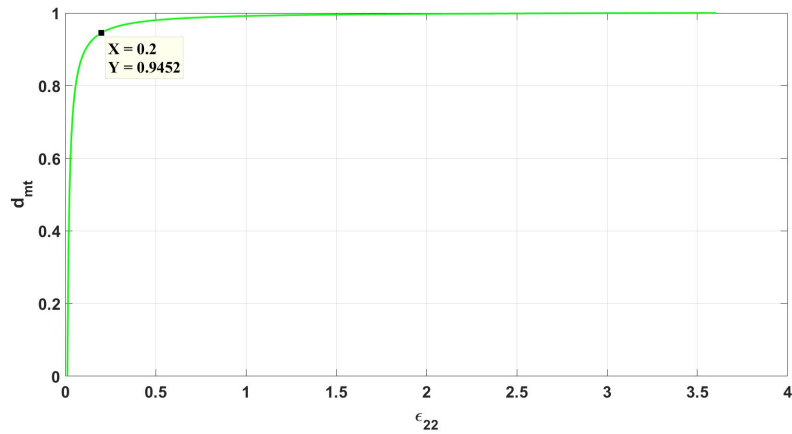


Fig. 5.4.2. Matrix traction damage evolution

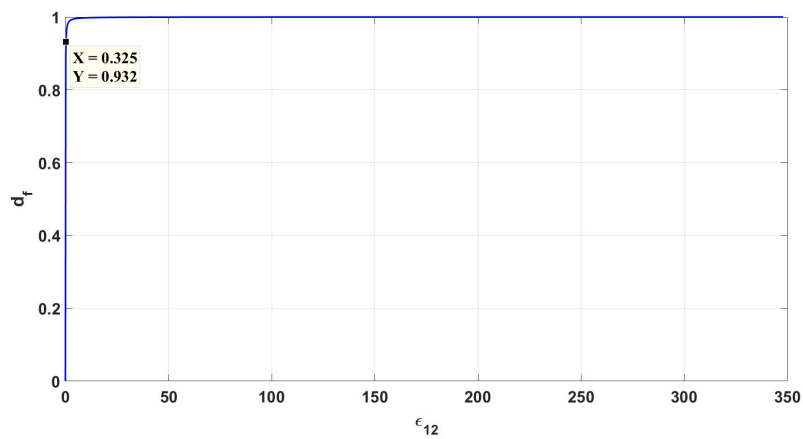


Fig. 5.4.3. Shear fibre damage evolution

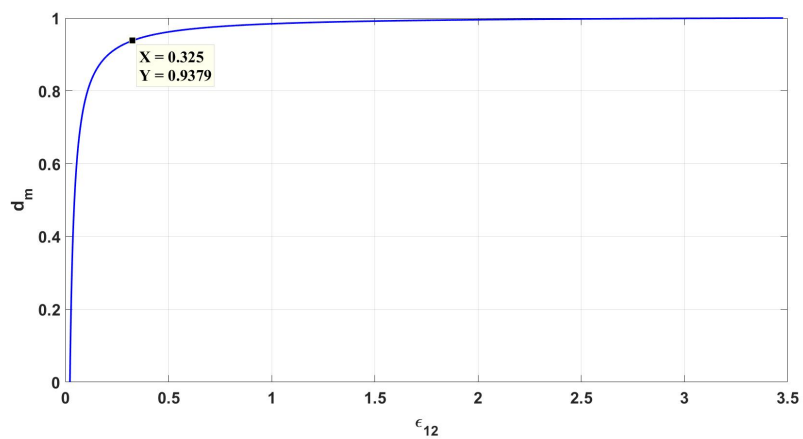


Fig. 5.4.4. Shear matrix damage evolution

In the case of the compression matrix, it is found that in the machining of 90° laminates suffer a high level of matrix compressive strain. Therefore if the elements in front of the tool are removed prematurely, it would avoid propagating the crack under the tool.

Therefore, it is decided that the value of $-\varepsilon_{22}$ should guarantee more severe damage than the previously mentioned range [0.9-0.95]. For this reason, the value of 0.99 is selected to slow down the elimination of these elements. In Fig. 5.4.5, we can appreciate how the value of 1.2 achieves this purpose.

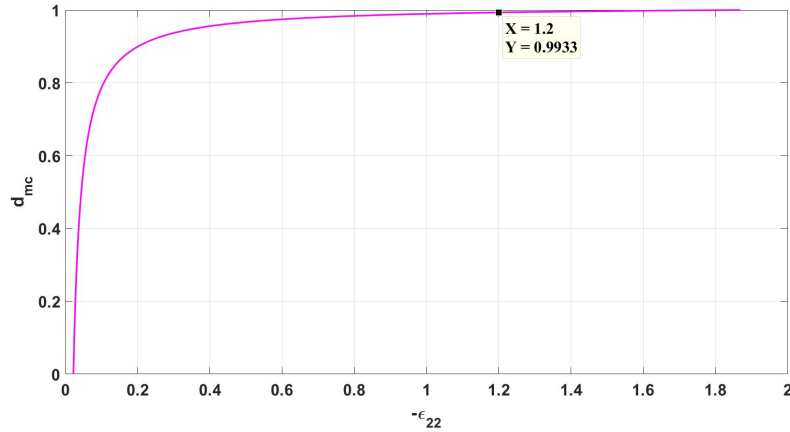


Fig. 5.4.5. Matrix compression damage evolution

Since the values of ε_{11} , ε_{33} , $-\varepsilon_{33}$, ε_{13} and ε_{23} are not associated with the composite damages modelled here; their limits are chosen to avoid element distortional problems. For this reason, a high strain limit is calculated in these components to avoid excessive distortion of an isolated element that suffers a great deformation in any of these directions. Therefore, a strain value of 2 is selected to ensure that the removal of the element occurs with damage values higher or close to 0.99, as shown in Figs. 5.4.6 to 5.4.10.

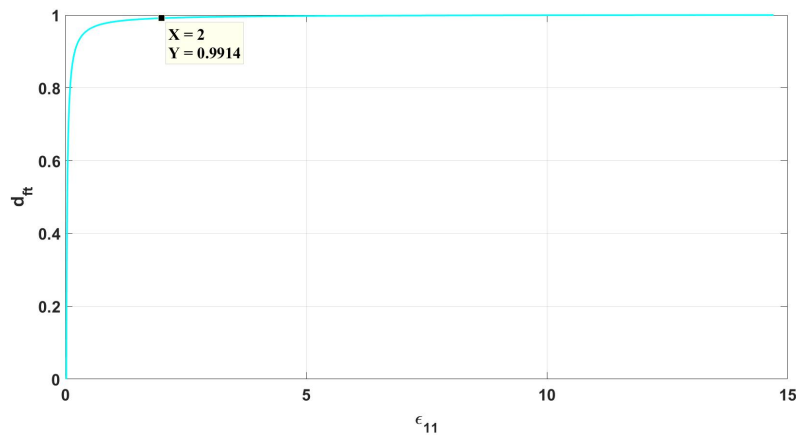


Fig. 5.4.6. Fibre traction damage evolution

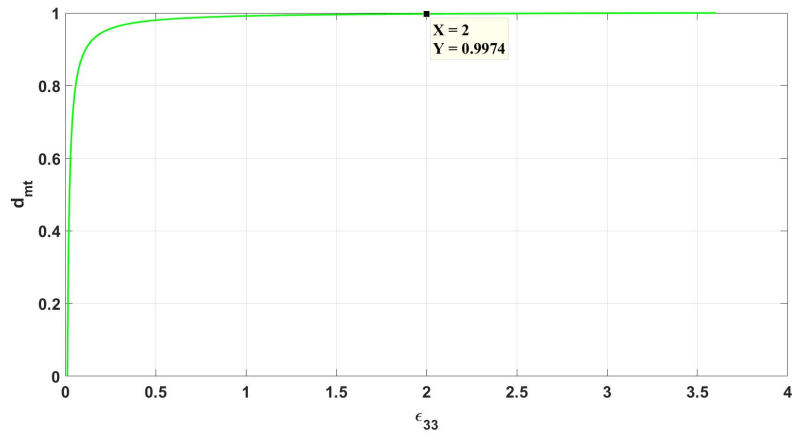


Fig. 5.4.7. Matrix traction damage evolution in the laminate thickness direction (3)

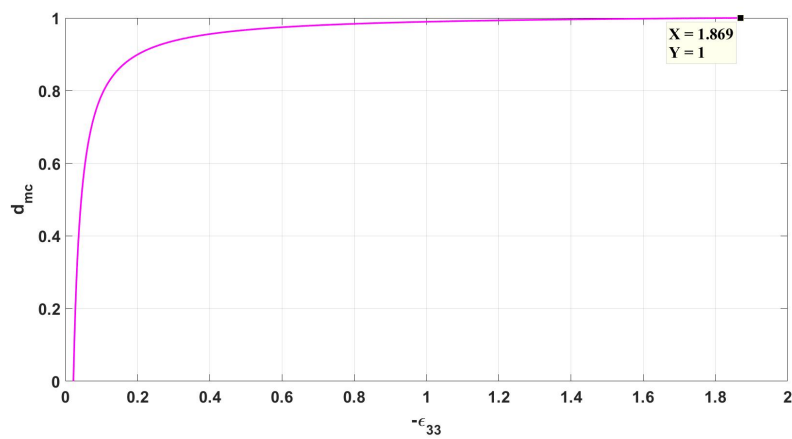


Fig. 5.4.8. Matrix compression damage evolution in the laminate thickness direction (3). The strain limit imposed (2) exceed the strain level to reach the total failure ($d_{mc} = 1$)

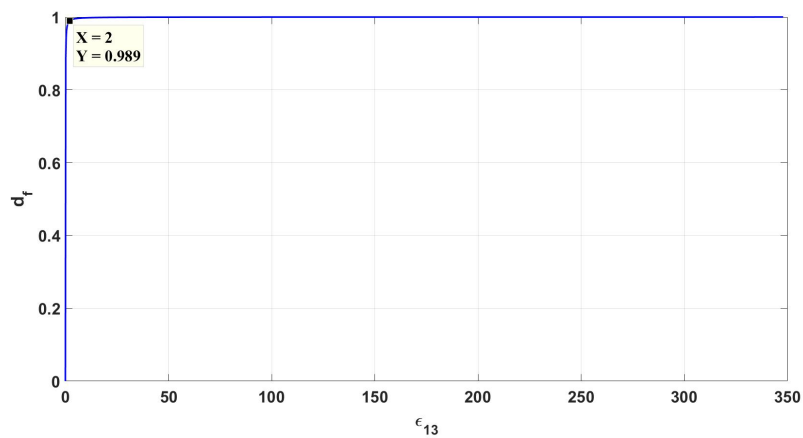


Fig. 5.4.9. Fibre shear damage evolution in plane 1-3

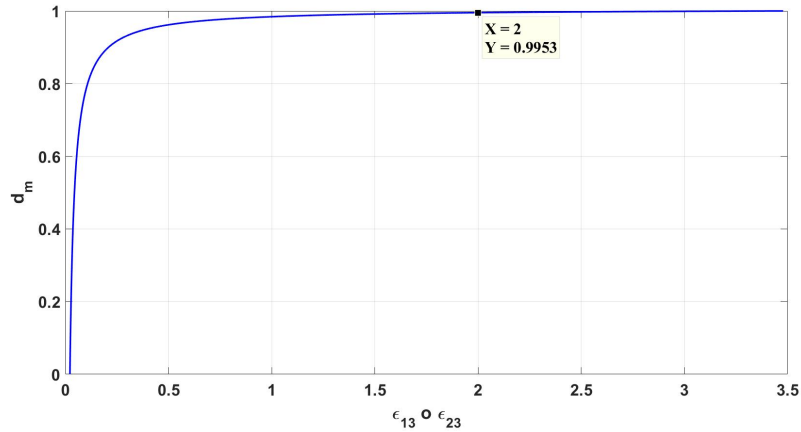


Fig. 5.4.10. Matrix shear damage evolution in planes 1-3 and 2-3

Finally, it was appreciated that the level of matrix traction strain of 0.2 was too high to simulate the chip's cantilever beam effect in 0° laminates. It occurs because elements in front of the tool edge break prematurely due to the tool's high longitudinal compression. Therefore, the traction matrix's failure must be anticipated by setting a new strain limit value of 0.15. This limit achieves a damage value inside the range of $[0.9 - 0.95]$, as shown in Fig. 5.4.11, and simulate the chip cantilever beam effect.

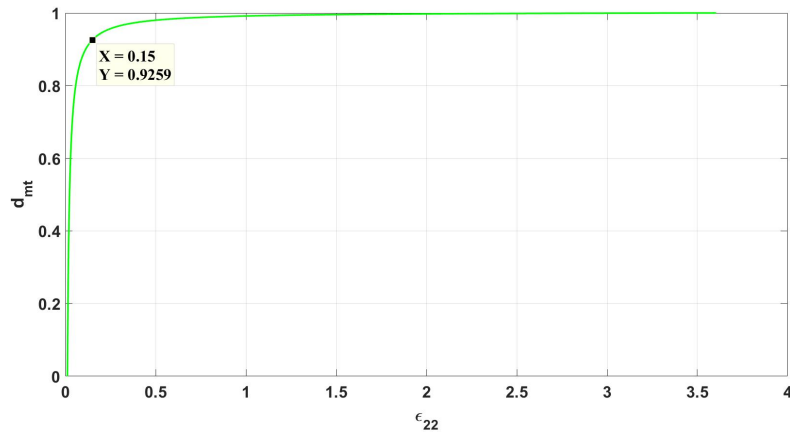


Fig. 5.4.11. Maximum damage calculated in the ideal configuration for matrix traction damage in the machining simulation of 0° with positive rake angle.

All strain limits used in this research are outlined in Table 5.4.1.

Table 5.4.1. Strain limits adopted to simulate the chip formation in all machining configurations studied

ϵ_{11}	$-\epsilon_{11}$	ϵ_{22}	$-\epsilon_{22}$	ϵ_{33}	$-\epsilon_{33}$	ϵ_{12}	ϵ_{13}	ϵ_{23}
2	0.2	0.15-0.2	1.2	2	2	0.325	2	2

5.4.2 Numerical assessment

Details about the modelling of the machining configurations described in the previous section are provided here. For this purpose, five different simulations are performed with the following fibre orientations: (1) 0° , (2) 0° and rake angle of 0° , (3) 45° , (4) 90° and (5) 135° . Particularities and numerical methodologies implemented in the simulation of every studied case are exposed below.

5.4.2.1 Fibre orientation of 0°

Although chip formation in this machining configuration consists of two phases: composite layer debonding and vertical fracture of the fibres, the simulation of the vertical fracture of the fibres is not modelled here. The laminate length in front of the cutting tool should be increased to generate the required bending moment to break the fibres to simulate this feature. Besides, it is necessary to simulate a thickness superior to the depth-of-cut to drive the chip upwards within the cutting plane and not in the thickness direction as it would be done in the current model. These changes would exponentially increase the model's computational cost; thus, the simulation of this feature is decided to be addressed in further investigations. The displacement in the thickness direction of one laminate lateral side is restricted to avoid this effect. The perspective and front views of the composite layer debonding simulated are presented in Fig. 5.4.12.

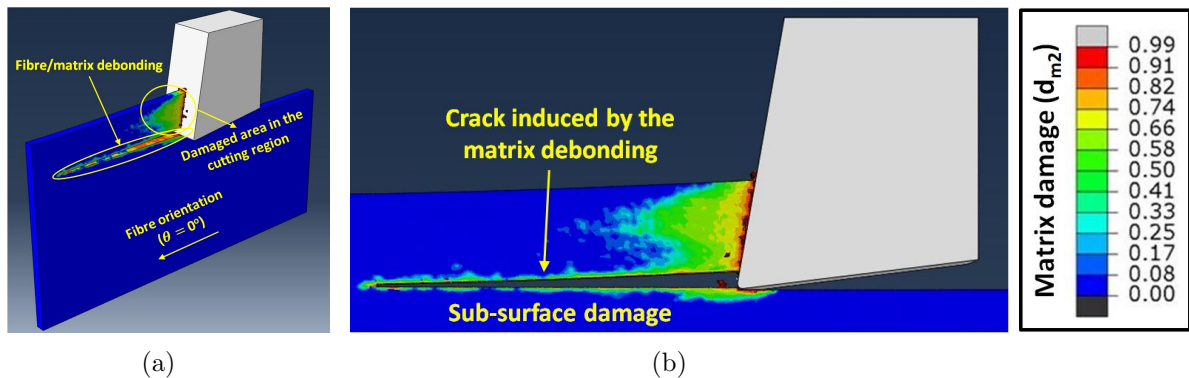


Fig. 5.4.12. Representation of the FE model simulated with a fibre orientation of 0° : (a) 3D perspective view (b) Front view

The composite layer debonding occurs in regions with high transversal strains to the fibre direction and substantial matrix traction damage. Therefore, to simulate this feature, the meshed elements with high transversal strain (ε_{22}) need to be deleted. In this work, the element's erosion is imposed when it reaches a value of $\varepsilon_{22} \geq 0.15$. As a result, the expected debonding is obtained using this methodology, observing high matrix traction damage ($d_{mt2} \in [0.9 - 0.99]$) in the deleted elements. These statements are visualised in Fig. 5.4.13 which represents the evolution of ε_{22} and d_{mt2} along the simulation time of a representative meshed element which is deleted during the simulation to generate the layer debonding.

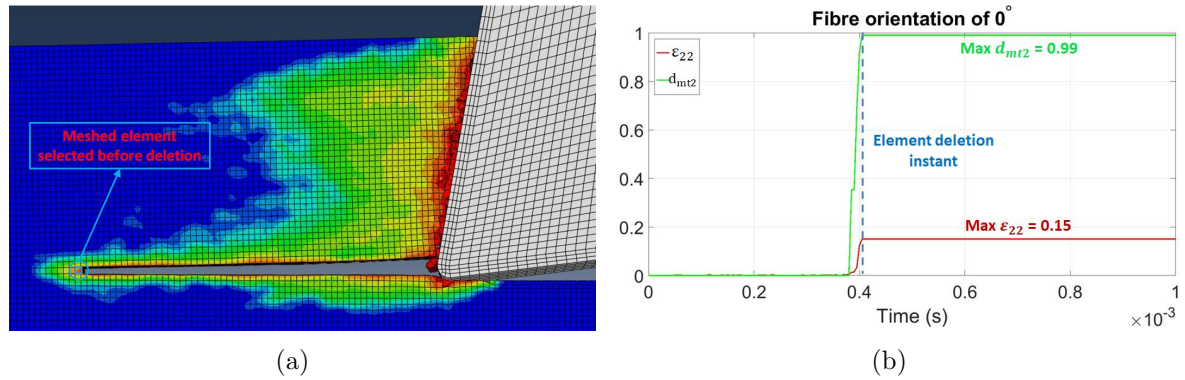


Fig. 5.4.13. Representation of a representative meshed element deleted to simulate the chip of a laminate with a fibre orientation of 0° : (a) Meshed element selected before deletion (b) Evolution of d_{mt2} and ε_{22} during the simulation time.

5.4.2.2 Fibre orientation of 0° with 0° rake angle

In this simulation, the fibre micro-buckling that takes place close to the cutting tool is accurately simulated. A significant large damaged area in front of the cutting tool is obtained due to the rake's abrupt contact with the laminate simultaneously, and the fibre micro-buckling represent an aggressive fracture. Both statements mentioned above are visualised in Fig. 5.4.14.

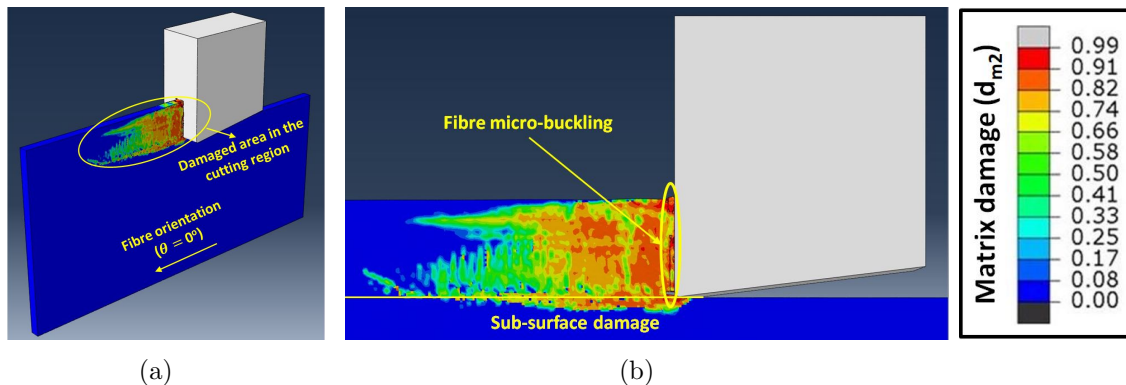


Fig. 5.4.14. Representation of the FE model simulated with a fibre orientation of 0° and a rake angle of 0° : (a) 3D perspective view (b) Front view

This fibre micro-buckling occurs after the fibre direction's mechanical properties are severely reduced with a high fibre compression damage ($d_{fc} \geq 0.9$). Therefore, for emulating this fracture behaviour, the deletion of elements with high fibre compression strain values of $-\varepsilon_{11} \geq 0.2$ is selected. These previous arguments are represented with the evolution of the variables $-\varepsilon_{11}$ and d_{fc} of one deleted element during the simulation time in Fig. 5.4.15

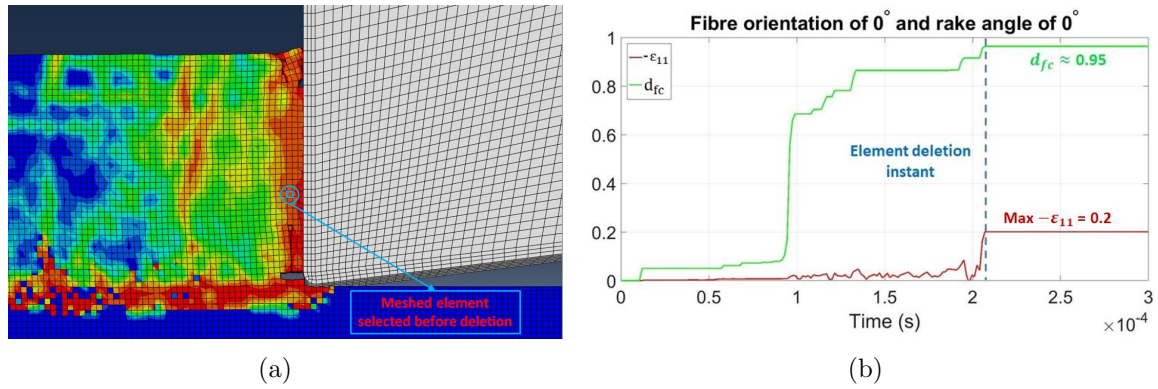


Fig. 5.4.15. Representation of a representative meshed element deleted to simulate the chip of a laminate with a fibre orientation of 0° and a rake angle of 0° : (a) Meshed element selected before deletion (b) Evolution of d_{fc} and ϵ_{11} during the simulation time.

5.4.2.3 Fibre orientation of 45°

A chip release fracture plane of 43° is achieved, as shown in Fig. 5.4.16(b). This fracture is produced because the deletion of elements is mainly occasioned by shear stresses which delete the elements mainly in the diagonal direction. However, occasionally they are deleted in horizontal inserting this small deviation of 2° concerning the fibre orientation during the crack growth due to the numerical errors in the damage transmission using this methodology to recreate the crack. A parallel alignment with the fibre orientation of the mesh might mitigate this defect. Finally, underlying the machined surface, it is appreciated that the damage distribution is parallel to the fibre as it occurs in reality (refer to Fig. 5.1.1(c)), see Fig. 5.4.16

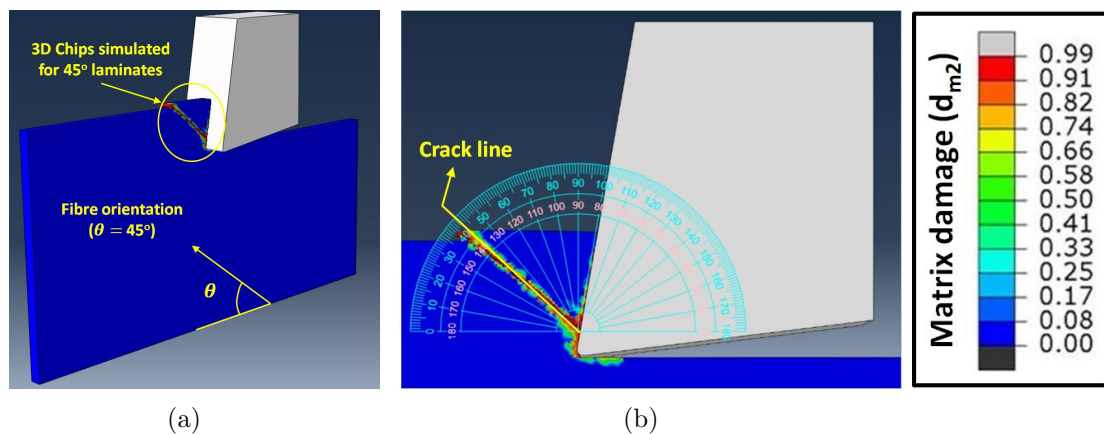


Fig. 5.4.16. Representation of the FE model simulated with a fibre orientation of 45° : (a) 3D perspective view (b) Front view

The chip fracture is generated because of the high shear stresses produced in the region where the chip slides out. Therefore, the deletion of element with a high in-ply shear strains (ϵ_{12}) values of $\epsilon_{12} \geq 0.325$. This statement is visualised in the evolution of ϵ_{12} of a representative deleted element eroded during the simulation in Fig. 5.4.17. In this case, both matrix and fibre damages could be high (0.9 or superior) in the chip release

region because shear stresses activate both damage types simultaneously. To support this argument, in Fig. 5.4.17(b) is represented the evolution of the d_{m2} . It is observed that this damage assessed achieves values higher than 0.9 before the final deletion.

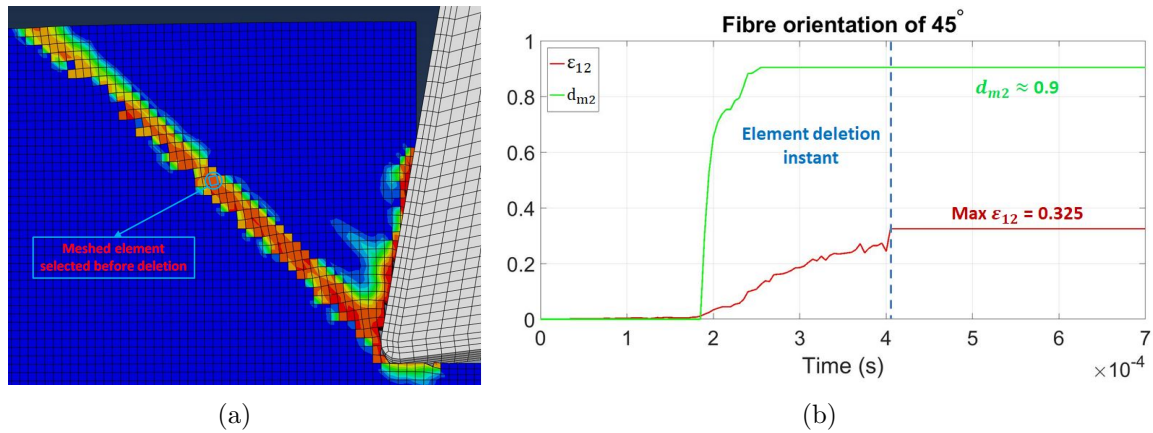


Fig. 5.4.17. Representation of a representative meshed element deleted to simulate the chip of laminates with a fibre orientation of 45° : (a) Meshed element selected before deletion (b) Evolution of d_{m2} and ϵ_{12} during the simulation time.

5.4.2.4 Fibre orientation of 90°

Two laminate fractures are modelled here: (1) small chip fragments in front of the tool and (2) fibre bending damage below the tool. The small chip fragments are simulated due to the high compression stresses produced because of the cutting tool's advance, while the fibre bending damage is originated because of the high matrix traction damage (d_{m2}). Both fractures are visualised in Fig. 5.4.18.

Two separate considerations in the deletion of elements are taken to simulate both fracture modes. A high compression value in the transversal compressive strains of $-\epsilon_{22} \geq 1.2$ is selected to simulate the small chip fragments in front of the cutting tool. In fibre bending damage, transverse tensile strain values of $\epsilon_{22} \geq 0.2$ are used. The representation of the evolution of the previous commented strain values for both studied fractures is represented in Fig. 5.4.19.

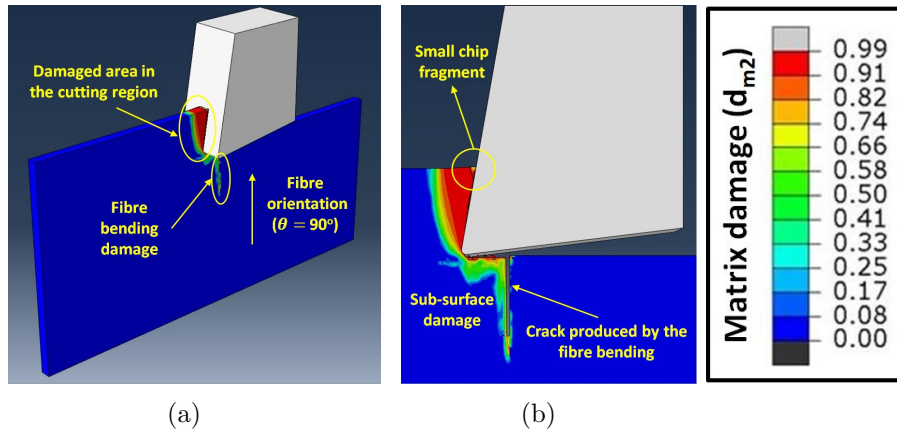


Fig. 5.4.18. Representation of the FE model simulated with a fibre orientation of 90° : (a) 3D perspective view (b) Front view

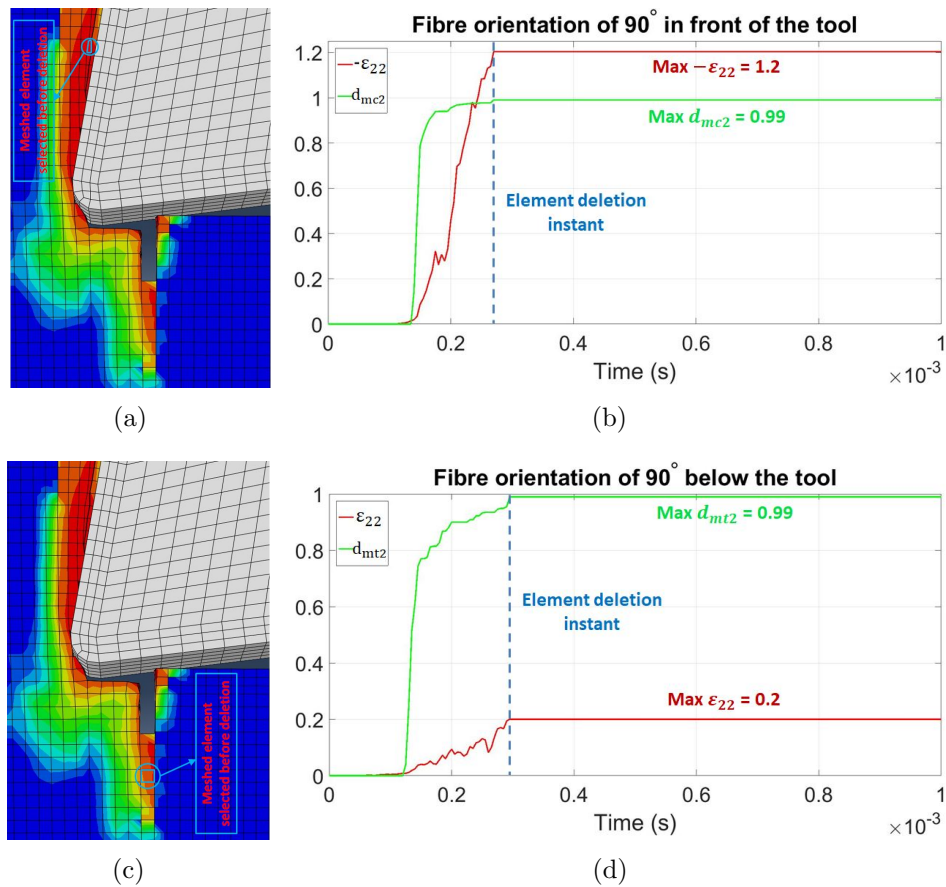


Fig. 5.4.19. Representation of a representative meshed element deleted to simulate the chip of laminates with a fibre orientation of 90° : (a) Meshed element selected in front of the cutting tool before deletion, (b) Evolution of d_{mc2} and ε_{22} during the simulation time, (c) Meshed element selected below of the cutting tool before deletion, (d) Evolution of d_{mt2} and ε_{22} during the simulation time.

5.4.2.5 Fibre orientation of 135°

A precise fracture perpendicular to the fibre direction is achieved in this simulation, as shown in Fig. 5.4.20(b). This fracture is motivated for the high shear stresses observed in the fracture zone. Furthermore, it is appreciated that the damage underlying the machined surface is parallel to the fibre direction as it is explained in the previous subsection of this manuscript, see Fig. 5.4.20.

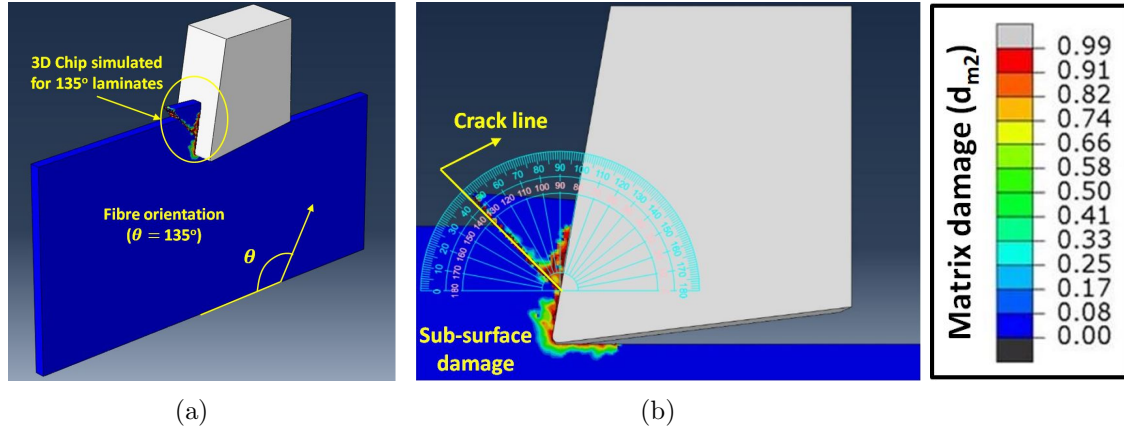


Fig. 5.4.20. Representation of the FE model simulated with a fibre orientation of 135°: (a) 3D perspective view (b) Front view

The fibre compression equation from Hashin's composite failure criteria exposed in Eq. (3.2.11) is modified to consider the shear effects to predict the fibre breakage. A factor of 0.8 is incorporated to address this matter leading to the final quadratic expression represented in Eq. (5.4.2). Expected results are reached as it is illustrated in Fig. 5.4.21, which illustrates the fibre compression damage (d_{fc}) is propagated through the laminate perpendicularly to the fibre direction.

- Fibre compression ($\sigma_{11} < 0$)

$$F_{ft} = \left(\frac{\sigma_{11}}{X_T} \right)^2 + 0.8 \left(\frac{\sigma_{12}}{S_{12}} \right)^2 + 0.8 \left(\frac{\sigma_{13}}{S_{13}} \right)^2 \geq 1 \quad (5.4.2)$$

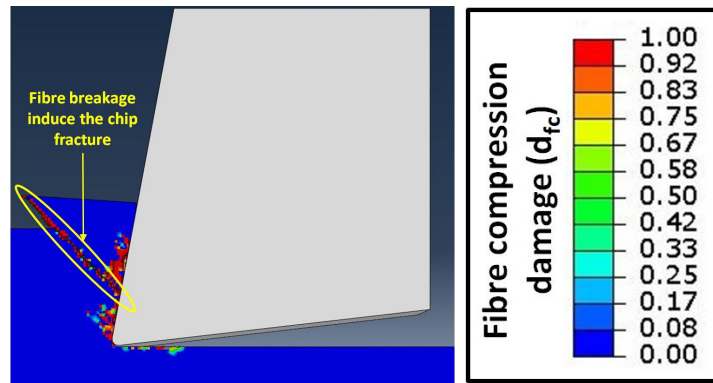


Fig. 5.4.21. Illustration of the fibre compression damage previous to the chip release in laminates with a fibre orientation of 135° .

The same strategy of element deletion in the chip formation of laminate with a fibre orientation of 45° is used here. Meshed elements are deleted when they achieve a shear strain levels of $\varepsilon_{12} \geq 0.325$. In this particular case, the fibre compression damage is the highest in the deleted elements achieving values close to 1, as appreciated in Fig. 5.4.22.

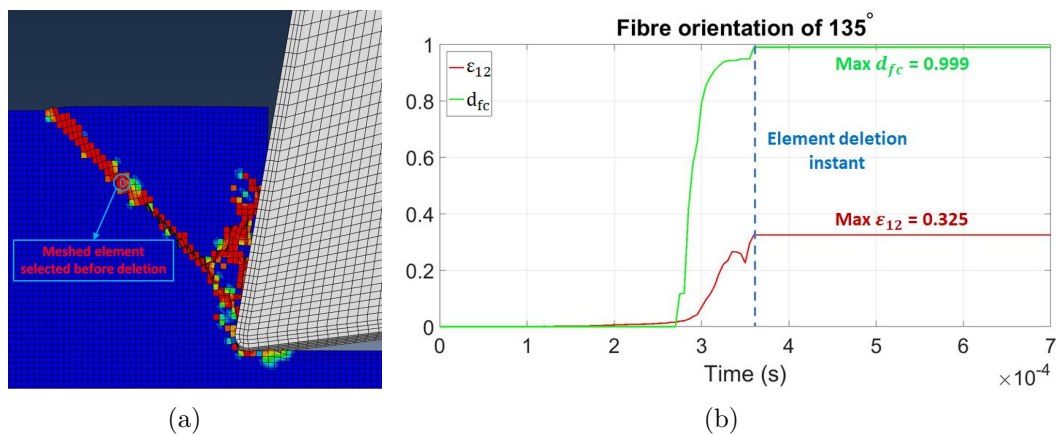


Fig. 5.4.22. Representation of a representative meshed element deleted to simulate the chip of laminates with a fibre orientation of 135° : (a) Meshed element selected before deletion (b) Evolution of d_{fc} and ε_{12} during the simulation time.

5.5 Concluding remarks

This chapter gives a novel research on the modelling of chip formation mechanisms in composite machining. This feature is essential to simulate a machining process and its implementation to the oncoming FE studies reliably. Additionally, this work offers an effective and feasible methodology for the implementation of the chip formation in the modelling of composite machining that could be applied to study more complex machining operations such as drilling, milling or edge trimming. Five machining configurations with fibre orientations of 0° , 0° and rake angle of 0° , 45° , 90° and 135° have been successfully modelled to cover various of the most common machining scenarios. A 3D energy-based composite damage model based on the continuum damage mechanics (CDM) theory is implemented herein to increase the deformation of the damaged elements and facilitate

their posterior deletion. After composite laminate elements are damaged, they are selectively eroded from the simulation using a specific strain limit criterion for every simulated case to mimic the chip shape obtained in real machining processes. Main conclusions extracted from the simulations carried out in this investigation are collected in the below bullet points.

- **Fibre orientation of 0° :** The layer debonding to generate the characteristic cantilever beam effect in this chip mechanism is simulated because of the high matrix traction damage increase the transversal strains of the damaged elements abruptly. These elements are deleted in this research after their transversal strain overcomes values of 0.15. The simulation of the fibre fracture which generate the chip release need to be addressed in further investigations.
- **Fibre orientation of 0° with 0° rake angle:** Fibre micro-buckling is successfully simulated obtaining high damage fibre compression damage levels. This achievement is reached with the implementation of a compressive longitudinal strain limit of 0.1. High damage levels are observed in the laminate as a consequence of the abrupt contact of the rake face of the cutting tool with the laminate and the high contact rigidity existent for this fibre orientation.
- **Fibre orientation of 45° :** This chip is obtained because of the high shear strain levels, 0.325 or superior, obtained in the crack path. As a result, high fibre and matrix damage levels are obtained in this particular case. A small deviation of 2° of the crack path is simulated in comparison with the experimental findings. This fact occurs because of the limitations provided by the deletion of element technique employed to track the crack path accurately.
- **Fibre orientation of 90° :** Two fracture modes are modelled here in front and below of the cutting tool. In front of the tool, small chip fragments are modelled deleting the elements with high matrix compression damage and a transversal compressive strain limit of 1.2. Below the cutting tool, the fibre bending is simulated eroding the elements with high matrix tensile damage which reach tensile transversal strains of 0.2 or higher.
- **Fibre orientation of 135° :** The chip release is generated because of the high shear strains reached in this case. This is motivated for the high fibre compression damage registered in the crack area. The fibre compression Hashin's failure criterion is modified to add the shear contributions. This is achieved with the use of a new quadratic formulation and multiplying the quadratic terms associated to the shear components by a factor of 0.8.

Chapter 6

Composite machining application: Edge trimming

6.1 Introduction

After contrasting the high efficiency of the composite damage model proposed to simulate the fundamentals in composite machining, such as chip formation and sub-surface damage, it is time to test this model's efficiency to model common machining operations such as milling. The cutting principles of a turning are quite similar to the cutting physics observed in orthogonal cutting and oblique cutting operations. Therefore, the machining physics observed in turning operations have been extensively studied developing orthogonal FE models due to their higher simplicity.

Drilling modelling investigations mostly assess the impact that machining factors have on the surface delamination of the outer plies [34,35]. Phadnis *et al.* [81] investigated that the selection of high cutting speeds and low feed rates reduce the delamination levels, torque and thrust force considerably. Later, Feito *et al.* [109] developed a simplified drilling FE model, which drastically reduced the computational time required for a complex drilling model in a simulation without a significant decrease in the accuracy of the predictions. Finally, the drill bit's morphology plays a relevant role to reduce the machining induce damage in drilling operations. For instance, Isbilir *et al.* [90] concluded that the use of high stage ratios in step drill bits is essential to decrease the push-out delamination.

In general, FE modeling of metal milling operations has been developed in numerous investigations in recent years. However, these models still offer important limitations. For instance, the development of advanced machining friction models is required to improve the feed force predictions quality [148]. The Johnson Cook model is the most used to define the plastic behavior of these metals with linear or exponential progressive damage models [149]. Many advances in this field have been achieved with these investigations. For example, Wojciechowski *et al.* [150] investigated that the cut-off transition between the burnishing regime and the chip formation regime is in a feed per tool range of 1-1.4 microns. Finally, Gao *et al.* [151] showed that the use of advanced modelling techniques such as the Coupled Eulerian-Lagrangian approach significantly improves the predictions quality in terms of chip shape and machining forces.

Although composite milling is one of the most common operations to achieve high quality

surfaces finishing in the industry; they have not been widely modelled so far. To study these operations simplified FE orthogonal cutting models are implemented because of the high difficulty of simulating explicitly the characteristic material failure and chip separation of a milling process [152]. Therefore, the development of sophisticated FE models capable of solving the doubts about the physical mechanism of failure concerning composite milling is necessary for oncoming investigations. Furthermore, the implementation of damage algorithms to mimic the characteristic progressive loss of mechanical properties and crack propagation observed in the damaged areas become vital to accomplish this matter [29].

The orientation of the cracks plays a fundamental role in the appearance of defects in the mechanical surface such as surface roughness or sub-surface damage. A clear increase in these variables is observed in fibre orientations greater than 90° due to the fact that the great bending effect causes the fibre breakage to occur in a very irregular way below the cutting surface as well as a significant increase in the fibre matrix debonding extension into the sub-surface damage [153, 154].

However, the orientation of the fibres is not the only factor that influences the increase in sub-surface damage, the wear of the tool tip also contributes significantly to the increase in the length of the cracks propagating into the machined surface. The impact of blunt tool tips (large tool edge radius) interacting with the fibre tends to push the fibres generating a significant bending effect rather than shearing them. This mechanism increases the size of the cracks produced by the fibre-matrix debonding below the machined surface, considerably reducing the structural integrity of the part [155]. Therefore, this tool wear must be quickly detected by evaluating variations in the mechanical responses. This information can be used to know when the worn tool inserts should be replaced for new ones avoiding the massive rejection of parts in a manufacturing production system. The most effective and easy-to-obtain indicator that shows the emergence of a severe tool wear is the visualisation of an increment in the cutting forces. Therefore, the investigation of the variations of the cutting forces caused by the tool wear during machining is necessary to enhance the final structural quality of the machined components.

This work develops a consistent FE study of the edge trimming of UD-CFRP laminates with 45° and 90° fibre orientations. The first aim of this work is to analyse the effect of tool wear on the machining forces. Laminate behaviour is modelled using a damage algorithm based on a hybrid Puck-Maximum stress failure criteria to determine composite damage onset and subsequently. The numerical implementation of the spring back phenomenon (partial thickness recovery of the machined surface) is essential to improve the numerical predictions' accuracy. Numerical results are validated using the experimental data collected in the trials developed by Duboust et al. [156]. Interesting conclusions from the evolution of global forces to the spindle axis (F_X and F_Y) and related forces to the cutting tool tooth (F_T and F_N) are collected in this research.

6.2 Experimental set-up

The milling process differs from orthogonal cutting in that there is a rotating tool with multiple cutting edges and intermittent contact of each cutting edge with the workpiece. Additionally, there is also a constantly changing thickness in the size of the removed chip as the tool is fed into the workpiece. A conventional edge trimming approach has been

applied in this experiment which means that the size of the chip will increase as the tool increases engagement with the workpiece. In a composite edge trimming process the milling kinematics means that there will be a new fragmented chip generated for every new pass of a cutting tooth. There will also be the effect of fibre orientation which will change in relative orientation to the cutting edge with the rotation of the milling tool, as shown in Fig. 6.2.1.

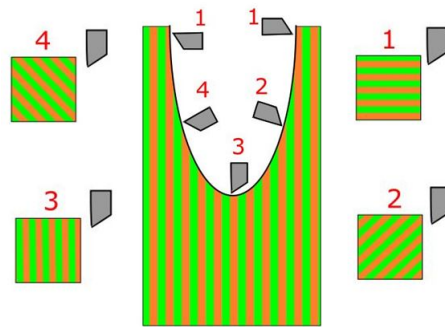


Fig. 6.2.1. Relative fibre orientation change in edge trimming - orange stripes = fibre, green stripes = matrix.

The edge trimming machining experiments were completed on a uni-directional laminate with two different fibre orientations – 45° and 90° fibre orientations. The carbon fibre laminates are manufactured by pre-preg hand layup and they are cured in an autoclave. A fibre type T700G and an epoxy matrix named Hexply M21 are employed. A five axis Computer Numerical Control (CNC) machine tool, Cincinnati FTV5-2500, Cincinnati machines, Ohio (EEUU), was used to machine the carbon fibre material, see Fig. 6.2.2.



Fig. 6.2.2. Five axis CNC machine tool, Cincinnati FTV5-2500.

A polycrystalline diamond (PCD) cutting tool was selected. Unidirectional CFRP laminates of 36 plies were vacuum bagged to be cured in an autoclave. The curing cycle selected is specified in the below list.

1. Apply full vacuum (1 bar).
2. Apply 7 bar gauge autoclave pressure.
3. Reduce vacuum to a safety value of -0.2 bar when the autoclave pressure reaches 1 bar gauge

4. Set heat-up rate from room temperature to $180^{\circ}\text{C} \pm 5^{\circ}\text{C}$ ($356^{\circ}\text{F} \pm 9^{\circ}\text{F}$) to achieve an actual component heat-up rate between $1\text{-}2^{\circ}\text{C}/\text{minute}$ ($2\text{-}4^{\circ}\text{F}/\text{minute}$).
5. Hold at $180^{\circ}\text{C} \pm 5^{\circ}\text{C}$ ($356^{\circ}\text{F} \pm 9^{\circ}\text{F}$) for 120 minutes ± 5 minutes.
6. Cool component at an actual cooldown rate of $2\text{-}5^{\circ}\text{C}/\text{minute}$ ($4\text{-}9^{\circ}\text{F}/\text{minute}$).
7. Vent autoclave pressure when the component reaches 60°C (140°F) or below.

This laminate was cut into samples (at the required fibre orientations), which had length, width and thickness – 160 mm, 63 mm and 6 mm, respectively. These samples were fixed using a clamping system as shown in Fig. 6.2.3 and attached to the CNC machine tool. The cutting forces were recorded during the experiment by using a Kistler dynamometer, which was attached to the base of the CNC machine as shown in Figure 6.2.3. The effect of cutting tool wear on the machining forces was recorded by measuring the F_X (feed force) and F_Y (thrust force), depicted in Figure 6.2.3.

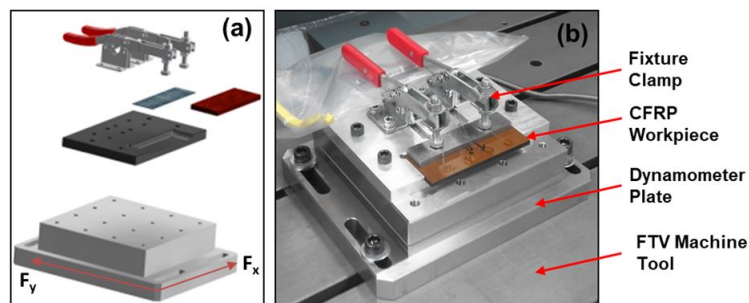


Fig. 6.2.3. Edge Trimming Set-up: (a) separate pieces and (b) assembled set.

The mean cutting forces were calculated then compared with numerical models, which were then used to validate FE cutting simulations. The PCD cutting tool had a zero helix angle and 10 mm diameter, as shown in Fig. 6.2.4. Two cutting tools were used in two different conditions in new and worn condition, with a $3\ \mu\text{m}$ and $10\ \mu\text{m}$ edge radius respectively. The tool tooth had a clearance angle of 22.4° , and a rake angle of 29.8° with a negative 1 mm offset from the centre line. Each test was repeated 2 times with each cutting tool condition. The samples were cut with a full thickness axial depth of cut (ap) of 6 mm and a radial depth of cut of 2 mm. A spindle speed of 6000 rpm and 1200 mm/min feed rate was applied using the three flute PCD cutting tool.



Fig. 6.2.4. Three flute Polycrystalline Diamond (PCD) Cutting Tool with Optical Edge Radius Measurements.

6.3 Model characteristics

This work has focused on analysing the tool wear influence on machining forces in composite edge trimming. It is achieved by developing 2D FE plane strain simulations in Abaqus/Explicit. In the FE model, just the cutting tool teeth of the three flute, zero helix, milling tool are simulated to reduce the computational cost. The initial laminate geometry is modelled to mimic the ideal initial conditions when one cutting edge starts the material removal, as shown in Fig. 6.3.3. CFRP mechanical and strength properties are shown in Tables 6.3.1 and 6.3.2, respectively.

Table 6.3.1. CFRP mechanical properties

Material	$E_1(GPa)$	$E_2(GPa)$	$G_{12}(GPa)$	ν_{12}
CFRP [156]	148	7.7	4.7	0.3

Table 6.3.2. CFRP strength properties.

Material	$X_T(MPa)$	$X_C(MPa)$	$Y_T(MPa)$	$Y_C(MPa)$	$S_{12}(MPa)$
CFRP [156]	2375	1465	51	119	112

Boundary conditions are selected to reproduce the cutting condition observed in real trials reliably. The displacement at the bottom of the laminate is fixed to simulate the fixtures' clamping conditions. The horizontal displacement is restricted to zero on the lateral sides to avoid the simulated laminate bending while the cutter is in contact with the workpiece. Quadrilateral CPS4R elements are employed in this research. The mesh employed is designed to guarantee the right balance between the accuracy and the model's computational cost. The element size of $10 \mu m$ in the cutting area is selected because it is appreciated that machining forces were converging around this element size, as shown in Figs. 6.3.1 and 6.3.2. Further to this region, the element sizes are gradually increased until achieving a maximum size of $200 \mu m$ at the laminate borders. The FE model partitions and meshed distribution used in this research are illustrated in Figs. 6.3.3 and 6.3.4.

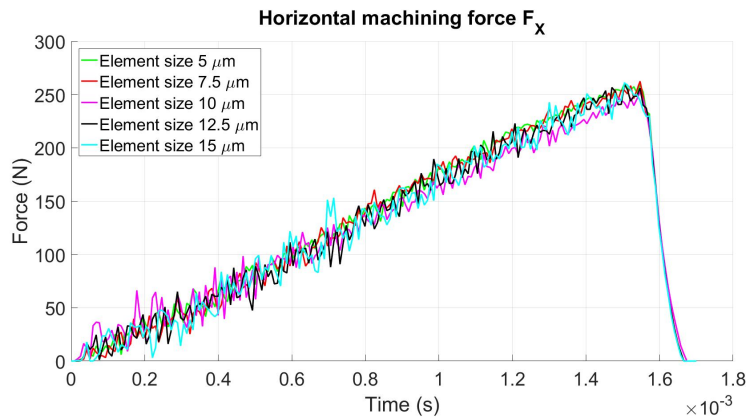


Fig. 6.3.1. Mesh sensitivity analysis of horizontal machining forces (F_x).

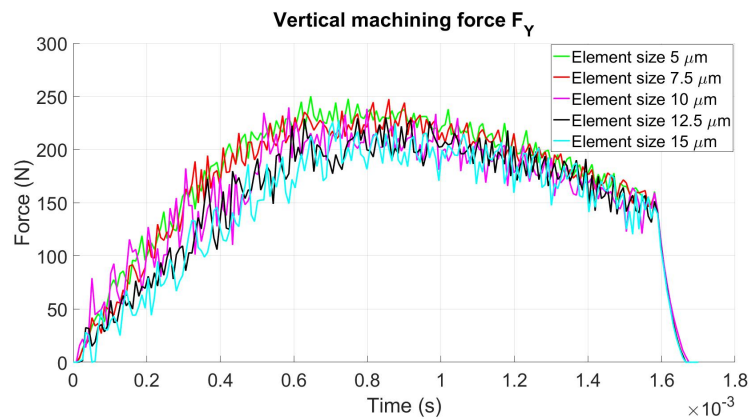


Fig. 6.3.2. Mesh sensitivity analysis of vertical machining forces (F_Y).

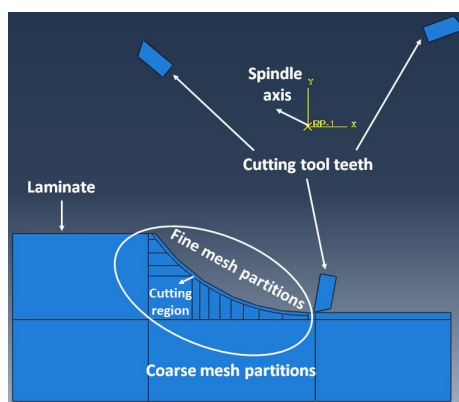


Fig. 6.3.3. Mesh zoom of the closed area next to the cutter tool edge.

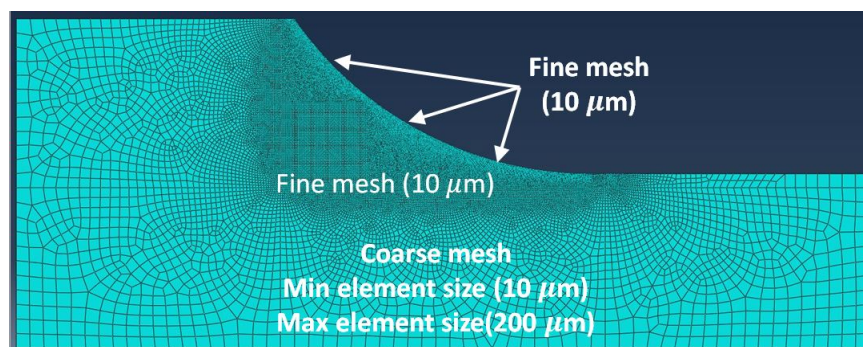


Fig. 6.3.4. Meshed elements distribution in the modelled laminate.

The cutting tool is treated as a solid rigid body to reduce the FE model's computational cost. This approach is plausible because of the high rigidity and hardness of the polycrystalline diamond (PCD) milling tool and the low deformations levels suffered at the cutting tool tip compared to the machined composite laminate. A constant Coulomb friction coefficient of 0.1 is used to model the friction between a PCD cutter and CFRP laminates accurately [147].

6.4 Damage model

The 2D FE damage model described in Chapter 3 is selected to fulfil all the requirements demanded in this work. The shear stresses contribution to determine the fibre damage initiation ($\alpha = 1$) in Hashin's failure criterion is considered. No element deletion is considered in this research due to this factor reduces the predictions accuracy limitation of the load transfer, which negatively affects the accuracy of the machine forces predicted. The fracture energies used to calculate the damage evolution are shown in Table Table 6.4.1.

Table 6.4.1. Values of critical fracture toughness selected

N/mm	G_{ft}^c	G_{fc}^c	G_{mt}^c	G_{mc}^c
Critical fracture toughness	100	100	1	1

As it is a novel investigation in this matter, there is not recommended values to select the limitation of damage in the literature. Therefore, the maximum d_s and d_m allowed were sequentially reduced until the distortional problems disappeared. Note that, a value of matrix damage of 95% is used because it is the value recommended in the literature [84] and later the d_s was reduce achieving values of 80% in the case of laminates of 90° . In the case of 45° laminates both damages were highly decreased to 50% until the distortional problems disappeared. This drastic limitation could be explained because the matrix compressive strength rates achieve for this laminate is high.

The chip separation is not studied in detail in this manuscript. In order to remove the material machined, strict strain-based criteria are chosen. All elements are removed when the element strain achieve a value higher of 1.2 in one of its components (ε_{11} , ε_{22} and ε_{12}). This value exceeds 100 times the order of magnitude of the strain levels required for an epoxy matrix to fail [133]. Nevertheless, it is maintained because the element erosion produces a total contact loss with the cutting tool in a discrete model. This fact significantly reduces the forces that the cutting tool received due to an important area in contact with the cutting tool is drastically removed. This factor significantly decreases the accuracy of the prediction of machining forces because the forces coming from the spring back phenomenon is not accounted [88]. Therefore, this element deletion criterion is taken in this research to simulate these spring-back forces.

6.5 Results and discussion

The cutting mechanism notably varies with tool wear, as shown in Fig. 6.5.1. A new tool cut the laminate shearing small chips away. For modelling this problem the fibre and matrix fracture mechanism should be included in the model to achieve a good quality in the numerical results. However, this configuration is not studied in this manuscript because this matter is out of the scope of this research.

A worn tool edge radius considerably reduces its effectiveness to cut the fibres. As a result, the tool edge removes the material due to the high rubbing forces with the laminate, as shown in Fig. 6.5.1 . The increment of tool/workpiece contact area increases abruptly the ploughing forces and sub-surface damage. The proposed FE model takes into account this phenomenon and check how the cutting forces increase because of the tool wear.

These results can be employed in real test to check the tool wear analysing the machining forces. Therefore, the inserts can be replace before the worn edges could induce excessive laminate damage.

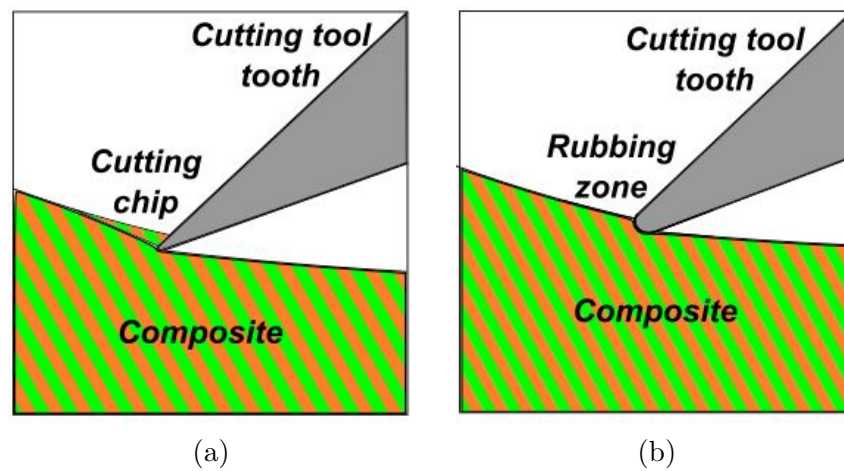


Fig. 6.5.1. Representation of the characteristic edge trimming cutting mechanisms using a (a) new tool and (b) worn tool

The simulations focus on the study of the action of the tool teeth on the material. Therefore, the simulation time selected is when one of the tool teeth is in contact with the laminate. A feed rate (f_r) of 1200 mm/min, spindle speed (w) of 6000 rpm and a radial depth of cut of 2 mm are modelled in this research, see Fig. 6.5.2(a). In this investigation, the tool edge wear is considered uniform; thus, the cutting tool edge will maintains a round shape. Five cutting-edge radii of 10 μm , 20 μm , 30 μm , 40 μm and 50 μm are investigated to assess the tool wear influence on the machining forces. Four distinct machining forces are analysed F_X , F_Y , F_T and F_N , which are represented in Fig. 6.5.2. F_X and F_Y denotes the horizontal and vertical forces, respectively. They are representative to analyse the machining forces experienced by the cutting tool in the spindle axis. In the case of F_T and F_N , they are the tangent and normal forces to the cutting tool edge trajectory, see Fig. 6.5.2(b), respectively. Henceforth, F_T will be named tangent force, and F_N will correspond to the normal force for clarity. These variables reliably represent the forces that the tool tooth undergoes during the machining process.

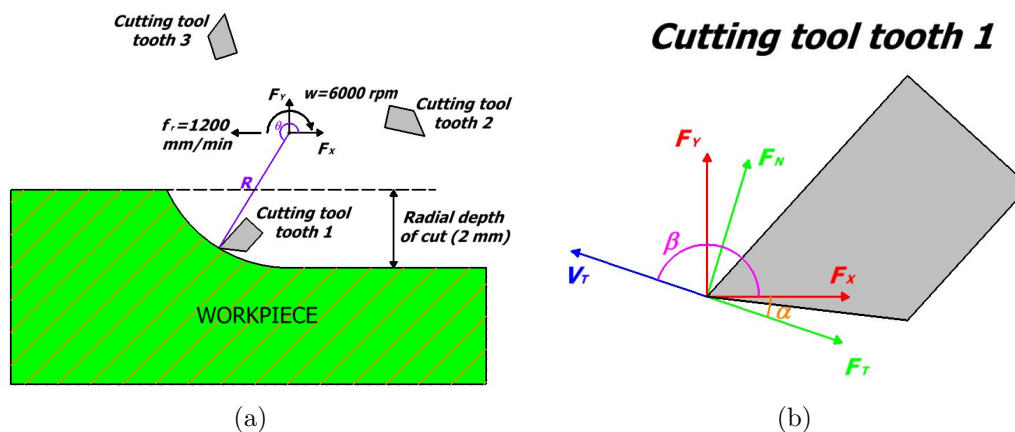


Fig. 6.5.2. Representation of relevant machining parameters analysed in this research: (a) FE model machining parameters employed and (b) tool tooth forces representation

In the above figure, θ represents the tool angle rotation. Variables w , f_r and R denote the cutting speed, feed rate and radius of the cutting tool, respectively. V_t is the tangent velocity at the tooltip. Finally, β and α correspond to the angles which indicate the orientation of V_t and the coordinate system to analyse F_t and F_n concerning the global coordinate system, respectively.

To transfer the machining forces obtained in the global coordinates, F_x and F_y to the relative coordinates F_t and F_n ; it is necessary to develop a vector base change. For this purpose, the angle that forms the tangent velocity at the tooltip (V_t) with the horizontal axis of the coordinate system (β) is calculated. The angle between the two vector bases (α) is established to transfer the forces obtained in the global coordinate system to the new coordinate axes. The relevant equations to complete the change of vector base are set out below.

$$\beta = \text{atan} \left(\frac{-wR\cos(\theta_0 - wt)}{wR\sin(\theta_0 - wt) - 20} \right) + \pi \quad \alpha = |\beta - \pi| = \left| \text{atan} \left(\frac{-wR\cos(\theta_0 - wt)}{wR\sin(\theta_0 - wt) - 20} \right) \right| \quad (6.5.1)$$

$$\begin{aligned} F_T &= F_X \cos(\alpha) - F_Y \sin(\alpha) \\ F_N &= F_X \sin(\alpha) + F_Y \cos(\alpha) \end{aligned} \quad (6.5.2)$$

In this work, the spring back phenomenon, which is the partial-thickness recovery after the cutter travel through the machined surface, is included. The insertion of this phenomenon in simulations is achieved, avoiding the deletion of the elements in contact with the cutting tool edge. The interaction between the laminate and the cutting tool is observed to displace the tool tooth normal to the workpiece surface, as shown in Fig. 6.5.3(a). This interaction inserts new forces not accounted for in previous studies, which improves the reliability of the predictions obtained, as discussed below.

Another relevant factor that influences the results is the machining relative angle. This factor is the angle between the tangent velocity of the cutting tooltip and the fibre orientation, see Fig. 6.5.3(b). Along with advancing the cutting tool tooth, this angle is progressively reduced, influencing notably in the machining forces obtained. For 45° laminates, the machining relative angle drops from 45° to -15°, while in 90° laminates go from 90° to 30°, as shown in Figs. 6.5.3(c) and 6.5.3(d).

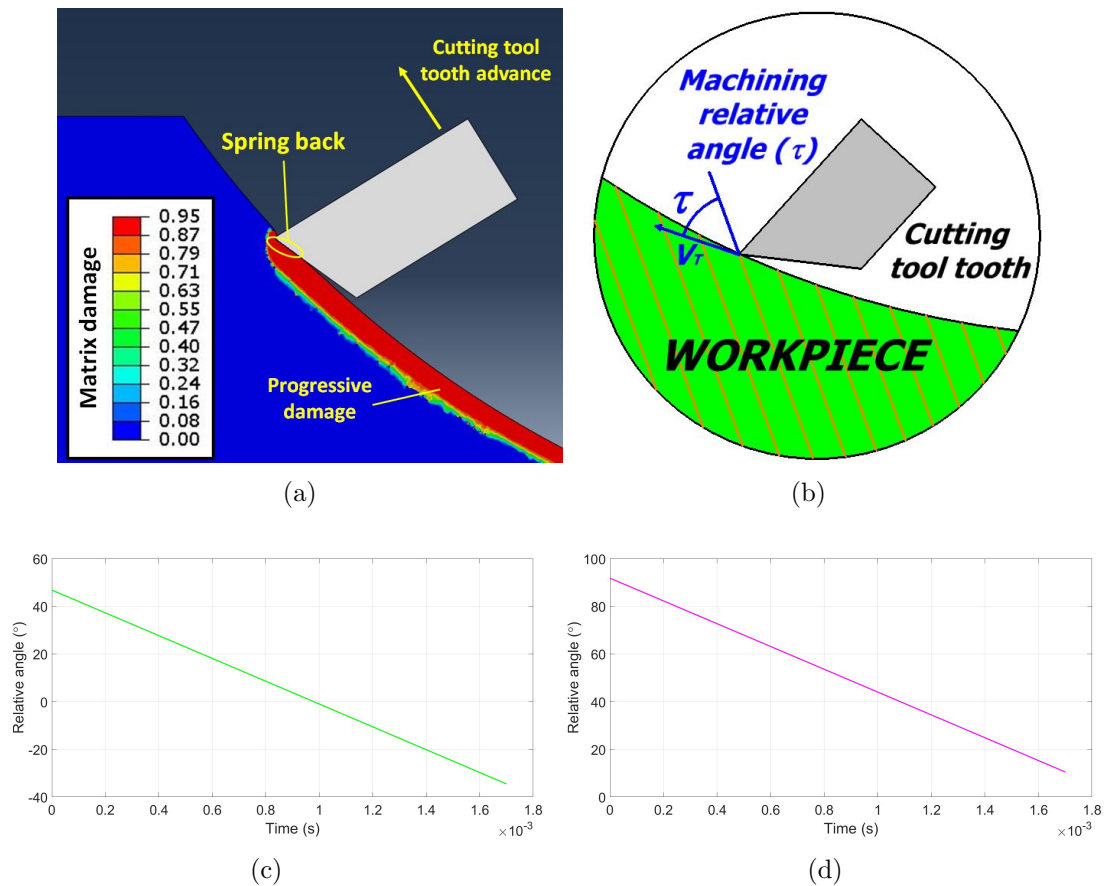


Fig. 6.5.3. Representation of relevant machining parameters analysed in this research: (a) spring back phenomenon (b) machining relative angle scheme, (c) machining relative angle distribution in the machining of 45° laminates and (d) machining relative angle distribution in the machining of 90° laminates

6.5.1 Numerical FE model validation

For the validation of this model, the average force data provided in the research of Duboust *et al.* [156] is used. All the machining configurations tested in the machining trials developed by Duboust *et al.* [156] with a cutting tool edge radius of 10 μm are simulated. In total, eight simulations with feed rates of 800 mm/min and 1200 mm/min, spindle speeds of 6000 rpm and 8000 rpm and fibre orientations of 45° and 90° are performed. The inclusion of the phenomenal spring back together with the limitation in the damage of shear and matrix applied can simulate trends in machining forces very similar to those obtained experimentally. Finally, a definite improvement is appreciated in comparison with the predictions made by Duboust *et al.* [156], as shown in Figs. 6.5.4 to 6.5.7.

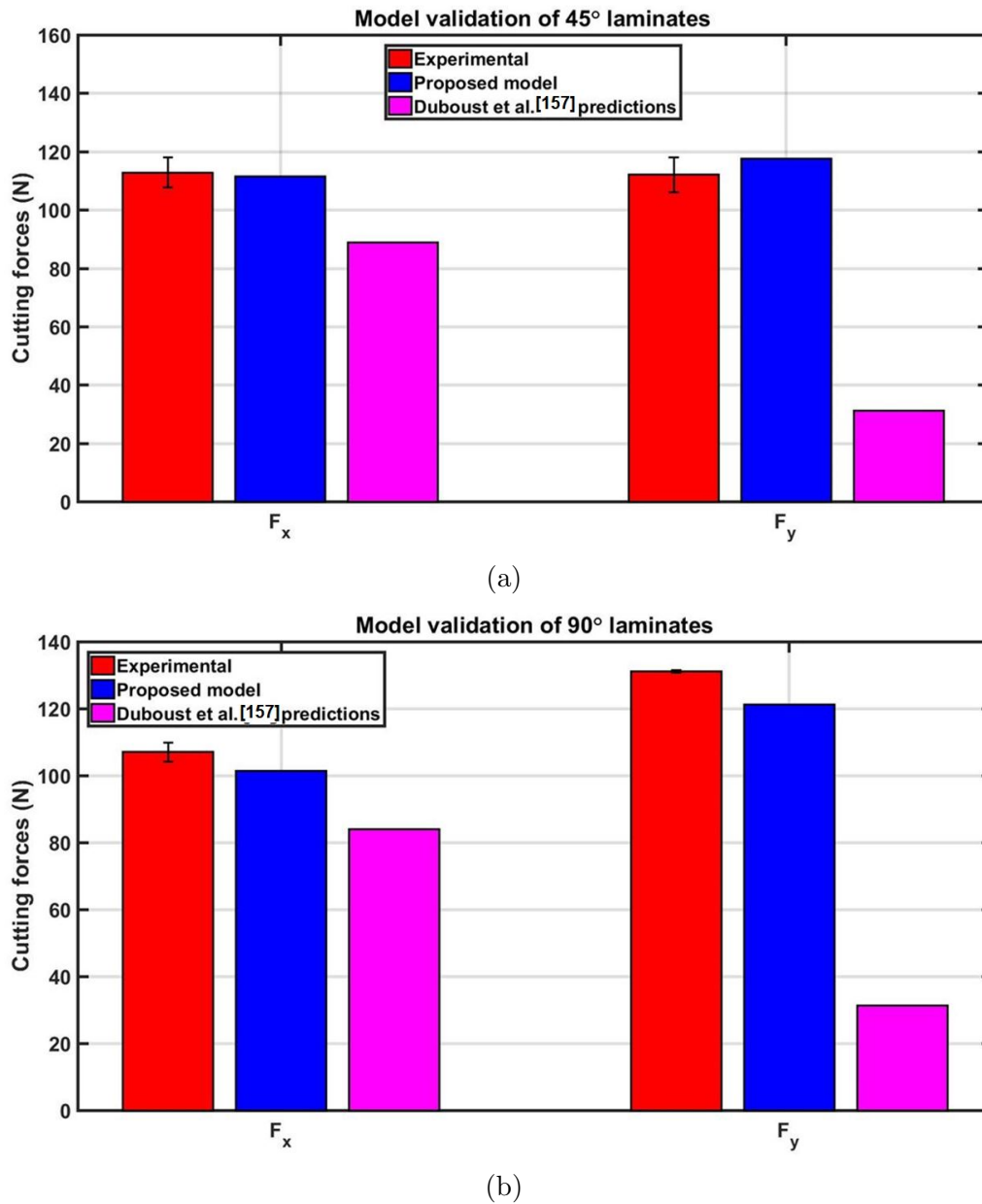


Fig. 6.5.4. Validation of FE predictions with $f_r=800$ mm/min, $w=6000$ rpm and fibre orientation of (a) 45° and (b) 90°

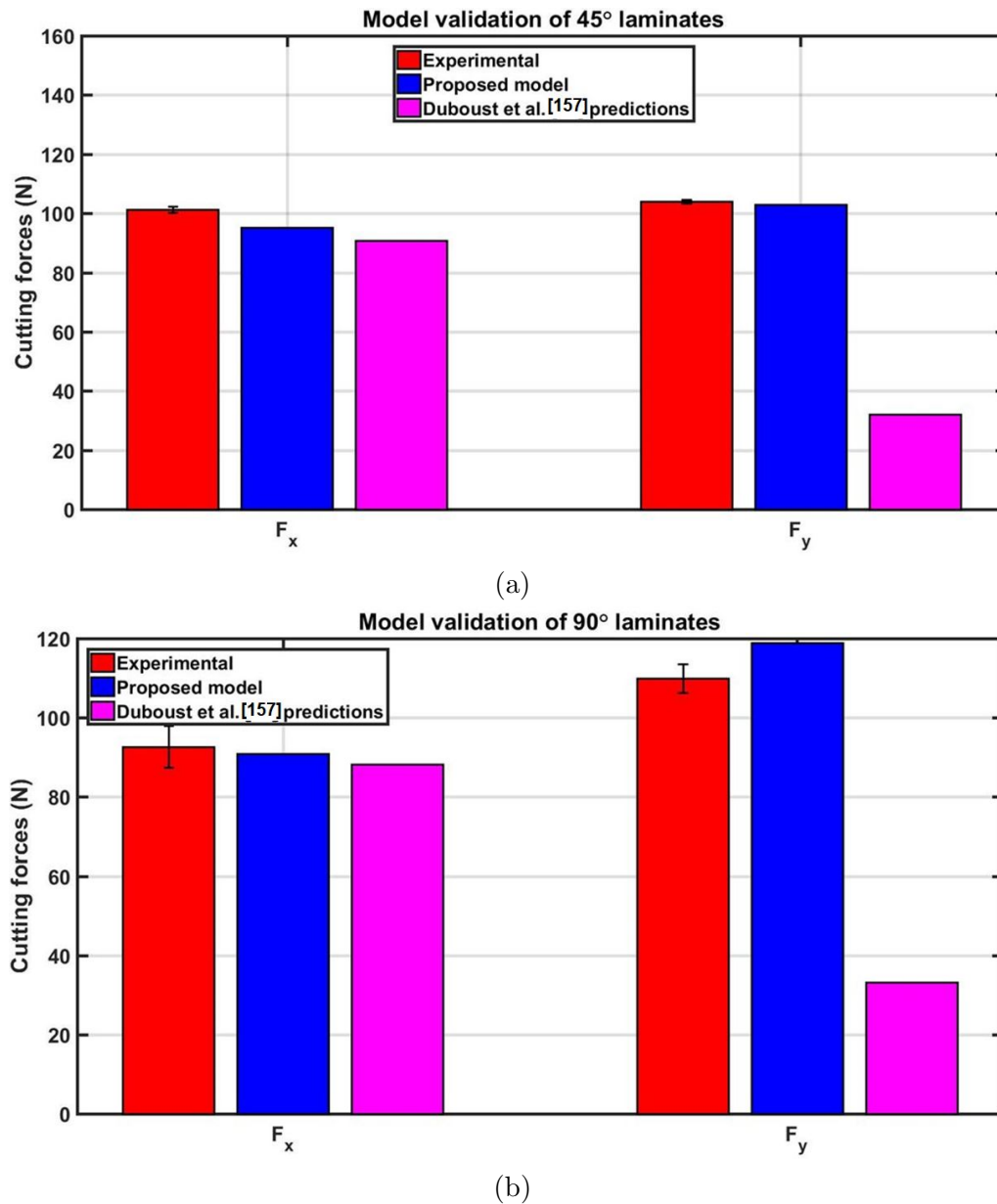


Fig. 6.5.5. Validation of FE predictions with $f_r=800$ mm/min, $w=8000$ rpm and fibre orientation of (a) 45° and (b) 90°

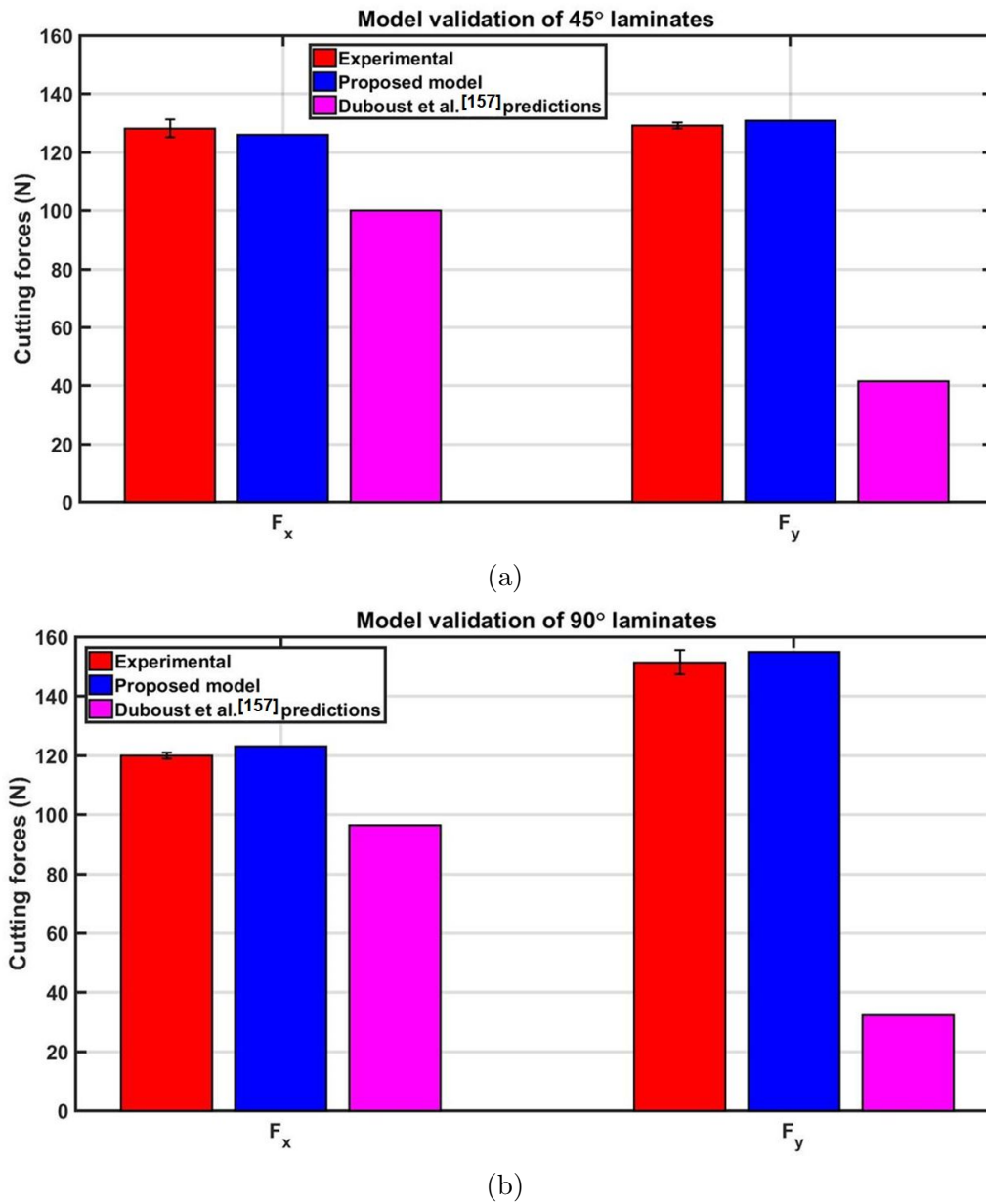


Fig. 6.5.6. Validation of FE predictions with $f_r=1200$ mm/min, $w=6000$ rpm and fibre orientation of (a) 45° and (b) 90°

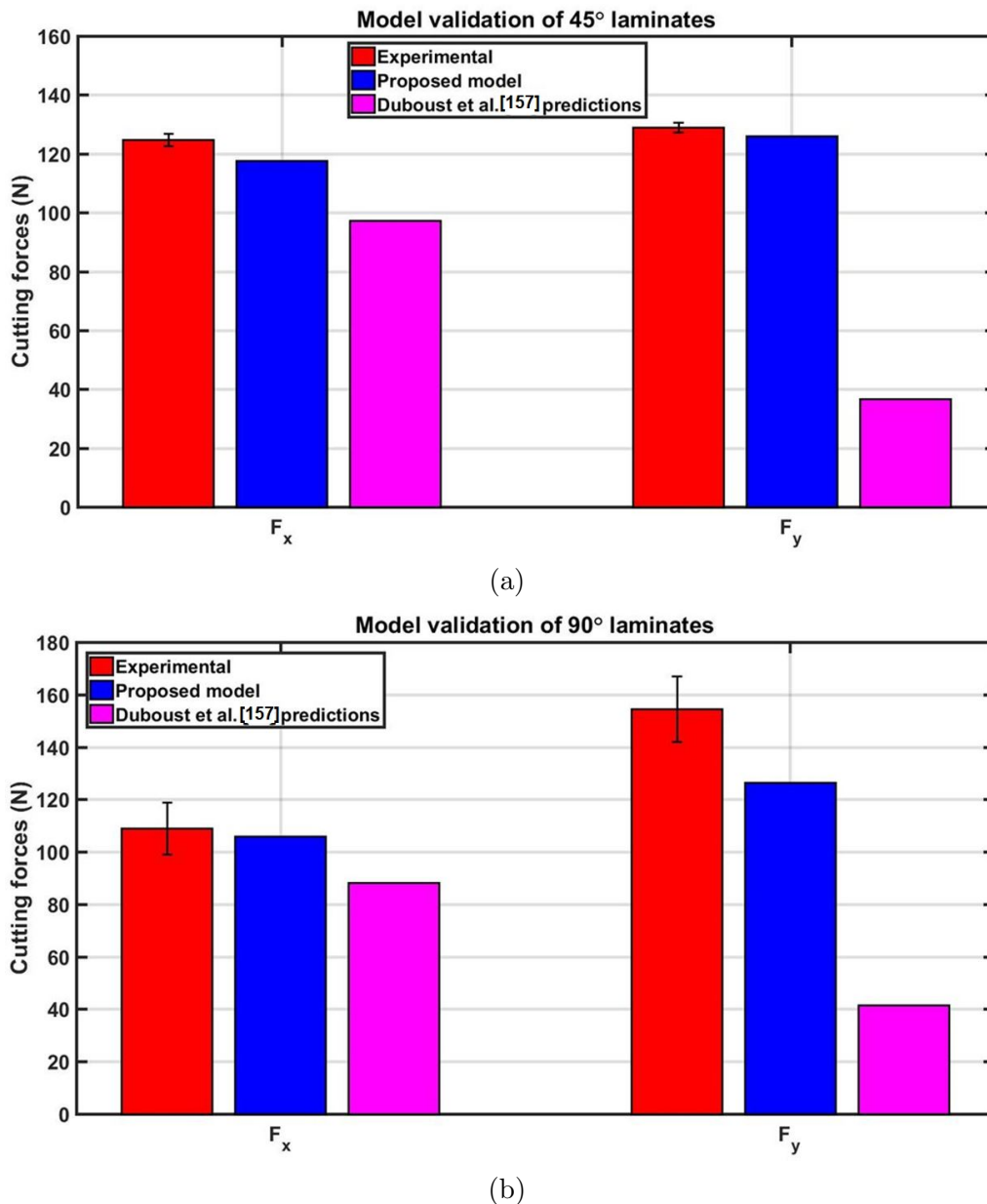


Fig. 6.5.7. Validation of FE predictions with $f_r=1200$ mm/min, $w=8000$ rpm and fibre orientation of (a) 45° and (b) 90°

The small error percentages simulated shows the reliability of this FE model to predict accurate machining forces in any cutting configuration. These errors do not exceed 10% in most of the average forces simulated, as shown in Table 6.5.1. Only the configuration with $f_r = 1200$ mm/min, $w = 8000$ rpm and 90° obtained an error higher than 10% in F_Y forces. However, a glance to Fig. 6.5.7 reveals that the standard deviation calculated for this trials is considerably bigger than the standard deviation obtained in the rest of the trials. Furthermore, the model predicts a similar trend observed in the experimental findings for F_X and F_Y forces. From these factors it is induced that a small error in the measurements of these forces could be the cause of this discrepancy.

Table 6.5.1. Numerical errors obtained with respect the experimental average forces measured by Duboust et al Duboust2017.

Parameters	Average $F_X 45^\circ$	Average $F_Y 45^\circ$	Average $F_X 90^\circ$	Average $F_Y 90^\circ$
$f_r=800$ mm/min $w=6000$ rpm	1.1%	5.03%	5.19%	7.58%
$f_r=800$ mm/min $w=8000$ rpm	5.98%	0.98%	1.87%	8.18%
$f_r=1200$ mm/min $w=6000$ rpm	1.61%	1.31%	2.64%	2.34%
$f_r=1200$ mm/min $w=8000$ rpm	5.67%	2.30%	2.97%	18.23%

6.5.2 Fibre orientation of 45°

Initially, vertical forces F_Y experience a steady growth mainly motivated by the spring back phenomenon. This trend is taken place because the range of machining relative angles given in the edge trimming of 45° laminates, from 45° to -15° refer to Fig. 6.5.3(c), generate similar thrust forces in machining [85]. Later, a parabolic decrease of the forces is observed because the spring back forces have a more considerable contribution to the X-axis, which decreases notably the quantity measured in the vertical component. Horizontal forces F_X experience a parabolic raise due to the spring-back contribution to the horizontal axis. An analysis of this result reveals that cutting forces are not significant compared to spring-back forces which are the leading cause that produces the F_X and F_Y forces distribution. The global machining forces simulated for cutting tool edge radius of $10 \mu m$, $20 \mu m$, $40 \mu m$ and $50 \mu m$ are presented in Fig. 6.5.8.

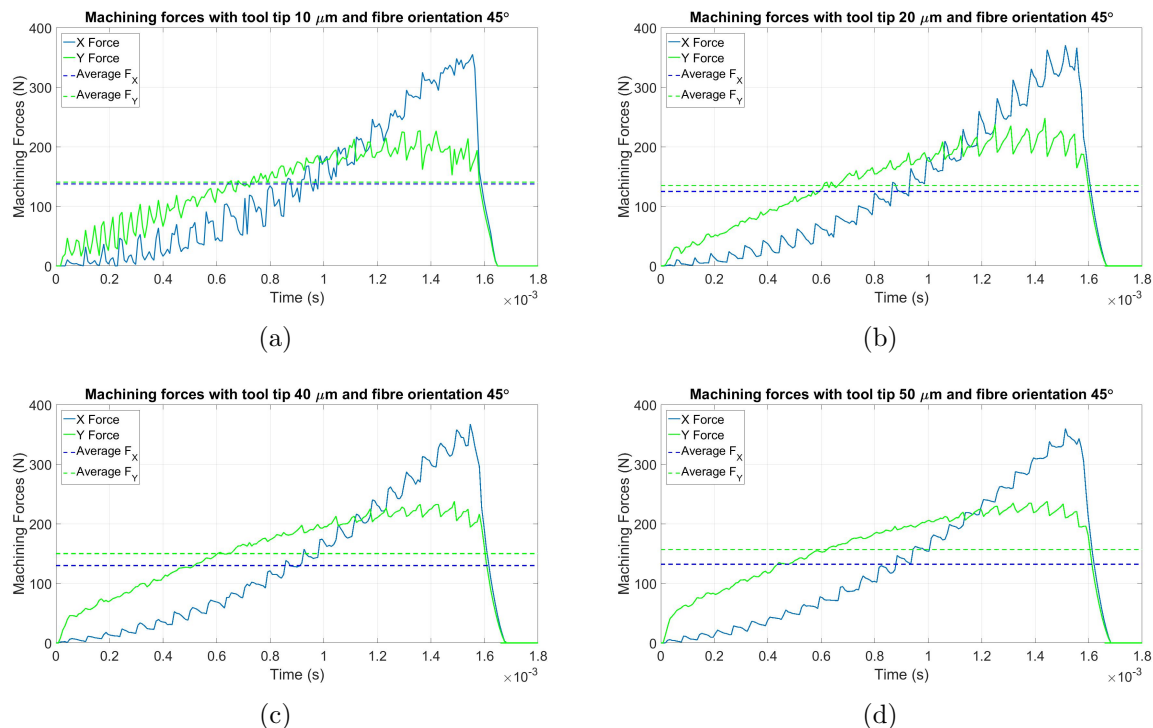


Fig. 6.5.8. F_X and F_Y forces simulated in laminates with a fibre orientation of 90° and tool edge radius of (a) 10 μm , (b) 20 μm , (c) 40 μm , (d) 50 μm .

Note that the cutting forces recorded in the simulations do not follow a smooth distribution with the tool's advancement, but rather it is appreciated an irregular distribution full of saw teeth. These fluctuations occurs because the tool teeth induces damage underneath the tool tip. The tool and the laminate have a group of element in contact which induces this peak of forces when the tool teeth travel from regions with damage elements to ahead no damage regions. Basically, first the elements below the tool have no damage increasing notably the cutting forces registered. After the first contact take place, these elements are damage and reduce their stiffness reducing the forces registered. Finally, the tool teeth advance and contact with a new set without damaged element increasing notably the forces again. It is observed how for higher tool edge radius the amplitude of these fluctuations decreases notably, as shown in Fig. 6.5.9. The reduction of the element sizes in the laminate lead to increase the frequency of these fluctuations and reduce their amplitude, see Fig. 6.5.10. These fluctuations magnitude increases notably with the implementation of higher contact stiffness and could create element distortion problems using high values. In this research, a linear contact rigidity of 10 GPa is employed to avoid this problem.

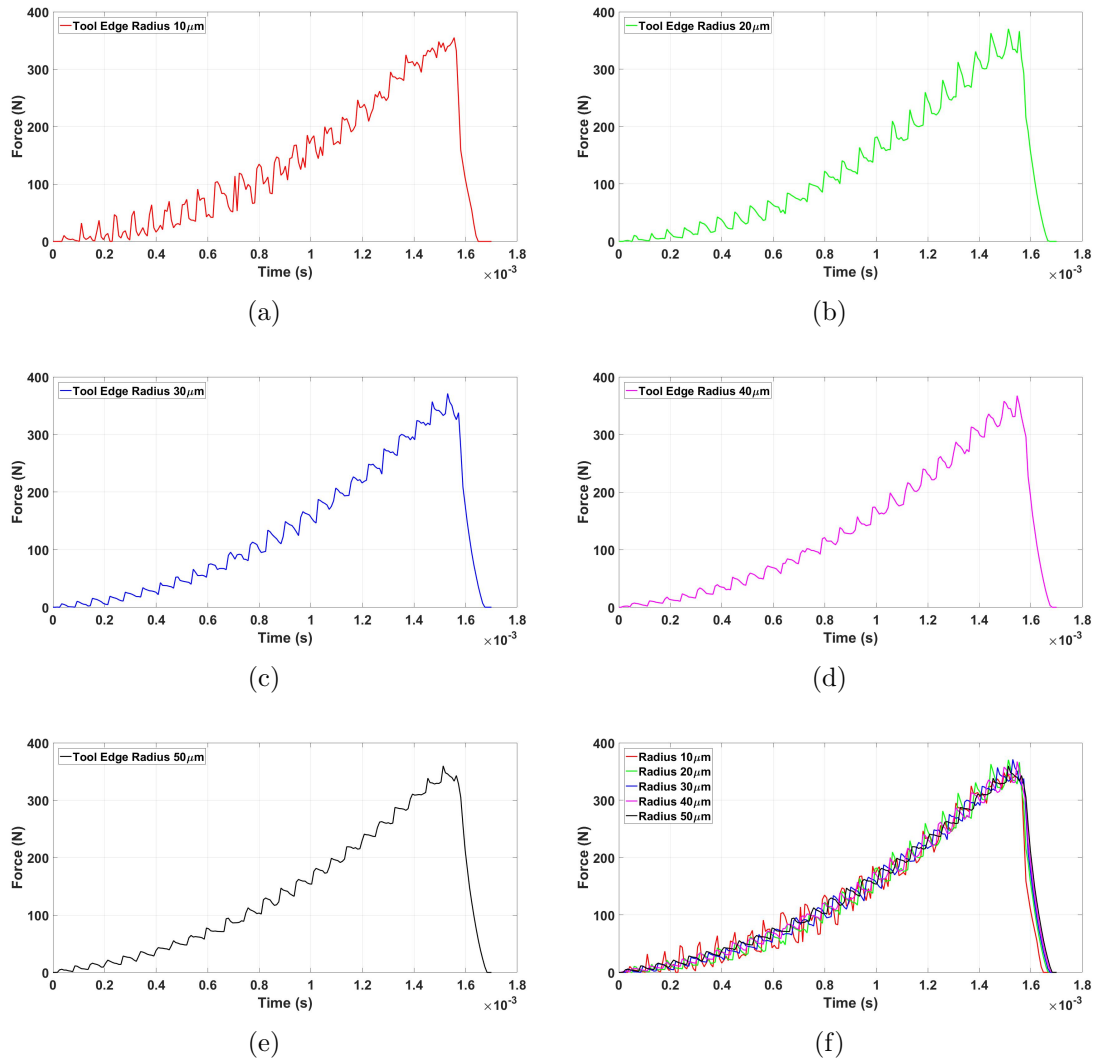


Fig. 6.5.9. F_X representation in 45° laminates and element sizes of $10\mu\text{m}$ for several tool edge radius: (a) 10 μm , (b) 20 μm , (c) 30 μm , (d) 40 μm , (e) 50 μm and (f) 10-50 μm .

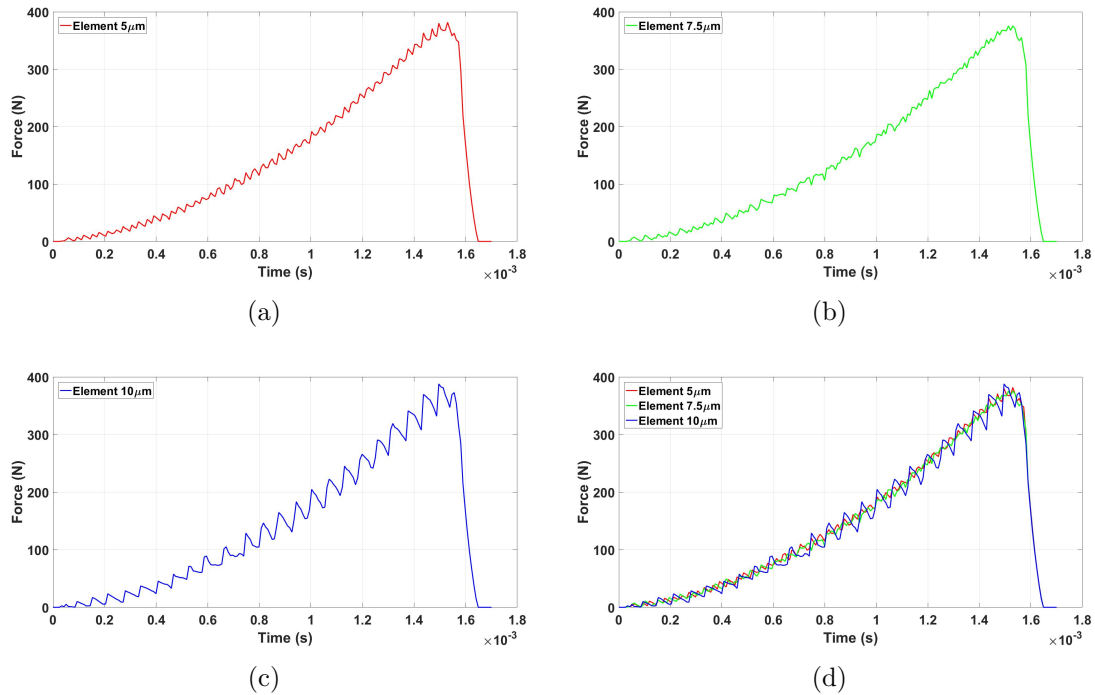


Fig. 6.5.10. F_X representation in 45° laminates and tool edge radius of 10 μm for several element sizes: (a) 10 μm, (b) 20 μm, (c) 40 μm, (d) 5-10 μm.

Regarding the forces F_T and F_N , two steady rises with distinct slopes are observed. Therefore, it is concluded that the variation of the effect of the changes in machining relative angles is not crucial for this configuration. As discussed above, it is observed that spring back forces responsible for the increment of F_N forces are higher than the cutting forces that govern the F_T forces evolution. The representation of all graphs measuring these forces is showcased in Fig. 6.5.11.

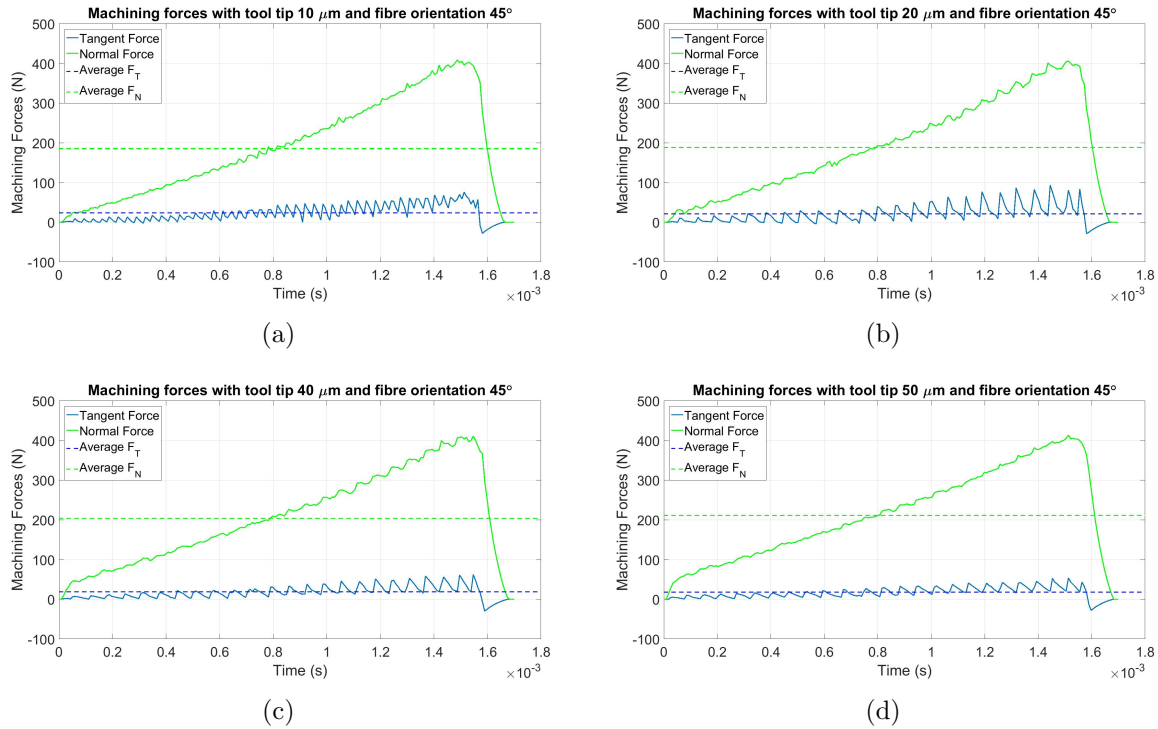


Fig. 6.5.11. F_T and F_N forces simulated in laminates with a fibre orientation of 45° and tool edge radius of (a) $10 \mu m$, (b) $20 \mu m$, (c) $40 \mu m$, (d) $50 \mu m$.

From the analysis of the results, it is inferred that tool wear does not increase significantly (less than 20%) the machining forces in the edge trimming of 45° laminates. The most significant increments are observed in forces F_N and F_Y with maximum raises of 19.90% and 13.76%, respectively. Forces F_X keeps stable with small increments below 5%. Finally, forces F_T are calculated low compared to the other forces analysed; they experience a slight decrease from 23.63 N to 17.78 N. The average machining forces simulated in this work are presented in Fig. 6.5.15, while the force increments obtained concerning the unworn cutting tool, tool edge radius of $10 \mu m$, are collected in Table 6.5.2.

Table 6.5.2. Average forces and increments percentage because of the tool wear simulated

Tool edge radius	Average $F_X(N)$	Average $F_Y(N)$	Average $F_T(N)$	Average $F_N(N)$
$10 \mu m$	126.13(-%)	130.89(-%)	23.63(-%)	185.43(-%)
$20 \mu m$	124.97(-0.91%)	134.95(3.09%)	20.98(-11.18%)	188.06(1.41%)
$30 \mu m$	127.81(1.33%)	143.27(9.45%)	19.33(-18.19%)	196.82(6.14%)
$40 \mu m$	129.86(2.96%)	150.02(14.61%)	18.68(-20.93%)	203.63(9.81%)
$50 \mu m$	132.12(4.75%)	156.94(19.90%)	17.78(-24.73%)	210.95(13.76%)

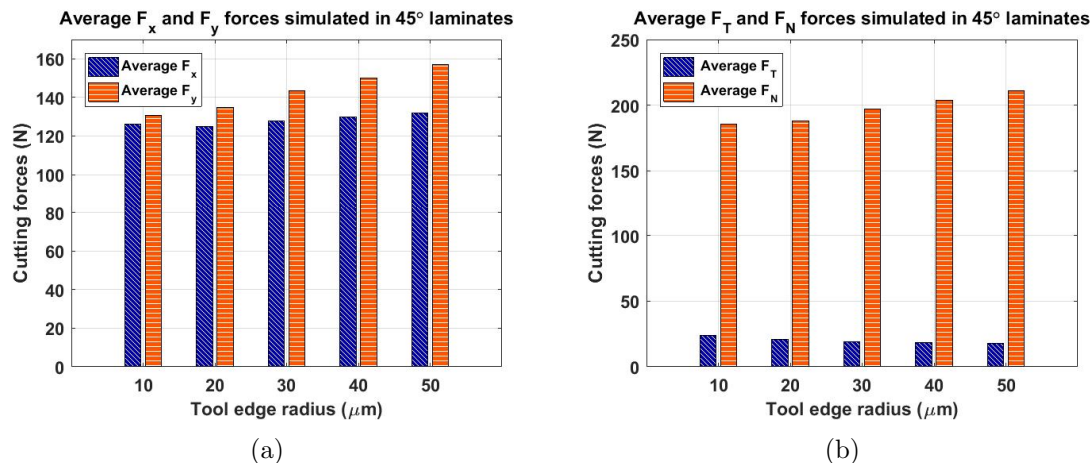


Fig. 6.5.12. Representation of the average machining forces simulated with a fibre orientation of 45° : (a) F_X and F_Y (b) F_T and F_N

6.5.3 Fibre orientation of 90°

An observation of the vertical forces obtained reveals that these initially undergo a steep rise due to the spring-back's effect that pushes the cutting tool in the normal direction to the machined surface. This steep rise slope occurs because the cutting tool is initially pushed with the characteristic high rigidity of laminates loaded parallel to the fibre. After this sharp rise, there is a decrease in this curve slope until it reaches a significant drop attributable to two factors. The first factor that causes this drop is that the contribution of forces produced by the spring back phenomenon in the vertical component decreases appreciably with the cutting tool tooth's advance. The second factor is that the machining process's cutting forces are added in the negative component of the vertical axis.

Horizontal force steady rises because of the horizontal contributions given during the spring-back and cutting forces simulation. The horizontal cutting forces are primarily increased because of the increase in chip thickness as the tool rotates. Subsequently, the forces coming from spring back raise their contribution in the horizontal axis while cutting force contribution becomes less relevant with the cutter tooth's advance. Below, in Fig. 6.5.13 are visualised the global machining forces collected for cutting tool edge radius of $10 \mu\text{m}$, $20 \mu\text{m}$, $40 \mu\text{m}$ and $50 \mu\text{m}$ where the above-commented statements discussed are appreciated.

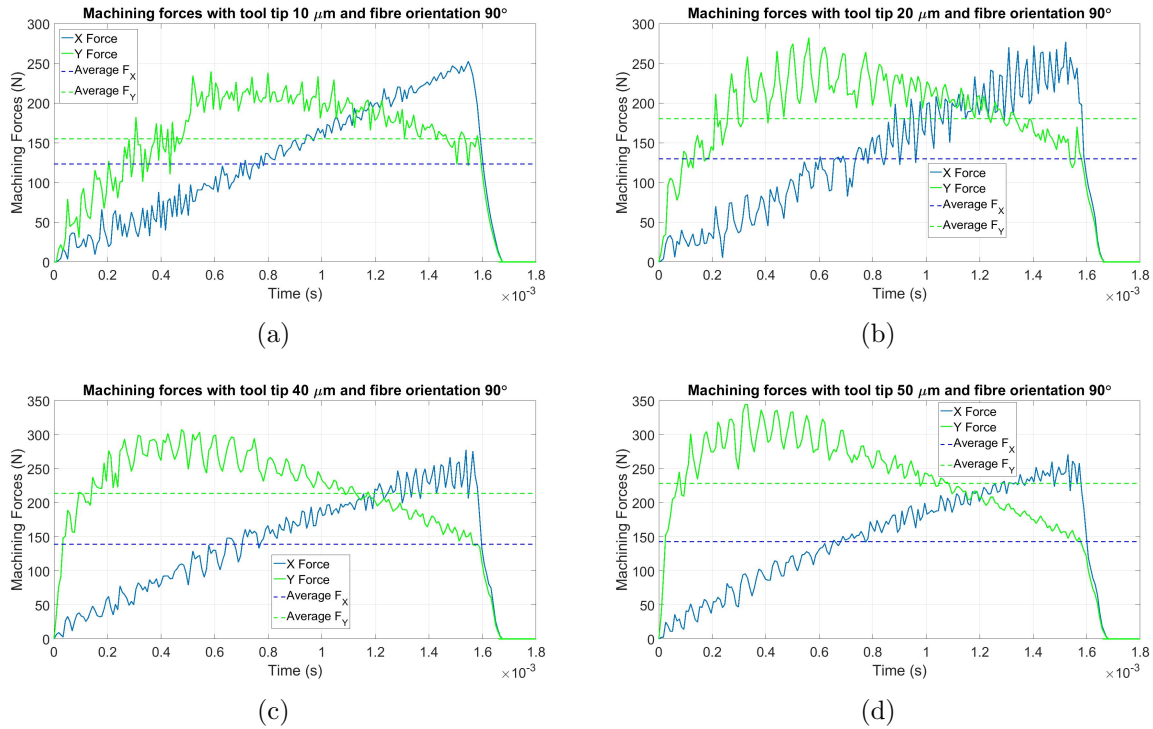


Fig. 6.5.13. F_X and F_Y forces simulated in laminates with a fibre orientation of 90° and tool edge radius of (a) $10 \mu m$, (b) $20 \mu m$, (c) $40 \mu m$, (d) $50 \mu m$.

Regarding the forces measured in the cutting tool's tooth, F_N and F_T , they reach a stable level of force over which they fluctuate. Different reasons explain this trend for both investigated forces. In the case of F_N , this force is obtained due to the spring back phenomenon. Initially, a rapid force increase is observed because the penetration stiffness is high when the tool pushes the laminate in a direction parallel to the fibre. As the tool advances, the relative machining angle decreases in a range from 90° to 30° , refer to Fig. 6.5.3(d), softening the workpiece/cutting tool contact and substantially reducing the contact stiffness. The level of force previously obtained is maintained due to the deeper penetration of the cutting tool tooth (with an increase in chip thickness). However, this is compensated by the contact stiffness reduction when the cutting tool tooth advances. An identical mechanism occurs with the tangential forces F_T , where the cutting forces decrease with relative cutting angles lower than 90° . Nevertheless, this factor is compensated by the more considerable amount of material removed when the simulation goes ahead in this analysis. As seen in Fig. 6.5.14, the reached force levels of F_N are significantly higher than those of F_T because each pass of the tool tooth has a small depth-of-cut.

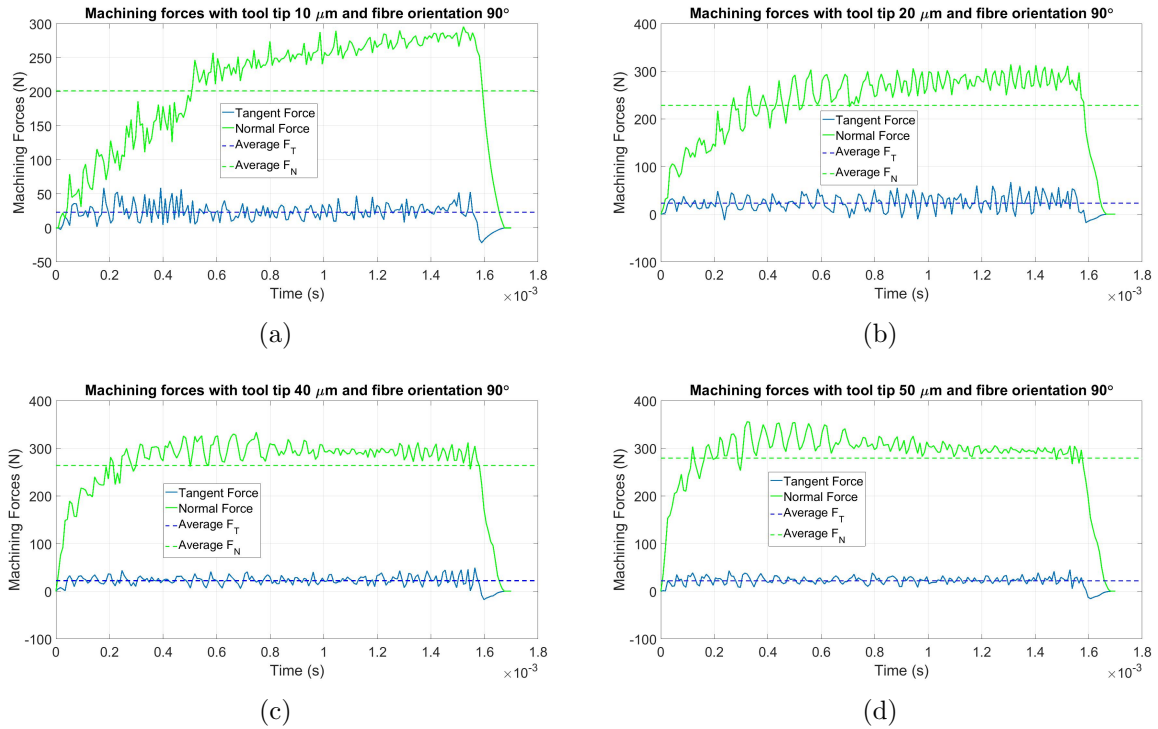


Fig. 6.5.14. F_T and F_N forces simulated in laminates with a fibre orientation of 90° and tool edge radius of (a) $10 \mu m$, (b) $20 \mu m$, (c) $40 \mu m$, (d) $50 \mu m$.

The average forces simulated in this investigation highlight several assertions. The machining forces experience a linear increment produced by the cutting tool wear. A gradual and significant increase in the forces F_N and F_Y caused by tool wear is observed, increasing maximum forces of 38.79% and 47.45%, respectively. This rise is less pronounced for F_X forces, achieving a maximum increment of 16.12%, while the F_T forces do not show a significant variation due to the wear of the cutting tool. This effect is due to the increased contact area between the workpiece and the worn cutting tool. All the data obtained in the simulations performed are illustrated in Fig. 6.5.15, while the force increases obtained compared to the forces obtained with the unworn tool, tool edge radius of $10 \mu m$, are shown in Table 6.5.3.

Table 6.5.3. Average forces and increments percentage because of the tool wear simulated

Tool edge radius	Average $F_X(N)$	Average $F_Y(N)$	Average $F_T(N)$	Average $F_N(N)$
$10 \mu m$	123.17(-%)	155.04(-%)	23.01(-%)	201.26(-%)
$20 \mu m$	129.71(5.31%)	180.41(16.36%)	23.44(1.86%)	228.45(13.51%)
$30 \mu m$	135.51(10.02%)	196.43(26.69%)	23.62(2.65%)	245.66(22.06%)
$40 \mu m$	139.03(12.88%)	213.74(37.85%)	22.34(-2.92%)	263.60(30.97%)
$50 \mu m$	143.02(16.12%)	228.62(47.45%)	22.09(-3.99%)	279.34(38.79%)

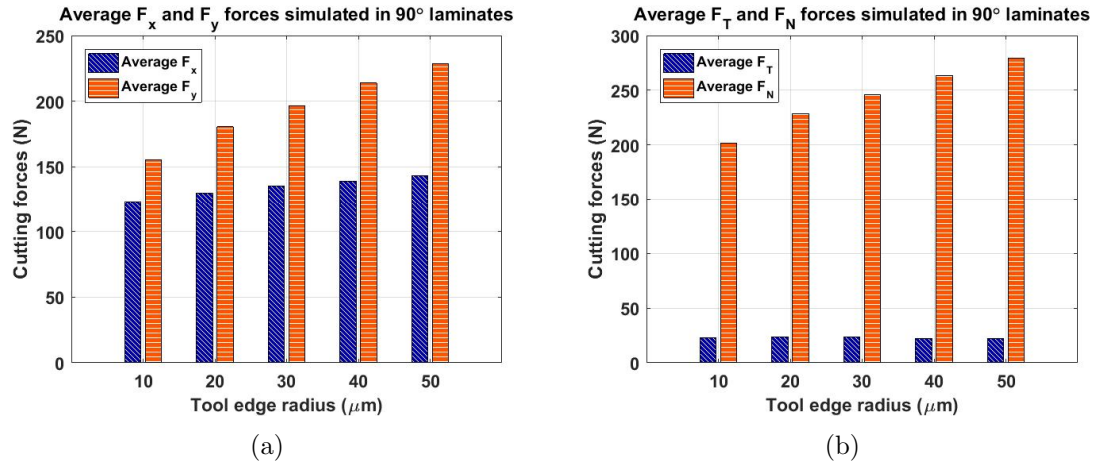


Fig. 6.5.15. Representation of the average machining forces simulated with a fibre orientation of 90°: (a) F_X and F_Y (b) F_T and F_N

A deeper analysis of the results simulated in 45° and 90° laminates yield the following conclusions. The increment of the machining forces occurs because the tool edge wear decrease the fibre cutting effectiveness. A worn tool instead of shearing the fibres away tends to bend the fibres increasing the machining forces and sub-surface damage. Generally, the increment of machining forces occurs because the tool/workpiece contact area is increased. This factor increase the spring back forces and frictional forces. The spring back forces increase significantly because a bigger area of the tool penetrates inside the laminates adding a substantial force in the normal component (F_N). The tangential force (F_T) changes are smaller because despite the friction forces increase due to this contact area increment, the tangential component of the spring back forces is contrary to the frictional force. Therefore, both effects are counteracted avoiding a clear trend in the tangential forces. Horizontal and vertical forces (F_X and F_Y) increments are result of the projections of the spring back force big increment. In general, the increments of F_Y caused by tool wear are more severe than the force increments observed in F_X .

6.6 Concluding remarks

This study develops a novel study in modelling edge trimming of CFRP laminates using a worn cutting tool. Tool wear effect on machining forces is successfully modelled in 45° and 90° laminates. A composite damage algorithm based on hybrid Puck-Maximum stress criteria has been used to calculate damage initiation with a linear energy-based degradation of the mechanical properties and mimic the composite behaviour. Validation of average machining forces predictions is achieved by obtaining relatively small errors (within 10%) compared to experimental data. These predictions notably enhance the numerical results achieved in previous investigations in this matter. These improvements are obtained because of the numerical implementation of the spring back phenomenon, which adds to the simulation machining forces not previously considered. Several relevant conclusions extracted from this study are summarised in the below bullet points.

- In all developed simulations, the normal forces (F_N) simulated are much higher than

the tangential forces (F_T). It means that spring back forces are predominant to the cutting forces in these analyses.

- The raise observed in F_N , F_X and F_Y is result of the increment of spring back forces, while F_T keeps stable because the increment of spring back and frictional forces are compensated.
- Increment in F_Y caused by tool wear are observed to be more severe than increments in F_X . Therefore, the evolution of vertical forces should be checked to determine the moment of a correct worn insert replacement.
- A steady increase in normal (F_N) and vertical (F_Y) average forces because the effect of the tool wear is observed in both studied laminates. These increments are more severe in 90° laminates.
- Normal and tangential machining forces depict a steady raise in 45° laminates. It happens because the range of machining relative angles from 45° to -15° does not modify the spring-back significantly or cutting forces. Therefore, this raise is governed by the progressive increment of the depth-of-cut when the cutting tool tooth advances.
- Normal machining forces of 90° laminates have an initial steep rise to later fluctuate between a stable value. In the normal force, the cutting tool tooth is pushing down the laminate parallel to the fibre finding a high contact rigidity that decreases significantly when the machining relative angle is far from this 90° .

Note that interesting technical applications could be achieved using the FE model developed in this investigation. For instance, it could detect the point where the tool should be replaced, thus saving manufacturing time and optimising the tool's use. Apart from this point, another analysis could be developed using this framework. The FE model developed in this research offers an excellent capability to analyse how other relevant cutting parameters such as feed rate, cutting speed, fibre orientation or rake and relief angles affect the machining forces. Therefore, this FE model or similar FE models can be used in oncoming composite milling investigations to quantify the effects of cutting edge rounding and CFRP machining failure mechanisms.

Chapter 7

Conclusions and future work

In this chapter, a broad summary of the thesis is performed. The foundations of all the written chapters are explained and the outcomes obtained and possible improvements of the work performed. Three sections are proposed to fulfil this task. Firstly, the thesis aims and the research direction taken are justified. Subsequently, all the results and conclusions drawn from this thesis are exposed in detail. Finally, the possible improvements to enhance the quality of this work are discussed.

7.1 Thesis aims

This thesis's principal aim is to use the finite element method to study composite material processing operations. The development of numerical research that implements advanced modelling techniques has significantly reduced costs (expensive test equipment, operator costs, materials) and reduce problems that draw clear conclusions from experimental tests (manufacturing of laminates, internal defects, measurement limitations). Therefore, developing a robust composite finite element model has brought tremendous progress to industry and academia. In addition to bringing substantial economic savings to the industry, it can also ensure that these operations' physical processes are carried out with higher precision.

This research is focused on the novel study of the physics of the interaction between long fibre reinforced polymers laminates and the cutting tool. This interaction is difficult to predict because the fibre's different behaviour and the matrix induce different failure modes simultaneously. Apart from this factor, the morphology of the tool generates non-uniform stress distributions in the cutting region. Therefore, all these factors should be considered in the numerical simulation to obtain accurate prediction.

It is achieved with the development of an algorithm that customises the composite behaviour to fulfil this thesis's objectives. This algorithm is implemented in a user-defined Vumat Fortran subroutine, linked to the FE model developed in Abaqus/Explicit. It includes a damage model based on the CDM approach with a progressive linear degradation of mechanical properties that considers the fracture energy of each failure mode. Fibre and matrix damage initiation is calculated using a hybrid model including Hashin's and Puck's failure criteria. The validation of this damage model is developed with the simulation of tensile test of specimens with fibre orientations of 0° and 90° . The results

reveal that the model predicts the different fibre and matrix damages with great accuracy in single load configurations. Therefore, the model is suitable for calculating more complex load situations that occur in composite machining. Finally, this algorithm includes a strain-based model that eliminates the elements by emulating the laminate fracture to recreate the different modes of fracture in composite machining.

An extensive study of the works published in the literature reveals the following three aspects that are poorly researched, and that should be improved in composite machining FE macro-mechanical models.

- Development of composite machining FE models with consistent sub-surface damage validations.
- Modelling of chip formation mechanism.
- Numerical assessment of complex machining operations such as edge trimming.

Therefore, the content developed in this thesis focuses on the modelling of the three previous aspects and the results obtained are discussed in the next section.

7.2 Thesis outcomes

As mention in Section 7.1 this thesis is focused on the modelling of three separate blocks: (1) sub-surface damage assessment, (2) chip formation mechanisms and (3) tool wear localisation in edge trimming. The conclusions extracted from these works are detailed below.

7.2.1 Modelling of sub-surface damage

In this investigation, the effect of several cutting parameters on the underlying damage below the cutting surface is assessed. This investigation validates its results using a combination of the experimental machining forces and sub-surface damage. This purpose is successfully achieved by modelling the spring-back phenomenon due to it achieve an enhancement in the thrust force and sub-surface damage predictions. Additionally, the versatile composite damage algorithm employed demonstrates that matrix damage modes cause the initial cracks' nucleation. Three main areas around the cutting tool position are distinguished:

- Below the tool edge: shear stresses govern matrix damage developed in this region; thus, matrix cracking and crushing are predicted simultaneously for this reason.
- Behind the tool edge: the strong push exerted by the tool on the laminate causes the appearance of strong tensile stresses in this area. Therefore, matrix cracking occurs mostly in this region.
- In front of the tool: tool compresses this area of the laminate before shearing the chip away; then, in this zone, a high degree of matrix crushing is appreciated

Several simulations have been developed to analyse the influence of fibre orientation, rake and relief angle, tool wear, and material on the underlying cutting surface damage. The below statements are outlined:

- **Fibre orientation:** In fibre orientations of 15° and 30° the damage does not dangerously penetrate inside the laminate because their fibre bending failure is not severe. However, the damage increments progressively for higher fibre orientations because the fibre bending failure becomes more important when this variable increases until 90° .
- **Material:** Because of the superior stiffness exhibited by the UD-CFRP, these laminates experience lower sub-surface damages and higher machining forces than UD-GFRP laminates.
- **Tool wear:** It is predicted a substantial sub-surface damage increment when the tool edge radius exceeds the $15\ \mu\text{m}$ in 90° laminates.
- **Relief angle:** The use of high relief angles has been proven to reduce sub-surface damage considerably. It occurs because this factor reduces the predicted vertical predicted forces; thus, the penetration of the damage inside of the laminate is stopped.
- **Rake angle:** The simulations developed in this research do not show any clear tendency of this variable's influence on the machining induced damage.

7.2.2 Modelling of chip formation

After simulating composite machining subsurface damage with great accuracy, the next step is to model chip fracture. Because chip fracture is directly related to machining forces and sub-surface damage, its modelling is vital to increase the predictions' quality. This work develops a straightforward methodology to simulate this feature in the most usual composite machining scenarios. Furthermore, it has a straightforward implementation in complex and common machining operations such as drilling or milling. This chip fracture is modelled by implementing a novel strain-based element deletion algorithm that erodes the elements after their mechanical properties have been progressively degraded. The study of the machining of five cutting configurations with different chip fracture mechanisms is successfully addressed. These configurations are defined as the machining of laminates with positive rake angles and fibre orientations of 0° , 45° , 90° and 135° and the machining of 0° laminate with a rake angle of 0° . The most relevant outcomes are summarised below.

- **Fibre orientation of 0° :** The typical chip cantilever beam effect before the total fracture is achieved because of the high matrix cracking observed in the debonded elements. This damage abruptly raises these elements' transversal strain until their deletion, when they exceed a value of 0.15. The final fibre shear failure should be investigated in the future to generate the chip release.
- **Fibre orientation of 0° with 0° rake angle:** In this configuration, high fibre compressive stress causes the fibre micro-buckling failure of the elements in front of the tool. This matter generates the rapid propagation of fibre compression damage,

which finally infer the elements' deletion exceed a longitudinal compressive strain of 0.2.

- **Fibre orientation of 45°:** Matrix shear failure plays a relevant role to fracture this chip. Elements are removed when their shear strain overcomes a value of 0.325 to generate a chip fracture plane parallel to the fibre direction.
- **Fibre orientation of 90°:** Two fracture mechanism are simulated in this configuration. In front of the tool, small chip fragments are generated due to the high matrix crushing in these elements. The fracture is obtained, deleting the elements that transversal compressive strains of 1.2. Additionally, a vertical crack is modelled due to the push that the cutting tool exerts on the laminate. The crack formation is caused due to the high levels of matrix cracking, removing the element with higher transversal strain levels than 0.2.
- **Fibre orientation of 135°:** Hashin's failure criterion is modified to add the shear stress contribution in the fibre fracture. A new quadratic formulation is proposed to achieve this purpose. The chip generated is perpendicular to the fibre direction, and it is formed with the deletion of elements that achieve a fibre shear strain limit of 0.325.

7.2.3 Edge trimming numerical results

Finally, the composite cutting FE model developed throughout this thesis to predict the machining induced damage and chip formation is applied in a common composite edge trimming operation. The evolution of the machining forces because of steady increments of tool wear is addressed. To achieve this purpose, the 2D FE model include the spring-back phenomenon and strict element deletion criteria. The average cutting forces are validated, obtaining an incredible small error below the 10% in comparison with the experimental trials. The conclusions obtained from this research are showcased in the below bullet points.

- Normal forces (F_N) are much higher than tangential forces (F_T). Therefore, spring back forces are more significant than cutting forces in edge trimming.
- The spring back forces increment induce an increment in F_N , F_X and F_Y forces. The evolution of tangential forces F_T due to tool wear is not severely affected because both increments of spring back and frictional forces which modify this force are compensated.
- Increment in F_Y caused by tool wear are observed to be more severe than increments in F_X . Therefore, the evolution of vertical forces should be checked to determine the moment of a correct worn insert replacement.
- A progressive increase in normal (F_N) and vertical (F_Y) average forces due to tool wear is simulated.
- The evolution of normal and tangential machining forces shows a steady increment in 45° laminates. This trend is obtained due to the progressive increment in the depth-of-cut.

- Normal machining forces in 90° laminates have an initial steep rise to later fluctuate between a stable value. It occurs due to initially the cutting tool tooth is pushing down the laminate parallel to the fibre finding a high contact rigidity. This contact rigidity decreases significantly when the machining relative angle is far from this 90° achieving a consistent force stabilisation.

7.3 Future work

Revising the literature review developed in chapter 3 it could be inferred that related oncoming works might obtain more valuable predictions if the following statements are addressed.

- **Development of multi-scale mechanical models:** The development of robust FE multi-scale models is necessary to combine knowledge of machining operations. In general terms, both macro-mechanical and micro-mechanical models offer limitations that prevent the development of a simulation that describes the events that occur in a machining operation with great accuracy. This type of studies with multi-scale models would enable an advanced study of the damage that occurs at the ply level using macro-mechanical models that incorporate behaviour equations that consider the micro-mechanical behaviour of the composite constituents. It is achieved by extracting the terms of its stiffness matrix from the simulations with different load configurations of an RVE of the woven or unidirectional composite studied. Additionally, from the macro-mechanical model results, local fibre and matrix damage could be inferred at each point of the laminate by applying their load and strain levels in the micro-mechanical model.
- **Modelling of complex machining problems:** Only simple orthogonal cutting operations and a few drilling operations with a simple tool morphology have been successfully simulated. It occurs because the large machining dimensions and the fibres' micro-metric nature make the simulation of this type of model extremely heavy, making its simulation an arduous task even with the increasing computational power of current computers. Therefore, finding solutions that solve or partially reduce this problem is necessary to model more common and complex machining operations that help companies optimise cutting parameters.
- **Use of alternative numerical approaches:** Although the element removal technique eliminates element distortion problems and can recreate chip formation mechanisms with some accuracy, this technique presents significant limitations that must be mitigated using more advanced modelling techniques. These limitations are because removing the element is a drastic process that considerably limits the transmission of charge or heat between the elements adjacent to the deleted element. This fact causes a prediction's accuracy reduction in the cutting forces and damages. Modelling approaches such as XFEM partially mitigate this problem by introducing discontinuities in an element, increasing these measurements' accuracy. However, the difficulty in implementing the equations required to apply this approach is very complex and has considerably slowed the development of works using this methodology. In the future, the development of FE models using XFEM or another advanced modelling approach that increases the predictions' accuracy is necessary.

Bibliography

- [1] J. Fraga, “Boeing 787 from the Ground Up,” *AERO Magazine*, pp. 17–23, 2006.
- [2] Mike and P. Brady, “Technology developments in automotive composites,” *Reinforced Plastics*, vol. 54, no. 6, pp. 25–29, 2010.
- [3] R. Nelson, C. Composites, and T. Oclv, “Bike frame races carbon consumer goods forward,” *Reinforced Plastics*, vol. 47, no. 7, pp. 36–40, 2003.
- [4] S. Kalpakjian and S. R. Schmid, *Manufacturing Engineering and Technology*. 2009.
- [5] Leuco, “Composite machinng,” 2018.
- [6] R. Allwin, K. Gobivel, K. Vijay Sekar, and K. Suresh, “High Speed Turning of Carbon Fiber – Epoxy Composite Material,” *8th International Conference on Science, Engineering and Technology (SET)*, pp. 50–53, 2014.
- [7] S. Gordon and M. T. Hillery, “A review of the cutting of composite materials,” *Proceedings of the Institution of Mechanical Engineers Part L: Journal of Materials: Design and Applications*, vol. 217, no. 1, pp. 35–45, 2003.
- [8] G. Gudimani, *Oblique machining of unidirectional carbon fiber reinforced polymer composites*. PhD thesis, 2011.
- [9] K. Kerrigan, J. Thil, R. Hewison, and G. E. O’Donnell, “An integrated telemetric thermocouple sensor for process monitoring of CFRP milling operations,” *5th CIRP Conference on High Performance Cutting 2012*, vol. 1, no. 1, pp. 449–454, 2012.
- [10] W. Hintze and F. Brüggmann, “Influence of Curved Workpiece Contours on Delamination during end Milling of FRP,” *10th CIRP Conference on Intelligent Computation in Manufacturing Engineering - CIRP ICME ’16*, vol. 62, pp. 62–67, 2017.
- [11] N. Duboust, H. Ghadbeigi, C. Pinna, S. Ayvar-Soberanis, A. Collis, R. Scaife, and K. Kerrigan, “An optical method for measuring surface roughness of machined carbon fibre-reinforced plastic composites,” *Journal of Composite Materials*, vol. 51, no. 3, pp. 289–302, 2017.
- [12] N. Duboust, D. Melis, C. Pinna, H. Ghadbeigi, A. Collis, S. Ayvar-Soberanis, and K. Kerrigan, “Machining of Carbon Fibre: Optical Surface Damage Characterisation and Tool Wear Study,” *Procedia CIRP*, vol. 45, pp. 71–74, 2016.
- [13] J. Xu, A. Mkaddem, and M. El, “Recent advances in drilling hybrid FRP / Ti composite : A state-of-the-art review,” *Composite Structures*, vol. 135, pp. 316–338, 2016.

-
- [14] S. O. Ismail, H. N. Dhakal, E. Dimla, and I. Popov, "Recent advances in twist drill design for composite machining: A critical review," *Proceedings of the Institution of Mechanical Engineers, Part B: Journal of Engineering Manufacture*, vol. 231, no. 14, pp. 2527–2542, 2017.
- [15] T. Rajasekaran, K. Palanikumar, and B. K. Vinayagam, "Application of fuzzy logic for modeling surface roughness in turning CFRP composites using CBN tool," *Production Engineering*, vol. 5, no. 2, pp. 191–199, 2011.
- [16] K. Palanikumar, "Application of Taguchi and response surface methodologies for surface roughness in machining glass fiber reinforced plastics by PCD tooling," *International Journal of Advanced Manufacturing Technology*, vol. 36, no. 1-2, pp. 19–27, 2008.
- [17] M. A. Azmir and A. K. Ahsan, "A study of abrasive water jet machining process on glass/epoxy composite laminate," *Journal of Materials Processing Technology*, vol. 209, no. 20, pp. 6168–6173, 2009.
- [18] D. Herzog, P. Jaeschke, O. Meier, and H. Haferkamp, "Investigations on the thermal effect caused by laser cutting with respect to static strength of CFRP," *International Journal of Machine Tools and Manufacture*, vol. 48, no. 12-13, pp. 1464–1473, 2008.
- [19] W. S. Lau, M. Wangt, and W. B. Lee, "Electrical Discharge Machining of Carbon Fibre Composite Materials," *Int. J. Mach. Tools Manufact*, vol. 30, no. 2, pp. 297–308, 1990.
- [20] V. A. Phadnis, A. Roy, and V. V. Silberschmidt, "A finite element model of ultrasonically assisted drilling in carbon/epoxy composites," *14th CIRP Conference on Modeling of Machining Operations (CIRP CMMO)*, vol. 8, pp. 141–146, 2013.
- [21] F. Makhadmeh, V. a. Phadnis, A. Roy, and V. V. Silberschmidt, "Effect of ultrasonically-assisted drilling on carbon-fibre-reinforced plastics," *Journal of Sound and Vibration*, vol. 333, no. 23, pp. 5939–5952, 2014.
- [22] J. Y. Sheikh-Ahmad, *Machining of Polymer Composites*. Boston, MA: Springer US, 2009.
- [23] U. Teicher, T. Rosenbaum, A. Nestler, and A. Brosius, "ScienceDirect Characterization of the surface roughness of milled carbon fiber reinforced plastic structures," vol. 66, pp. 199–203, 2017.
- [24] I. A. Shchurov, A. V. Nikonov, and I. S. Boldyrev, "SPH-Simulation of the Fiber-reinforced Composite Workpiece Cutting for the Surface Quality Improvement," *International Conference on Industrial Engineering, ICIE 2016*, vol. 150, pp. 860–865, 2016.
- [25] S. Samiezadeh, Z. Fawaz, and H. Bougherara, "Biomechanical properties of a structurally optimized carbon- fibre / epoxy intramedullary nail for femoral shaft fracture fixation," *Journal of the Mechanical Behavior of Biomedical Materials*, vol. 56, pp. 87–97, 2016.

- [26] N. A. Abdullah, J. L. Curiel-Sosa, Z. A. Taylor, B. Tafazzolimoghaddam, J. L. Martinez Vicente, and C. Zhang, "Transversal crack and delamination of laminates using XFEM," *Composite Structures*, vol. 173, pp. 78–85, 2017.
- [27] S. T. Pinho, P. Robinson, and L. Iannucci, "Fracture toughness of the tensile and compressive fibre failure modes in laminated composites," *Composites Science and Technology*, vol. 66, no. 13, pp. 2069–2079, 2006.
- [28] J. L. Curiel Sosa and N. Karapurath, "Delamination modelling of GLARE using the extended finite element method," *Composites Science and Technology*, vol. 72, no. 7, pp. 788–791, 2012.
- [29] J. L. Curiel-sosa, B. Tafazzolimoghaddam, and C. Zhang, "Modelling fracture and delamination in composite laminates : Energy release rate and interface stress," *Composite Structures*, vol. 189, no. January, pp. 641–647, 2018.
- [30] D. J. Mortell, D. A. Tanner, and C. T. Mccarthy, "An experimental investigation into multi-scale damage progression in laminated composites in bending An experimental investigation into multi-scale damage progression in laminated composites in bending," *Composite Structures*, vol. 149, no. March, pp. 33–40, 2016.
- [31] J. Dong, P. Pomarède, L. Chehami, A. Locquet, F. Meraghni, N. F. Declercq, and D. S. Citrin, "Visualization of subsurface damage in woven carbon fiber-reinforced composites using polarization-sensitive terahertz imaging," *NDT and E International*, vol. 99, no. July, pp. 72–79, 2018.
- [32] A. Faraz, D. Biermann, and K. Weinert, "Cutting edge rounding: An innovative tool wear criterion in drilling CFRP composite laminates," *International Journal of Machine Tools and Manufacture*, vol. 49, no. 15, pp. 1185–1196, 2009.
- [33] B. Poddar, I. Automation, C. R. Bijudas, M. Mitra, and P. Mujumdar, "Damage detection in a woven-fabric composite laminate using time-reversed Lamb wave," *Structural Health Monitoring*, vol. 11, no. 5, pp. 602–6012, 2012.
- [34] N. Shetty, S. M. Shahabaz, S. S. Sharma, and S. Divakara Shetty, "A review on finite element method for machining of composite materials," *Composite Structures*, vol. 176, pp. 790–802, 2017.
- [35] G.-D. Wang and S. K. Melly, "Three-dimensional finite element modeling of drilling CFRP composites using Abaqus/CAE: a review," *The International Journal of Advanced Manufacturing Technology*, 2017.
- [36] C. R. Dandekar and Y. C. Shin, "Modeling of machining of composite materials: A review," *International Journal of Machine Tools and Manufacture*, vol. 57, pp. 102–121, 2012.
- [37] D. Che, I. Saxena, P. Han, P. Guo, and K. F. Ehmann, "Machining of Carbon Fiber Reinforced Plastics/Polymers: A Literature Review," *Journal of Manufacturing Science and Engineering*, vol. 136, no. 3, p. 034001, 2014.
- [38] O. O. Ochoa and J. N. Reddy, "Finite Element Analysis of Composite Laminates," pp. 37–109, Springer, Dordrecht, 1992.

-
- [39] R. D. Cook, D. S. Malkus, M. E. Plesha, and R. J. Witt, *Concepts and applications of finite element analysis*. fourth ed. ed., 2001.
- [40] F. Matthews, C. Soutis, D. Hitchings, and G. A. O. Davies, *Finite Element Modeling of Composite Materials and Structures*. Elsevier Science, 2000.
- [41] Y. W. Kwon, D. H. Allen, and R. Talreja, eds., *Multiscale Modeling and Simulation of Composite Materials and Structures*. Boston, MA: Springer US, 2008.
- [42] G. V. G. Rao, P. Mahajan, and N. Bhatnagar, “Three-dimensional macro-mechanical finite element model for machining of unidirectional-fiber reinforced polymer composites,” *Materials Science and Engineering A*, vol. 498, no. 1-2, pp. 142–149, 2008.
- [43] C. Santiuste, Díaz-Álvarez, X. Soldani, and H. Miguélez, “Modelling thermal effects in machining of carbon fiber reinforced polymer composites,” *Reinforced Plastics & Composites*, vol. 33, no. 8, pp. 758–766, 2014.
- [44] H. Cheng, J. Gao, O. L. Kafka, K. Zhang, B. Luo, and W. K. Liu, “A micro-scale cutting model for UD CFRP composites with thermo-mechanical coupling,” *Composites Science and Technology*, vol. 153, pp. 18–31, 2017.
- [45] T. Belytschko, W. Kam Liu, and B. Moran, *Nonlinear finite elements for Continua and Structures*. Wiley, first edit ed., 2000.
- [46] R. Talreja and C. V. Singh, *Damage and Failure of Composite Materials*. Cambridge: Cambridge University Press, 2012.
- [47] K. K. Chawla, *Composite Materials Science and Engineering*. New York, NY: Springer New York, 2012.
- [48] V. Phadnis, *Impact and blast response of polymer matrix laminates: finite-element studies*. PhD thesis, Loughborough University, 2013.
- [49] R. M. Jones, *Mechanics of Composite Materials*. CRC Press, oct 1999.
- [50] J. P. Davim, ed., *Machining Composite Materials*. Wiley, first edit ed., 2010.
- [51] J. A. Nairn, “Matrix Microcracking in Composites,” in *Comprehensive Composite Materials*, vol. 2, pp. 403–432, Elsevier, 2000.
- [52] M. Kashtalyan and C. Soutis, “Analysis of composite laminates with intra- and interlaminar damage,” *Progress in Aerospace Sciences*, vol. 41, pp. 152–173, feb 2005.
- [53] C. H. Hsueh, “Interfacial debonding and fiber pull-out stresses of fiber-reinforced composites. VIII: The energy-based debonding criterion,” *Materials Science and Engineering A*, vol. 159, no. 1, pp. 65–72, 1992.
- [54] L.-M. Zhou, J.-K. Kim, and Y.-W. Mai, “Interfacial debonding and fibre pull-out stresses,” *Journal of Materials Science*, vol. 27, no. 12, pp. 3155–3166, 1992.

- [55] B. Lauke, W. Beckert, and J. Singletary, "Energy release rate and stress field calculation for debonding crack extension at the fibre-matrix interface during single-fibre pull-out," *Composite Interfaces*, vol. 3, no. 4, pp. 263–273, 1995.
- [56] C. H. Hsueh, "Elastic load transfer from partially embedded axially loaded fibre to matrix," *Journal of Materials Science Letters*, vol. 7, no. 5, pp. 497–500, 1988.
- [57] N. S. Choi, A. J. Kinloch, and J. G. Williams, "Delamination fracture of multidirectional carbon-fiber/epoxy composites under mode I, mode II and mixed-mode I/II loading," 1999.
- [58] A. J. Brunner, B. R. Blackman, and P. Davies, "A status report on delamination resistance testing of polymer-matrix composites," *Engineering Fracture Mechanics*, vol. 75, no. 9, pp. 2779–2794, 2008.
- [59] A. C. Garg, "Delamination-a damage mode in composite structures," *Engineering Fracture Mechanics*, vol. 29, no. 5, pp. 557–584, 1988.
- [60] J. A. Nairn and S. Hu, "The initiation and growth of delaminations induced by matrix microcracks in laminated composites," *International Journal of Fracture*, vol. 57, no. 1, pp. 1–24, 1992.
- [61] C. C. Tsao, "Thrust force and delamination of core-saw drill during drilling of carbon fiber reinforced plastics (CFRP)," *International Journal of Advanced Manufacturing Technology*, vol. 37, no. 1-2, pp. 23–28, 2008.
- [62] T. N. Valarmathi, K. Palanikumar, and B. Latha, "Measurement and analysis of thrust force in drilling of particle board (PB) composite panels," *Measurement: Journal of the International Measurement Confederation*, vol. 46, no. 3, pp. 1220–1230, 2013.
- [63] R. K. Pandey and S. S. Panda, "Evaluation of Delamination in Drilling GFRP Composites," *Materials and Manufacturing Processes*, vol. 23, no. 7, pp. 858–864, 2008.
- [64] H. Shahrajabian, M. Hadi, and M. Farahnakian, "Experimental investigation of machining parameters on machinability of carbon fiber/epoxy composites," *Int. J. Eng. Innovative Technol*, vol. 2, no. 3, pp. 30–36, 2012.
- [65] E. U. Enemuoh, A. S. El-Gizawy, and A. Chukwujekwu Okafor, "An approach for development of damage-free drilling of carbon fiber reinforced thermosets," *International Journal of Machine Tools and Manufacture*, vol. 41, no. 12, pp. 1795–1814, 2001.
- [66] N. J. Pagano, "On the micromechanical failure modes in a class of ideal brittle matrix composites. Part 1. Coated-fiber composites," *Composites Part B: Engineering*, vol. 29, no. 2, pp. 93–119, 1998.
- [67] N. Pagano, "On the micromechanical failure modes in a class of ideal brittle matrix composites. Part 2. Uncoated-fiber composites," *Composites Part B: Engineering*, vol. 29, pp. 121–130, jan 1998.

-
- [68] R. Jamison, "On the Interrelationship Between Fiber Fracture and Ply Cracking in Graphite/Epoxy Laminates," in *Composite Materials: Fatigue and Fracture*, pp. 252–273, 100 Barr Harbor Drive, PO Box C700, West Conshohocken, PA 19428-2959: ASTM International, 1986.
- [69] R. Bucinell, ed., *Composite Materials: Fatigue and Fracture: 7th Volume*. 100 Barr Harbor Drive, PO Box C700, West Conshohocken, PA 19428-2959: ASTM International, jan 1998.
- [70] S. T. Pinho, L. Iannucci, and P. Robinson, "Physically based failure models and criteria for laminated fibre-reinforced composites with emphasis on fibre kinking. Part II: FE implementation," *Composites Part A: Applied Science and Manufacturing*, vol. 37, no. 5, pp. 766–777, 2006.
- [71] K. Kerrigan and G. E. O. Donnell, "On the relationship between cutting temperature and workpiece polymer degradation during CFRP edge trimming," *Procedia CIRP*, vol. 55, pp. 170–175, 2016.
- [72] C. R. Dandekar and Y. C. Shin, "Multiphase Finite Element Modeling of Machining Unidirectional Composites: Prediction of Debonding and Fiber Damage," *Journal of Manufacturing Science and Engineering*, vol. 130, no. 5, p. 051016, 2008.
- [73] G. V. G. Rao, P. Mahajan, and N. Bhatnagar, "Micro-mechanical modeling of machining of FRP composites - Cutting force analysis," *Composites Science and Technology*, vol. 67, no. 3-4, pp. 579–593, 2007.
- [74] J. Simo and T. Hughes, *Computational Inelasticity*, vol. 7 of *Interdisciplinary Applied Mathematics*. New York: Springer-Verlag, 1998.
- [75] J. R.M, *Mechanics of composite materials*. Virginia: Taylor & Francis, 2nd edition ed., 1995.
- [76] Z. Hashin and A. Rotem, "A Fatigue Failure Criterion for Fiber Reinforced Materials," *Journal of Composite Materials*, vol. 7, no. 4, pp. 448–464, 1973.
- [77] Z. Hashin, "Failure Criteria for Unidirectional FibreComposites," *Journal of Applied Mechanics*, vol. 47, no. June, pp. 329–334, 1980.
- [78] A. Puck and H. Schurmann, "Failure Analysis of Frp Laminates By Means of Physically Based Phenomenological Models *," *Composites Science and Technology*, vol. 3538, no. 96, pp. 1633–1662, 1998.
- [79] M. J. Hinton, A. S. Kaddour, and P. D. Soden, "A comparison of the predictive capabilities of current failure theories for composite laminates , judged against experimental evidence," *Composites Science and Technology*, vol. 62, pp. 1725–1797, 2002.
- [80] J. Hou, N. Petrinic, C. Ruiz, and S. Hallet, "Prediction of Impact Damage in Composite Plates," *Composites in Science and Technology*, vol. 60, no. February 1999, pp. 273–281, 2000.

- [81] V. A. Phadnis, F. Makhadmeh, A. Roy, and V. V. Silberschmidt, "Drilling in carbon / epoxy composites : Experimental investigations and finite element implementation," *Composites Part A: Applied Science and Manufacturing*, vol. 47, pp. 41–51, 2013.
- [82] N. Feito, J. Diaz-Álvarez, J. López-Puente, and M. H. Miguelez, "Numerical analysis of the influence of tool wear and special cutting geometry when drilling woven CFRPs," *Composite Structures*, vol. 138, pp. 285–294, 2016.
- [83] A. Abena, S. L. Soo, and K. Essa, "A finite element simulation for orthogonal cutting of UD-CFRP incorporating a novel fibre-matrix interface model," *15th CIRP Conference on Modelling of Machining Operations*, vol. 31, pp. 539–544, 2015.
- [84] L. Lasri, M. Nouari, and M. El Mansori, "Modelling of chip separation in machining unidirectional FRP composites by stiffness degradation concept," *Composites Science and Technology*, vol. 69, no. 5, pp. 684–692, 2009.
- [85] C. Santiuste, X. Soldani, and M. H. Miguélez, "Machining FEM model of long fiber composites for aeronautical components," *Composite Structures*, vol. 92, no. 3, pp. 691–698, 2010.
- [86] A. Kaddour and M. Hinton, "Maturity of 3D failure criteria for fibre- reinforced composites : Comparison between theories and experiments : Part B of WWFE-II," *Journal of Composite Materials*, 2013.
- [87] S. T. Pinho, C. G. Dávila, P. P. Camanho, L. Iannucci, and P. Robinson, "Failure Models and Criteria for FRP Under In-Plane or Three-Dimensional Stress States Including Shear Non-Linearity," *NASA*, 2005.
- [88] F. Cepero-Mejías, V. A. Phadnis, and J. L. Curiel-sosa, "Machining induced damage in orthogonal cutting of UD composites : FEA based assessment of Hashin and Puck criteria," *17th CIRP Conference on Modelling of Machining Operations*, vol. 82, pp. 332–337, 2019.
- [89] O. Isbilir and E. Ghassemieh, "Three-dimensional numerical modelling of drilling of carbon fiber-reinforced plastic composites," *Journal of Composite Materials*, vol. 48, no. 10, pp. 1209–1219, 2014.
- [90] O. Isbilir and E. Ghassemieh, "Numerical investigation of the effects of drill geometry on drilling induced delamination of carbon fiber reinforced composites," *Composite Structures*, vol. 105, pp. 126–133, 2013.
- [91] C. Santiuste, H. Miguélez, and X. Soldani, "Out-of-plane failure mechanisms in LFRP composite cutting," *Composite Structures*, vol. 93, no. 11, pp. 2706–2713, 2011.
- [92] C. Santiuste, J. Diaz-Alvarez, X. Soldani, and H. Miguelez, "Modelling thermal effects in machining of carbon fiber reinforced polymer composites," *Journal of Reinforced Plastics and Composites*, vol. 33, pp. 758–766, dec 2013.
- [93] I. Lapczyk and J. A. Hurtado, "Progressive damage modeling in fiber-reinforced materials," *Composites Part A: Applied Science and Manufacturing*, vol. 38, no. 11, pp. 2333–2341, 2007.

-
- [94] F. Guo-dong, L. Jun, and W. Bao-lai, “Progressive damage and nonlinear analysis of 3D four-directional braided composites under unidirectional tension,” *Composite Structures*, vol. 89, no. 1, pp. 126–133, 2009.
- [95] J. Reinoso, G. Catalanotti, A. Blázquez, P. Areias, P. P. Camanho, and F. París, “A consistent anisotropic damage model for laminated fiber-reinforced composites using the 3D-version of the Puck failure criterion,” *International Journal of Solids and Structures*, vol. 126-127, no. July, pp. 37–53, 2017.
- [96] C. S. Lopes, P. P. Camanho, Z. Gürdal, P. Maimí, and E. V. González, “Low-velocity impact damage on dispersed stacking sequence laminates. Part II: Numerical simulations,” *Composites Science and Technology*, vol. 69, no. 7-8, pp. 937–947, 2009.
- [97] J. L. C. Sosa, N. Petrinic, and J. Wiegand, “A three-dimensional progressive damage model for fibre-composite materials,” *Mechanics Research Communications*, vol. 35, pp. 219–221, 2008.
- [98] J. L. Curiel Sosa, S. Phaneendra, and J. J. Munoz, “Modelling of mixed damage on fibre reinforced composite laminates subjected to low velocity impact,” *International Journal of Damage Mechanics*, vol. 22, no. 3, pp. 356–374, 2013.
- [99] X. Soldani, C. Santiuste, A. Muñoz-Sánchez, and M. H. Miguélez, “Influence of tool geometry and numerical parameters when modeling orthogonal cutting of LFRP composites,” *Composites Part A: Applied Science and Manufacturing*, vol. 42, no. 9, pp. 1205–1216, 2011.
- [100] M. V. Hosur, J. Alexander, U. K. Vaidya, and S. Jeelani, “High strain rate compression response of carbon / epoxy laminate composites,” *Composite Structures*, vol. 52, pp. 405–417, 2001.
- [101] F. Cepero, I. G. García, J. Justo, V. Mantič, and F. París, “An experimental study of the translaminal fracture toughnesses in composites for different crack growth directions , parallel and transverse to the fiber direction,” *Composites Science and Technology*, vol. 181, no. February, p. 107679, 2019.
- [102] A. K. Salve and S. N. Jalwadi, “Implementation of Cohesive Zone in ABAQUS to Investigate Fracture Problems,” *National Conference for Engineering Post Graduates RIT*, no. November, pp. 60–66, 2016.
- [103] S. Abrate, J. F. Ferrero, and P. Navarro, “Cohesive zone models and impact damage predictions for composite structures,” *Meccanica*, no. 1, 2015.
- [104] K. Song, C. Davila, and C. Rose, “Guidelines and parameter selection for the simulation of progressive delamination,” *2008 ABAQUS User’s Conference*, pp. 1–15, 2008.
- [105] A. Turon, P. P. Camanho, J. Costa, and J. Renart, “Accurate simulation of delamination growth under mixed-mode loading using cohesive elements: Definition of interlaminar strengths and elastic stiffness,” *Composite Structures*, vol. 92, no. 8, pp. 1857–1864, 2010.

- [106] X. F. Hu, B. Y. Chen, M. Tirvaudey, V. B. Tan, and T. E. Tay, “Integrated XFEM-CE analysis of delamination migration in multi-directional composite laminates,” *Composites Part A: Applied Science and Manufacturing*, vol. 90, pp. 161–173, 2016.
- [107] A. Quintanas-corominas, J. Reinoso, E. Casoni, A. Turon, and J. A. Mayugo, “A phase field approach to simulate intralaminar and translaminar fracture in long fiber composite materials,” *Composite Structures*, vol. 220, no. January, pp. 899–911, 2019.
- [108] I. Scheider, “Cohesive model for crack propagation analyses of structures with elastic – plastic material behavior Foundations and implementation,” 2001.
- [109] N. Feito, J. López-Puente, C. Santiuste, and M. H. Miguélez, “Numerical prediction of delamination in CFRP drilling,” *Composite Structures*, vol. 108, no. 1, pp. 677–683, 2014.
- [110] D. Nayak, N. Singh, N. Bhatnagar, and P. Mahajan, “An Analysis of Machining Induced Damages in FRP Composites — A Micromechanics Finite Element Approach,” *AIP Conference Proceedings*, vol. 712, pp. 327–331, 2004.
- [111] G. Venu Gopala Rao, P. Mahajan, and N. Bhatnagar, “Machining of UD-GFRP composites chip formation mechanism,” *Composites Science and Technology*, vol. 67, no. 11-12, pp. 2271–2281, 2007.
- [112] G.-D. Wang, S. K. Melly, and S. K. Ahmed, “Finite element study into the effects of fiber orientations and stacking sequence on drilling induced delamination in CFRP/Al stack,” *Science and Engineering of Composite Materials*, vol. 0, no. 0, 2016.
- [113] C. Santiuste, A. Olmedo, X. Soldani, and H. Migue, “Delamination prediction in orthogonal machining of carbon long fiber-reinforced polymer composites,” *Journal of Reinforced Plastics and Composites*, vol. 31 (13), pp. 875–885, 2012.
- [114] N. Moes, J. Dolbow, and T. Belytschko, “A finite element method for crack growth without remeshing,” *Int. J. Numer. Meth. Engng.*, vol. 46, no. February, pp. 131–150, 1999.
- [115] G. Francfort and J. Marigo, “Revisiting brittle fracture as an energy minimization problem,” *J. Mech. Phys. Solids*, vol. 46, pp. 1319–1342, 1998.
- [116] J. Bleyer and R. Alessi, “Phase-field modeling of anisotropic brittle fracture including several damage mechanisms,” *Comput. Methods Appl. Mech. Engrg.*, vol. 336, pp. 213–236, 2018.
- [117] R. Rentsch, O. Pecat, and E. Brinksmeier, “Macro and micro process modeling of the cutting of carbon fiber reinforced plastics using FEM,” *ICM11*, vol. 10, pp. 1823–1828, 2011.
- [118] N. Bhatnagar, D. Nayak, I. Singh, H. Chouhan, and P. Mahajan, “Determination of machining-induced damage characteristics of fiber reinforced plastic composite laminates,” *Materials and Manufacturing Processes*, vol. 19, no. 6, pp. 1009–1023, 2004.

-
- [119] D. Arola and M. Ramulu, “Orthogonal cutting of fiber-reinforced composites: a finite element analysis,” *Int. J. Mech. Sci.*, vol. 39, no. 5, pp. 597–613, 1997.
- [120] S. Zenia, L. Ben Ayed, M. Nouari, and A. Delamézière, “Numerical analysis of the interaction between the cutting forces, induced cutting damage, and machining parameters of CFRP composites,” *International Journal of Advanced Manufacturing Technology*, vol. 78, no. 1-4, pp. 465–480, 2015.
- [121] S. Zhang and J. S. Strenkowski, “An Eulerian Orthogonal Cutting Model for Unidirectional Fiber-Reinforced Polymers,” *Journal of Manufacturing Science and Engineering*, vol. 140, pp. 1–8, 2018.
- [122] J. Xu, M. El Mansori, and J. Voisin, “Numerical Modeling and FE Analysis of CFRP/Ti Stack Orthogonal Cutting,” *7th HPC 2016 – CIRP Conference on High Performance Cutting*, vol. 46, pp. 67–70, 2016.
- [123] J. Xu and M. El Mansori, “Numerical modeling of stacked composite CFRP/Ti machining under different cutting sequence strategies,” *International Journal of Precision Engineering and Manufacturing*, vol. 17, no. 1, pp. 99–107, 2016.
- [124] M. Benhassine, E. Rivière-lorphèvre, P.-j. Arrazola, P. Gobin, and D. Dumas, “2D simulations of orthogonal cutting of CFRP: Effect of tool angles on parameters of cut and chip morphology,” *AIP Conference Proceedings*, vol. 070005, pp. 1–6, 2018.
- [125] F. P. Van der Meer and L. J. Sluys, “Continuum models for the analysis of progressive failure in composite laminates,” *Journal of Composite Materials*, vol. 43, no. 20, pp. 2131–2156, 2009.
- [126] L. Li, W. Liu, and R. Wang, “Study on Damage Evaluation and Machinability of UD-CFRP for the Orthogonal Cutting Operation Element Method,” *Materials*, vol. 10, pp. 204–224, 2017.
- [127] A. Abena, S. L. Soo, and K. Essa, “Modelling the orthogonal cutting of UD-CFRP composites: Development of a novel cohesive zone model,” *Composite Structures*, vol. 168, pp. 65–83, 2017.
- [128] K. A. Calzada, S. G. Kapoor, R. E. Devor, J. Samuel, and A. K. Srivastava, “Modeling and interpretation of fiber orientation-based failure mechanisms in machining of carbon fiber-reinforced polymer composites,” *Journal of Manufacturing Processes*, vol. 14, no. 2, pp. 141–149, 2012.
- [129] J. Marigo, “Modelling of brittle and fatigue damage for elastic material by growth of microvoids,” *Engineering Fracture Mechanics*, vol. 21, pp. 861–874, 1985.
- [130] V. Tvergaard, “Effect of Fibre Debonding in a Whisker-reinforced Metal,” *Materials Science and Engineering*, vol. 125, pp. 861–874, 1990.
- [131] N. Feito, J. Díaz-Álvarez, J. López Puente, and M. Miguelez, “Effect of cutter geometry on machining induced damage in orthogonal cutting of ud polymer composites : Fe study,” *Composite Structures*, vol. 184, pp. 1147–1155.
- [132] Z. P. Bažant and B. H. Oh, “Crack band theory for fracture of concrete,” *Matériaux et Constructions*, vol. 16, pp. 155–177, may 1983.

- [133] F. Paris Carballo, J. Cañas, and J. Marín, *Introducción al análisis y diseño con materiales compuestos*. Sevilla: Universidad de Sevilla, Escuela Técnica Superior de Ingenieros, 2008.
- [134] ASTM D3039/D3039M17, *Standard Test Method for Tensile Properties of Polymer Matrix Composite Materials*. 2017.
- [135] ASTM D3410/D3410M16, *Standard Test Method for Compressive Properties of Polymer Matrix Composite Materials with Unsupported Gage Section by Shear Loading*. 2016.
- [136] ASTM D3518/D3518M-94, *Standard Test Method for In-Plane Shear Response of Polymer Matrix Composite Materials by Tensile Test of a 45° Laminate*. 1994.
- [137] P. P. Camanho, P. Maimí, and C. G. Dávila, “Prediction of size effects in notched laminates using continuum damage mechanics,” *Composites Science and Technology*, vol. 67, no. 13, pp. 2715–2727, 2007.
- [138] F. Stojcevski, T. Hilditch, and L. C. Henderson, “A modern account of Iosipescu testing,” *Composites Part A: Applied Science and Manufacturing*, vol. 107, pp. 545–554, apr 2018.
- [139] G. Odegard and M. Kumosa, “Determination of shear strength of unidirectional composite materials with the Iosipescu and 10 off-axis shear tests,” *Composites Science and Technology*, vol. 60, pp. 2917–2943, dec 2000.
- [140] D5379/D5379M-19, “ASTM D5379 Standard Test Method for Shear Properties of Composite Materials by the V-Notched,” *Annual Book of ASTM Standards*, vol. i, no. March, pp. 1–13, 2005.
- [141] A. Koplev, A. Lystrup, and T. Vorm, “The cutting process, chips, and cutting forces in machining CFRP,” *Composites*, vol. 14, no. 4, pp. 371–376, 1983.
- [142] C. Zhang, E. A. Duodu, and J. Gu, “Finite element modeling of damage development in cross-ply composite laminates subjected to low velocity impact,” *Composite Structures*, vol. 173, no. 9, pp. 219–227, 2017.
- [143] D. H. Wang, M. Ramulu, and D. Arola, “Orthogonal cutting mechanisms of graphite/epoxy composite. Part I: unidirectional laminate,” *International Journal of Machine Tools and Manufacture*, vol. 35, no. 12, pp. 1623–1638, 1995.
- [144] H. Li, X. Qin, G. He, Y. Jin, D. Sun, and M. Price, “Investigation of chip formation and fracture toughness in orthogonal cutting of UD-CFRP,” *The International Journal of Advanced Manufacturing Technology*, vol. 82, pp. 1079–1088, feb 2016.
- [145] D. Iliescu, D. Gehin, I. Iordanoff, F. Girot, and M. E. Gutiérrez, “A discrete element method for the simulation of CFRP cutting,” *Composites Science and Technology*, vol. 70, no. 1, pp. 73–80, 2010.
- [146] A. Mondelin, B. Furet, and J. Rech, “Characterisation of friction properties between a laminated carbon fibres reinforced polymer and a monocrystalline diamond under dry or lubricated conditions,” *Tribology International*, vol. 43, no. 9, pp. 1665–1673, 2010.

- [147] G. Chardon, O. Klinkova, J. Rech, S. Drapier, and J. M. Bergheau, "Characterization of friction properties at the work material/cutting tool interface during the machining of randomly structured carbon fibers reinforced polymer with Poly Crystalline Diamond tool under dry conditions," *Tribology International*, vol. 81, pp. 300–308, 2015.
- [148] X. Jin and Y. Altintas, "Prediction of micro-milling forces with finite element method," *Journal of Materials Processing Technology*, vol. 212, no. 3, pp. 542–552, 2012.
- [149] M. N. Nasr and M. M. Ammar, "An Evaluation of Different Damage Models when Simulating the Cutting Process Using FEM," *Procedia CIRP*, vol. 58, pp. 134–139, 2017.
- [150] S. Wojciechowski, M. Matuszak, B. Powalka, M. Madajewski, R. W. Maruda, and G. M. Królczyk, "Prediction of cutting forces during micro end milling considering chip thickness accumulation," *International Journal of Machine Tools and Manufacture*, vol. 147, no. 2019, 2019.
- [151] Y. Gao, J. H. Ko, and H. P. Lee, "3D coupled Eulerian-Lagrangian finite element analysis of end milling," *International Journal of Advanced Manufacturing Technology*, vol. 98, no. 1-4, pp. 849–857, 2018.
- [152] S. Ghafarizadeh, J.-F. Chatelain, and G. Lebrun, "Finite element analysis of surface milling of carbon fiber-reinforced composites," *The International Journal of Advanced Manufacturing Technology*, vol. 87, pp. 399–409, oct 2016.
- [153] C. Wang, L. Wen, W. Ming, Q. An, and M. Chen, "Experimental study on effects of fiber cutting angle in milling of high-strength unidirectional carbon fiber-reinforced polymer laminates," *Proceedings of the Institution of Mechanical Engineers, Part B: Journal of Engineering Manufacture*, vol. 232, no. 10, pp. 1813–1824, 2018.
- [154] N. Duboust, M. Watson, M. Marshall, G. E. O'Donnell, and K. Kerrigan, "Towards intelligent CFRP composite machining: Surface analysis methods and statistical data analysis of machined fibre laminate surfaces," *Proceedings of the Institution of Mechanical Engineers, Part B: Journal of Engineering Manufacture*, 2020.
- [155] R. M. Saoubi, D. Axinte, S. Leung, C. Nobel, H. Attia, G. Kappmeyer, S. Engin, and W.-m. Sim, "Manufacturing Technology High performance cutting of advanced aerospace alloys and composite materials," *CIRP Annals - Manufacturing Technology*, vol. 64, no. 2, pp. 557–580, 2015.
- [156] N. Duboust, C. Pinna, H. Ghadbeigi, S. Ayvar-Soberanis, V. A. Phadnis, A. Collis, and K. Kerrigan, "2D and 3D Finite Element Models for the Edge Trimming of CFRP," *16th CIRP Conference on Modelling of Machining Operations*, vol. 58, pp. 233–238, 2017.

Appendices

Appendix A

Scientific publications

A.1 Conference papers

A.1.1 Paper 1

Title: *Análisis numérico de la formación de la viruta en operaciones de mecanizado de fibra de carbono*

Conference: *Congreso Español de la Fractura 2019.*

Year of publication: *2019*

Abstract

Finite element (FE) method offers an exceptional low cost alternative for the study of important cutting parameters in the machining of composites. This paper deals with a study of the chip formation in orthogonal cutting operations in unidirectional (UD) carbon fibre laminates using 2D FE models. For this purpose, different UD carbon fibre laminates with fibre orientations between 0° and 135° with respect to the cutting direction are assessed. Damage initiation is determined using the maximum stress criterion for the fibre, while to predict matrix failure Puck criterion is employed. After damage condition for the fibre or matrix is reached, a linear strain-based softening is applied the mechanical properties of the element damaged until its total degradation and fracture. It is observed that the fracture of the material occurs in the fibre / matrix interface for laminates between 15° - 75° , while for laminates with negative fibre orientation 105° - 135° , it propagates in a direction perpendicular to the fibre. For fibre orientation of 0° , a clean cut surface with a large chip length is obtained. Finally, 90° carbon fibre laminates produce small chips with a large amount of machining induced damage.

ANÁLISIS NUMÉRICO DE LA FORMACIÓN DE LA VIRUTA EN OPERACIONES DE MECANIZADO DE FIBRA DE CARBONO

F. Cepero-Mejías^{1,2,3*}, J.L. Curiel-Sosa^{2,3}, V.A. Phadnis⁴

¹ Industrial Doctorate Centre in Machining Science, The University of Sheffield, S1 3JD, UK.

² Computer-Aided Aerospace & Mechanical Engineering (CA2M) Research Group, S1 3JD, UK

³ Department of Mechanical Engineering, The University of Sheffield, S1 3JD, UK.

⁴ AMRC with Boeing, Advanced Manufacturing Park, S605TZ, UK.

* Persona de contacto: fmcepero1@sheffield.ac.uk

RESUMEN

El método de los elementos finitos (EF) ofrece una excepcional alternativa de bajo coste para el estudio de parámetros de corte importantes en el mecanizado de composites. Este trabajo aborda un estudio de la formación de la viruta proveniente de las operaciones de corte ortogonal en laminados unidireccionales de fibra de carbono usando modelos de EF 2D. Con este propósito, diferentes laminados unidireccionales de fibra de carbono con orientaciones de fibra entre 0° y 135° con respecto a la dirección de corte son evaluados. La iniciación del daño es determinada por el criterio de Hashin en el caso de las fibras, mientras el criterio de Puck es usado para predecir el fallo en la matriz. Una vez la condición de daño para la fibra o matriz es alcanzada, las propiedades mecánicas del elemento dañado son reducidas linealmente con el incremento de la deformación hasta su total degradación y fractura. Se observa que la fractura del material se produce en la interface fibra/matriz para laminados entre 15°-75°, mientras que para laminados con orientación de fibra negativa 105°-135° grados se propaga en dirección perpendicular a la fibra. Para fibras con 0° un corte claro del laminado con una gran longitud de viruta es apreciado. Finalmente, las fibras de 90° producen virutas pequeñas con una gran magnitud de daño inducido por el mecanizado.

PALABRAS CLAVE: Mecanizado, Composite, Corte ortogonal, Elementos finitos, Fibra de carbono

ABSTRACT

Finite element (FE) method offers an exceptional low cost alternative for the study of important cutting parameters in the machining of composites. This paper deals with a study of the chip formation in orthogonal cutting operations in unidirectional (UD) carbon fibre laminates using 2D FE models. For this purpose, different UD carbon fibre laminates with fibre orientations between 0° and 135° with respect to the cutting direction are assessed. Damage initiation is determined using the maximum stress criterion for the fibre, while to predict matrix failure Puck criterion is employed. After damage condition for the fibre or matrix is reached, a linear strain-based softening is applied to the mechanical properties of the element damaged until its total degradation and fracture. It is observed that the fracture of the material occurs in the fibre / matrix interface for laminates between 15°-75°, while for laminates with negative fibre orientation 105°-135°, it propagates in a direction perpendicular to the fibre. For fibre orientation of 0°, a clean cut surface with a large chip length is obtained. Finally, 90° carbon fibre laminates produce small chips with a large amount of machining induced damage.

KEYWORDS: Machining, Composite, Orthogonal cutting, Finite element, Carbon fibre

INTRODUCCIÓN

En estos últimos años, el uso de materiales compuestos de fibra de carbono (MCFC) se ha visto incrementado notablemente en diversas aplicaciones industriales, debido a su excelente compromiso peso-resistencia. Esta tendencia está especialmente aplicada en el sector aeronáutico, donde por ejemplo, el fuselaje del modelo Boeing 787 ha sido fabricado con un porcentaje en peso superior al 50%, eliminando 1500 láminas de aluminio

y entre 40000-50000 remaches, consiguiendo un importante ahorro de peso y de consumo de combustible [1].

A pesar de que las piezas de materiales compuestos son fabricadas con dimensiones similares a las de uso, las estrictas tolerancias dimensionales y de ensamblaje demandadas frecuentemente hace imprescindible la utilización de operaciones de mecanizado. Sin embargo, los compuestos de fibra de carbono no son materiales

fácilmente mecanizables. Este hecho se debe principalmente al alto grado de desgaste que sufre la herramienta a consecuencia de la fricción con las fibras y la alta concentración de calor que se da en la herramienta debido a la baja conductividad térmica normalmente encontradas en la resina del composite. Las herramientas desgastadas excesivamente empujan las fibras, extendiendo de forma remarcable el daño en el interior del laminado, en vez de cortarlas limpiamente por cizalladura.

Además, la no correcta elección de los parámetros de corte, puede traer consigo la aparición de importantes daños en el composite que afectan frontalmente a la integridad física y a calidad superficial del laminado. Algunos de los daños más usuales en composites son la delaminación, el despegue fibra-matriz, y la rotura de la matriz [2]–[4].

Por lo tanto, es preciso un minucioso estudio de cómo afectan todas las variables de corte a la estructura del laminado. Sin embargo, el alto coste de los composites y herramientas usados en la industria, junto a la complejidad de realizar el alto número de pruebas requeridas, hacen que abordar este proceso de forma experimental sea muy caro y laborioso. Por tanto el uso de otras vías debe ser seriamente considerado para el correcto desarrollo de este cometido. El método de los elementos finitos ofrece una alternativa muy efectiva en términos de coste y tiempo para recrear este tipo de experimentos fielmente. Varios trabajos han analizado las respuestas del laminado a distintos parámetros del corte ortogonal usando modelos de elementos finitos.

Santiuste et al. [5] concluyeron que al mecanizar laminados de fibra de carbono experimentaba una fractura frágil con un daño inducido bajo, mientras que los laminados de fibra de vidrio muestra un comportamiento más dúctil con un daño mayor en la superficie inferior. El efecto de la orientación de la fibra, el ángulo de ataque y la profundidad de corte sobre la propagación del daño interno y las fuerzas de corte fue investigado por Zenia et al. [6]. El estudio de la FE concluyó que las elevadas orientaciones de la fibra y la alta profundidad de corte aumentan el daño inducido por el mecanizado y las fuerzas de corte, mientras que el incremento del ángulo de ataque reduce estas respuestas. Recientemente, Cepero-Mejias et al. [7] desarrollo un novedoso análisis de la influencia de distintos parámetros de corte (ángulo de alivio, ángulo de ataque, radio de herramienta, orientación de fibra...) en daño inducido en el mecanizado. Interesantes conclusiones fueron extraídas de este trabajo, como la considerable reducción del daño con grandes ángulos de alivio o el mecanizado de láminas con orientaciones de fibra de 15° o 30°. Esto ayudó a comprender mejor la selección de parámetros de corte apropiados para laminados compuestos unidireccionales de fibras de vidrio y carbono.

Sin embargo, en conocimiento de los autores no existe en la literatura ningún trabajo que simule la formación de la viruta en composites, característica primordial tanto para entender el mecanismo interno de fractura del laminado y para analizar la calidad superficial de los laminados. Por lo tanto, la introducción de esta clase de estudios se hace muy necesaria para ampliar esta inexplorada rama del conocimiento.

Este trabajo contiene un estudio numérico de la formación de la viruta en laminados unidireccionales de fibra de carbono con distintas orientaciones de fibra comprendidas entre 0° y 135°. La fractura del laminado se modela con el uso de una subrutina VUMAT, la cual implementa un novedoso algoritmo de daño en el mecanizado de composites. En las siguientes secciones, los parámetros más importantes del modelo de elementos finitos y modelo de daño empleado son convenientemente descritos. Posteriormente, es realizado el análisis de los resultados de las distintas fracturas de laminados obtenidas en este trabajo, para terminar remarcando las conclusiones más importantes que se pueden extraer de este artículo.

CARACTERÍSTICAS PRINCIPALES DEL MODELO DE ELEMENTOS FINITOS

Todas las simulaciones llevadas a cabo en este trabajo, se han desarrollado en modelos de elementos finitos de tensión plana 2D con el software numérico Abaqus/Explicit. Las propiedades mecánicas y de resistencia del laminado de fibra carbono simulado se están convenientemente recogidas en la Tablas 1 y 2, respectivamente.

A modo ilustrativo, los parámetros de corte que juegan un papel importante en las operaciones de corte ortogonal están esquematizados en la figura 1, así como los valores específicos empleados en las simulaciones están recopilados en la Tabla 3.

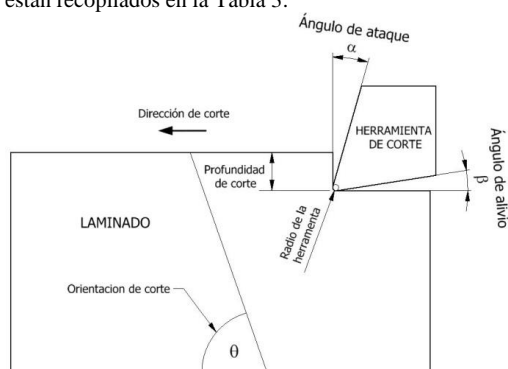


Figura 1. Parámetros de corte considerados en operaciones de corte ortogonal.

Debido a las altas exigencias computacionales el modelo numérico empleados consta de unas reducidas dimensiones de 2 mm de largo y 1 mm de alto. El

desplazamiento del lado inferior del laminado está completamente prohibido, mientras que en los lados laterales solo el desplazamiento horizontal no está permitido.

Tabla 1.- Propiedades mecánicas empleadas

Material	$E_{11}(\text{GPa})$	$E_{22}(\text{GPa})$	$G_{12}(\text{GPa})$	ν_{12}
MCFC	127	9.1	5.6	0.31

Tabla 2.- Propiedades de fallo utilizadas

MCFC	X_T	X_C	Y_T	Y_C	S
(MPa)	2720	1690	111	214	115

Tabla 3.- Parámetros de mecanizado empleados

Parámetros	Valores
Ángulo de ataque	15°
Ángulo de alivio	10°
Radio de la herramienta	30 μm
Profundidad de corte	200 μm
Velocidad de corte	100 mm/s
Orientación de fibra	0-135°

Con el objetivo de reproducir fielmente la fractura de la viruta de composite proveniente de operaciones de corte ortogonal, se modela una fina malla en la zona superior de con un tamaño de elemento de 5 μm. Debajo de esta capas superior, una malla más basta en las capas inferiores del laminado para reducir el coste computacional es utilizada, como se muestra en la figura 2.



Figura 2. Malla empleada en este trabajo.

La herramienta es tratada como un sólido rígido para para reducir el coste computacional para todas las orientaciones de fibra estudiadas exceptuando la orientación de 0°. Esta hipótesis es aceptable debido a la alta rigidez de las piezas de corte industriales (400-600 GPa). En el caso de los laminados de 0° se modela la herramienta como un material isotrópico con una rigidez de 400 GPa para relajar la rigidez de contacto herramienta-laminado y mejorar la calidad de las simulaciones. Para modelar la fricción entre la herramienta y el laminado un coeficiente de Coulomb de 0.5 es empleado.

MODELO DE DAÑO Y FRACTURA

El uso de una subrutina VUMAT es empleado con el objetivo de introducir todas las variables de degradación de propiedades y fractura necesarias para llevar a cabo este análisis. Cuatro tipos de daño son implementados en la matriz de rigidez siguiendo la misma metodología usada por Lapczyk and Hurtado [8]. Estos daños de los componentes del composite se identifican como:

- Daño por fibra a tracción (d_f)
- Daño por fibra a compresión (d_{fc})
- Daño por matriz a tracción (d_{mt})
- Daño por matriz a compresión (d_{mc})

Todas estas variables de daños se mantienen con un valor de cero (material no dañado) en cada elemento mientras las condiciones de inicio de daño no tengan lugar. Para determinar estas condiciones se implementan unas funciones de activación de daño (F_i con $i=ft, fc, mt$ y mc) que inicializan el daño cuando el criterio de fallo propuesto por Hashin [9] (véase expresiones (1) y (2)) es alcanzado en el caso de la fibra y el criterio de Puck [10] en el caso de la matrix. Como se puede apreciar en las expresiones (3-5) el criterio de Puck tiene asociados tres tipos de fallos (Modo A, Modo B y Modo C) en vez de los dos daños estudiados en este trabajo. El daño a tracción es asociado al Modo A, mientras que el daño a compresión es activado cuando se cumple cualquiera de los criterios de fallo englobados en el Modo B y el Modo C. Por motivos de ahorro de espacio, las variables mostradas en los criterios de fallo de Puck no serán explicadas en este documento, los lectores interesados en conocerlas en detalle están invitados a leer la referencia [10].

Fibra a tracción ($\sigma_{11} \geq 0$)

$$F_{ft} = \left(\frac{\sigma_{11}}{X_T}\right)^2 + \alpha \left(\frac{\sigma_{12}}{S}\right)^2 \geq 1 \tag{1}$$

Fibra a compresión ($\sigma_{11} < 0$)

$$F_{fc} = \left(\frac{\sigma_{11}}{X_C}\right)^2 \geq 1 \tag{2}$$

Matriz Mode A ($\sigma_{22} \geq 0$)

$$F_{mma} = \sqrt{\left(\frac{\sigma_{12}}{R_{11}^A}\right)^2 + \left(1 - \frac{p_{11}^{(+)} R_{11}^{(+)} A}{R_{11}^{(+)} A}\right)^2 \left(\frac{\sigma_{22}}{R_{11}^{(+)} A}\right)^2} + \frac{p_{11}^{(+)} \sigma_{22}}{R_{11}^A} \geq 1 \tag{3}$$

Matriz Mode B ($\sigma_{22} < 0$ y $\sigma_{22} > -R_{11}^A$)

$$F_{mmb} = \sqrt{\left(\frac{\sigma_{12}}{R_{11}^A}\right)^2 + \left(\frac{p}{R}\right)^2 \sigma_{22}^2 + \left(\frac{p}{R}\right) \sigma_{22}} \geq 1 \tag{4}$$

Matriz Mode C ($\sigma_{22} < -R_{11}^A$)

$$F_{mmc} = \frac{1}{2\left[1 + \left(\frac{p}{R}\right) \frac{R_{11}^A}{R_{11}^A}\right]} \left[\left(\frac{\sigma_{12}}{R_{11}^A}\right)^2 + \left(\frac{\sigma_{22}}{R_{11}^A}\right)^2 \right] \frac{R_{11}^A}{-\sigma_{22}} \geq 1 \tag{5}$$

Cuando uno de los daños es iniciado, un progresivo incremento lineal entre un desplazamiento equivalente

inicial ($\delta_{I,eq}^0$) y el desplazamiento equivalente final ($\delta_{I,eq}^f$) es aplicado como se puede leer en la expresión (7).

$$d_I = \frac{\delta_{I,eq}^f(\delta_{I,eq} - \delta_{I,eq}^0)}{\delta_{I,eq}(\delta_{I,eq}^f - \delta_{I,eq}^0)} \quad (6)$$

La variable d_I se calcula como el desplazamiento inicial cuando una condición de fallo es alcanzada, mientras la variable $\delta_{I,eq}$ se calcula teniendo en cuenta la energía crítica de fractura (G_f^c) asociada a ese modo de daño, como se puede apreciar en la expresión (7).

$$\delta_{I,eq}^f = \frac{2G_f^c F_I}{\sigma_{I,eq}} \quad ; \quad \delta_{I,eq}^0 = \frac{\delta_{I,eq}}{F_I} \quad (7)$$

Los valores de energía de fractura crítica considerados en este trabajo están recogidos en la tabla 4. Los valores de daño máximos permitidos son para la matriz y la fibra son de 0.95. Estos valores máximos se aplican para evitar los problemas de distorsión de elementos así como para simular la resistencia remanente que las láminas totalmente fracturadas aportan al conjunto del laminado [11]. Finalmente para producir la fractura la eliminación de los elementos que superan una deformación cortante (ϵ_{12}) superior a 0.5 es aplicada para obtener los resultados discutidos en la siguiente sección.

Tabla 4.- Valores de la energía de fractura crítica empleados

G_f^c	G_{ft}^c	G_{fc}^c	G_{mt}^c	G_{mc}^c
N/mm	10	10	1	1

DISCUSIÓN DE LOS RESULTADOS

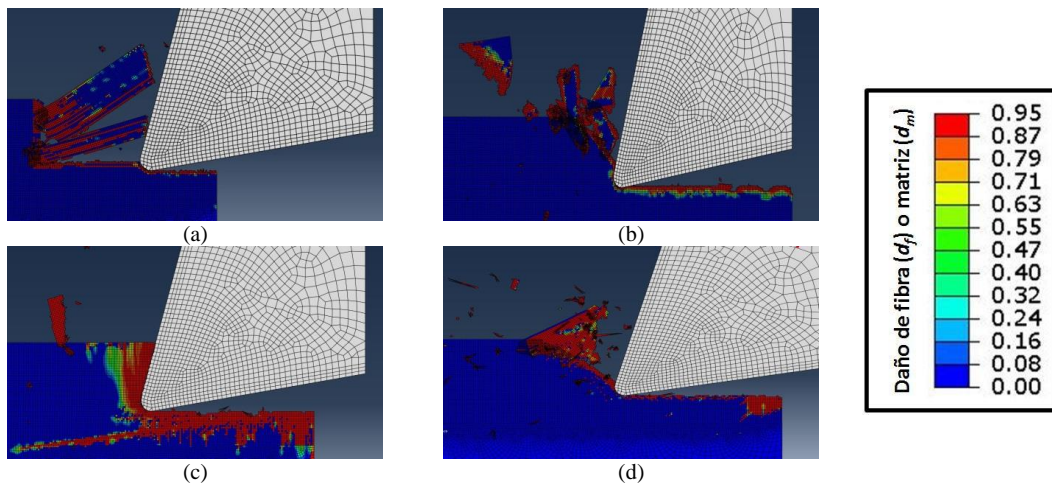


Figura 3.- Ilustraciones de los distintos tipos de viruta formados estudiados en este trabajo con sus respectivos daños de fibra (d_f) o matriz (d_m): $0^\circ(d_m)$, $45^\circ(d_m)$, $90^\circ(d_m)$ y $135^\circ(d_f)$

En este trabajo, la formación de virutas laminadas de fibra de carbono con una orientación de fibra entre 0 y 135 con intervalos de 15 es estudiada. En términos generales cuatro tipos de fractura son observados, los cuales se enumeran y explican en más detalle a continuación.

- Rotura en la interface matriz/fibra en laminados.

Para orientaciones de fibra entre 15° y 75° reduciéndose sustancialmente la longitud de la viruta formada. Este mecanismo de fractura se produce por las fuertes deformaciones cortantes que se producen en la matriz en dirección paralela a la fibra y se aprecia claramente en la figura 1 (b).

- Formación de la viruta perpendicular a la dirección de fibra.

En el caso de los laminados con orientaciones de fibra entre 105° y 135° la formación de una viruta de tamaño pequeño es observada. La fractura se produce perpendicular a las fibras debido al fuerte esfuerzo cortante que se aprecia en ellas. Esta tendencia se puede observar en la figura 1 (d).

- Corte limpio con formación de viruta larga

La viruta obtenida en los laminados con orientación de fibra de 0° grados es bastante larga como es ilustrado en la figura 1 (a). Se aprecian dos procesos claramente separados en su formación: (1) fractura horizontal de la matriz a la altura de la punta de la herramienta y (2) corte perpendicular debido al fuerte cortante que sufre la fibra después del despegue de la viruta en las capas inferiores.

- Formación de pequeña viruta con gran propagación de daño interno

Finalmente, para orientaciones de fibra de 90° la viruta formada es de un tamaño pequeño produciéndose la fractura paralela a la dirección de la fibra como es apreciada en la figura 1 (c). Finalmente, es apreciado un mayor daño inducido por el mecanizado que para otras orientaciones debido a que el empuje que ejerce la herramienta sobre las fibras provoca un gran efecto de despegue matriz-fibra en este particular caso.

CONCLUSIONES

Este artículo desarrolla la implementación de un modelo de elementos finitos para modelar operaciones de corte ortogonal en laminados de fibra de carbono. El interés de este trabajo se centra en el análisis de los mecanismos de formación de viruta que se desarrollan para laminados con distintas orientaciones de fibra, estudiando los laminados con fibras en un rango entre 0° y 135°.

Se prueba la eficacia del algoritmo de daño empleado, que combina el uso de los criterios de fallo de Hashin y Puck con una degradación lineal de las propiedades basadas en criterios energéticos, para simular este tipo de problema. Cuatro distintos tipos de viruta son observados, los cuales se especifican a continuación.

- Rotura en la interface matriz/fibra en laminados. (15-75°)
- Formación de la viruta perpendicular a la dirección de fibra. (105-135°)
- Corte limpio con formación de viruta larga. (0°)
- Formación de pequeña viruta con gran propagación de daño interno. (90°)

Este modelo será empleado en el futuro para obtener información útil en la selección de los parámetros de corte apropiados para mitigar el daño inducido por el mecanizado en materiales compuestos.

AGRADECIMIENTOS

Los autores desean agradecer a las instituciones del IDC (Industrial Doctoral Centre) de Sheffield y el EPSRC (Engineering and Physical Sciences Research Council) por hacer posible este trabajo financiando el doctorado del primer autor con la beca EP/L016257/1.

REFERENCIAS

[1] Boeing, "Boeing 787 Dreamliner," 2018. [Online].

Available: <https://aviationbenefits.org/case-studies/boeing-787-dreamliner/>. [Accessed: 07-Dec-2018].

- [2] J. L. Curiel-sosa, B. Tafazzolimoghaddam, and C. Zhang, "Modelling fracture and delamination in composite laminates: Energy release rate and interface stress," *Compos. Struct.*, vol. 189, no. January, pp. 641–647, 2018.
- [3] N. A. Abdullah, J. L. Curiel-Sosa, Z. A. Taylor, B. Tafazzolimoghaddam, J. L. Martinez Vicente, and C. Zhang, "Transversal crack and delamination of laminates using XFEM," *Compos. Struct.*, vol. 173, pp. 78–85, 2017.
- [4] C. Zhang, J. L. Curiel-sosa, and T. Quoc, "Meso-scale progressive damage modeling and life prediction of 3D braided composites under fatigue tension loading," *Compos. Struct.*, vol. 201, no. June, pp. 62–71, 2018.
- [5] C. Santiuste, X. Soldani, and M. H. Miguélez, "Machining FEM model of long fiber composites for aeronautical components," *Compos. Struct.*, vol. 92, no. 3, pp. 691–698, 2010.
- [6] S. Zenia, L. Ben Ayed, M. Nouari, and A. Delamézière, "Numerical analysis of the interaction between the cutting forces, induced cutting damage, and machining parameters of CFRP composites," *Int. J. Adv. Manuf. Technol.*, vol. 78, no. 1–4, pp. 465–480, 2015.
- [7] F. Cepero-mejías, J. L. Curiel-sosa, C. Zhang, and V. A. Phadnis, "Effect of cutter geometry on machining induced damage in orthogonal cutting of UD polymer composites: FE study," *Compos. Struct.*, vol. 214, no. February, pp. 439–450, 2019.
- [8] I. Lapczyk and J. A. Hurtado, "Progressive damage modeling in fiber-reinforced materials," *Compos. Part A Appl. Sci. Manuf.*, vol. 38, no. 11, pp. 2333–2341, 2007.
- [9] Z. Hashin, "Failure Criteria for Unidirectional FibreComposites," *J. Appl. Mech.*, vol. 47, no. June, pp. 329–334, 1980.
- [10] A. Puck and H. Schurmann, "Failure Analysis of Frp Laminates By Means of Physically Based Phenomenological Models *," *Compos. Sci. Technol.*, vol. 3538, no. 96, pp. 1633–1662, 1998.
- [11] F. Paris Carballo, *Introducción al análisis y diseño con materiales compuestos*. Sevilla: Universidad de Sevilla, Escuela Técnica Superior de Ingenieros, 2008.

A.1.2 Paper 2

Title: *Comparación experimental de la tenacidad a fractura intralaminar en materiales compuestos para crecimiento de grietas en diferentes direcciones en el plano*

Conference: *Congreso Español de la Fractura 2019.*

Year of publication: *2019*

Abstract

In this work, the intralaminar fracture toughness of a crack growing parallel and perpendicular to the fibers in a unidirectional composite laminate is compared experimentally. The test carried out consists of a three-point bending test (TPB) in which a pre-crack has been made to the specimens on the tension side. The results show that the intralaminar fracture toughness is greater when the crack grows parallel to the direction of the fiber than when it grows perpendicular.

COMPARACIÓN EXPERIMENTAL DE LA TENACIDAD A FRACTURA INTRALAMINAR EN MATERIALES COMPUESTOS PARA CRECIMIENTO DE GRIETAS EN DIFERENTES DIRECCIONES EN EL PLANO

F. Cepero^{1,2,3,4}, I. García¹, J. Justo^{1*}, V. Mantić¹, F. París¹

¹ Grupo de Elasticidad y Resistencia de Materiales.
Escuela Técnica Superior de Ingeniería. Universidad de Sevilla.
Camino de los Descubrimientos s/n, 41092. Sevilla-España.

²Industrial Doctorate Centre in Machining Science, The University of Sheffield.
Sir Frederick Mappin Building Mappin Street, S1 3JD Sheffield, United Kingdom.

³Computer-Aided Aerospace \& Mechanical Engineering (CA2M) Research Group.
Sir Frederick Mappin Building Mappin Street, S1 3JD Sheffield, United Kingdom.

⁴Department of Mechanical Engineering, The University of Sheffield.
Sir Frederick Mappin Building Mappin Street, S1 3JD Sheffield, United Kingdom.

*Persona de contacto: jjusto@us.es

RESUMEN

En este trabajo se compara experimentalmente la tenacidad a la fractura intralaminar de una grieta que crece a lo largo de las direcciones paralela y perpendicular a las fibras en un laminado unidireccional de material compuesto reforzado con fibras largas. El ensayo realizado consiste en un ensayo de flexión en tres puntos (TPB) al que se ha realizado una pre-grieta a las probetas en la cara de tracción. Los resultados muestran que la tenacidad a la fractura intralaminar es mayor cuando la grieta crece paralelamente a la dirección de la fibra que cuando crece perpendicular.

PALABRAS CLAVE: Materiales compuestos, tenacidad a fractura, ensayos

ABSTRACT

In this work, the intralaminar fracture toughness of a crack growing parallel and perpendicular to the fibers in a unidirectional composite laminate is compared experimentally. The test carried out consists of a three-point bending test (TPB) in which a pre-crack has been made to the specimens on the tension side. The results show that the intralaminar fracture toughness is greater when the crack grows parallel to the direction of the fiber than when it grows perpendicular.

KEYWORDS: Composites, fracture toughness, testing

1. INTRODUCCIÓN

El uso extensivo de los materiales compuestos en estructuras primarias ha conllevado la necesidad de un conocimiento profundo de sus propiedades. Dentro de las mismas, tiene gran importancia la tenacidad a fractura intralaminar, debido a la cada vez más habitual aparición de cargas fuera del plano en este tipo de piezas y a su influencia en los mecanismos de fallo asociados a estas cargas. Generalmente, se habla de tenacidad a fractura interlaminar, refiriéndose a la propagación de las grietas entre capas. Sin embargo, la grieta se puede propagar en otras direcciones [1], siendo habitual el caso de propagación intralaminar, pudiendo darse ésta en la dirección paralela a las fibras, que aquí denotaremos por G_{1cL} (ver figura 1), o en la dirección perpendicular a las fibras, aquí denotado por G_{1cT} (ver figura 2).

Dado que únicamente hay normativa relativa a la determinación de la tenacidad a fractura interlaminar (como por ejemplo la ISO 15024 [2] o la AITM 1-0053 [3]), la comunidad científica, habitualmente, asume iguales los valores de la tenacidad para ambos casos de propagación intralaminar, igualándolos al valor de la tenacidad a fractura interlaminar, medida mediante el ensayo de doble viga en voladizo (DCB). Obviamente, el hecho de que estos valores puedan ser diferentes afectaría en gran medida a la predicción del comportamiento de piezas de material compuesto. Este hecho manifiesta la necesidad de una caracterización en profundidad de ambos valores.

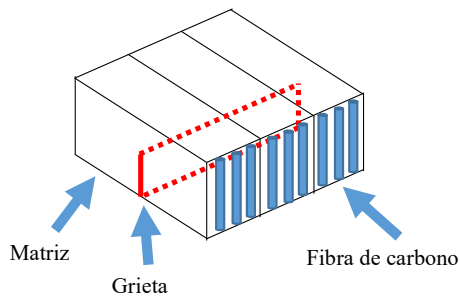


Figura 1. Esquema de la disposición del laminado en la que la grieta crece de forma intralaminar paralela a las fibras.

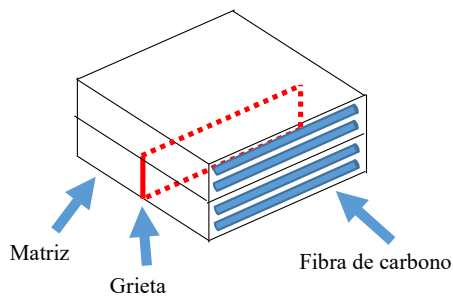


Figura 2. Esquema de la disposición del laminado en la que la grieta crece de forma intralaminar perpendicular a las fibras.

En este trabajo se pretende poner de manifiesto la diferencia entre los valores de tenacidad a la fractura intralaminar cuando la grieta se propaga en la dirección de las fibras o perpendicular a las mismas. Para ello, se fabricarán y ensayarán dos tipos de especímenes, en los que se fuerce a las grietas a crecer según estas direcciones. Si bien existe un ensayo normalizado para la determinación de G_{IcL} , los autores han comprobado experimentalmente que éste no es válido para la determinación de G_{IcT} , dada su poca resistencia ante cargas fuera del plano, que producen el arrancamiento de parte del espécimen antes del comienzo de la propagación de la grieta. En este caso, se ha elegido un ensayo de flexión en tres puntos, en el que la grieta se genera y propaga en la dirección de la carga aplicada (ver figura 3).

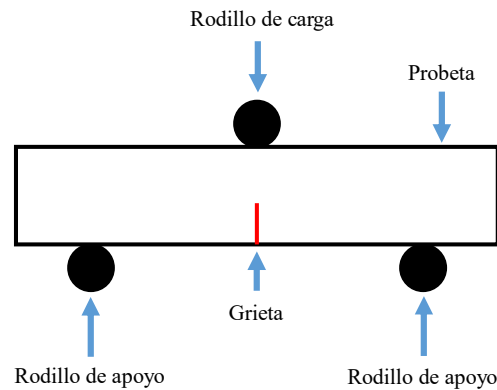


Figura 3. Esquema del ensayo de flexión en tres puntos.

En la sección 2 se comenta la fabricación de las probetas, continuando en la sección 3 con los ensayos realizados y sus resultados y finalizando con una discusión sobre los mismos y las conclusiones derivadas del trabajo en la sección 4.

2. FABRICACIÓN DE LAS PROBETAS

Las probetas, para el ensayo de flexión en tres puntos, tienen la configuración mostrada en la figura 4. La geometría y dimensiones se han elegido en base a las limitaciones que ofrecen las dos disposiciones de la fibra respecto de las grietas. Dado que las probetas se fabrican apilando capas unidireccionales de pre-impregnado, en base a experiencias anteriores [4], [5] y con el fin de asegurar una correcta fabricación, se optó por fijar como máximo un alto de 19 mm para las probetas, limitado por el caso de las probetas de G_{IcT} , en el que las láminas se apilan en esa dirección del alto de la probeta (que coincide con la dirección de propagación de la grieta). De este modo, las dimensiones son las mostradas en la figura 4.

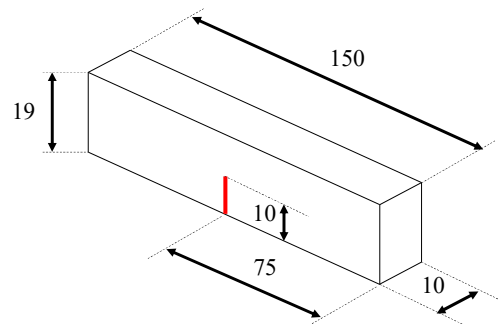


Figura 4. Dimensiones de la probeta de flexión en tres puntos. Dimensiones en mm.

Con el fin de obtener las probetas, se han fabricado todas juntas en forma de paneles, que posteriormente se han mecanizado con una sierra de disco de diamante (véanse las figuras 5 y 6).

De modo similar al ensayo descrito en las normas [2], [3], las probetas aquí ensayadas deben tener una pre-grieta, que dará lugar a una grieta tras la aplicación de la carga. Esta pre-grieta se fabrica insertando una lámina de material desmoldeante dentro del material compuesto antes de fabricar el mismo, de modo que, una vez curado y solidificado, aparezca una interfase clara de separación dentro del material. Tal como se muestra en el esquema de la figura 4, la pre-grieta tiene una longitud aproximada de 10mm.

Una vez fabricadas las probetas y tras una inspección visual, se descartaron varias debido al desalineamiento de la pre-grieta con respecto de la dirección de la carga (véase como ejemplo las probetas marcadas de 1 a 9 de la figura 6).

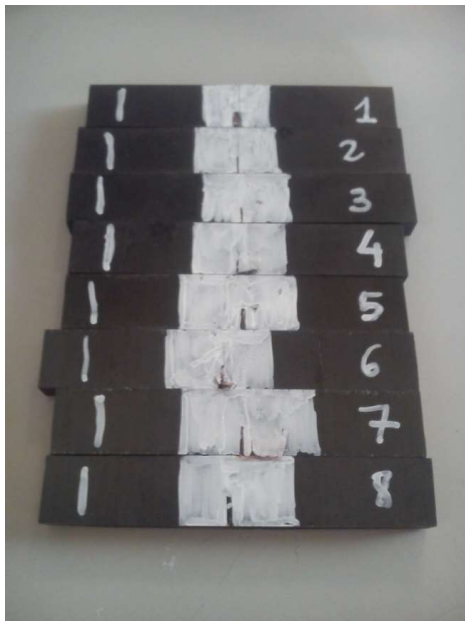


Figura 5. Vista de las probetas en las que la grieta crecerá paralela a la dirección de las fibras tras los procesos de fabricación y mecanizado.



Figura 6. Vista de las probetas en las que la grieta crecerá perpendicular a la dirección de las fibras tras los procesos de fabricación y mecanizado.

3. ENSAYOS

3.1. Realización del ensayo

Los ensayos se han realizado en una máquina universal de ensayos electromecánica Instron 4482, con una célula de carga de 500 kg. Para inducir la flexión en tres puntos, se ha utilizado un útil específico de la propia compañía Instron (ver figura 7).



Figura 7. Vista de la rotura de una probeta con crecimiento de la grieta paralelo a las fibras, en el ensayo de flexión en tres puntos.

En todos los ensayos, para ambos tipos de probeta, se han utilizado unos rodillos de carga y apoyo de 5 mm de diámetro, con una luz entre apoyos de 76 mm (el rodillo central, dispuesto simétricamente, se emplazó a 38 mm de cada lado, situándose bajo el mismo la pre-grieta generada en la probeta).

El ensayo consta de dos fases. En una primera, se carga la probeta a 0.2 mm/min hasta que se consigue iniciar la grieta a partir de la pre-grieta fabricada. Una vez se obtiene una grieta real, se procede a la descarga del espécimen a 0.5 mm/min. A continuación, se vuelve a cargar la probeta a 0.2 mm/min hasta que se produce la rotura de la misma, obteniendo en esta fase un crecimiento estable de la grieta que posibilita su seguimiento, pudiéndose relacionar en cada instante la longitud de la grieta con la carga aplicada y el desplazamiento de la cruceta de la máquina de ensayo.

Durante los ensayos, se registraron en la máquina de ensayos la carga aplicada y el desplazamiento de la cruceta. El avance de la grieta se registró por inspección ocular.

La tenacidad a fractura, para ambos tipos de probetas, se ha calculado como la energía disipada en un ciclo virtual de carga-crecimiento de grieta-descarga entre dos valores de la longitud de grieta. Este valor se divide por la nueva superficie de grieta, obteniéndose de ese modo la energía disipada por unidad de área de nueva grieta.

Ejemplos de curvas fuerza/desplazamiento obtenidas durante los ensayos pueden verse en las figuras 8 y 9, para el crecimiento de la grieta paralelo y perpendicular a las fibras, respectivamente.

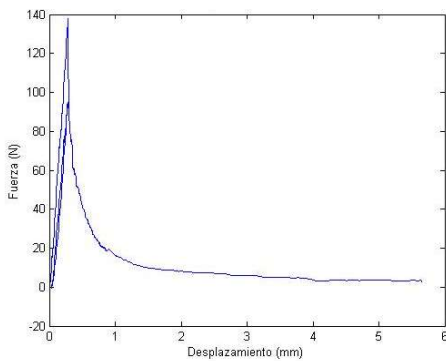


Figura 8. Curva fuerza-desplazamiento característica de un ensayo de flexión en tres puntos para una probeta con crecimiento de la grieta paralelo a las fibras.

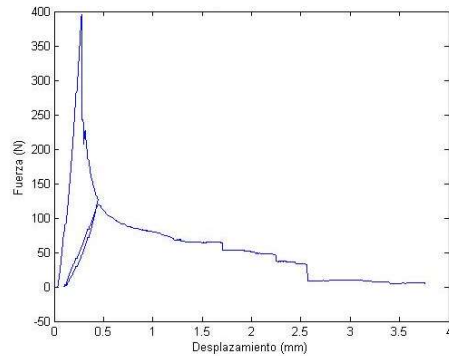


Figura 9. Curva fuerza-desplazamiento característica de un ensayo de flexión en tres puntos para una probeta con crecimiento de la grieta perpendicular a las fibras.

En las gráficas de las figuras 8 y 9, se aprecia, tras una primera zona de ajuste entre el útil de flexión y la probeta, un crecimiento lineal hasta llegar al pico máximo. En este momento se abre la grieta y se produce un descenso brusco de la carga. Tras esto se puede ver la descarga realizada y la consiguiente carga en la que se da lugar al crecimiento estable de la grieta hasta el fallo. Durante este crecimiento estable la carga va bajando gradualmente a medida que la longitud de grieta se hace mayor.

De estas curvas fuerza-desplazamiento puede observarse que, si bien el pico máximo en las probetas en que la grieta crece perpendicular a las fibras es más elevado que en el caso de crecimiento paralelo, el descenso en la carga es mucho más rápido, generando un área bajo la curva (y, por tanto, disipando una energía) significativamente menor.

3.2. Resultados de los ensayos

Se han ensayado ocho probetas para cada una de las configuraciones, debiéndose descartar cinco para el caso de crecimiento paralelo a las fibras y tres para el caso perpendicular a las fibras debido a roturas catastróficas tras la generación de la grieta.

La rotura de las probetas ha sido la esperada, propagándose la grieta en la dirección de la carga desde la pre-grieta hasta el extremo opuesto del espesor de la probeta, donde se encuentra el rodillo de carga. Esto ha sucedido tanto para el crecimiento paralelo a las fibras como para el perpendicular a las fibras, como puede verse en las figuras 7 y 10, respectivamente.



Figura 10. Vista de la rotura de una probeta con crecimiento de la grieta perpendicular a las fibras, en el ensayo de flexión en tres puntos.

Los valores medios de la tenacidad a fractura para ambos tipos de ensayo, así como sus correspondientes desviación estándar y coeficiente de variación se muestran en la tabla 1.

Tabla 1. Resumen de los valores de tenacidad a fractura obtenidos en el ensayo de flexión en tres puntos. Se presentan la media, desviación estándar y coeficiente de variación.

Ensayo	Tenacidad a fractura (J/m ²)	DST (J/m ²)	CV (%)
TPB longitudinal	561.99	36.55	6.5
TPB transversal	408.53	16.07	3.93

Como puede comprobarse, a partir de los coeficientes de variación expuestos en la tabla 1, los resultados obtenidos muestran una muy baja dispersión, lo que permite dar validez a los mismos.

4. DISCUSIÓN Y CONCLUSIONES

Se ha evaluado la tenacidad a fractura transversal en un material compuesto propiciando la propagación de las grietas en sentido paralelo a las fibras (G_{IcL}) y perpendicular a las mismas (G_{IcT}). A la vista de los resultados recogidos en la tabla 1, puede determinarse que ambos valores de la tenacidad a fractura son considerablemente diferentes, siendo mayor para el caso de propagación de la grieta en la dirección paralela a las fibras.

La diferencia entre tenacidades a fractura intralaminares puede explicarse con el camino que se va encontrando la grieta a medida que se va propagando. Mientras que cuando la grieta se propaga paralela a las fibras, debe seguir el camino marcado por éstas con el fin de evitar romper fibras, en el caso de propagación perpendicular la grieta es más libre de elegir un camino más favorable, en términos de disipación de energía y de acuerdo a la distribución de tensiones presente en el laminado. De este modo, el valor de la tenacidad a fractura intralaminar en la propagación perpendicular a las fibras es menor que en el caso longitudinal.

Por otro lado, un daño entre fibras no involucra la rotura de ninguna fibra y los dos casos estudiados corresponden a daño entre fibras. Un daño entre fibras, aceptando un modelo simple en el que se tiene fibra, matriz y una intercara entre ambas (es decir, no hay interfase física entre fibra y matriz), se puede producir involucrando rotura de la matriz y despegues entre fibra y matriz. Es obvio que el caso de crecimiento del daño paralelo a las fibras tiene más posibilidades de producirse con rotura casi exclusiva de matriz mientras que el daño transversal a las fibras involucra con toda seguridad despegues entre fibras y matriz. Al menos, puede decirse que este segundo tipo de daño tiene más probabilidad de tener más daño de despegues que de rotura frente a la misma relación para el caso de daño paralelo. Como normalmente las propiedades de la interfase son inferiores a las de la matriz, ello justifica que el valor de G_{IcL} sea mayor que el de G_{IcT} , aceptando que la relación entre propiedades matriz-intercara sea la indicada. En todo caso, esto abre una discusión acerca de la no universalidad de los resultados obtenidos, porque si se tuviera un material compuesto con valores inversos, esto es, mejores propiedades de la intercara que de la matriz, el resultado, invocando este razonamiento, debería ser el opuesto.

Independientemente de esto, la otra razón que se puede invocar es la diferente incidencia de los modos de fractura I, II y III en el mecanismo de propagación del daño en los dos casos de propagación. Este estudio, no obvio en cuanto a los resultados, requeriría la realización de modelos tridimensionales de los dos modelos de crecimiento en estudio.

Los valores obtenidos demuestran que en ningún caso debe tratarse por igual, desde el punto de vista de la tenacidad a fractura, la propagación de grietas intralaminar en direcciones perpendicular y paralela a las fibras, tal como se ha venido haciendo hasta ahora.

Un posible avance sobre los resultados aquí obtenidos sería realizar ensayos de tenacidad a fractura interlaminar, tal como los descritos en las normas [2], [3], y comparar los valores con las tenacidades calculadas en este trabajo.

AGRADECIMIENTOS

Los autores desean agradecer su contribución a D. Alberto Barroso, Prof. José Cañas y D. Antonio Cañas. Este trabajo ha sido financiado por el Ministerio de Ciencia e Innovación (Proyecto MAT2009-14022), el Ministerio de Economía y Competitividad y el Fondo Europeo de Desarrollo Regional (Proyectos MAT2012-37387, MAT2015-71036-P y MAT2016-80879-P) y por la Consejería de Innovación, Ciencia y Empresa de la Junta de Andalucía y el Fondo Social Europeo (Proyecto P08-TEP-4051).

REFERENCIAS

- [1] Pinho, S.T., P. Robinson, and L. Iannucci. Developing a four point bend specimen to measure the mode I intralaminar fracture toughness of unidirectional laminated composites. *Composites Science and Technology* (2009) 69(7-8): 1303-1309.
- [2] Airbus. Carbon Fibre Reinforced Plastics. Determination of fracture toughness energy of bonded joints. Mode I. G1C. Issue 1. AITM 1-0053 2006.
- [3] ISO Standard. Fibre-reinforced plastic composites - Determination of mode I interlaminar fracture toughness, G1C, for unidirectionally reinforced materials. Geneva, Switzerland. ISO 15024 2001.
- [4] F. Cepero, I.G. García, J. Justo, V. Mantič, F. París, A. Barroso. Comparación experimental de la tenacidad a fractura transversal de laminados unidireccionales correspondientes al crecimiento longitudinal o transversal de grietas. *Actas del XI Congreso Nacional de Materiales Compuestos, MATCOMP 15* (2015) 1165-1170.
- [5] F. Cepero, I.G. García, J. Justo, V. Mantič. Experimental comparison between the transverse fracture toughness of a unidirectional laminate corresponding to either longitudinal or transverse crack growth. *16th European Conference on Composite Materials, ECCM16* (2014).

A.1.3 Paper 3

Title: *Comparación experimental de la tenacidad a fractura transversal de laminados unidireccionales correspondientes al crecimiento longitudinal o transversal de grietas*

Conference: *XI Congreso Nacional de Materiales Compuestos*

Year of publication: *2015*

Abstract

The objective of the work is to determine and compare, in unidirectional laminates, the transverse fracture toughness corresponding to two directions of crack growth, parallel ($G_{Ic,par}$) and perpendicular ($G_{Ic,perp}$) to the fibers. For this purpose, two types of specimens have been designed and manufactured for the three and four point bending test, with equal dimensions but with different fiber orientations with respect to the initial crack. The main difficulty encountered during manufacturing has been the generation of cracks. This article describes the different techniques implemented to generate the cracks and the problems encountered. The results show that the toughness values for both directions of propagation are close, a slightly higher value being detected when the direction of propagation is parallel to the fibre.



Comparación experimental de la tenacidad a fractura transversal de laminados unidireccionales correspondientes al crecimiento longitudinal o transversal de grietas

F. Cepero¹, I.G. García^{1,2}, J. Justo¹, V. Mantič¹, F. París¹, A. Barroso¹

^a Grupo de Elasticidad y Resistencia de Materiales, Escuela Técnica Superior de Ingeniería, Universidad de Sevilla, España.

^b Departamento de Ingeniería Mecánica y Diseño Industrial, Escuela Superior de Ingeniería, Universidad de Cádiz, España.

RESUMEN

El objetivo del trabajo es determinar y comparar, en laminados unidireccionales, las tenacidades a fractura transversal correspondientes a dos direcciones de crecimiento de grieta, paralela ($G_{I_{\text{cpar}}}$) y perpendicular ($G_{I_{\text{cperp}}}$) a las fibras. Con este propósito, se han diseñado y fabricado dos tipos de probetas para el ensayo de flexión a tres y cuatro puntos, con dimensiones iguales pero con distintas orientaciones de fibras con respecto a la grieta inicial. La principal dificultad encontrada durante la fabricación ha sido la generación de grietas. En este artículo se describen las diferentes técnicas implementadas para la generación de las grietas y los problemas encontrados. Los resultados muestran que los valores de la tenacidad para ambas direcciones de propagación son cercanos, detectándose un valor ligeramente más alto cuando la dirección de propagación es paralela a la fibra.

PALABRAS CLAVE: Tenacidad a fractura transversal, laminados unidireccionales.

1. INTRODUCCIÓN

La tenacidad a fractura transversal es una magnitud clave para comprender y poder predecir el fallo de las capas transversales en laminados de fibra de carbono. Sin embargo, el método experimental usado para la medida de esta magnitud, recogido en documentos como [1], sólo permite medir la tenacidad correspondiente a la hipótesis de que la dirección de crecimiento de la grieta es paralela al eje de la fibra, asumiendo que la tenacidad a fractura transversal con crecimientos de grieta perpendiculares a la dirección de las fibras presenta un valor similar.

Sin embargo, ante la falta de evidencias físicas, no se puede afirmar si se está realizando una aproximación razonable de esta magnitud. En la práctica, este desconocimiento se traduce en una fuente de incertidumbre para todo modelo que pretenda, utilizando esta propiedad, predecir la fractura de este tipo de materiales.



El presente trabajo, propone un método experimental para calcular y comparar G_{Icpar} y G_{Icperp} basándose en los resultados obtenidos anteriormente en [2]. En particular, se describen los procedimientos de fabricación, ensayo de probetas y obtención de los datos buscados. Finalmente se muestran las conclusiones obtenidas de este trabajo.

2. FABRICACIÓN DE PROBETAS, ENSAYOS Y RESULTADOS OBTENIDOS

Con el fin de poder utilizar la misma geometría de probeta para obtener las dos tenacidades a la fractura que se desean comparar se propone el ensayo de flexión de 3 o 4 puntos. En la figura 1, se puede observar un esquema del ensayo que se ha realizado para las dos probetas que se estudian en este trabajo. Las dimensiones de las probetas son de 10 mm de espesor, 19 mm de altura, y 150 mm de longitud. La relación entre altura y espesor se escoge de acuerdo a las recomendaciones recogidas en [3]. Las pregrietas, tienen una longitud de 10 mm. Todas las probetas se fabrican usando el material Hexcel® AS4-8852. Se realizan 3 series de ensayos que se detallan a continuación.

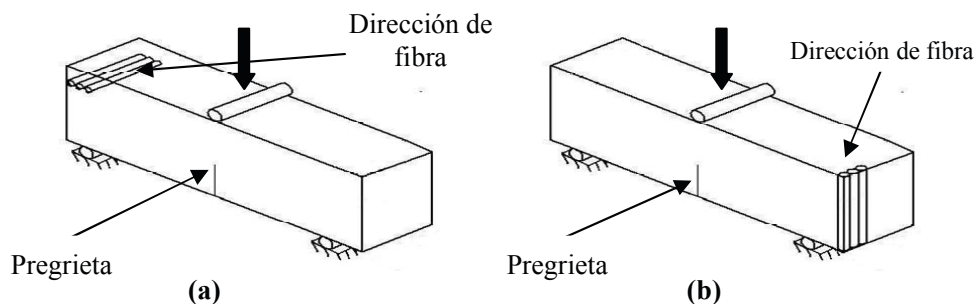


Fig. 1. Probetas con distintas direcciones de fibra con respecto al crecimiento de grieta: (a) crecimiento perpendicular a la dirección de fibra, (b) crecimiento paralelo a la dirección de fibra

2.1 Fabricación y ensayos de las probetas de la serie 1

Con vistas a verificar la funcionalidad de la técnica de generación de la grieta se fabrican inicialmente dos probetas con crecimiento paralelo a la dirección de fibra, denominadas en adelante serie 1. La grieta se genera a partir de la introducción de una cuchilla cubierta de una capa de nylon. La figura 2 ilustra el laminado antes de ser fabricado, con las cuchillas en posición.



Fig. 2. Laminado con fibras paralelas a la grieta de la serie 1

Una vez realizado el laminado, se introduce en el autoclave, y se somete al ciclo de curado recomendado por el fabricante. Posteriormente, se procede al proceso de corte de las probetas del laminado, para obtener las dos probetas de este laminado. Tras la fabricación, se observa que se produce una ligera inclinación de la grieta a lo largo del



espesor de la probeta. Finalmente, se ensayan estas probetas en un ensayo de flexión a cuatro puntos con distancias entre los rodillos inferiores de 120 mm y entre los superiores de 30 mm.

2.2 Fabricación y ensayos de las probetas de la serie 2

Una vez probada como satisfactoria la técnica utilizada en la serie 1, se decide realizar una serie con mayor número de probetas de los dos tipos que se quieren ensayar.

Para la evaluación de la tenacidad transversal con dirección de propagación paralela a la dirección de la fibra (Laminado paralelo), se han realizado 4 laminados iguales al fabricado en la serie 1, con 56 láminas y dimensiones de 170x70 mm cada uno. Las fibras siguen la dirección del lado corto del laminado, introduciendo dos pregrietas en sus bordes en la mitad de su lado largo. De esta forma se obtienen 8 probetas.

Para la evaluación de la tenacidad transversal con dirección de propagación perpendicular a la dirección de la fibra (Laminado perpendicular), se fabrica un laminado que dispone de 105 láminas de dimensiones de 170x100 mm. Las fibras siguen el sentido del lado corto y se realiza la pregrieta insertando, al igual que en el caso anterior siguiendo la dirección de fibra en la mitad del laminado obteniendo 8 probetas de este laminado.

Tras el proceso de curado y recantado se observa, de nuevo, una ligera inclinación de la grieta. Estas probetas son ensayadas a 3 y 4 puntos. Las probetas con fibras paralelas a la dirección de propagación de la grieta tienen una inclinación de grieta grande en el espesor y hace que los ensayos tengan propagación de grieta inestable, tanto si la flexión es en 3 o 4 puntos.

Para las probetas con fibras perpendiculares a la grieta, los ensayos realizados han sido de flexión a tres puntos, con una distancia de separación de los rodillos inferiores de 100 mm. La figura 3 muestra imágenes de los laminados y ensayos realizados.

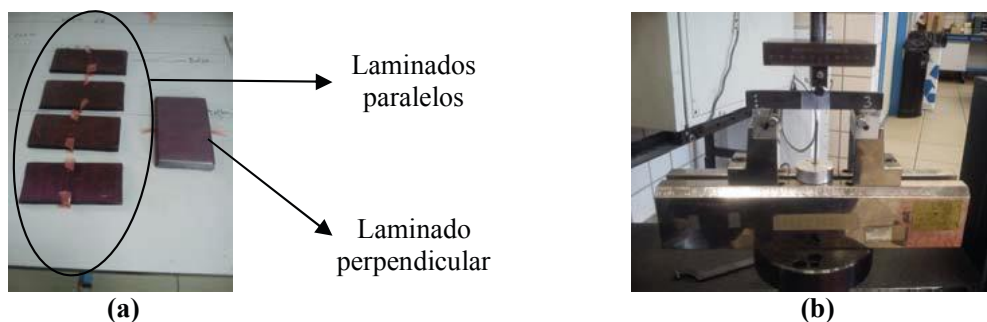


Fig. 3. Fabricación y ensayo de probetas de la serie 2: (a) laminados serie 2, (b) ensayo de la probeta 3 con fibras perpendiculares a la propagación de la grieta

2.3 Fabricación y ensayos de las probetas de la serie 3

En esta ocasión, para fabricar las probetas con fibra en la misma dirección de la grieta (Laminado paralelo), se han realizado cuatro laminados, con las mismas dimensiones y de la misma forma que en la serie 2, con la salvedad de que ahora se han utilizado útiles



que impidan la inclinación en las pregrietas. Estos útiles son perfiles rectangulares de aluminio con una ranura en su zona central, donde se aloja la cuchilla que posteriormente genera la pregrieta, introduciendo las cuchillas de la misma forma que en los laminados de este tipo de la serie 2.

En cuanto a los laminados para fabricar las probetas con fibras perpendiculares a la dirección de propagación de la grieta (Laminado perpendicular), se han realizado dos laminados de 105 láminas y dimensiones 170x70 mm cada uno. La cuchilla se introduce a una profundidad de 10 mm siguiendo la dirección de la fibra en la sección central del laminado y en sus bordes se fijan a unos perfiles rectangulares de aluminio, ver figura 4.

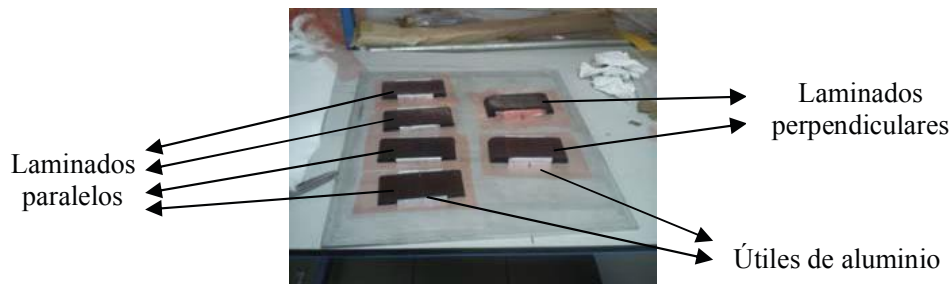


Fig. 4. Laminados de la serie 3

Los útiles que se emplean para realizar las pregrietas en los laminados son distintos para cada tipo de laminado. En el laminado paralelo se usan dos útiles en los bordes de lado largo, de forma que introduce la cuchilla en la mitad de este lado.

Para los laminados perpendiculares, el útil tiene una cuchilla que recorre la sección central del laminado y en sus bordes hay dos perfiles de aluminio que alojan a la cuchilla en una ranura. En la figura 5 se pueden observar ambos útiles.



Fig. 5. Útiles de aluminio de la serie 3: (a) útil del laminado perpendicular, (b) útil del laminado paralelo.

De estos laminados se obtienen 9 probetas con fibras perpendiculares a la grieta y 7 probetas con fibras paralelas a la grieta. Estas probetas se ensayan a flexión en tres puntos, con distancia entre rodillos de 120 mm para las probetas con fibras paralelas a la grieta y 100 mm para las probetas con fibras perpendiculares a la grieta.

Todos los ensayos se realizaron con velocidad de mordaza de 0,2 mm/min, hasta que la



grieta avanza varios milímetros de forma inestable. Una vez detectado este crecimiento, se descarga a 0,5 mm/min y se vuelve a cargar a 0.2 mm/min avanzando la grieta de forma estable hasta la rotura, observándose *bridging* durante los ensayos. En la figura 6 se muestra un ejemplo de un ensayo con estas probetas.

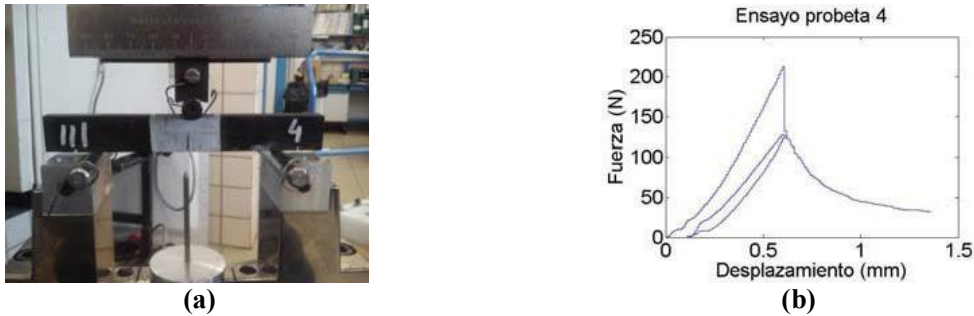


Fig. 6. Ensayo de la probeta 4 con fibras paralelas a la propagación de la grieta de la serie 3: (a) foto del ensayo, (b) registros de fuerza-desplazamientos obtenidos en el ensayo

3. RESULTADOS DE G_{Icpar} Y G_{Icperp} EN LAS DISTINTAS SERIES

Para calcular la tenacidad a fractura transversal en estos dos tipos de probetas se calcula la energía disipada cuando la grieta crece de forma estable. Este valor se obtiene a partir del área encerrada en la gráfica de fuerza-desplazamiento desde que la grieta empieza a crecer de forma estable hasta 1 mm antes de su rotura. Posteriormente, se divide entre la nueva superficie de grieta creada. Las tablas 1 y 2 muestran los resultados obtenidos.

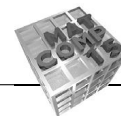
Tabla 1. Valores obtenidos en las series 1 y 3 de G_{Icpar} .

$G_{Icpar}(J/ m^2)$					
Serie 1		Serie 3			Media
Probeta 1	Probeta 2	Probeta 3	Probeta 4	Probeta 7	
514,23	551,52	596,72	577,78	511,47	550,34

Tabla 2. Valores obtenidos en las series 2 y 3 de G_{Icperp} .

$G_{Icperp}(J/ m^2)$	Serie 2	Serie 3
Probeta 1	503,75	395,29
Probeta 2	521,00	368,45
Probeta 3	517,63	-
Probeta 4	525,86	405,91
Probeta 5	-	428,68
Probeta 6	-	425,02
Probeta 7	-	387,75
Media	517,06	401,85

Para calcular G_{Icpar} , se obtienen las medidas de dos probetas de la serie 1, estos ensayos fueron con un ensayo de flexión a cuatro puntos y tres medidas más de la serie 3 con ensayos de flexión a tres puntos, obteniendo una media de **550,34 J/m²**. El intervalo de confianza (IC) es [517,20; 583,49] y su coeficiente de variación (CV) de 6,87%.



En cuanto a $G_{Ic\text{perp}}$, de la serie 2 se obtienen cuatro medidas con una media de **517,06 J/m²**, su IC es [507,76; 526,36] y un CV de 1,84%. De la serie 3 se obtienen seis medidas con una media de **401,85 J/m²**, su IC es [383,50; 420,20] y su CV es 5,71%, todos estos ensayos han sido de flexión a tres puntos. Se observa CV_s inferiores al 10% e IC_s bastante próximos que indican que las medidas tomadas son bastante homogéneas.

Los resultados de $G_{Ic\text{par}}$ son superiores a los valores de $G_{Ic\text{perp}}$ obtenidos en las distintas series, para las probetas de la serie 2 son un 6,44% superiores y para las probetas de la serie 3, un 36,95% superiores. Esta diferencia se debe a que las probetas de la serie 2 tienen una inclinación a lo largo del espesor indeseada.

4. CONCLUSIONES

En este trabajo se han realizado ensayos para comparar la tenacidad a fractura intralaminar en materiales compuestos cuando el crecimiento de la grieta es paralelo y perpendicular a las fibras. Se han ensayado tres series distintas de probetas utilizando diferentes técnicas para la generación de la grieta inicial.

Se obtienen dos valores apreciablemente distintos de $G_{Ic\text{perp}}$, uno para cada una de las dos series de probetas fabricadas con propagación de grieta perpendicular a la fibra, por diferencias en la fabricación de las probetas seguidas en las distintas series. El resultado obtenido de $G_{Ic\text{par}}$, es siempre superior a los dos obtenidos de $G_{Ic\text{perp}}$. Esto se puede deber a fenómenos macroscópicos como el bridging observado en ambos tipos de probetas que deberán ser revisados en futuros ensayos. Por otra parte, un análisis microestructural de la propagación de la grieta en ambos casos permitiría evaluar la influencia de la microestructura en esta diferencia.

AGRADECIMIENTOS

Este trabajo fue financiado por el Ministerio de Educación (FPU 2009/3968), el Ministerio de Ciencia e Innovación (Proyecto MAT2009-14022), el Ministerio de Economía y Competitividad y el Fondo Europeo de Desarrollo Regional (Proyecto MAT2012-37387), la Junta de Andalucía y el Fondo Social Europeo (Proyecto P08-TEP-4051).

REFERENCIAS

1. International Series. Fibre-reinforced plastic composites-Determination of mode I interlaminar fracture toughness, G_{Ic} , for unidirectionally reinforced materials, ISO 15024; 2001.
2. CEPERO, F., GARCÍA, I.G., JUSTO, J., MANTIČ, V. Experimental comparison between the transverse fracture toughness of a unidirectional laminate corresponding to either longitudinal or transverse crack growth (2014) 16th European Conference on Composite Materials, ECCM 2014.
3. GARG A. Intralaminar and interlaminar fracture in graphite/epoxy laminates. *Engineering Fracture Mechanics*; 23(4) 1986: 719-733.

A.1.4 Paper 4

Title: *Experimental comparison between the transverse fracture toughness of a unidirectional laminate corresponding to either longitudinal or transverse crack growth*

Conference: *ECCM16 – 16th European Conference on Composite Materials*

Year of publication: *2014*

Abstract

A test is developed to compare the transverse fracture toughness of a crack growing along the longitudinal and transverse directions of long-fiber-reinforced laminates. The test proposed is based on a three point bending (TPB) test. The starter crack will be generated inserting a non-adhesive nylon film prior to the curing process. Once the specimens are cured, this precrack will grow by a first static loading. Two different test specimens will be fabricated with the same dimensions and two different fibre orientations. In the first specimen configuration the fibres are orientated parallel the direction of crack growth whereas in the second one the fibres are perpendicular to the direction of crack growth. The comparison of the results for both specimens will enable to evaluate the influence of the direction of crack propagation on the transverse fracture toughness.

EXPERIMENTAL COMPARISON BETWEEN THE TRANSVERSE FRACTURE TOUGHNESS OF A UNIDIRECTIONAL LAMINATE CORRESPONDING TO EITHER LONGITUDINAL OR TRANSVERSE CRACK GROWTH.

F. Cepero, I.G. García*, J. Justo, V. Mantič

*Grupo de Elasticidad y Resistencia de Materiales, Escuela Técnica Superior de Ingeniería.
Universidad de Sevilla, Camino de los Descubrimientos s/n, 41092 Sevilla, Spain*

**Corresponding Author: israelgarcia@us.es*

Keywords: unidirectional lamina, laminate fracture toughness, transverse failure, testing

Abstract.

A test is developed to compare the transverse fracture toughness of a crack growing along the longitudinal and transverse directions of long-fiber-reinforced laminates. The test proposed is based on a three point bending (TPB) test. The starter crack will be generated inserting a non-adhesive nylon film prior to the curing process. Once the specimens are cured, this pre-crack will grow by a first static loading. Two different test specimens will be fabricated with the same dimensions and two different fibre orientations. In the first specimen configuration the fibres are orientated parallel the direction of crack growth whereas in the second one the fibres are perpendicular to the direction of crack growth. The comparison of the results for both specimens will enable to evaluate the influence of the direction of crack propagation on the transverse fracture toughness.

1. Introduction

The transverse fracture toughness of unidirectional laminates has received a considerable attention in the composite community given its influence on the failure mechanisms associated to off-axis loading. In general, the term transverse fracture toughness refers to the value measured for a crack propagating parallel to the fibre direction, denoted here as G_{Icl} . In fact, this is the only value which can be obtained employing the available standards, see e.g. ISO 15024 [1]. The absence of procedures to measure the value for a crack growing perpendicular to the fibre direction G_{Ict} is caused by the lack of experimental results in the literature. In practical applications, a large part of the engineering community assumes that both values of transverse fracture toughness, G_{Icl} and G_{Ict} , are identical in spite of the lack of experimental evidences justifying it.

The differences between the values of fracture toughness corresponding to different directions of crack growth could affect significantly the prediction of the overall performance of the structural components. Therefore, it is important to evaluate experimentally the adequacy of the hypothesis that assumes that these two values are identical. In order to carry out the pertinent comparison, two types of specimens, having the same dimensions, will be

fabricated. The only difference between these two specimens will be the fibre orientation. These specimens will be based on the classic three point bending beam (TPB) specimens, see Figure 1. A pre-crack will be generated by the insertion of a demolding nylon film before the curing process.

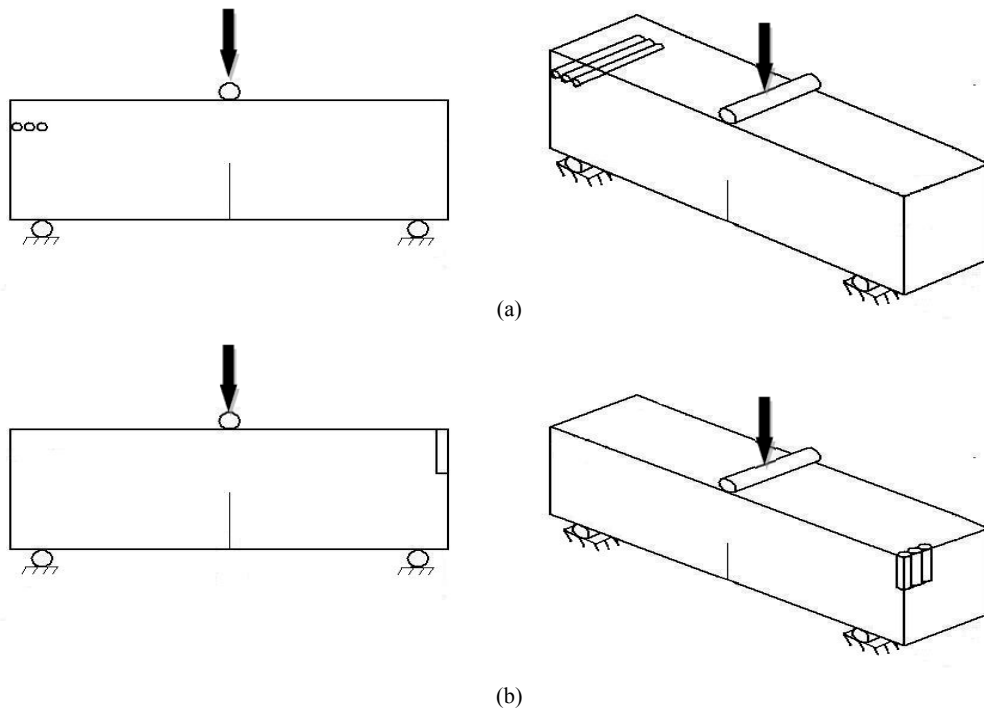


Figure 1. Three point bending beam (TPB) specimens proposed to measure the transverse fracture toughness of a crack growing either (a) perpendicular or (b) parallel to the fibre direction, G_{Ict} and G_{Icl} , respectively.

The present work proposes an experimental study aimed at giving information about the similarity of G_{Ict} and G_{Icl} . Details regarding specimen fabrication and pre-insertion of the demolding nylon film will be described in the next section. Subsequently, the testing procedure is detailed in Section 3. Finally, Section 4 discusses the techniques which will be employed to obtain the values of the properties through the postprocessing of the experimental results.

2. Specimens fabrication

The test specimens are fabricated from AS4-8852 unidirectional fibre carbon/epoxy tape pre-preg, manufactured by Hexcel. Two laminates are fabricated, one of them with dimensions 150 mm x 150 mm, composed by 100 plies and the other one with dimensions 30 mm x 1200 mm with 53 plies. After the stacking process, the demolding film is inserted and subsequently the laminates are cured employing the autoclave curing cycle recommended by the manufacturer. Finally, the specimens are cut up from the laminates employing a diamond saw blade.

The TPB specimens is 100 mm long (the distance between supports will be 80 mm), with a thickness of 10 mm and height of 19 mm. The ratio between these dimensions is in accordance with the recommendations found in the literature, e.g. [2]. Considering these ratios as fixed, the size of the specimen is chosen by taking into account the limitations given by the stacking process and the requirements for a satisfactory curing process.

In the case of the laminate that is used to measure G_{IcI} , 53 layers are stacked. The future specimens with 100 mm length are situated next to each other in the laminate along the longitudinal direction in the laminate, and are cut up after the curing process. A cut of at least 8 mm depth is made in the middle of each future specimen before the curing process in order to insert the demolding film.

In the case of the laminate that is used to measure G_{IcI} , a single cut has to be made since the future specimens are situated next to each other along the thickness direction. The cut is at least 8 mm deep in the middle of one of the faces of the laminate.

In both cases, the demolding film is inserted, with its distance to the edge fixed by an adhesive film. Since no fibres are broken in the cutting process, a possible small excess in the depth of cut is not relevant since the resin fill possible discontinuities during the curing process.

Once both laminates are cured, the irregular edges are cut with a diamond saw blade. Employing the same tool, the laminates are cut up to get the dimensions described previously.

3. Testing procedure

Once the specimens has been cut up, the symmetric situation of the crack tip in both edges of the specimen is verified in order to assure the correct alignment of the demolding film. For this purpose, an optical microscope is employed. Subsequently, the edges are whitened in order to enable the measurement of the advance of the crack tip.

The tests are performed by employing a TPB fixture especially designed for this type of tests. The distance between supports is fixed to 80 mm. The crack is situated at the same distance of the two supports, and aligned in the direction of the applied load. This alignment is verified carefully since this is a key factor for the accuracy of measurements. The TPB fixture is attached to a universal testing machine.

An initial monotonic loading is applied in order to generate a sharp crack by growing the initial pre-crack produced by the insertion of the demolding film. The specimen is unloaded when the crack reaches a length of 9 mm. Subsequently, the symmetry of the crack is verified again by measuring the crack length at the two opposed edges.

A second monotonic loading is applied until reaching the total failure of the specimen. The load and displacements are recorded along with the crack length. These results are employed to estimate the values of the transverse fracture toughness.

4. Estimation of the transverse fracture toughness from the experimental results

The estimation of the transverse fracture toughness with longitudinal growth (G_{lcl}) and transverse growth (G_{lct}) is based on two different methods: the first method is based on the variation of the compliance, whereas in the second one the area under the load-displacement curve is computed.

The first method is based on the change of the compliance (C) with the crack length. Under a displacement-controlled test, the value of the transverse fracture toughness can be obtained as,

$$G_{1c} = \frac{1}{2} \cdot \frac{U^2}{C^2} \cdot \frac{\partial C}{\partial A} \quad (1)$$

where U is the displacement corresponding to a certain crack length a , A is the crack area and $C(a)=U/F$ is the compliance, with F being the applied load. Typically, the compliance is considered as a function of the crack length a . The compliance values are obtained from the measured values of displacement U and load F . These compliance values are fitted by a quadratic function

$$C(a) = C_0 + C_1 \cdot \left(\frac{a}{w}\right) + C_2 \cdot \left(\frac{a}{w}\right)^2 \quad (2)$$

where w is a reference length of the specimen, e.g. the final length of the crack at the end of the test. C_0 , C_1 and C_2 are coefficients to be fitted to the experimental results.

The second method is based on computing the area below the load-displacement curve between fictitious unloading processes from the points corresponding to certain values of the crack length. The area obtained can be identified with the energy dissipated during the increment of crack area between the two consecutive points. Thus, the transverse fracture toughness can be obtained by dividing this area on the load-displacement curve by the increment of crack area.

Finally, the results obtained for the two transverse fracture toughnesses, G_{lcl} and G_{lct} , will be compared. In addition, these results will be contrasted with the results obtained for a test carried out on the same material according to the ISO 15024 standard [1].

5. Conclusions

A test is proposed to compare the transverse fracture toughness of a long-fibre-reinforced composite for the crack growing either longitudinally or transversely to the fibre direction. The main advantage of this test is the ability to measure these two properties by employing the same test specimen and procedure. This enables a comparison between the two types of propagation avoiding the possible influence of the test type on the comparison results. The specimen fabrication and testing along with the results postprocessing are briefly discussed.

Acknowledgements

The work was supported by the Junta de Andalucía and European Social Fund (Project P08-TEP-4051), the Spanish Ministry of Economy and Competitiveness (Project MAT2012-37387).

References

- [1] International Standard. Fibre-reinforced plastic composites-Determination of mode I interlaminar fracture toughness, G_{Ic} , for unidirectionally reinforced materials, ISO 15024; 2001.
- [2] Garg A. Intralaminar and interlaminar fracture in graphite/epoxy laminates. *Engineering Fracture Mechanics*; 23(4) 1986: 719-733.

A.2 Conference posters

A.2.1 Poster 1

Conference: 5th Annual Machining Science Student Conference, 2020.



The University of Sheffield.

Finite Element Method investigation in the edge trimming of CFRP laminates

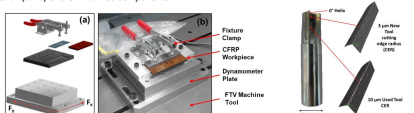
F. Cepero-Mejias^{a,b,c}, J.L. Curiel-Sosa^{b,c}, N. Duboust^d, V.A. Phadnis^e and K. Kerrigan^d

^aIndustrial Doctorate Centre in Machining Science, The University of Sheffield, Sir Frederick Mappin Building, Mappin Street, S1 3JD Sheffield, United Kingdom.
^bComputer-Aided Aerospace & Mechanical Engineering (CA2M) Research Group, Sir Frederick Mappin Building, Mappin Street, S1 3JD Sheffield, United Kingdom.
^cDepartment of Mechanical Engineering, The University of Sheffield, Sir Frederick Mappin Building, Mappin Street, S1 3JD Sheffield, United Kingdom.
^dAMRC with Boeing, Advanced Manufacturing Park, Wallis Way, Catfild, Rotherham, S605TZ, United Kingdom.

Tool wear in composite edge trimming

Introduction

The impact of blunt tool tips (large tool edge radius) interacting with the fibre tends to push the fibres generating a significant bending effect rather than shearing them. This mechanism increases the size of the cracks produced by the fibre-matrix debonding below the machined surface, considerably reducing the structural integrity of the part [1]. Therefore, this tool wear must be quickly detected by evaluating variations in the mechanical responses of the machining process to avoid the massive rejection of parts in a manufacturing production system. The most effective and easy-to-obtain indicator that indicates the emergence of a severe tool wear is the visualisation of an increment in the cutting forces [2]. Therefore, the investigation of the variations of the cutting forces because of the tool wear during machining is necessary to improve the final structural quality of the machined components.



Damage algorithm

- Experimental investigations are expensive and time consuming to optimize cutting configuration.
- FE models offer a viable option to enhance the machining design.
- Complex damage algorithms are required.

Constitutive equations

$$\begin{bmatrix} \sigma_{11} \\ \sigma_{22} \\ \sigma_{12} \end{bmatrix} = \frac{1}{D} \begin{bmatrix} (1-d_f)E_{11} & (1-d_f)(1-d_m)v_{12}E_{11} & 0 \\ (1-d_f)(1-d_m)v_{12}E_{11} & (1-d_m)E_{22} & 0 \\ 0 & 0 & (1-d_f)G_{12} \end{bmatrix} \begin{bmatrix} \epsilon_{11} \\ \epsilon_{22} \\ \gamma_{12} \end{bmatrix}$$

where $D = 1 - (1-d_f)(1-d_m)v_{12}v_{21}$; $d_f = 1 - (1-d_f)(1-d_f)(1-d_m)$; $d_m = \max(d_{f1}, d_{f2})$; $d_{f1} = \max(d_{f1}, d_{f2})$; $d_{f2} = \max(d_{f1}, d_{f2})$; $d_{f1} = \max(d_{f1}, d_{f2})$; $d_{f2} = \max(d_{f1}, d_{f2})$; $d_{f1} = \max(d_{f1}, d_{f2})$; $d_{f2} = \max(d_{f1}, d_{f2})$

Damage initiation

Fibre (Hashin)

$$F_{f1} = \frac{\sigma_{11}^2 + \sigma_{22}^2}{S^2} = 1$$

$$F_{f2} = \frac{\sigma_{12}^2}{S_c^2} = 1$$

Damage propagation

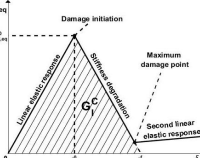
$$d_f = \frac{\sigma_{11}^2 + \sigma_{22}^2}{S^2} + \frac{\sigma_{12}^2}{S_c^2}$$

Matrix (Plane stress Puck criterion)

$$F_{m1} = F_{m2} = \frac{\sigma_{11}^2 + \sigma_{22}^2}{S^2} + \frac{\sigma_{12}^2}{S_c^2} = 1$$

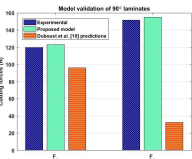
FE model characteristics

- A fine mesh with an element size of 10 µm is allocated in the cutting region.
- Bottom side is totally fixed and lateral sided horizontal movement is restricted.
- Fibre orientations of 45 and 90 degrees are studied.
- Excellent cutting force agreement with experimental findings is achieved.
- Spring back effect is considered to increase the quality of thrust force predictions.
- Tool edge radius between 10-50 microns are simulated in this research.

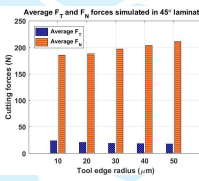


FE model characteristics

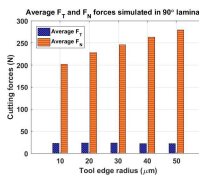
Model validation of 90° laminates



Average Fx and Fy forces simulated in 45° laminates



Average Fx and Fy forces simulated in 90° laminates



Conclusions and future work

Conclusions

- Efficiency of the damage model used is proved and its main capabilities are:
 - Inclusion of spring back phenomenon increase the predictions quality.
 - Normal forces are predominant in edge trimming.
 - The relative machining angle plays a relevant role in the evolution of machining forces.
 - Tool wear effect is more significant in 90° laminates than in 45° laminates.

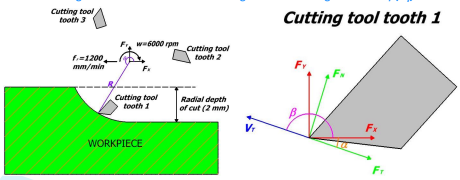
Future works

- Development of a 3D FEA of more complex composite milling processes.
- Introduction of strain rate and thermal matrix effects.
- Include chip formation in the simulation and study other fibre orientations.

Results and discussion

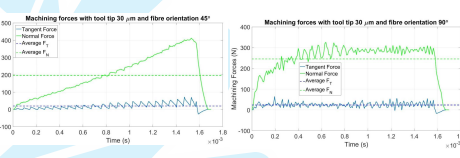
Normal (F_N) and tangential (F_T) forces and definitions

- A three flute cutting tool with zero helix angle 10 mm diameter and radial depth of cut of 2mm is modelled.
- A feed rate of 1200 mm/min and a spindle speed of 6000 rpm is studied.
- Normal and tangential forces are normal and tangent to the cutting tool velocity (V_c)



Cutting forces evolution

- Normal forces are much higher than tangential forces (spring back effect).
- In 45° laminate normal and tangential forces increase gradually due to the relative machining angles stay always in values where these forces are stable.
- Initial normal force peak is motivated because fibres push parallel to the cutting tool.
- Normal forces are notably higher in 90° laminates



Results and conclusions

- The normal forces and its increment due to tool wear is higher for 90° laminates.
- Tangential forces keeps stable and similar in both laminates.
- In general the tool wear is more visualised in normal forces for 90° laminates

Conclusions and future work

Conclusions

- Efficiency of the damage model used is proved and its main capabilities are:
 - Inclusion of spring back phenomenon increase the predictions quality.
 - Normal forces are predominant in edge trimming.
 - The relative machining angle plays a relevant role in the evolution of machining forces.
 - Tool wear effect is more significant in 90° laminates than in 45° laminates.

Future works

- Development of a 3D FEA of more complex composite milling processes.
- Introduction of strain rate and thermal matrix effects.
- Include chip formation in the simulation and study other fibre orientations.

References

[1] R. M. Saoubi et al., "Manufacturing Technology High performance cutting of advanced aerospace alloys and composite materials," *CIRP Ann. - Manuf. Technol.*, vol. 64, no. 2, pp. 557-580, 2015.

[2] N. Duboust, S. Ayyar, K. Kerrigan, and R. Scaife, "FE modelling of CFRP machining: prediction of the effects of cutting edge rounding," *17th CIRP Conf. Model. Mach. Oper. FE*, 2019.

A.2.2 Poster 2

Conference: 2nd CIRP Conference on Composite Material Parts Manufacturing (CIRP-CCMPM 2019), 2019.

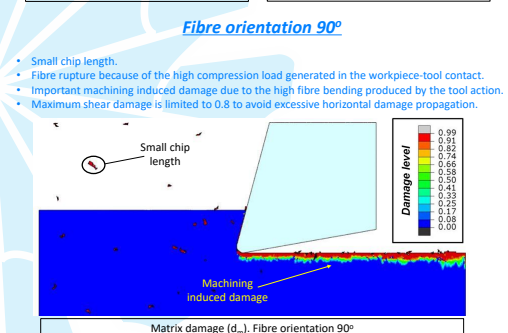
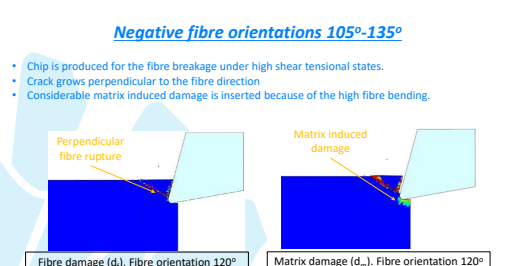
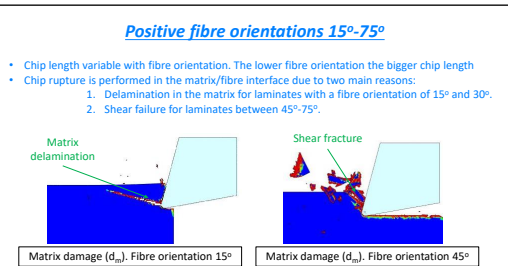
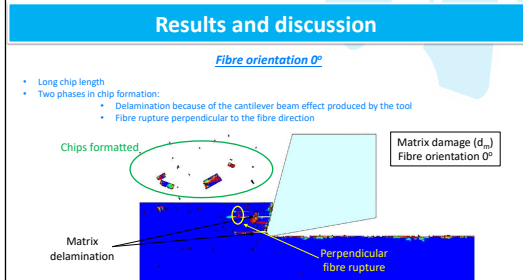
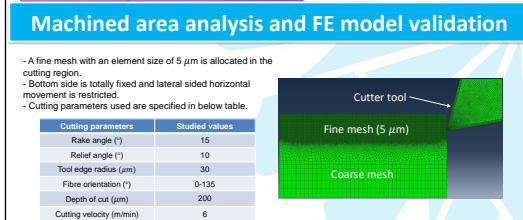
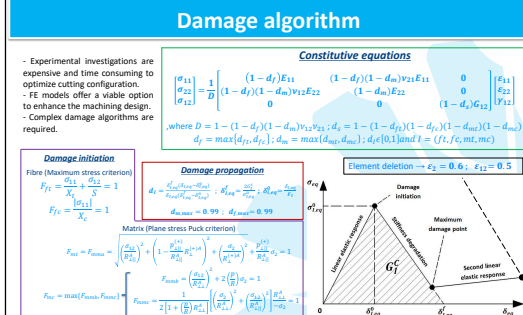
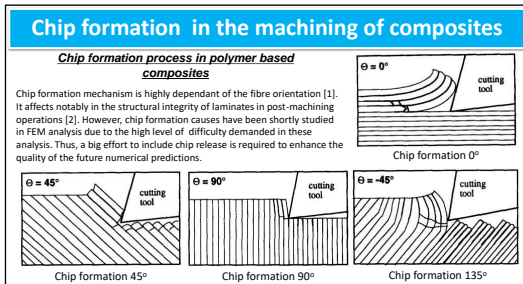


Chip formation in machining of UD polymer based composites: FEM based assessment

F. Cepero-Mejias^{a,b,c}, J.L. Curiel-Sosa^{b,c}, V.A. Phadnis^d and K. Kerrigan^d



^aIndustrial Doctorate Centre in Machining Science, The University of Sheffield, Sir Frederick Mappin Building, Mappin Street, S1 3JD Sheffield, United Kingdom.
^bComputer-Aided Aerospace & Mechanical Engineering (CA2M) Research Group, Sir Frederick Mappin Building, Mappin Street, S1 3JD Sheffield, United Kingdom.
^cDepartment of Mechanical Engineering, The University of Sheffield, Sir Frederick Mappin Building, Mappin Street, S1 3JD Sheffield, United Kingdom.
^dAMRC with Boeing, Advanced Manufacturing Park, Walls Way, Catciff, Rotherham, S605TZ, United Kingdom.



Conclusions and future work

Conclusions

Efficiency of the damage model used is proved and its main capabilities are:

- Good prediction of delamination and fibre rupture in laminates of 0°.
- Detection of different failure modes in laminates with positive fibre orientations.
- Accurate prediction of machining induced damage and chip formation for laminates with negative fibre orientations.
- Correct simulation of fibre bending effect in the machining of 90° laminates.

Future works

Development of a 3D FEA of orthogonal cutting, drilling and milling processes. Introduction of strain rate and thermal matrix effects. Tool degradation and cross ply laminates delamination assessment.

[1] D. H. Wang, M. Ramulu, and D. Arola, "Orthogonal cutting mechanisms of graphite/epoxy composite. Part I: unidirectional laminate," *Int. J. Mach. Tools Manufact.*, vol. 35, no. 12, pp. 1623–1638, 1995.
 [2] X. M. Wang and L. C. Zhang, "An experimental investigation into the orthogonal cutting of unidirectional fibre reinforced plastics," *International Journal of Machine Tools and Manufacture*, vol. 43, no. 10, pp. 1015–1022, 2003.



A.2.3 Poster 3

Conference: Congreso del Grupo Español de la fractura, 2019.



Escuela Técnica Superior de
INGENIERÍA DE SEVILLA

Congreso del Grupo Español de Fractura 2019, Sevilla, 2 al 5 de abril de 2019



COMPARACIÓN EXPERIMENTAL DE LA TENACIDAD A FRACTURA INTRALAMINAR EN MATERIALES COMPUESTOS PARA CRECIMIENTO DE GRIETAS EN DIFERENTES DIRECCIONES EN EL PLANO

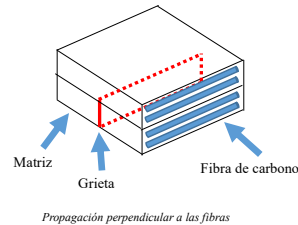
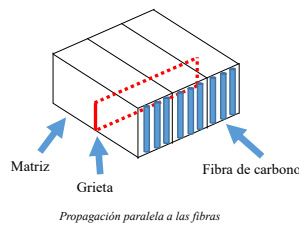
F. Cepero^{1,2}, I. G. García¹, J. Justo^{1*}, V. Mantić¹, F. Paris¹

¹Grupo de Elasticidad y Resistencia de Materiales. Escuela Técnica Superior de Ingeniería. Universidad de Sevilla. Camino de los Descubrimientos s/n, 41092. Sevilla-España.

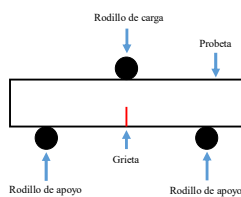
²The University of Sheffield. Sir Frederick Mappin Building Mappin Street, S1 3JD Sheffield, United Kingdom.

* Persona de contacto: jjusto@us.es

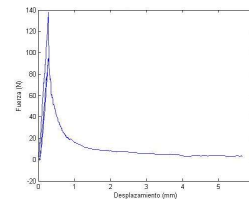
Propagación intralaminar de la grieta según dos direcciones respecto de las fibras



Caracterización de la tenacidad a fractura mediante un ensayo de flexión en tres puntos

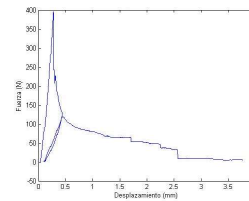
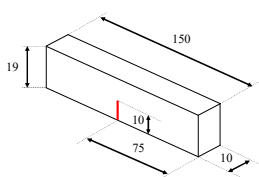


Ensayos de flexión y curvas fuerza-desplazamiento



Ensayo con crecimiento de grieta paralelo a las fibras

Dimensiones de las probetas (cotas en mm)



Ensayo con crecimiento de grieta perpendicular a las fibras

Se genera una pre-grieta introduciendo una lámina antiadherente en los laminados durante el apilado del material

Resultados de los ensayos de flexión a tres puntos

Ensayo	Tenacidad a fractura (J/m ²)	DST (J/m ²)	CV (%)
Paralelo a las fibras	561.99	36.55	6.5
Perpendicular a las fibras	408.53	16.07	3.93

Conclusiones

Se ha evaluado la tenacidad a fractura transversal en un material compuesto propiciando la propagación de las grietas en sentido paralelo a las fibras ($G_{I,cl}$) y perpendicular a las mismas ($G_{I,ct}$). A la vista de los resultados, puede determinarse que ambos valores de la tenacidad a fractura son considerablemente diferentes, siendo mayor para el caso de propagación de la grieta en la dirección paralela a las fibras, demostrando que en ningún caso debe tratarse por igual, desde el punto de vista de la tenacidad a fractura, la propagación de grietas intralaminar en direcciones perpendicular y paralela a las fibras, tal como se ha hecho tradicionalmente.

Agradecimientos

Este trabajo ha sido financiado por el Ministerio de Ciencia e Innovación (Proyecto MAT2009-14022), el Ministerio de Economía y Competitividad y el Fondo Europeo de Desarrollo Regional (Proyectos MAT2012-37387, MAT2015-71036-P y MAT2016-80879-P) y por la Consejería de Innovación, Ciencia y Empresa de la Junta de Andalucía y el Fondo Social Europeo (Proyecto P08-TEP-4051).

Referencias

- [1] Pinho, S.T., P. Robinson, and L. Iannucci. Developing a four point bend specimen to measure the mode I intralaminar fracture toughness of unidirectional laminated composites. Composites Science and Technology (2009) 69(7-8): 1303-1309.
- [2] Airbus. Carbon Fibre Reinforced Plastics. Determination of fracture toughness energy of bonded joints. Mode I, G_{IC}. Issue 1. AITM 1-0053 2006.
- [3] ISO Standard. Fibre-reinforced plastic composites - Determination of mode I interlaminar fracture toughness, G_{IC} for unidirectionally reinforced materials. Geneva, Switzerland. ISO 15024 2001.
- [4] F. Cepero, I.G. García, J. Justo, V. Mantić, F. Paris, A. Barros. Comparación experimental de la tenacidad a fractura transversal de laminados unidireccionales correspondientes al crecimiento longitudinal o transversal de grietas. MATCOMP 15 (2015) 1165-1170.
- [5] F. Cepero, I.G. García, J. Justo, V. Mantić. Experimental comparison between the transverse fracture toughness of a unidirectional laminate corresponding to either longitudinal or transverse crack growth. 16th European Conference on Composite Materials, ECCM16 (2014).

A.2.4 Poster 4

Conference: *Tech Fellows, 2018.*



Effect of cutter geometry on machining induced damage in orthogonal cutting of UD polymer composites : FE study

F. Cepero-Mejias^{a,b,c}, J.L. Curiel-Sosa^{b,c} and V.A. Phadnis^d

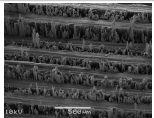
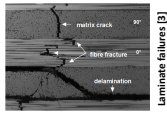
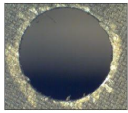
^aIndustrial Doctorate Centre in Machining Science, The University of Sheffield, Sir Frederick Mappin Building, Mappin Street, S1 3JD Sheffield, United Kingdom.
^bComputer-Aided Aerospace & Mechanical Engineering (CA2M) Research Group, Sir Frederick Mappin Building, Mappin Street, S1 3JD Sheffield, United Kingdom.
^cDepartment of Mechanical Engineering, The University of Sheffield, Sir Frederick Mappin Building, Mappin Street, S1 3JD Sheffield, United Kingdom.
^dAMRC with Boeing, Advanced Manufacturing Park, Wallis Way, Catliff, Rotherham, S605TZ, United Kingdom.

Composite machining failures

Post-machining damages in polymer based composites

Composite machining operations are required to meet with the strict dimensional tolerance and assembly demands. However, these operations produce materials defects which affect the structural and dimensional requirements. Main damage modes are:

- Fibre buckling and breakage
- Fibre pull-out
- Fibre-matrix debonding
- Matrix compression and traction
- Delamination
- Matrix thermal degradation



Damage model

- Experimental investigations are expensive and time consuming to optimize cutting configuration.
- FE models offer a viable option to enhance the machining design.
- Complex damage algorithms are required.

Constitutive equations

$$\begin{bmatrix} \sigma_{11} \\ \sigma_{22} \\ \sigma_{12} \end{bmatrix} = \frac{1}{D} \begin{bmatrix} (1-d_f)E_{11} & (1-d_f)(1-d_m)v_{12}E_{11} & 0 \\ (1-d_f)(1-d_m)v_{12}E_{11} & (1-d_m)E_{22} & 0 \\ 0 & 0 & (1-d_f)G_{12} \end{bmatrix} \begin{bmatrix} \epsilon_{11} \\ \epsilon_{22} \\ \epsilon_{12} \end{bmatrix}$$

where $D = 1 - (1-d_f)(1-d_m)v_{12}v_{21}$; $d_f = 1 - (1-d_{f1})(1-d_{f2})(1-d_{mc})$; $d_m = \max\{d_{m1}, d_{m2}\}$; $d_{f1} = \max\{d_{f1}, d_{f2}\}$ and $d = (f_1, f_2, m, mc)$

Damage initiation

Fibre (Maximum stress criterion)

$$F_{f1} = \frac{\sigma_{11}}{X_t} = 1$$

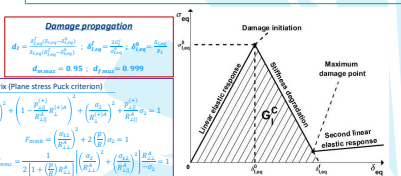
$$F_{f2} = \frac{|\sigma_{22}|}{X_c} = 1$$

Matrix (Plane stress Puck criterion)

$$F_{m1} = F_{m2} = \left(\frac{\sigma_{11}}{X_{t1}} \right)^2 + \left(1 + \frac{v_{12}^2}{X_{t1}^2} \right) \left(\frac{\sigma_{12}}{X_{t1}} \right)^2 + \left(\frac{\sigma_{22}}{X_{c1}} \right)^2 = 1$$

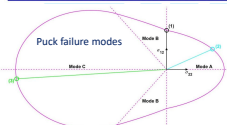
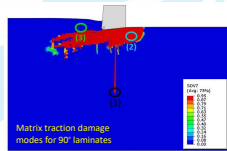
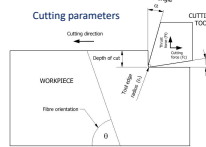
$$F_{m2} = \left(\frac{\sigma_{22}}{X_{t2}} \right)^2 + \left(1 + \frac{v_{21}^2}{X_{t2}^2} \right) \left(\frac{\sigma_{12}}{X_{t2}} \right)^2 + \left(\frac{\sigma_{11}}{X_{c2}} \right)^2 = 1$$

$$F_{mc} = \max\{F_{m1}, F_{m2}\}$$

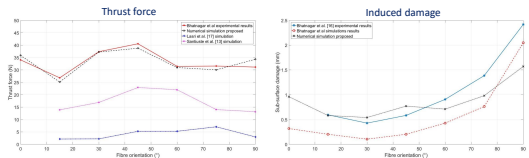


Machined area analysis and FE model validation

- Different tool edge radius, rake and relief angles and CFRP and GFRP laminates are studied.
- Matrix induced damages are predominant.
- Three damage zones are distinguished:
 - Zone 1: Shear fail.
 - Zone 2: Matrix traction.
 - Zone 3: Matrix compression.



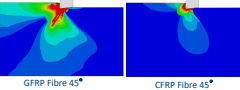
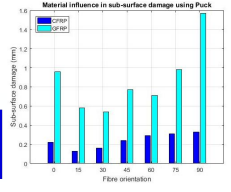
Damage model and bouncing back (partial thickness recovery) implementation enhanced other previous thrust force and induced damage numerical predictions.



Results and discussion

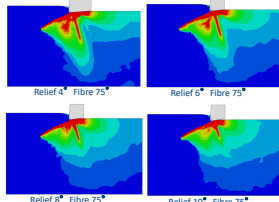
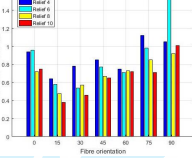
Workpiece material

- Important reduction of induced damage is obtained machining CFRP composites
- All fibre orientations reduced damage levels 2 or 3 times machining a CFRP laminate.



Relief angle

Relief angle influence in sub-surface damage using Puck

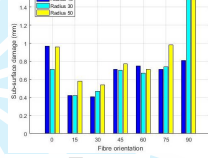


Observations

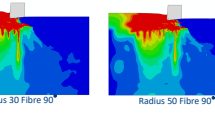
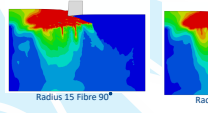
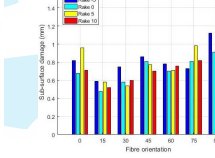
- In general, high the use of high relief angles is recommended to reduce laminate damage.
- For the fibre orientation of 60° the relief angle effects in laminate damage are negligible.
- Relief angle of 6° increase significantly the damage for fibre orientation of 90°.

Rake angle and tool edge radius

Edge tool radius influence in sub-surface damage using Puck



Rake angle influence in sub-surface damage using Puck



Observations

- In general terms, the rake angle and tool edge radius studied did not affect considerably to the induced damage.
- Rake angle of 0° is recommend to decrease the sub-surface damage levels.
- The damage is doubled when tool edge radius pass from 15 μm to 30 μm for a fibre orientation of 90°.

Conclusions and future work

Conclusions
 CFRP shows more brittle and better machined surface quality than GFRP composites. High relief angles reduce considerably the levels of induced machining damage. Rake angle and tool edge radius simulated did not show a remarkable influence on the sub-surface damage.

Future works
 Development of a 3D FEA of orthogonal cutting and drilling operations. Introduction of plastic and thermal matrix effects. Tool degradation and delamination assessment.

References

- S. T. Pinho, P. Robinson, and L. Iannucci, "Fracture toughness of the tensile and compressive fibre failure modes in laminated composites," *Composites Science and Technology*, vol. 66, no. 13, pp. 2069–2079, 2006.
- Sandvik Coromat, "Machining carbon fibre materials", 2010.
- D. Svensson, Experimental methods to determine model parameters for failure modes of CFRP. PhD thesis, Chalmers University of Technology, 2013.
- D. I. Mortell, D. A. Tanner, and C. T. McCarthy, "An experimental investigation into multi-scale damage progression in laminated composites in bending." *Composite Structures*, vol. 149, no. March, pp. 33–40, 2016.

A.2.5 Poster 5

Conference: *Tech Fellows, 2017.*



Damage model design for composite materials



F. Cepero^a, J.L. Curiel-Sosa^b and V.A. Phadnis^c

^aIndustrial Doctorate Centre in Machining Science, The University of Sheffield.
^bDept. of Mechanical Engineering, The University of Sheffield
^cThe Advanced Manufacturing Research Centre, The University of Sheffield.

Context

Advanced composite materials

- High strength-weight ratio
- Excellent resistance to fatigue and corrosion
- Satisfactory durability

However, its potential is not fully exploited:

- High security factors
- Many experimental tests (e.g. 10,000 tests for certification)

However, modelling failure in advanced composite materials have limitations:

- Stability problems in FE models due to the drastic loss of properties after failure
- Not accurate behaviour predicted after failure assumption
- Damage model necessary to be inserted

Better computational tools

- Reduce tests
- Reduce costs

Different composite failure criteria

- Some articles like [2] and [3] develop some damage criteria for composites based on famous failure criteria developed in some machining operations.
- The damage design of this work is based on Hashing criteria for the fibre and in the Puck criteria for the matrix, taken equations from [1] for only plane stress problems.

Fibre Hashing criterion

$$\left(\frac{\sigma_{11}}{X_t}\right)^2 + \left(\frac{\sigma_{12}}{S}\right)^2 = 1 \quad (\sigma_{11} > 0)$$

$$|\sigma_{11}| = X_c \quad (\sigma_{11} < 0, X_c > 0)$$

Matrix Puck criterion

$$\sqrt{\left(\frac{\sigma_{12}}{R_{12}}\right)^2 + \left(1 - \frac{p_{12}^{(1)}}{R_{22}^{(1)}} R_{11}^{(1)A}\right)^2 + \left(\frac{\sigma_{22}}{R_{22}^{(1)A}} + \frac{p_{12}^{(1)}}{R_{22}^{(1)}}\right)^2} \sigma_2 = 1 \quad \text{Mode A}$$

$$\left(\frac{\sigma_{12}}{R_{12}}\right)^2 + 2 \left(\frac{p_{12}}{R}\right) \sigma_2 = 1 \quad \text{Mode B}$$

$$\frac{1}{2} \left[\frac{(\sigma_{12})^2}{R_{12}^2} + \left(\frac{\sigma_{22}}{R_{22}^{(1)}}\right)^2 \right] = 1 \quad \text{Mode C}$$

Damage implementation

- Variable "Dam" denote the level of damage between 0 (no damage) and 1 (failure).
- Variable "exp" is introduced in order to obtain multiple damage models.
- Strain domain equation is calculated introducing a linear damage in the constitutive equations of a composite material.

Stress Domain

Strain Domain

Matrix Puck criterion

$$\frac{D}{2} \sigma_{12}^2 + \frac{E}{2} (\sigma_{11} + \frac{E}{2} (1 - \text{Dam})^{\text{exp}})^2 = (1 - \text{Dam})^{\text{exp}} \quad \text{Mode A}$$

$$D \sigma_{12}^2 + 2B \sigma_{12} (1 - \text{Dam})^{\text{exp}} = (1 - \text{Dam})^{\text{exp}} \quad \text{Mode B}$$

$$0 (\sigma_{12} + 7(1 - \text{Dam})^{\text{exp}}) + 1 \sigma_{22}^2 = (1 - \text{Dam})^{\text{exp}} \quad \text{Mode C}$$

Fibre Hashing criterion

$$\left(\frac{\sigma_{11}}{X_t}\right)^2 + \left(\frac{\sigma_{12}}{S}\right)^2 = (1 - \text{Dam})^{\text{exp}} \quad (\sigma_{11} > 0)$$

$$-\frac{\sigma_{11}}{X_c} = (1 - \text{Dam})^{\text{exp}} \quad (\sigma_{11} < 0, X_c > 0)$$

Matrix Puck criterion

$$\frac{D}{2} \left[(1 - \text{Dam})^{\text{exp}} \sigma_{12}^2 + \left(1 - \text{Dam} \left(\frac{p_{12}^{(1)}}{R_{22}^{(1)}} R_{11}^{(1)A} + \frac{E}{2} (1 - \text{Dam})^{\text{exp}} \right) \right)^2 + \left(\frac{\sigma_{22}}{R_{22}^{(1)A}} + \frac{p_{12}^{(1)}}{R_{22}^{(1)}} \right)^2 \right] = (1 - \text{Dam})^{\text{exp}} \quad \text{Mode A}$$

$$D \sigma_{12}^2 + 2B \sigma_{12} (1 - \text{Dam})^{\text{exp}} + 2 \left[(1 - \text{Dam})^{\text{exp}} \sigma_{12} + (1 - \text{Dam})^{\text{exp}} \left(\frac{p_{12}^{(1)}}{R_{22}^{(1)}} R_{11}^{(1)A} + \frac{E}{2} (1 - \text{Dam})^{\text{exp}} \right) \right] \sigma_{22} = (1 - \text{Dam})^{\text{exp}} \quad \text{Mode B}$$

$$0 \left[(1 - \text{Dam})^{\text{exp}} \sigma_{12} + (1 - \text{Dam})^{\text{exp}} \left(\frac{p_{12}^{(1)}}{R_{22}^{(1)}} R_{11}^{(1)A} + \frac{E}{2} (1 - \text{Dam})^{\text{exp}} \right) \right] + \sigma_{22}^2 = (1 - \text{Dam})^{\text{exp}} \quad \text{Mode C}$$

Fibre Hashing criterion

$$\left[(1 - \text{Dam})^{\text{exp}} \sigma_{12}^2 + \left(1 - \text{Dam} \left(\frac{p_{12}^{(1)}}{R_{22}^{(1)}} R_{11}^{(1)A} + \frac{E}{2} (1 - \text{Dam})^{\text{exp}} \right) \right)^2 + \left(\frac{\sigma_{22}}{R_{22}^{(1)A}} + \frac{p_{12}^{(1)}}{R_{22}^{(1)}} \right)^2 \right] = (1 - \text{Dam})^{\text{exp}} \quad (\sigma_{12} > 0)$$

$$\left[(1 - \text{Dam})^{\text{exp}} \sigma_{12}^2 + \left(1 - \text{Dam} \left(\frac{p_{12}^{(1)}}{R_{22}^{(1)}} R_{11}^{(1)A} + \frac{E}{2} (1 - \text{Dam})^{\text{exp}} \right) \right)^2 + \left(\frac{\sigma_{22}}{R_{22}^{(1)A}} + \frac{p_{12}^{(1)}}{R_{22}^{(1)}} \right)^2 \right] = (1 - \text{Dam})^{\text{exp}} \quad (\sigma_{12} < 0, X_c > 0)$$

Multiple damage models obtained

- The better damage behaviour must be determined with previous results from previous simple test.
- Only the results with lower damage values are taken into account.
- More realistic damage evolution is obtained for values of exp next to 2.

Stress-Damage Evolution

Strain-Damage Evolution

Stress-Strain Evolution

Multiple damage models obtained

- The failure damage surfaces obtained of the damage model with **exp=1.85** are shown as example.

Fibre Damage

Stress Domain

Strain Domain

Matrix Damage

Stress Domain

Strain Domain

Conclusions and future works

Conclusions

- Design of a damage model with different failure modes.
- High flexibility for adapting the model to different test.

Future works

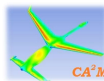
- Implementation damage model in Abaqus subroutines.
- Verification of this damage model with some experimental test

References

- [1] F. París, J. Cañas, J.C. Marin, A. Barroso, Introducción al análisis y diseño con materiales compuestos, Escuela técnica superior de ingenieros (Universidad de Sevilla).
- [2] Vaibhav A. Phadnis, Farrukh Makhdom, Anish Roy, Vadim V. Silberschmidt, Drilling in carbon/ epoxy composites: Experimental investigations and finite element implementation, Composites: Part A 47 (2013) 41–51.
- [3] C. Santiuste, A. Olmedo, X. Soldani, H. Migueluez, Delamination prediction in orthogonal machining of carbon long fiber-reinforced polymer composites, Journal of Reinforced Plastics and Composites 31(13) 875–885.



Advanced Manufacturing Research Centre



Computer-Aided Aerospace & Mechanical Engineering (CA²M) Research Group
www.ca2m.group.shef.ac.uk



Engineering and Physical Sciences Research Council

This work was co-funded through the EPSRC Centre for Doctoral Training in Machining Science (EP/I01800X/1) and by [name of sponsoring company].

Appendix B

Matrix traction failure exposure factors F_{mt} images at the end of the simulation

Standard cutting configuration

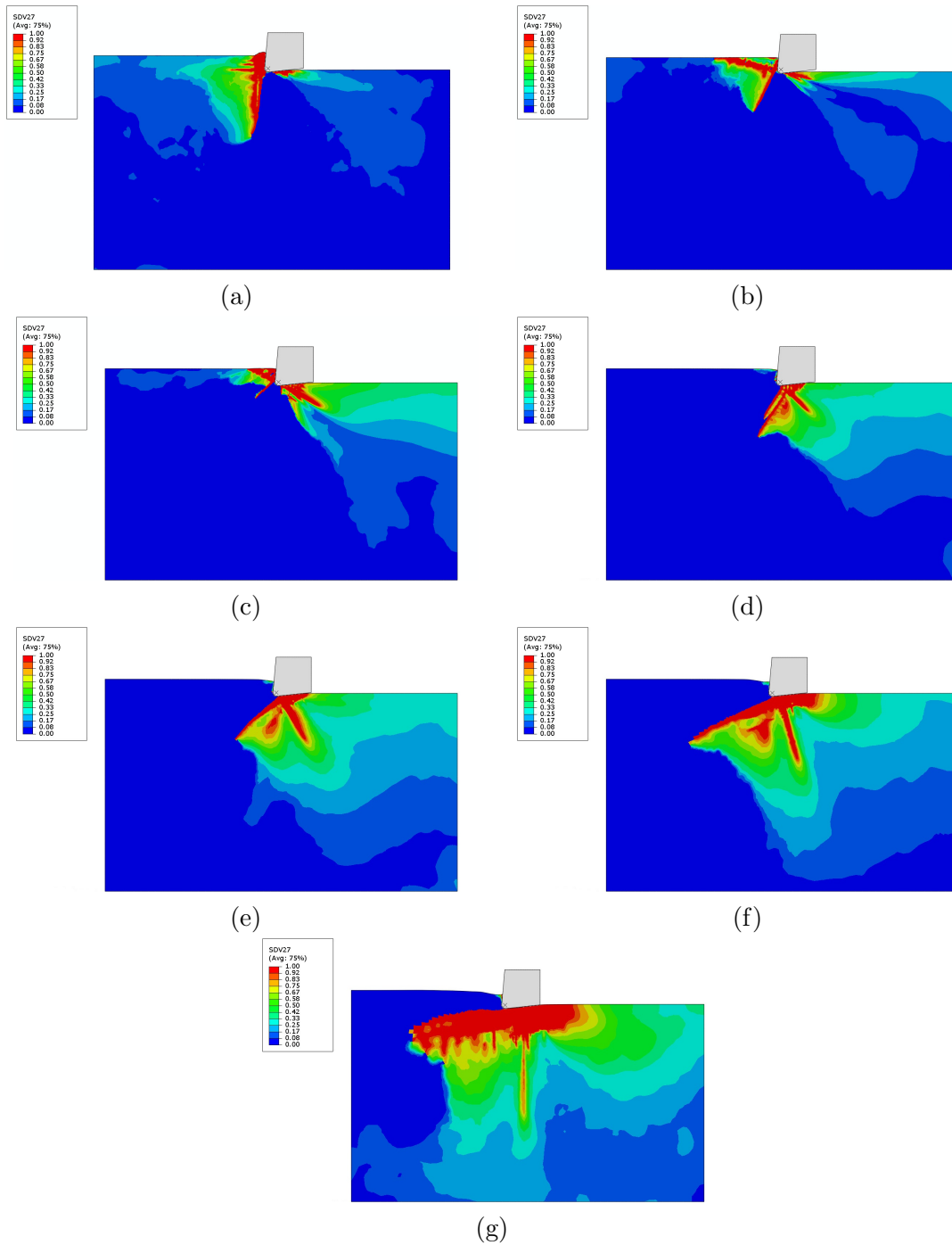


Fig. B.0.1. F_{mt} obtained for fibre orientations (a) 0° (b) 15°, (c) 30°, (d) 45°, (e) 60°, (e) 75° and 90° at final simulation time with the standard cutting configuration.

Cutting configuration with a rake angle of -5°

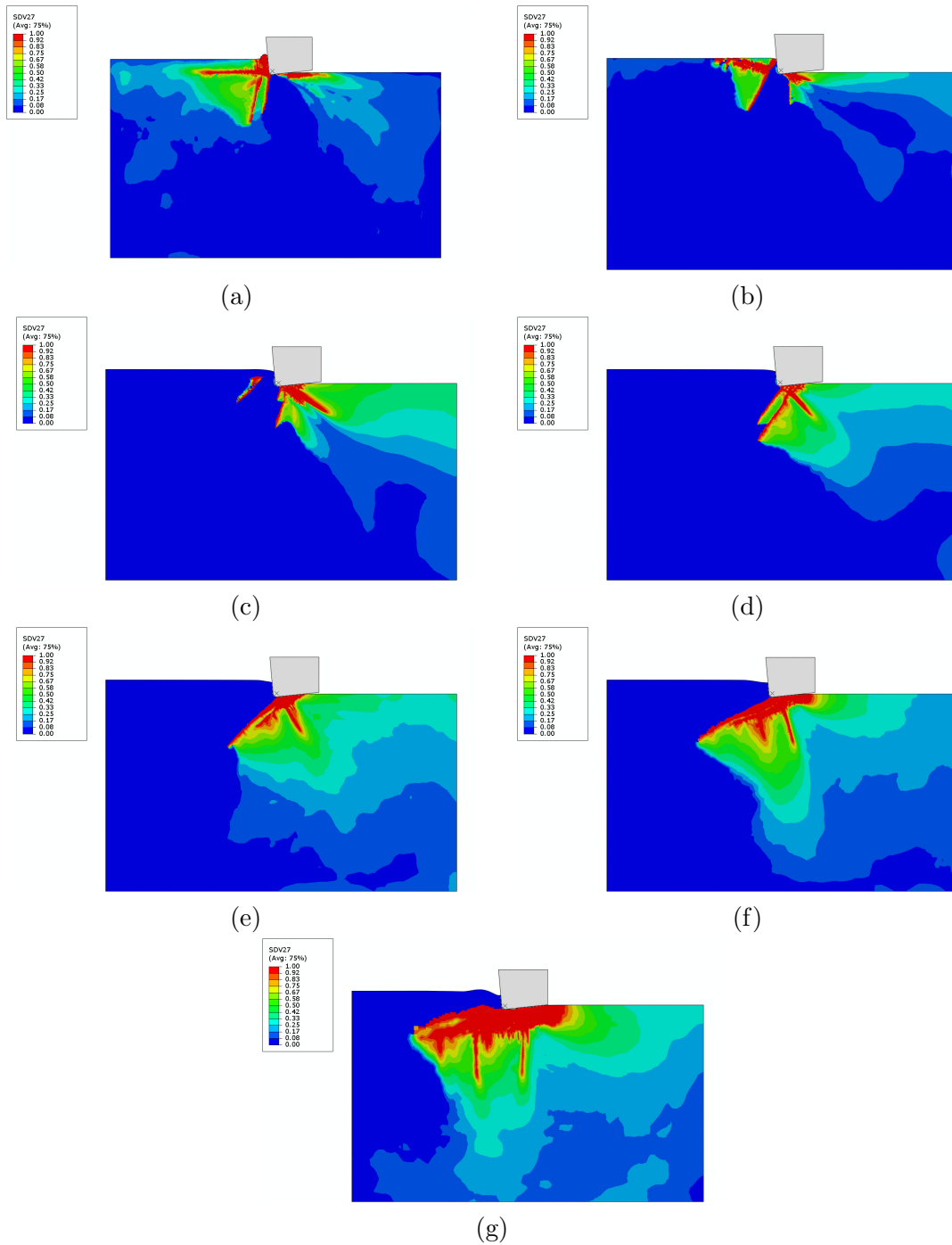


Fig. B.0.2. F_{mt} obtained for fibre orientations (a) 0° (b) 15° , (c) 30° , (d) 45° , (e) 60° , (e) 75° and 90° at final simulation time using a rake angle of -5° .

Cutting configuration with a rake angle of 0°

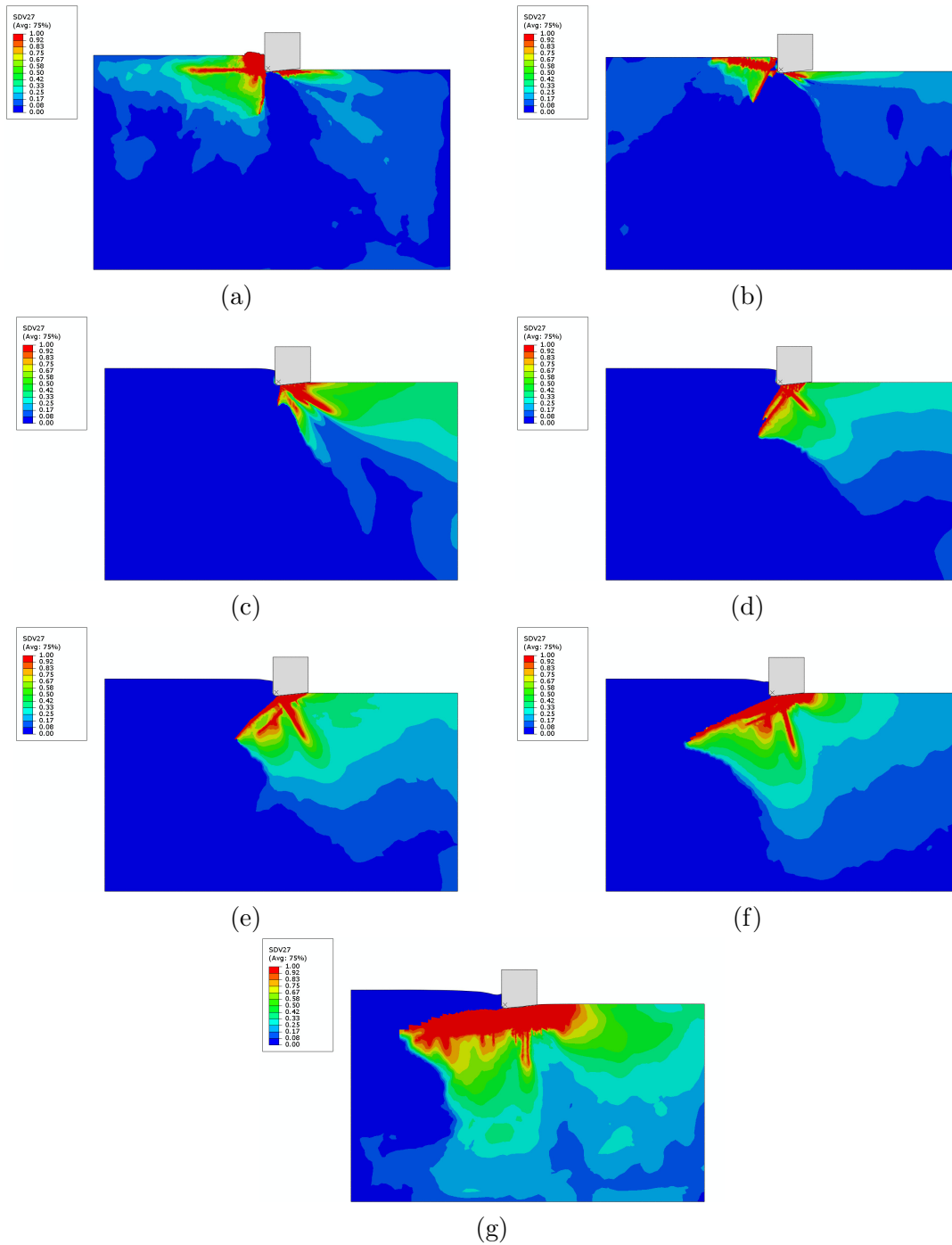


Fig. B.0.3. F_{mt} obtained for fibre orientations (a) 0° (b) 15° , (c) 30° , (d) 45° , (e) 60° , (e) 75° and 90° at final simulation time using a rake angle of 0° .

Cutting configuration with a rake angle of 10°

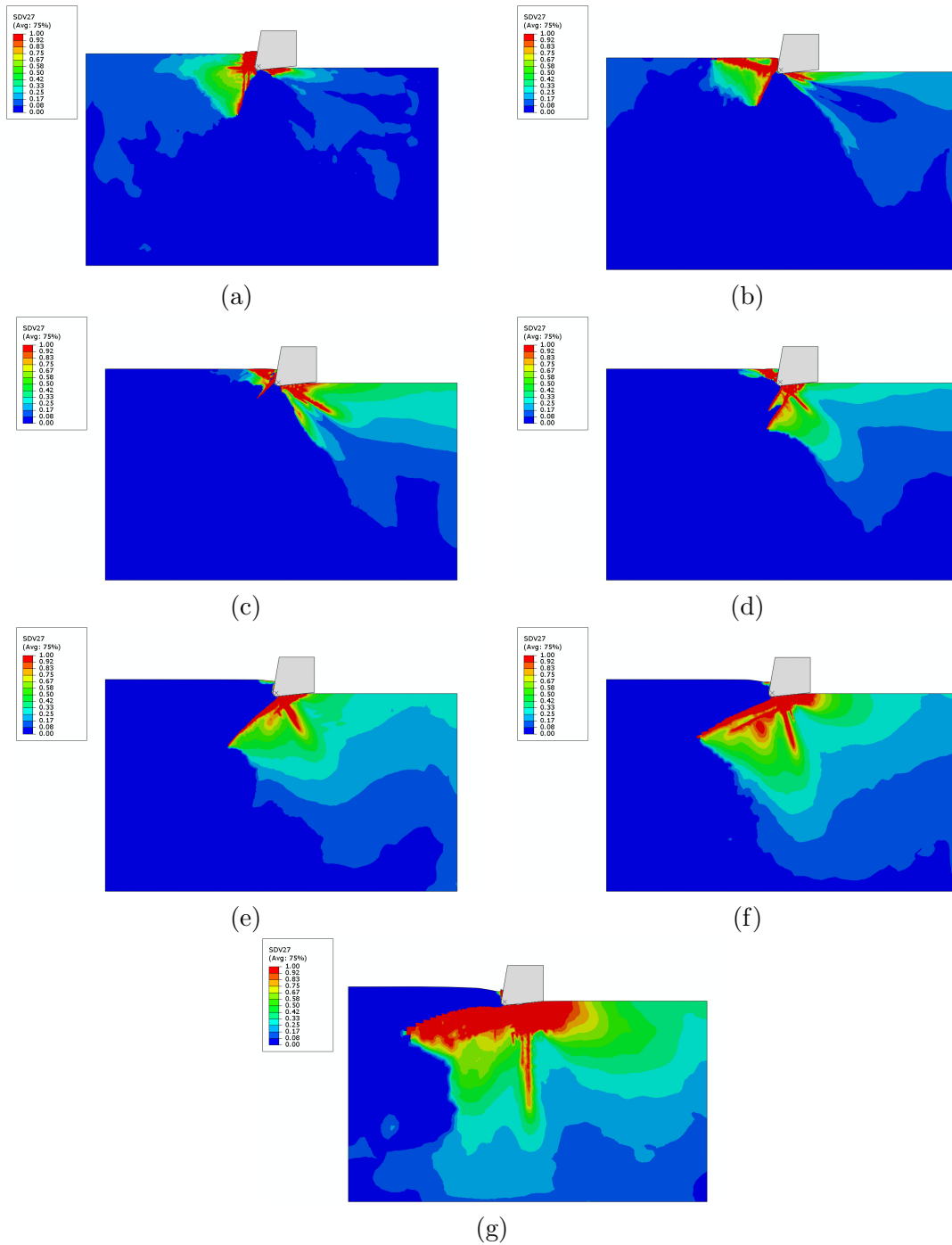


Fig. B.0.4. F_{mt} obtained for fibre orientations (a) 0° (b) 15° , (c) 30° , (d) 45° , (e) 60° , (e) 75° and 90° at final simulation time using a rake angle of 10° .

Cutting configuration with a rake angle of 4°

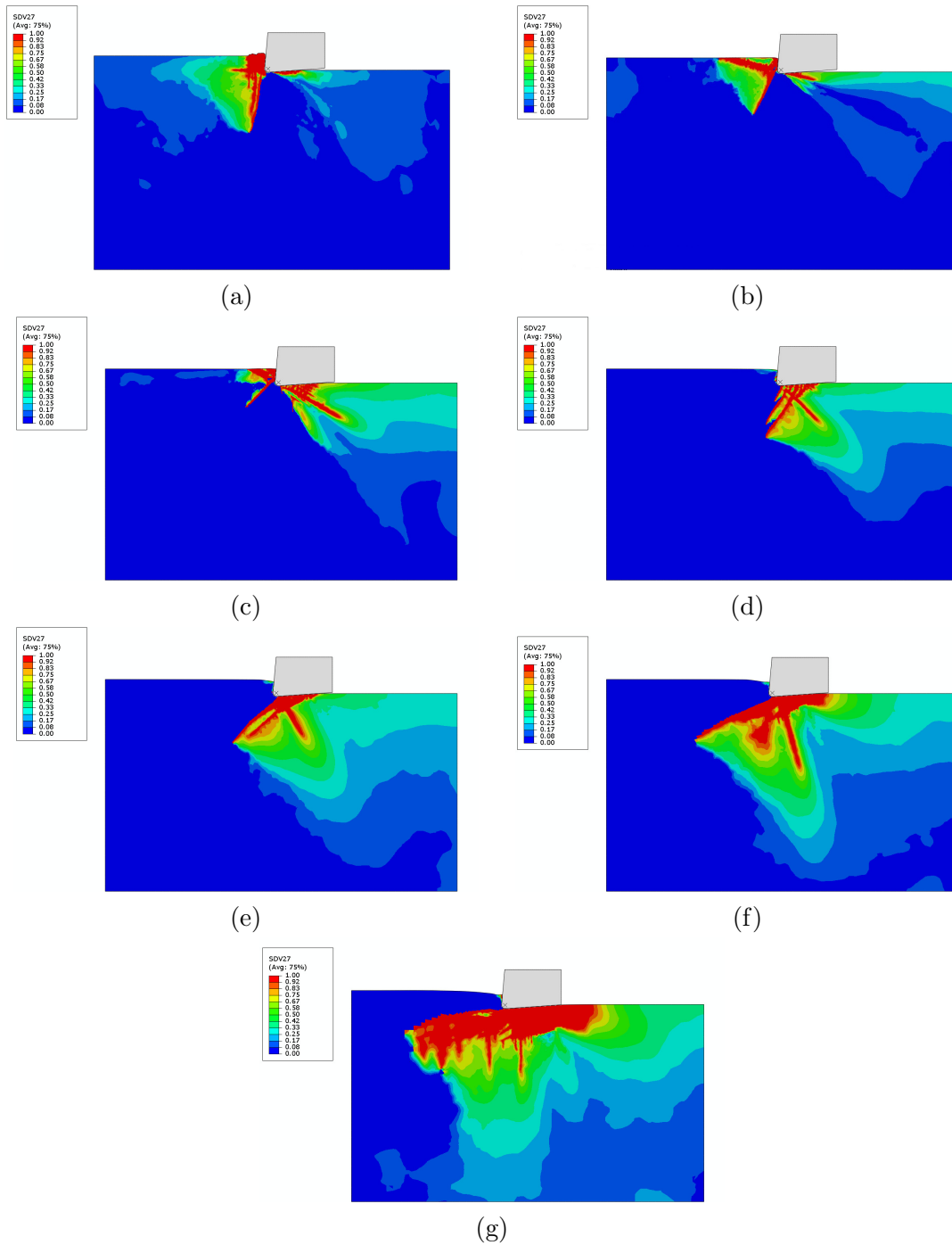


Fig. B.0.5. F_{mt} obtained for fibre orientations (a) 0° (b) 15° , (c) 30° , (d) 45° , (e) 60° , (e) 75° and 90° at final simulation time using a relief angle of 4° .

Cutting configuration with a rake angle of 8°

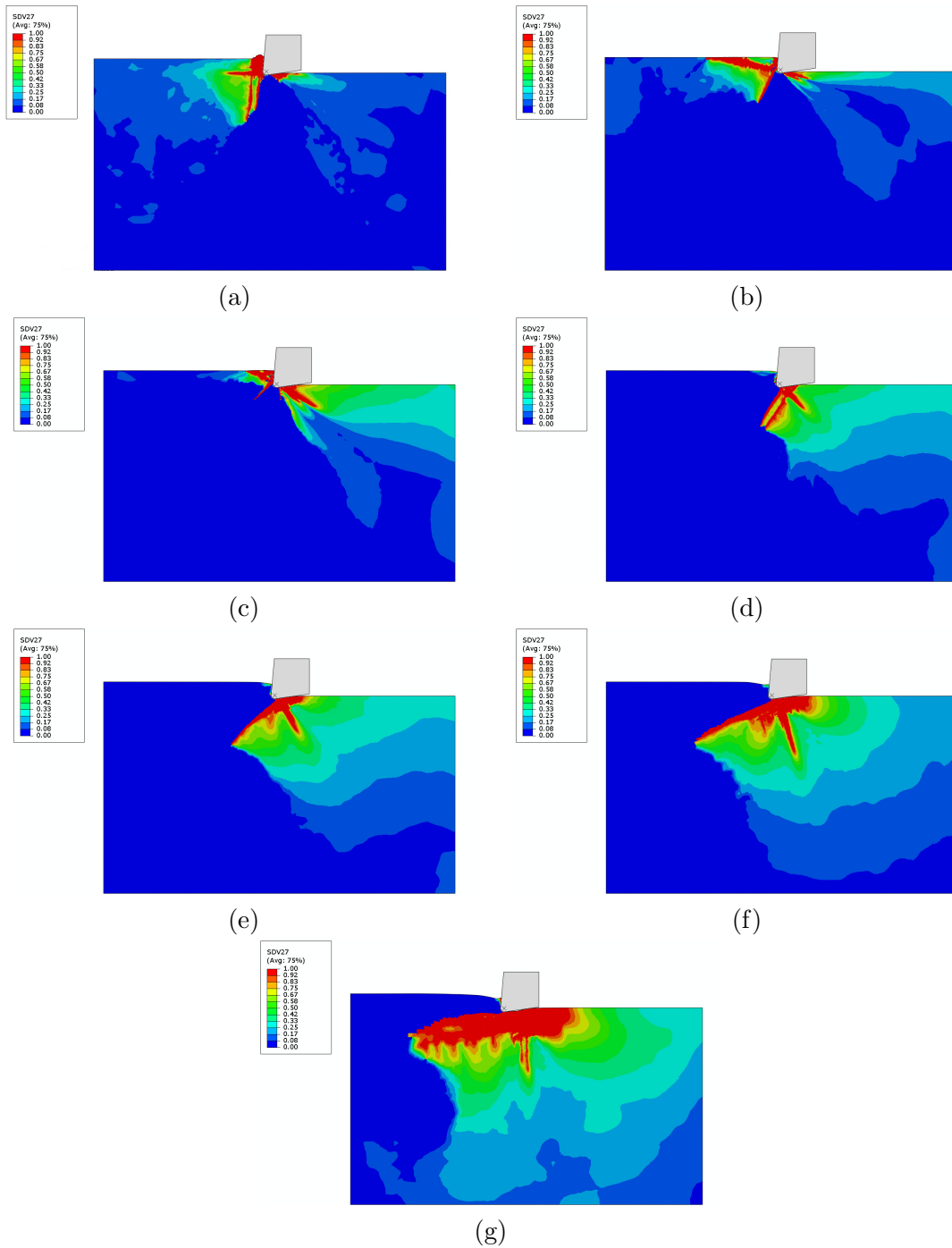


Fig. B.0.6. F_{mt} obtained for fibre orientations (a) 0° (b) 15° , (c) 30° , (d) 45° , (e) 60° , (e) 75° and 90° at final simulation time using a relief angle of 8° .

Cutting configuration with a rake angle of 10°

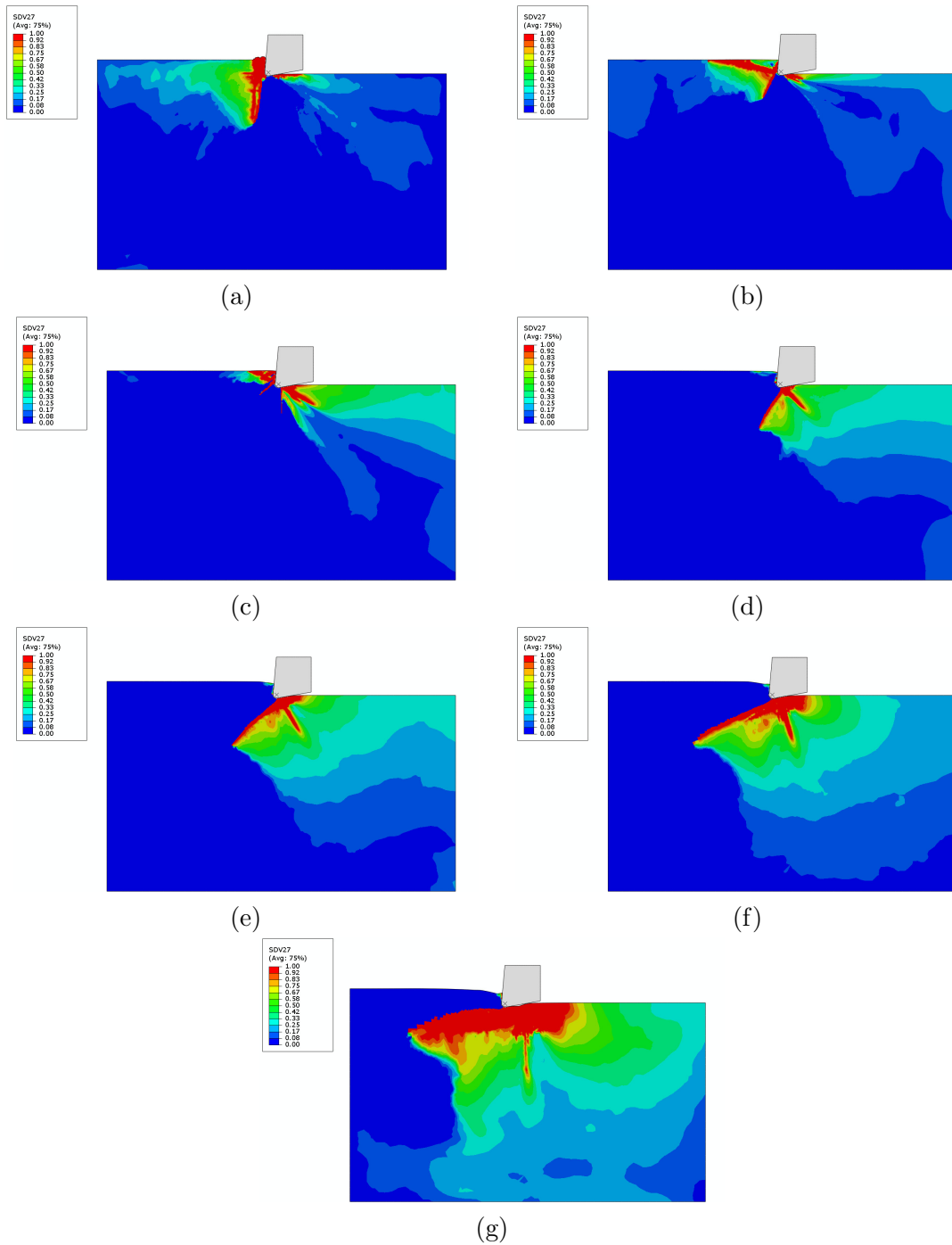


Fig. B.0.7. F_{mt} obtained for fibre orientations (a) 0° (b) 15° , (c) 30° , (d) 45° , (e) 60° , (e) 75° and 90° at final simulation time using a relief angle of 10° .

Cutting configuration with a UD-CFRP workpiece

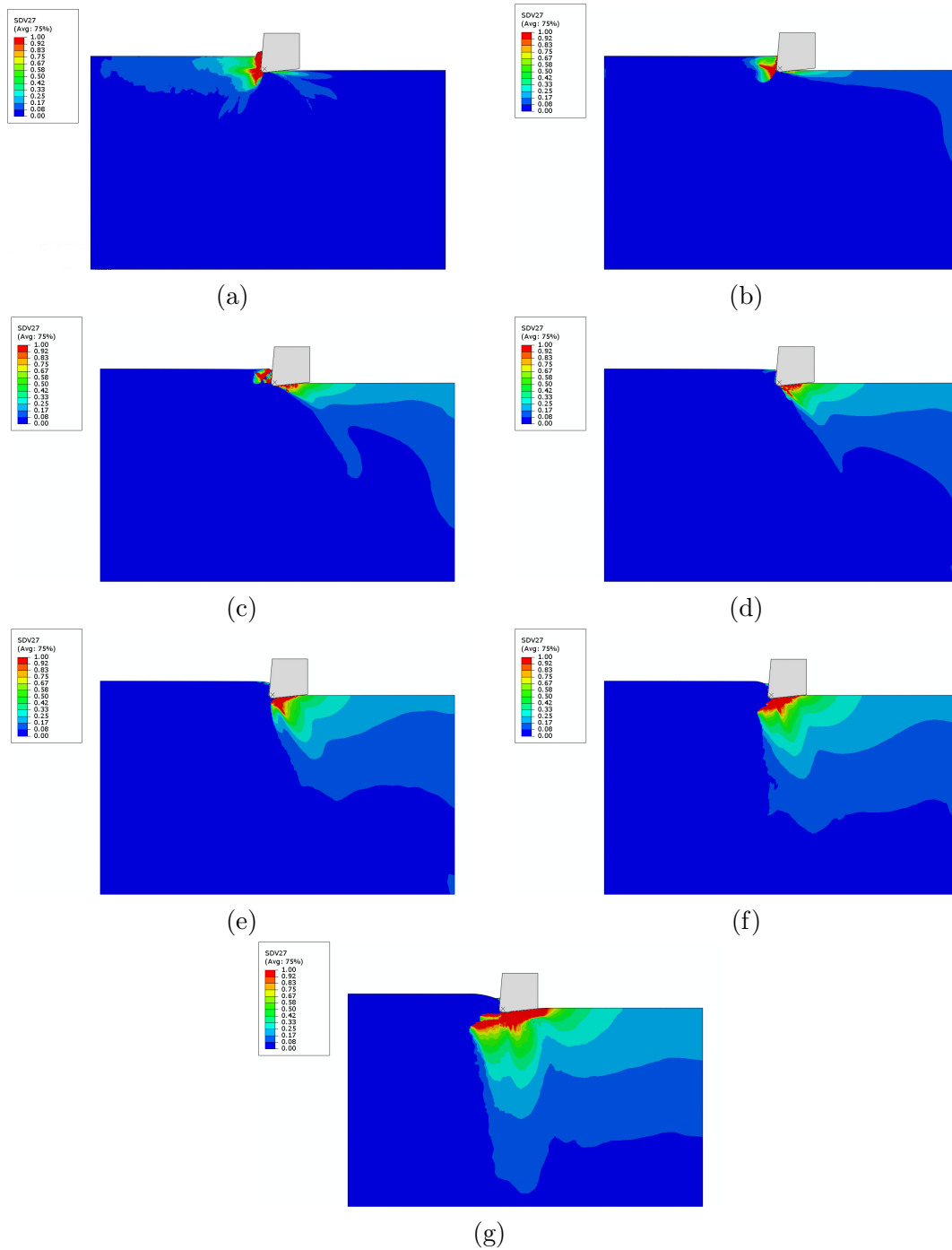


Fig. B.0.8. F_{mt} obtained for fibre orientations (a) 0° (b) 15°, (c) 30°, (d) 45°, (e) 60°, (e) 75° and 90° at final simulation time with a UD-CFRP workpiece.

Cutting configuration with a tool edge radius of $15\mu m$

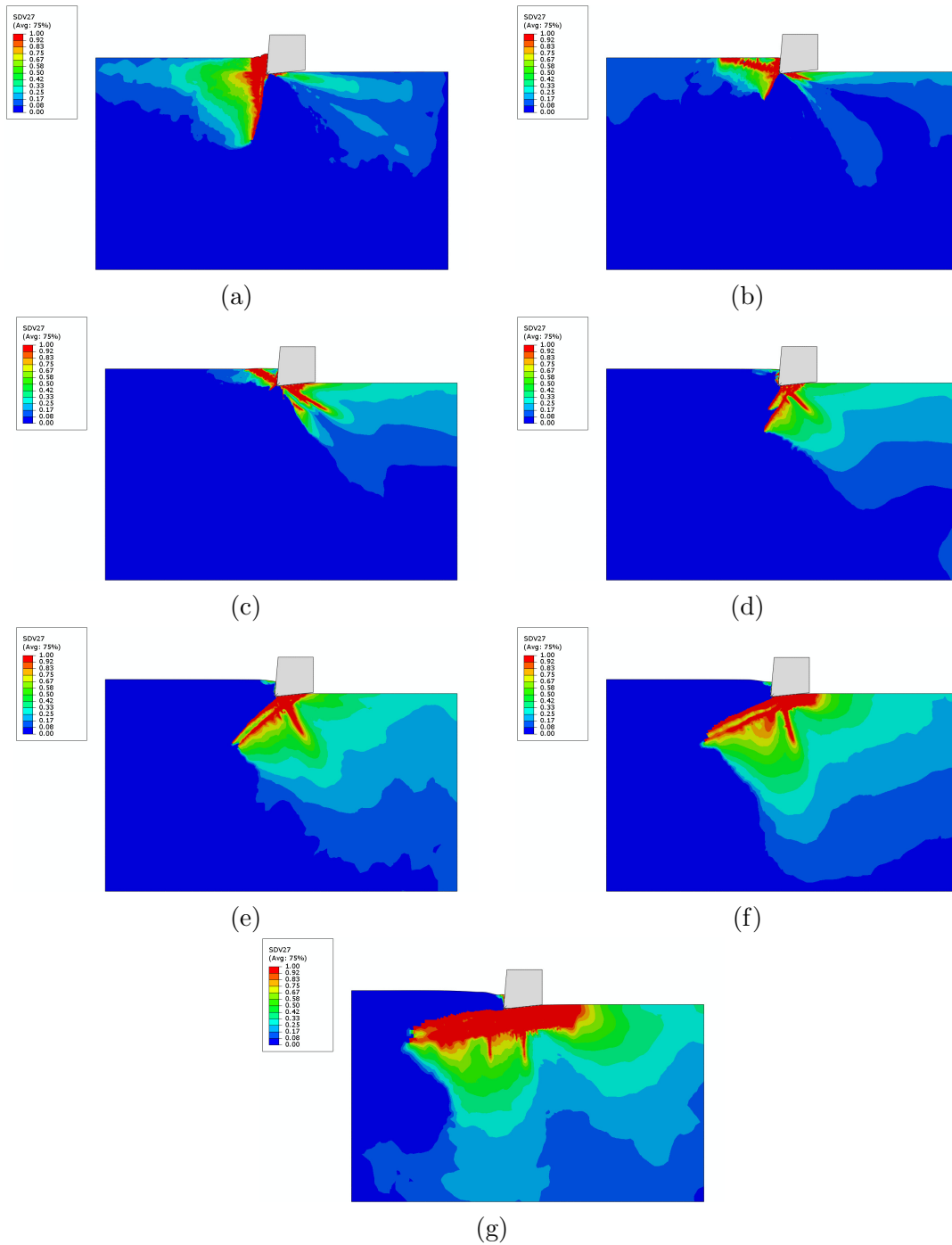


Fig. B.0.9. F_{mt} obtained for fibre orientations (a) 0° (b) 15° , (c) 30° , (d) 45° , (e) 60° , (e) 75° and 90° at final simulation time with a tool edge radius of $15\mu m$.

Cutting configuration with a tool edge radius of $30\mu m$

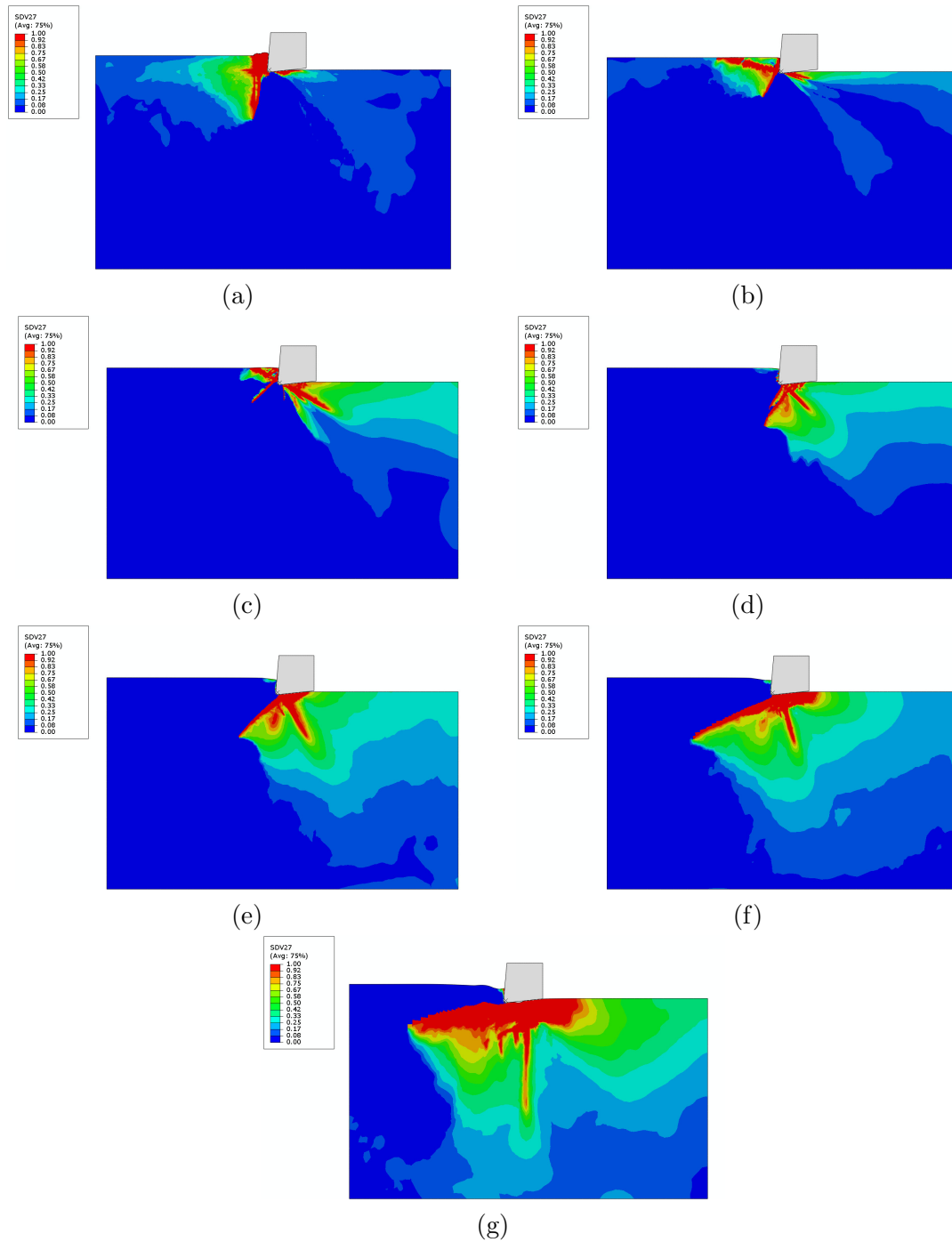


Fig. B.0.10. F_{mt} obtained for fibre orientations (a) 0° (b) 15° , (c) 30° , (d) 45° , (e) 60° , (e) 75° and 90° at final simulation time with a tool edge radius of $30\mu m$.

Appendix C

Matrix compression failure exposure factors F_{mc} images at the end of the simulation

Standard cutting configuration

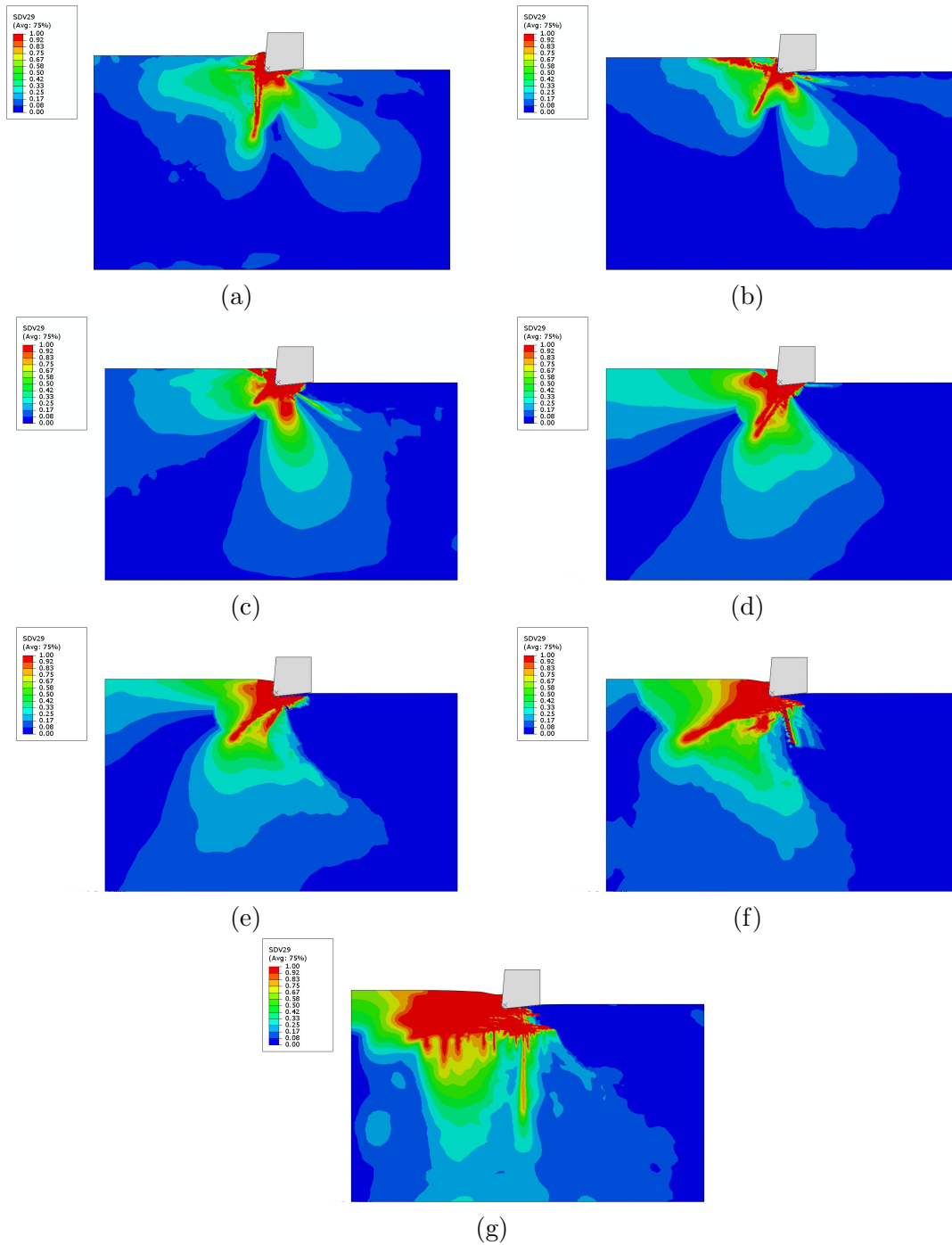


Fig. C.0.1. F_{mc} obtained for fibre orientations (a) 0° (b) 15°, (c) 30°, (d) 45°, (e) 60°, (e) 75° and 90° at final simulation time with the standard cutting configuration.

Cutting configuration with a rake angle of -5°

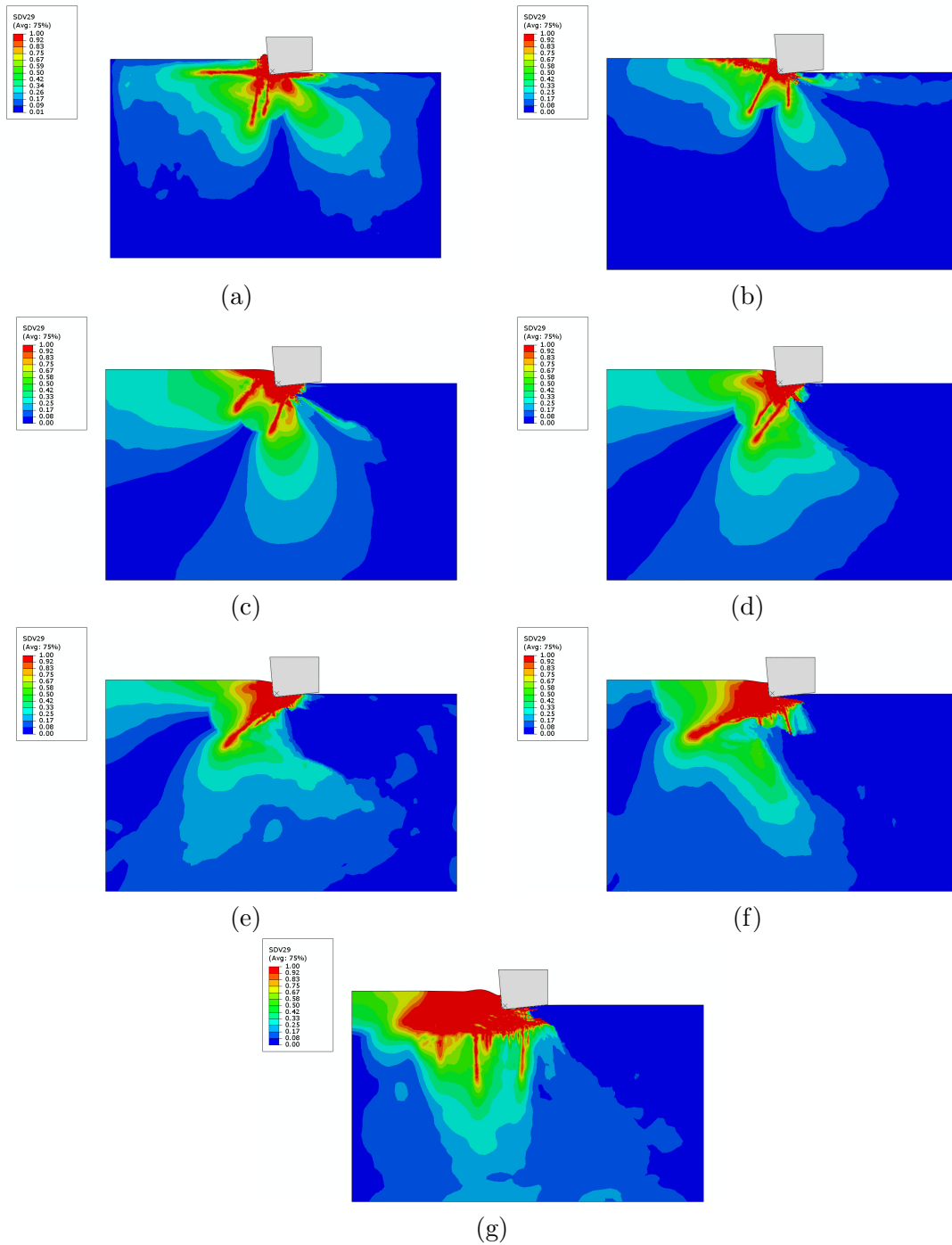


Fig. C.0.2. F_{mc} obtained for fibre orientations (a) 0° (b) 15° , (c) 30° , (d) 45° , (e) 60° , (e) 75° and 90° at final simulation time using a rake angle of -5° .

Cutting configuration with a rake angle of 0°

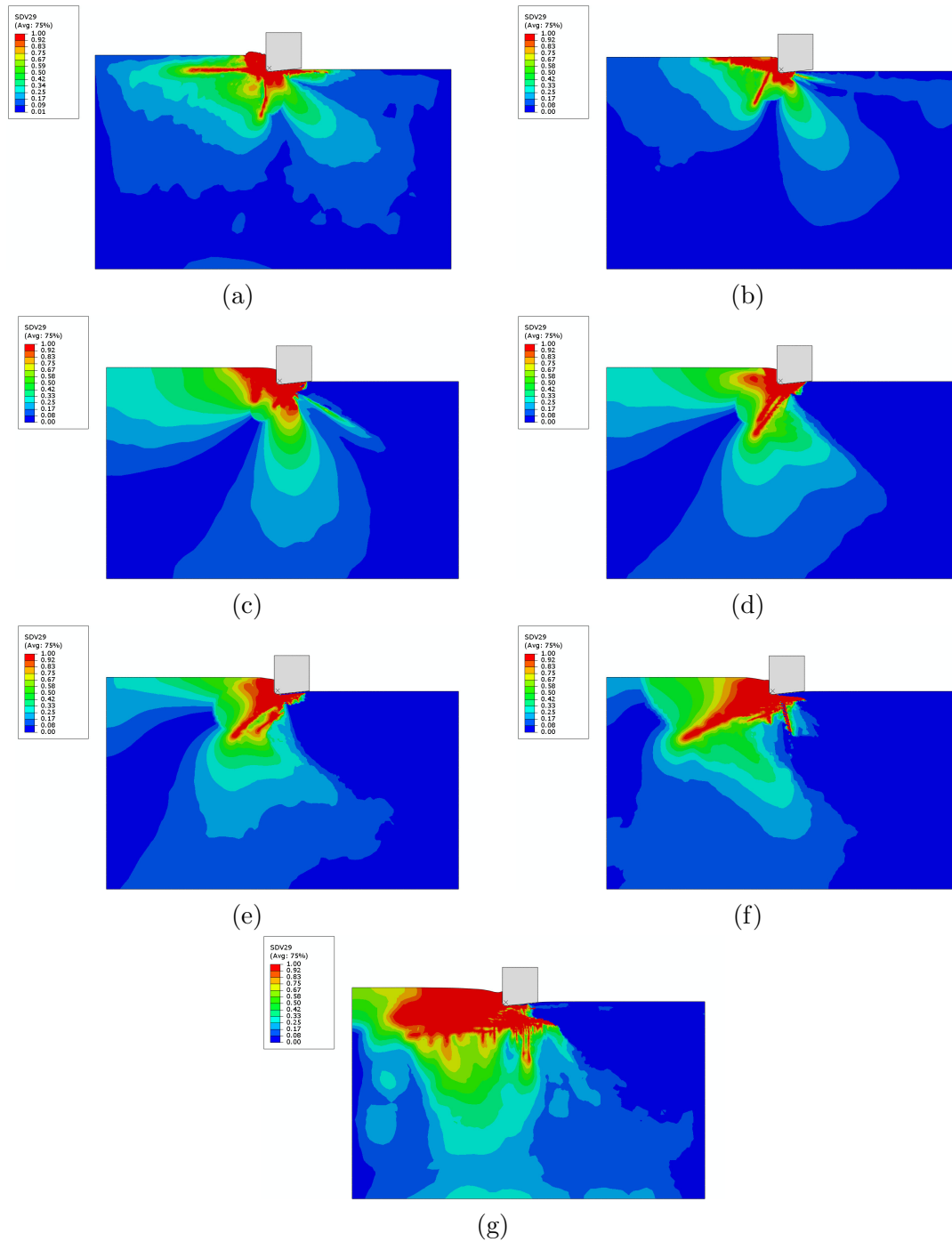


Fig. C.0.3. F_{mc} obtained for fibre orientations (a) 0° (b) 15° , (c) 30° , (d) 45° , (e) 60° , (e) 75° and 90° at final simulation time using a rake angle of 0° .

Cutting configuration with a rake angle of 10°

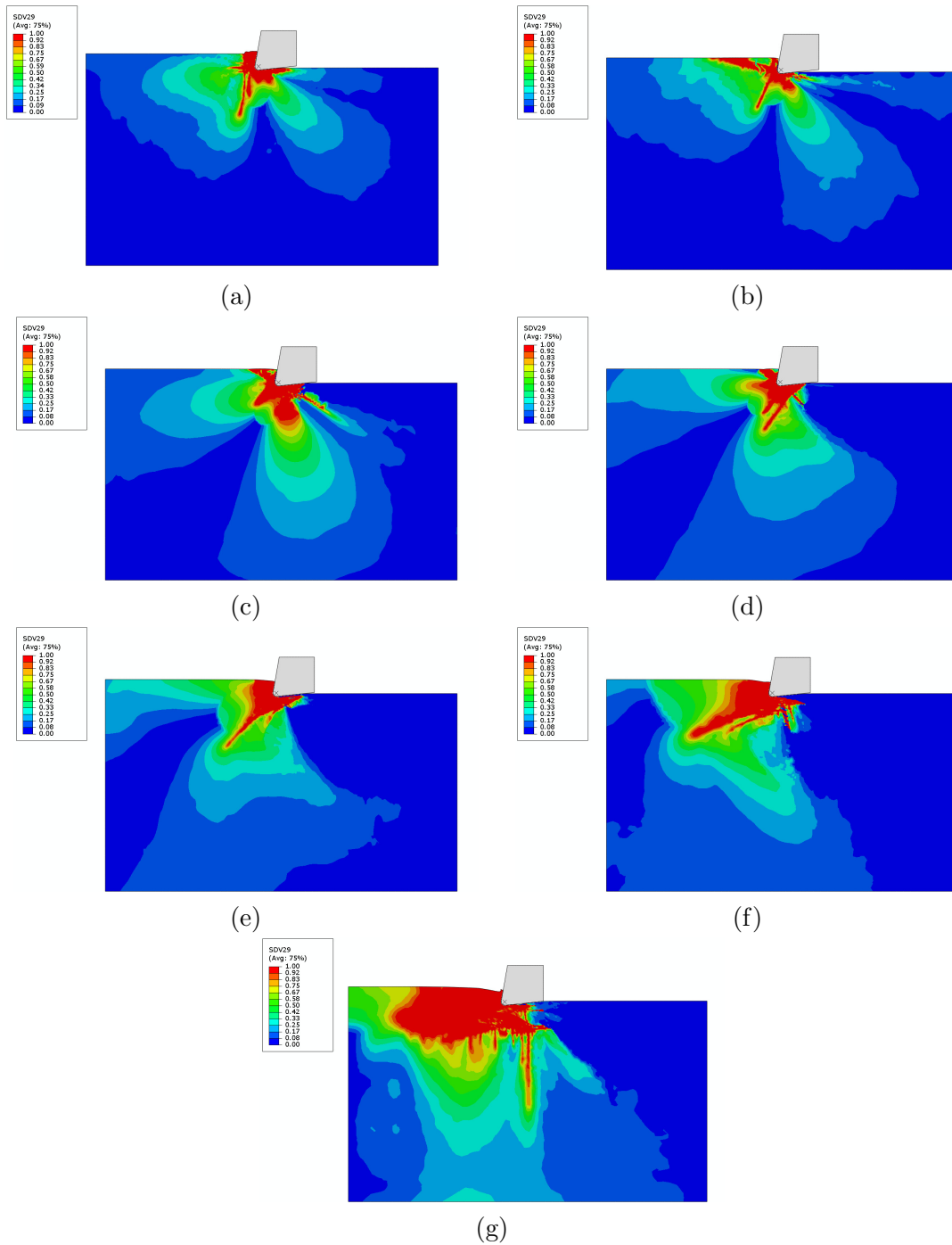


Fig. C.0.4. F_{mc} obtained for fibre orientations (a) 0° (b) 15° , (c) 30° , (d) 45° , (e) 60° , (e) 75° and 90° at final simulation time using a rake angle of 10° .

Cutting configuration with a relief angle of 4°

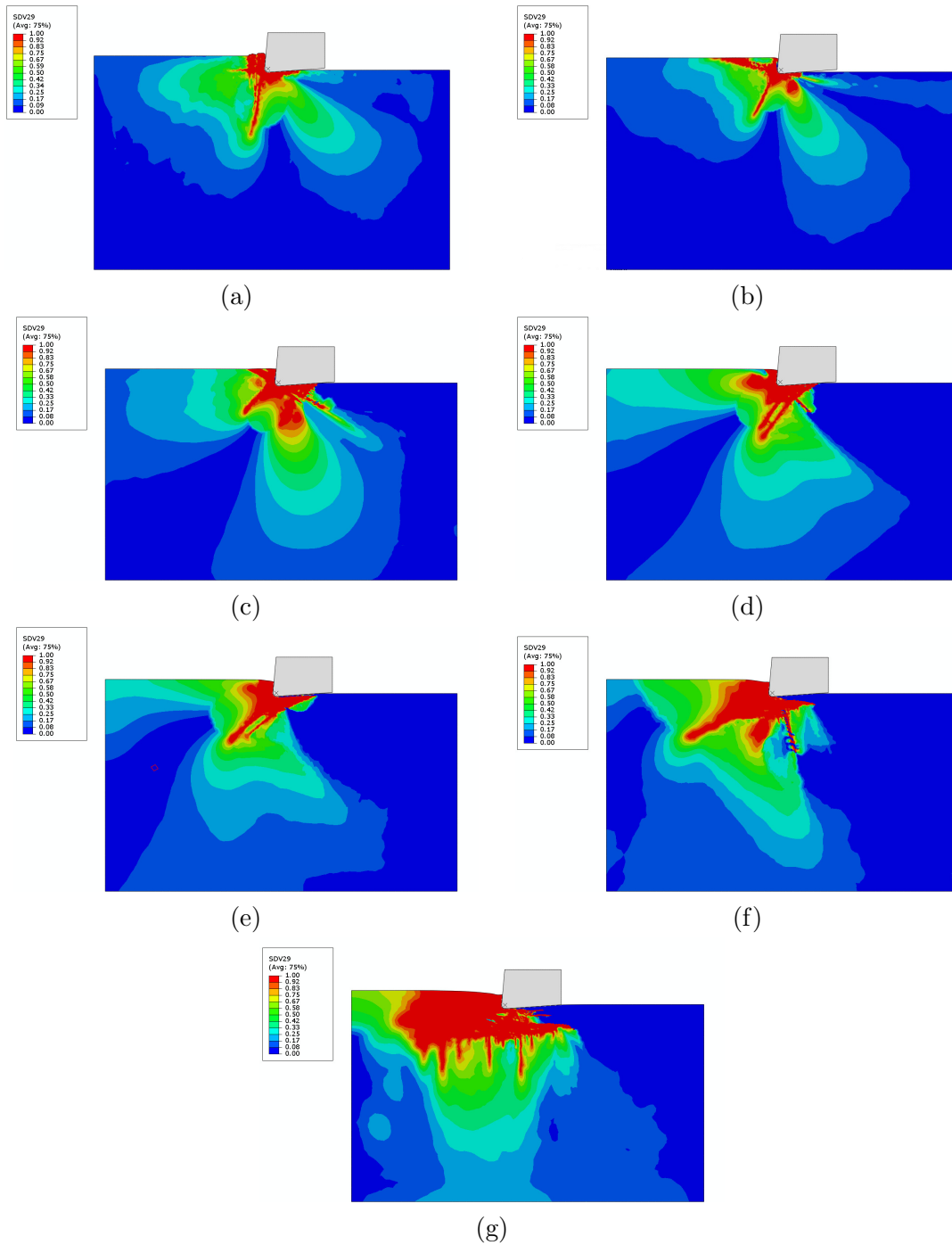


Fig. C.0.5. F_{mc} obtained for fibre orientations (a) 0° (b) 15° , (c) 30° , (d) 45° , (e) 60° , (e) 75° and 90° at final simulation time using a relief angle of 4° .

Cutting configuration with a relief angle of 8°

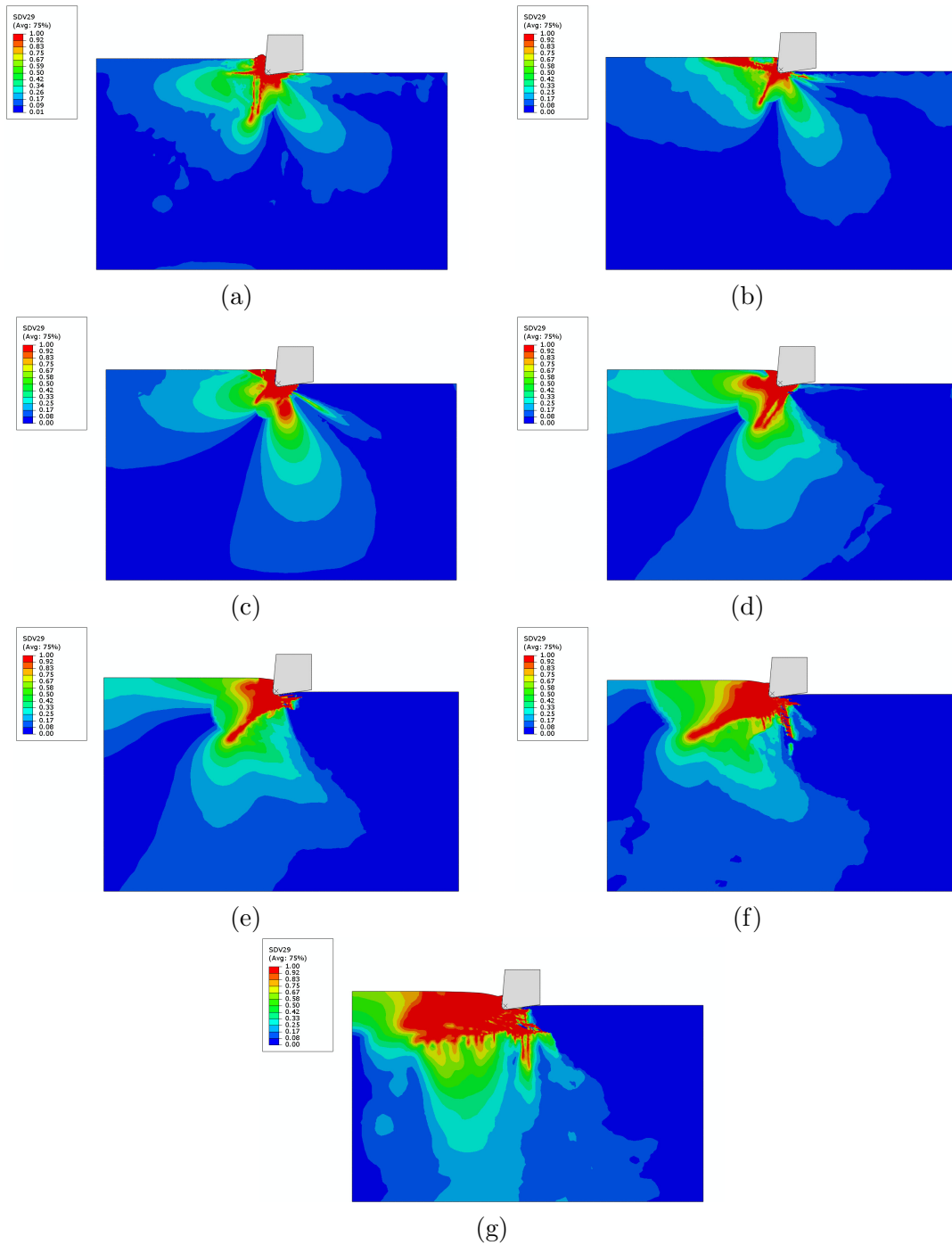


Fig. C.0.6. F_{mc} obtained for fibre orientations (a) 0° (b) 15° , (c) 30° , (d) 45° , (e) 60° , (e) 75° and 90° at final simulation time using a relief angle of 8° .

Cutting configuration with a relief angle of 10°

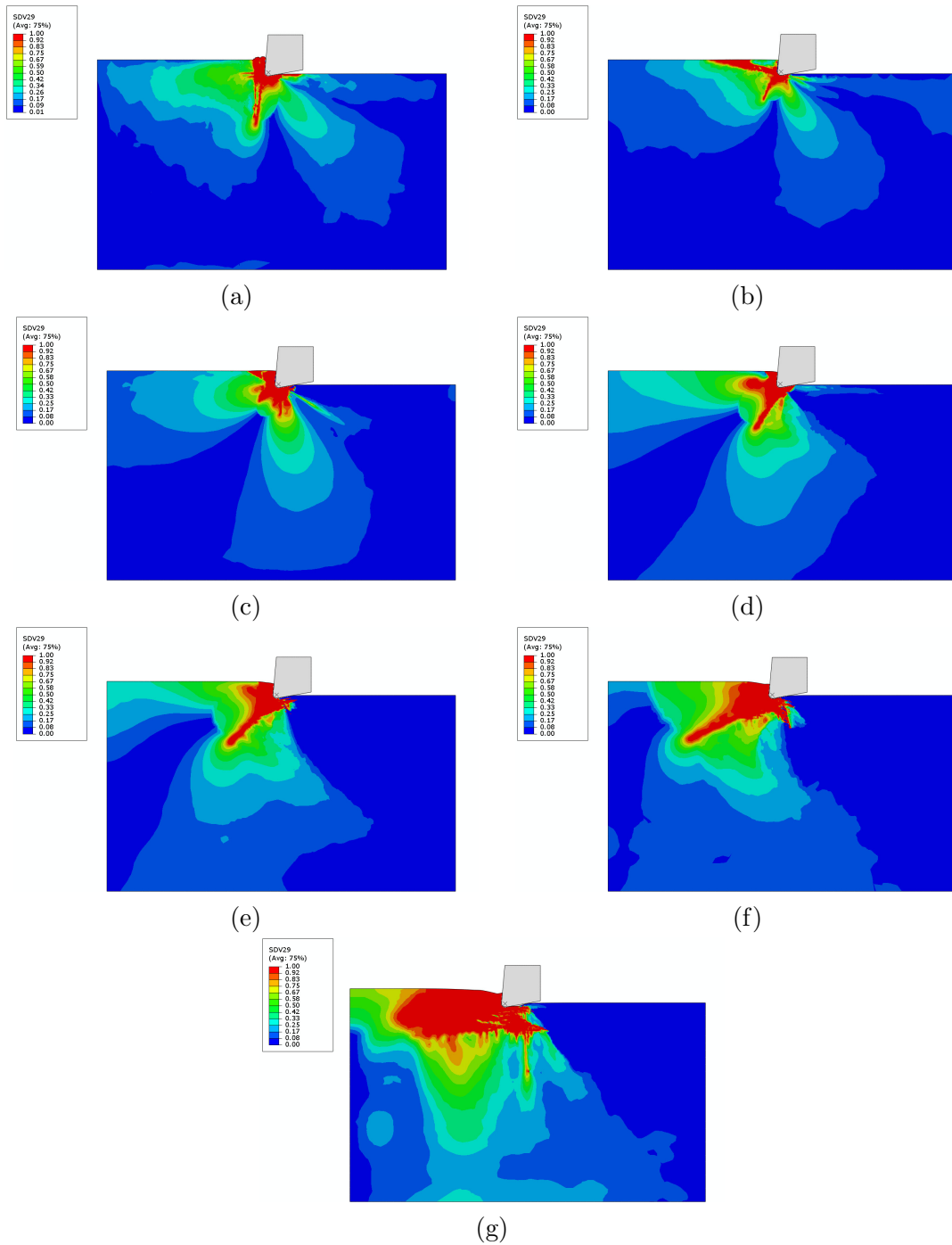


Fig. C.0.7. F_{mc} obtained for fibre orientations (a) 0° (b) 15° , (c) 30° , (d) 45° , (e) 60° , (f) 75° and (g) 90° at final simulation time using a relief angle of 10° .

Cutting configuration with a UD-CFRP workpiece

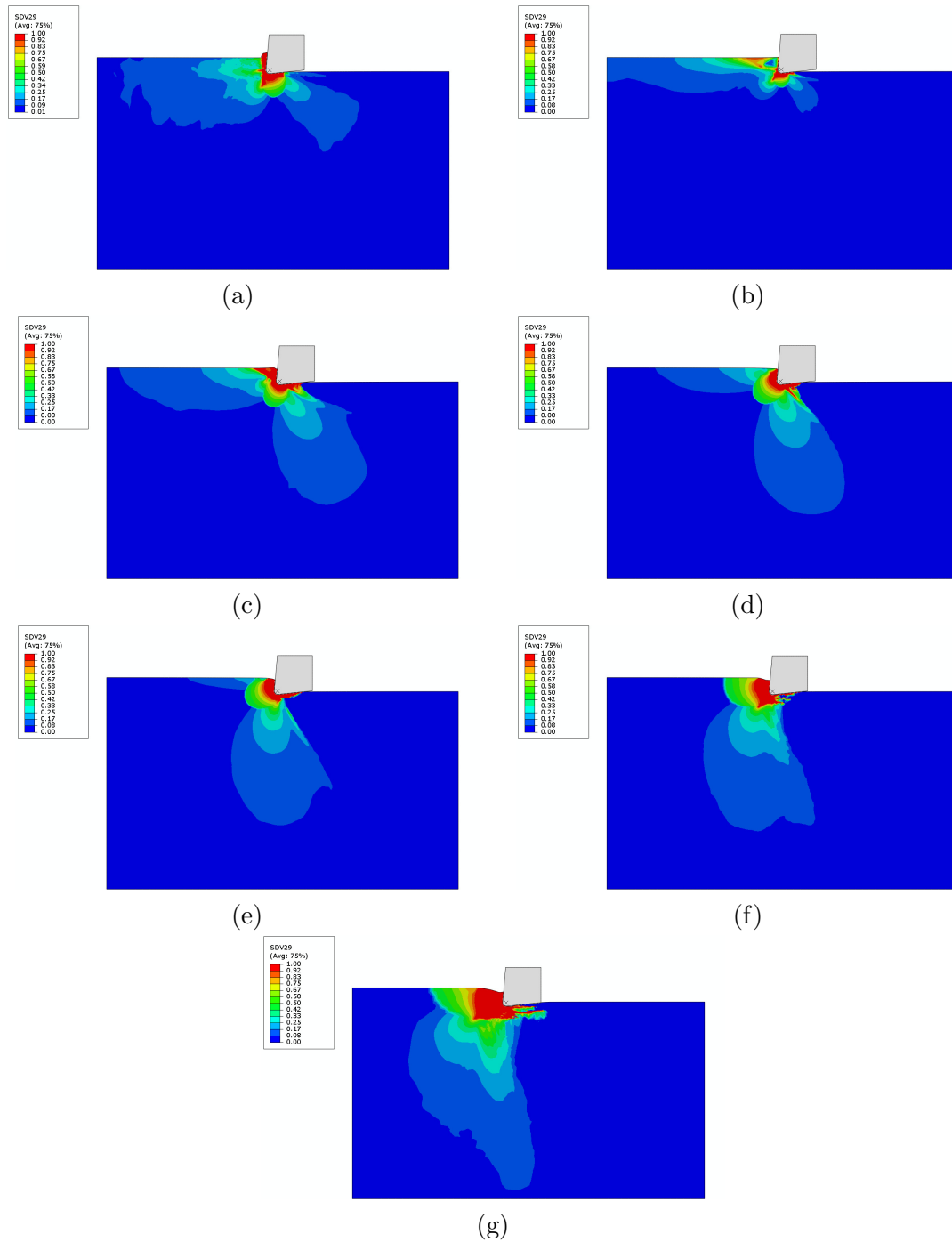


Fig. C.0.8. F_{mc} obtained for fibre orientations (a) 0° (b) 15°, (c) 30°, (d) 45°, (e) 60°, (e) 75° and 90° at final simulation time with a UD-CFRP workpiece.

Cutting configuration with a tool edge radius of $15\mu m$

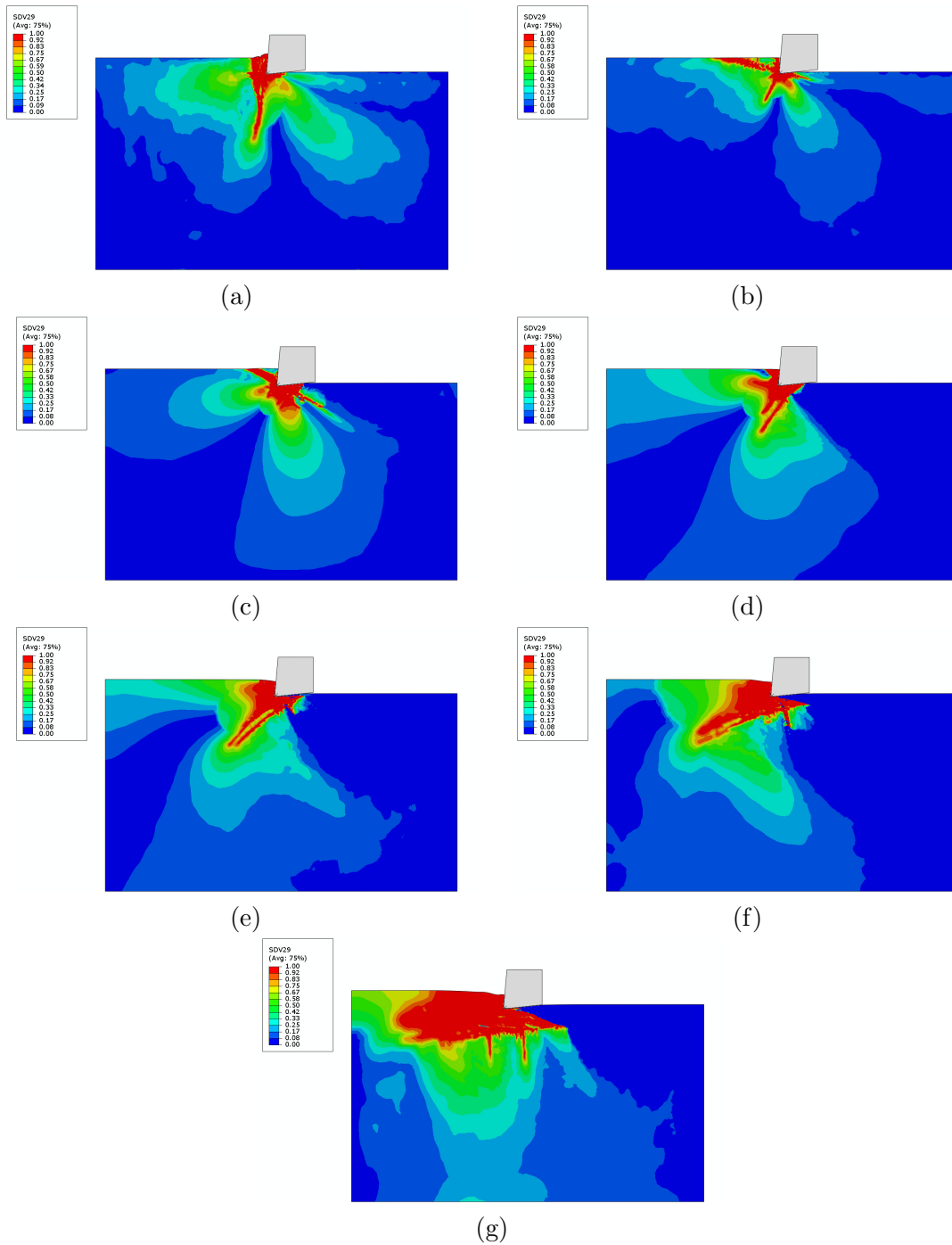


Fig. C.0.9. F_{mc} obtained for fibre orientations (a) 0° (b) 15° , (c) 30° , (d) 45° , (e) 60° , (e) 75° and 90° at final simulation time with a tool edge radius of $15\mu m$.

Cutting configuration with a tool edge radius of $30\mu m$

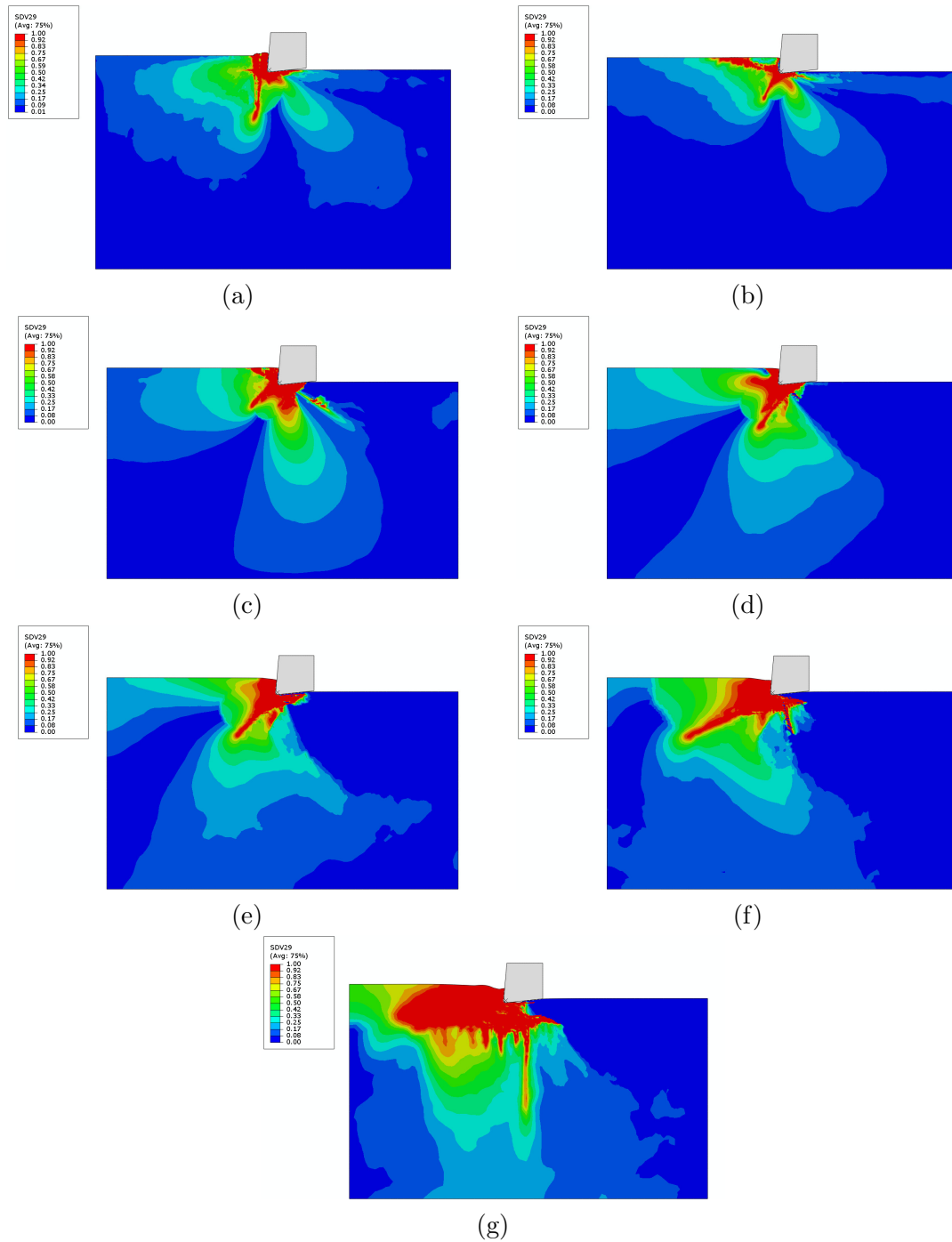


Fig. C.0.10. F_{mc} obtained for fibre orientations (a) 0° (b) 15° , (c) 30° , (d) 45° , (e) 60° , (e) 75° and 90° at final simulation time with a tool edge radius of $30\mu m$.